Experimental study and FEM of RC shear walls with internal FRP reinforcement

by

Hamid Rahman

A thesis submitted in partial fulfilment of the requirements for the degree of

Doctor of Philosophy

in

Structural Engineering

October 2020

Abstract

Earthquakes claim thousands of lives around the world annually due to the poor design of lateral load resisting systems, mainly shear walls. Additionally, corrosion of the steel reinforcement in concrete structures is one of the main challenges in the construction industry. Fibre-reinforced polymer (FRP) reinforcement can be used as an alternative to traditional steel reinforcement. FRP has several excellent mechanical properties than steel, such as high resistance to corrosion, high tensile strength, light self-weight and electromagnetic neutrality.

This thesis is about the result of experimental research incorporating testing of medium-scale concrete shear wall samples; reinforced with Basalt-FRP (BFRP), Glass-FRP (GFRP), and steel bars as a control sample. The samples are tested under quasi-static-cyclic loading following the modified ATC-24 protocol for seismic loading. The results of the samples are compared to allow a judgment about the performance of BFRP/GFRP reinforced in comparison with the conventional steel-reinforced concrete shear wall (RCSW).

The results of the conducted researches show that the load-displacement and energy dissipation graphs for BFRP and GFRP RCSWs are lower in comparison to steel RCSWs. However, the close-range FRP results provide momentum toward utilisation of the FRP as an alternative to traditional steel reinforcement to improve durability with suitable energy dissipation in the RCSWs.

Additionally, presented is the results of finite element (FE) models developed for the RCSWs utilising Ansys mechanical. Two models including “Solid65” and Microplane are developed which are capable of modelling the cracking/crushing and strain-softening, respectively. The FE results are validated with experimental results, and parametric studies are conducted on the FE models. The outcome of FE modelling show Ansys “Solid65” model can capture the hysteresis response of the samples until the failure point. And the Microplane model can simulate the strain-softening behaviour of the samples under pushover analysis. Overall the modelling outcomes show a good correspondence with experimental results, and the models are used for parametric studies.

The key findings from the experimental study show that BFRP and GFRP can be utilized as a replacement to the traditional rebars in RCSWs as it has a similar hysteresis response. The theoretical studies confirm the experimental findings of FRP reinforced shear walls under cyclic and pushover loads. Furthermore, theoretical models can be used in the parametric studies of the shear wall responses under indicated loading.

Table of Contents

List of Tables

List of Figures

List of Symbols

A_s	Area of steel reinforcement
A_h	Areas of horizontal reinforcement
A_v	Area of vertical reinforcement
c	Damping coefficient
d^{mic}	Damage evolution normalized for microplane model
d_w	Distance from the extreme compression face
E_c	Elastic Modulus
F	Applied force for iteration
F_1	Internal residual force after iteration
f_1	Biaxial crushing stress (positive) under the ambient hydrostatic stress state
f_2	Uniaxial crushing stress (positive) under ambient hydrostatic stress state
f_c	Mean compressive strength
f_{cb}	Biaxial crushing stress (positive)
f_t	Mean tensile strength and
gap	Gaping size for interface element
h_w	Height of the wall
I_1	First invariant of strain tensor for microplane model
J_2	Second invariant of the deviatoric part of the strain tensor
K1, K2	Stiffness constant for interface element Combin40
k_0, k_1 and k_2	Damage function parameters for microplane model
l_w	Length of the wall
m	Mass applied on interface element
M_s	Surface Wave Magnitude
M_b	Body Wave Magnitude
M_w	Moment Magnitude
T_c	Stiffness multiplier for cracked tensile condition
t_w	Thickness of the wall
X	Result of convergence force (F)
X_1	Result of residual force (F_1)
v	Poisson's Ratio
α^{mic}	Maximum degradation for microplane model
β^{mic}	Rate of damage evolution for microplane model
β_c	Shear transfer coefficients for a closed crack
β_t	Shear transfer coefficients for an open crack
γ_0^{mic}	Equivalent strain on which damage starts.
Φ^{mic}	Damage status for microplane model
η^{mic}	Damage function for microplane model
ε	Strain at any stress
ε_0 =	Strain at the ultimate compressive strength f_c
σ =	Stress at any strain
σ_h^a	Ambient hydrostatic stress state
σ_{xp}	Stress in x direction
σ_{yp},	Stress in y direction
σ_{zp},	Stress in z direction

Definitions and Abbreviations

ACI	American Concrete Institute
AFRP	Aramid Fibre Reinforced Polymer
AMMP	Average Maximum and Minimum Points
ASME	American Society of Mechanical Engineers
ATC	Applied Technology Council
B6	Shear wall specimen with 6 mm diameter BFRP rebars
B10	Shear wall specimen with 10 mm diameter BFRP rebars
BA6	Shear wall specimen with 6 mm diameter BFRP rebars anchored
BA10	Shear wall specimen with 10 mm diameter BFRP rebars anchored
BFRP	Basalt Fibre Reinforced Polymer
CBF	Concentrically braced frames
CED	Cumulative Energy Dissipation
CFRP	Carbon Fibre Reinforced Polymer
CFS	Carbon Fibre Sheets
CPU	Central Processing Unit
CSRCW	Composite shear wall with steel enchased profile
CVS	Comma separated values
DOF	Degrees of Freedom
ECC	Engineered Cementitious Composites
ED	Energy Dissipation
EBF	Eccentrically braced frames
EBR	Externally Bonded Reinforcement
Epicentre	Point of earth surface vertically above hypocentre (refer to hypocentre)
Exp	Experimental
FD	Force Displacement
FE	Finite Element
FEA	Finite Element Analysis
FEM	Finite Element Method
FEMA	Federal Emergency Management Agency
FRP	Fibre Reinforced Polymer
FRPRCS	Fibre-Reinforced Polymer Reinforcement for Concrete Structures
G1	Group one tested shear walls (includes i1S6, i1B6, i2S6 and i2B6 specimens)
G2	Group two testes shear walls (includes S6 and B6 specimens)
G3	Group three tested shear walls (includes SA6, BA6, GA6 and BA10 specimens)
G4	Group four tested shear walls (includes S10 and B10 specimens)
GA6	Shear wall specimen with 6 mm diameter GFRP rebars anchored
GC-6	Isopropyl alcohol surface cleanser for application of micro strain gauges
GFRP	Glass Fibre Reinforced Polymer
GUI	Graphical User Interface
HLPV	Hysteresis Loop Peak Value
HSFG	High Strength Friction Grip
Hypocentre	location below earth surface where earthquake has originated
IBC	International Building Code

i1S6	First shear wall specimens with 6 mm diameter steel rebars for pilot study
i1B6	First shear wall specimens with 6 mm diameter BFRP rebars for pilot study
i2S6	Second shear wall specimens with 6 mm diameter steel rebars for pilot study
i2B6	Second shear wall specimens with 6 mm diameter BFRP rebars for pilot study
ISIS	Intelligent Sensing for Innovative Structures
KUL	Kingston University London
LLRC	Lateral Load Resisting System
LVDT	Linear Variable Displacement Transducers
M-200 Catalyst	Liquid for quick hardening of adhesive
M-Bond 200	Strain gauge adhesive package
M-Prep Conditioner	Surface cleanser for application of micro strain gauges
M-Prep Neutralizer	Surface neutralizer for application of micro strain gauges
MDF	Micro Defect Free
MRF	Moment Resisting Frame
NAFEMS	National Agency for Finite Element Methods and Standards
NEHRP	National Earthquake Hazard Reduction Program
NSM	Near Surface Mounting
NR	Newton-Raphson
P-Delta	Gravity multiplied by the displacement
PFC	Parallel Flanged Channels
PL-60-11	Purpose built strain gauges for surface of concrete
Plate tectonic	Movement of earth plates relative to each other
POA	Pushover Analysis (application of force at top of a structure until it collapse)
PRCWP	Precast Reinforced Concrete Wall Panels
PRESSS	Precast Seismic Structural System
PS	Pilot Study
PTC	Performance Test Code
Pultrusion	FRP rebars production process
RC	Reinforced Concrete
RCSW	Reinforced Concrete Shear Wall
RSH	Rectangular Hollow Section
RS-Pro	Two-part epoxy risen adhesive for concrete surface
Richter	A scale of 1-9 to for measuring magnitude of earthquakes
S6	Shear wall specimen with 6 mm diameter steel rebars
S10	Shear wall specimen with 10 mm diameter steel rebars
SA6	Shear wall specimen with 6 mm diameter steel rebars anchored
SG	Strain Gauge
SI	System International
SPSW	Steel Plate Shear Wall
TML	Tokyo Measuring Instruments Lab
UBC	Uniform Building Code
V&V	Verification and Validation
WCEE	World Conference on Earthquake Engineering

APDL Syntax

,	Separates commands, arguments and values
!	Do not read command following this mark
ADPTKY	Uses adaptive decent methodology for iteration
ALLSEL	Select all entities
AREA	Defines area size
AUTOTS	Applies automatic time steps
BISO	Applies bilinear isotropic material properties
CEINTF	Creates constraint equation between nodes
CMSEL	Selects component of a model
COMBIN39	Interface element with nonlinear force-displacement capability
COMBIN40	Interface element with sliding, damping, gaping, mass, rotation capabilities
CONCR	Concrete material model capable of cracking and crashing
CONTA174	Contact element for surface of a 3D contact
CPT215	3D element with elasticity, stress stiffening, large deflection capabilities
DELTIM	Specifies time step size
EALIVE	Activates an element
EINTF	Creates interface element between nodes
EKILL	Deactivates an element
ELEM	Element
ESTIF	Changes an element stiffness
ET	Defines an element type
EX	Elastic Modulus
KEYOPT	Assigns key options to the element
MISO	Applies multilinear isotropic material properties
MPC	Applies multi-point constraints formulation to contacts
MPLANE	Concrete material microplane model capable of strain-softening
MATID	Default name for assigning element and material properties to the model
NEQIT	Specifies the number of maximum iterations before bisection
NLGEOM	Activates or deactivates geometric nonlinearity
NODE	Nodes
NROPT	Selects types of Newton-Raphson iteration e.g. non-symmetric.
NSUBST	Specifies number of substeps
PLCRACK	Maps location of cracking and crushing
POST1	Enters postprocessor module
R (Command)	Assigns real constant to the model (up to 6 constants)
R (argument)	Additional set of components
PREP7	Entering preprocessor module
PRXY	Poisson's Ratio
REAL	Assigns all real constant sets to MATID
RMORE	Assigns more real constant to the model (up to 6 constant each)
S (argument)	New set of components
SOLID65	3D element capable of cracking, crushing, large strain & stress stiffening
SOLU	Enter solver module

SECDATA	Defines section property
SECTYPE	Defines section type
TARGE170	Target element for surface of a 3D element
TB	Assigns material model type table to the model
TBDATA	Assigns material properties table to the model
TBPT	Assigns table data points
TEMP	Assigns temperature
TYPE	Assigns element type to MATID
UNSYM	Newton-Raphson iteration option for unsymmetrical stiffness matrices

Dedication

This work is dedicated to my family including my father, my mother, my aunt, my wife, my brother and my sisters who’re love and support encouraged me to continue my commitments in my research studies. Without them, it would not have been possible.

Acknowledgement

I would like to express my great gratitude to the director of my studies Dr Ted Donchev who's comprehensive, countless, and continuous support has made every difference to make this research possible. I would like to thank Dr Diana Petkova for enriching and enhancing this work with her invaluable and unique experiences enabling me to end this endeavour.

My sincere thanks to Dr Gul Afghan Saleh who has generously and boundlessly gifted his valuable time by advising me as an external supervisor. My ample and abundant appreciation goes to Eng. Meena Ghalib and her engineering team for continuous consulting and sharing of her enriching and enhancing engineering experiences with me throughout this study.

I would like to take the opportunity to thank Mr Daren Chapman, Ms Tracy Davies, Mr George Hopartean, and their respectful team of technical staff for their unwavering and untiring support; during the preparation of the samples, at the structural laboratory of Kingston University.

1. Introduction

1.1. General

Earthquakes claim thousands of lives around the world due to the poor design of lateral load resisting systems, mainly shear walls. Additionally, the problem of steel corrosion can be solved by alternative reinforcement of fibre reinforced polymer (FRP) bars which are more durable against corrosion, have lighter weight, reduced carbon footprint during production, and excellent mechanical properties. Additionally, nonconductive properties of internal FRP reinforcement can be useful for application in hospitals and other structures containing sensitive laboratory equipment where electromagnetic neutrality is an essential factor.

Change in the traditional design philosophy of concrete structures is needed for FRP reinforcement as the mechanical behaviour of FRP differs from the behaviour of conventional steel reinforcement. FRP materials are anisotropic and are characterised by high tensile strength and in the direction of the reinforcing fibres, which affects shear behaviour and dowel action of the FRP bars as well as bond performance. Furthermore, FRP materials do not yield, they are elastic until failure, and the design procedure must account for lack of ductility in structural concrete members reinforced with FRP bars.

Previous studies have been made on the steel-reinforced concrete shear walls (RCSWs) by many researchers proving the effective use of steel reinforcement for them (Chittiprolu and Kumar, 2014). However, the construction of shear walls in multi-storey buildings in the earthquake-prone regions reinforced with FRP bars calls for further investigation of their behaviour as a relatively small amount of research is conducted in this area.

Currently, there are areas with limited knowledge of the performance of FRP reinforcement, for example, hysteresis response, fire-resistance, durability in outdoor or severe exposure conditions, bond fatigue, and bond lengths for lap splices. These are the areas that need further research and additional information according to the ACI-440 committee reports on FRP reinforcement.

The current research investigates the behaviour of concrete shear wall internally reinforced with FRP bars under quasi-static lateral cyclic in the aspect of energy dissipation. The investigation shall be conducted by preparing and testing medium-scale shear wall specimens in the lab and utilising FE methodology to model such behaviour and conduct parametric studies.

1.2. Aim and Objectives

This research aims to investigate the behaviour of BFRP and GFRP RCSWs to identify the suitability of such reinforcements as an alternative to the conventional steel reinforcement and understand the effects of anchoring of the rebars and concrete strength on the behaviour of the RCSWs.

To achieve the aims, the main objectives of this research work are as followings:

1. To prepare BFRP and GFRP RCSW samples and test them under a seismic protocol of loading.
2. To investigate the effect of different types of FRP, and anchors on the behaviour of the samples.
3. To develop analytical models for the investigation of shear walls with innovative FRP and traditional steel internal reinforcement.
4. To investigate the crack generation patterns due to lateral forces on the shear wall specimens and models.
5. To conduct parametric studies on the behaviour of the FE models.

1.3. Thesis Outline

This thesis contains eight chapters, and this section gives a summary of each chapter's content.

Chapter 1 introduces the research with an overview, aims and objective of the work. It also gives a brief description of the contents in each chapter.

Chapter 2 provides a revision of the several past types of research in the literature conducted on the lateral load resisting system, particularly for shear walls, including experimental investigations and theoretical modelling.

Chapter 3 provides detailed information about the material properties, design and construction of the test samples, installation of the samples into the testing-rig; configuration of the system for the application of the quasi-static cyclic loading, instrumentation of strain gauges and linear variable displacement transducers (LVDTs), and configuration of data-logger and computer hardware and software for collection of information about the samples.

Chapter 4 presents an elaborated illustration and discussion of the experimental test results that are collected and analysed using tables, graphs and texts. The result of the samples tested is grouped based on the strength of the concrete and anchorage use.

Chapter 5 have an overview of the Ansys program, the fundamental principle behind the FE (Finite Element) method, FE analysis and FE procedures.

Chapter 6 consists of a thorough explanation of the FE “Solid65 model” development from geometry and element selection to material properties and FE discretisation. Additionally, analysis settings, loading and boundary conditions used in modelling are explained. Furthermore, the modelling results are presented and a conclusion is made for the chapter. The analysis type conducted in this chapter is the hysteresis response under cyclic loading.

Chapter 7 contains a detailed description of the “FE Microplane” model development and results similar to the previous chapter. The study type conducted in this chapter is the pushover analysis under the envelope of the cyclic load.

Chapter 8 provides a detailed discussion of the results and outcome of the experimental and FE modelling sections. The results are compared to the outcome of similar researches in the literature.

Chapter 9 presents a conclusion and recommendation based on experimental and modelling investigations in this study.

The last part includes a bibliography of the references used in this research study.

2. Literature Review

2.1. Earthquakes

Earth lithosphere is made up of the crust and upper mantle. The earth lithosphere is broken into plates that move against each other. When two plates of the earth suddenly move past each other, an earthquake happens. Hypocentre is the location below the earth surface where an earthquake is originated, and the epicentre is the location directly above the hypocentre on the earth surface. Where the plates meet each other, it is called the plate boundary. Plate boundaries are rough and have several faults that get stuck against each other while the rest of the plate is moving. When plates move far enough, the stuck part unsticks, and that is where the earthquake happens (Wald, 2014).

Earthquake magnitudes are measured using the Richter magnitude scale (also known as local magnitude M_L), first developed by Charles F. Richter of the California Institute of Technology in 1935. Magnitude is based on a logarithmic scale (base 10) meaning that for each whole number in the scale the amplitude of ground motion recorded by a seismograph goes up ten times. This scale means that a magnitude of 6 Richter earthquake would cause a ground motion ten times the level of ground motion due to a magnitude 5 Richter earthquake. A magnitude of 2.5 Richter or less will result in a ground motion small enough not to be noticed by many people. Richter grades can be categorised in order of effects it may have as per the following table.

Table 2.1 - Richter magnitudes, its effects and estimate number of recurrences per year [from www.geo.mtu.edu, 2014]

Magnitude	Earthquake effects	Estimated Number Each Year
2.5 or Less	Usually not felt, but can be recorded by seismograph	900,000
2.5 to 5.4	Often felt, but only causes minor damage	30,000
5.5 to 6.0	Slight damage to building and other structures	500
6.1 to 6.9	May cause a lot of damage in very populated areas	100
7.0 to 7.9	Major earthquakes serious damages	5
8.0 or greater	Great earthquakes. Can destroy communities near the epicentre	Once every 5 to 10 year time

The Richter magnitude scale makes an accurate representation of earthquakes up to 6.5, and anything over this number is progressively underestimated the actual energy release. In other words, the Richter scale is said to be “saturated” for earthquakes magnitude over 6.5 (McCalpin, 2014).

Magnitude scales such as Surface-Wave Magnitude, Body-Wave Magnitude and Moment Magnitude scales have been used in the past to improve the standard for expressing earthquake magnitude and describe larger scale magnitudes. The magnitudes that have not been able to be characterised by the Richter magnitude. In other words, overcome the “saturation” problem with the Richter magnitude scale.

Surface wave magnitude (M_s) scale measurement is similar to the measurement method in Richter magnitude except, peak waves amplitude is measured for surface waves that have a period of 20s. Surface wave magnitudes do not require a seismograph record within 100km of the epicentre, and it also saturates at an earthquake of over 8 M_s.

Body wave magnitude (M_b) is used for earthquakes measured at distances greater than 600km. This scale can be used for earthquakes at any depth; however, it saturates at magnitudes below that of a surface wave scale of 6 to 6.5 M_b.

The moment magnitude (M_w) is considered the best and for more massive earthquakes of over magnitude 8. This magnitude is measured over a broad range of frequencies present in a typical earthquake wave, unlike other magnitudes which are using a single frequency. The M_w was devised in the 1970s to overcome the problem of Richter magnitudes defining larger earthquakes, e.g., the Chilean earthquake in 1960 and the Alaskan earthquake in 1964, which both were at magnitudes over 8. The M_w takes into account the area of the fault’s rupture and slippage along the fault as well as the seismic wave records.

No matter how precise methods of measuring magnitudes is used, there will be some uncertainties involved in the determination of the final size of the earthquake. A significant number of recorded strong seismic ground motions over the past few decades indicates that characteristics of ground motions vary significantly between recording stations. The stations close to the epicentre have a magnified level of recording than farther stations. Therefore, two main regions with different types of ground motions are considered in the design, and an increased design force should be used in some cases.

Ground motions have caused disaster around the globe over the past few decades, which has resulted in the loss of thousands life and billions of properties. Table 2.2 below shows an example of the death tolls of ten earthquakes against the magnitudes around the globe. Figure 2.1 shows a picture taken at the scene of a magnitude 7.6 Richter in Taiwan in 1999 which claimed over 2.4 thousand lives.

Table 2.2 - Outlining earthquakes magnitude and death toll example around the globe [from www.earthquake.usgs.gov, 2014]

Date	Location	Deaths	Magnitude
11/03/2011	Japan 38.297 142.373	20896	9.0
12/01/2010	Haiti region 18.443 -72.571	316000	7.0
13/04/2010	Southern Qinghai, China 33.165 96.548	2200	6.9
30/09/2009	Southern Sumatra, Indonesia -0.720 99.867	1117	7.5
5/12/2008	Eastern Sichuan, China 31.002 103.322	87587	7.9
3/11/2008	Japan 38.322 142.369	28050	9
1/12/2007	Haiti region 18.445 -72.571	222570	7
9/30/2006	Southern Sumatra, Indonesia -0.720 99.867	1117	7.5
5/26/2006	Indonesia -7.961 110.446	5749	6.3
10/8/2005	Pakistan 34.53N 73.58E	86000	7.6

Figure 2.1 - Taiwan earthquake disasters 1999 [from www.earthquake.usgs.gov, 2014]

Lateral load resisting systems (LLRS) are required to resist forces on buildings due to earthquakes. Shear walls are part of LLRS and an example of failure mechanism schematics are given in Figure 2.2. The failure can be overturning, flexural, shear sliding or shear in a diagonal direction as it can be seen in Figure 2.2 (a), (b), (c) and (d), respectively. Yielding of the rebars can occur in the shear and flexural failure mechanism. To prevent the overturning of the wall a fully fixed strong bottom connection is required for a shear wall to resist the strong lateral forces applied at the top of the wall (Hosseini and Rao, 2017).

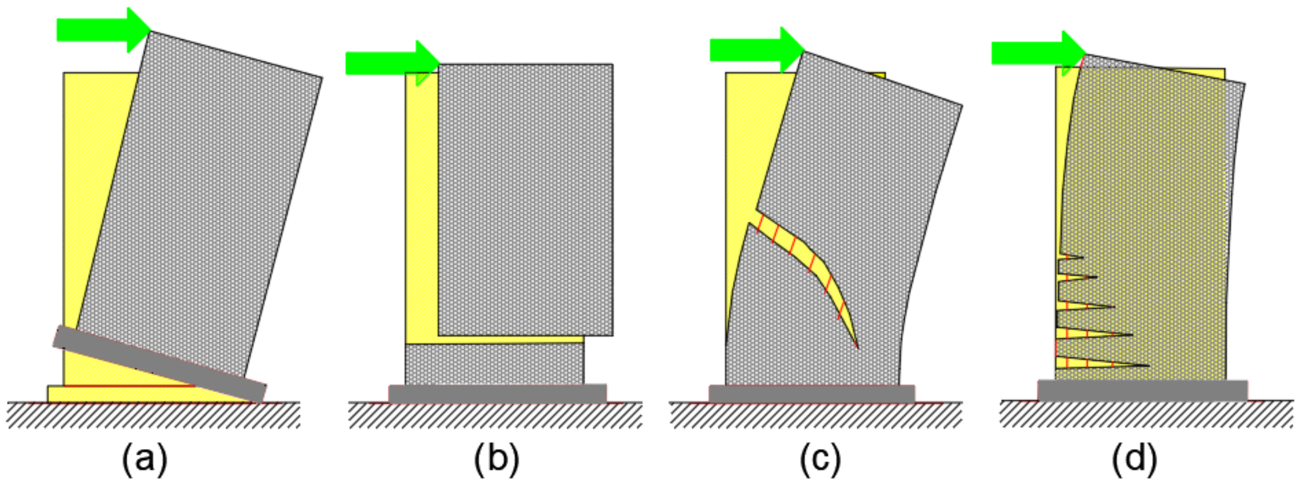

Figure 2.2 – RCSW failure mechanism (a) overturning, (b) sliding shear (c) diagonal shear, and (d) flexural (after Hosseini and Rao, 2017)

In this section earthquake mechanism, magnitudes, examples, and failure mechanisms of shear walls subject to lateral loads are described. In the next sub-chapter, different types of lateral load resisting systems are briefly described.

2.2. Lateral Load Resisting Systems

Lateral Load Resisting Systems (LLRS) are the first step in the design of buildings to resist earthquake loading as well as wind loading. Buildings can be considered as a big cantilever beam supported at one end only and the loads acting perpendicular to the beam. The LLRS shall be capable of responding to the ground motion producing lateral loads.

The system will be made up of one or a combination of the following (except the diaphragm which can only be in conjunction with the other) types of resisting systems;

- Shear Wall
    - Reinforced Concrete
    - Steel
    - Timber
    - Masonry
    - Coupled beam

  - Combination of above
- Frames
  - Moment resisting frame (MRF)
  - Braced frames
  - In-filled frames
- Tubular System
  - Tube-in-tube or Hull core
  - Bundle tubes
  - Braced tube
- Combination of the above
- Diaphragm

A shear wall is generally made up of one or a combination of the materials outlined above. Shear walls have high in-plane stiffness and are well suited to take the lateral load in tall buildings of generally about 35 stories. As shear walls do intrude the availability and desire for open spaces in a building, it is best suited to residential, and hotel type constructions, the best locations for shear walls are around elevators and stair cores. Shear walls in reinforced concrete buildings which are designed and appropriately detailed against the earthquakes have shown excellent performance in the past. The shear wall needs special detailing in high seismic regions; however, even a poorly detailed wall that had a sufficient number of reinforcement distribution were saved from the collapse.

Shear walls are easy to construct, and a prevalent choice in earthquake-prone countries to resist lateral loads. They are efficient in construction cost and a longer-term minimisation of earthquake damages to structural and nonstructural components of a building. Coupled shear walls are made up of two or more shear walls in-plane of each other coupled with stiff beams or slabs at each floor, tend to behave like a moment frame with highly stiff columns. The coupling effect reduces lateral deflection, where forces in the coupling elements can be quite large.

Frames can be either moment-resisting, braced, or in-filled type. Moment frames are made of columns and beam joined by moment resisting connections components, the lateral stiffness of which depends on the stiffness of the above components. Moment resisting frames are economical for building up to about 25 stories and are well suited for reinforced concrete construction due to the inherited continuity in the connection (Figure 2.3).

Braced frames are also known as vertical trusses, and they are exclusively made up of steel and timber; it is a highly efficient type of construction since after construction of the frames to resist prime axial loads. Very little additional material is required to add stiffness to the frame and eventually to the building, braced frames are suitable for any height, intrusion to the spatial constraints can be reduced by applying bracing to the building's perimeter frames. Bracings can be single, double, chevron, knee bracing type, and can be single or multiple stories and bays (Figure 2.5).

In-filled frames are the most common type of construction in many countries, used for buildings up to 30 stories; they are either steel or masonry infilled with concrete or masonry, which will behave much like a strut in compression. However, due to the nature of masonry infill, it is not easy to establish the stiffness and strength of this system and no standard method of analysis for infilled frames acquiring general acceptance has been identified.

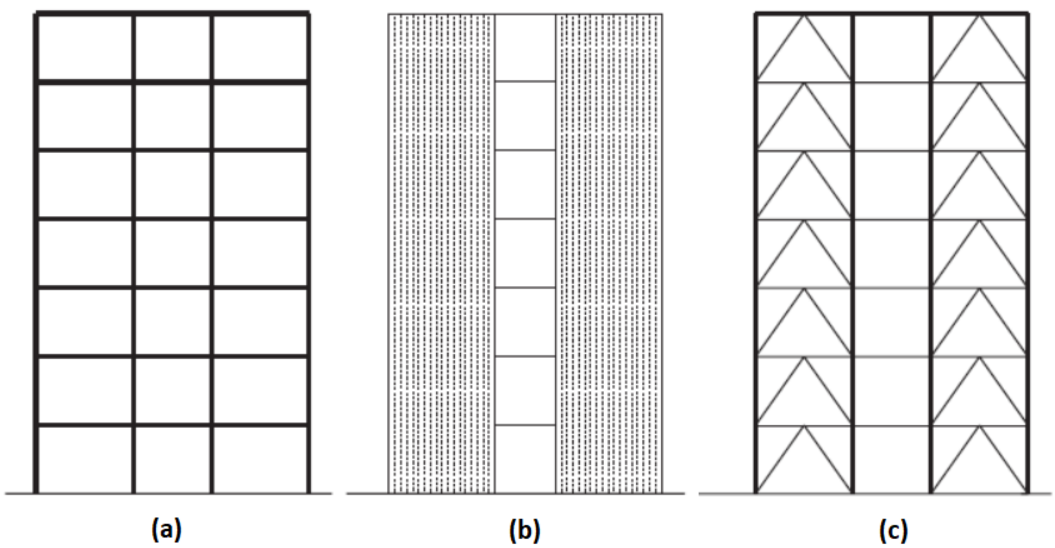

Figure 2.3 - Three common LLRS (a) MRF, (b) shear wall, (c) braced frame (Rai, 2012)

The tubular system is based on the idea of forming a rectangular tube with the perimeter of the building by closely spacing the columns connected by stiff spandrel beams creating very stiff moment frames. The frames perpendicular to the direction of the lateral force will act as the flanges. This system is easy to construct due to repetitive frames and is best applied to rectangular or circular plans, concrete or steel for buildings up to 40 stories or more. In tube-in-tube or hull-core, the inner tube is usually located around the elevator, stair, or service core. Bundle-tubes introduces additional frames acting like the web of a column reducing shear lag, making flanges more efficient. And braced tubes can utilise a large-scaled braced frame in place of a rigid frame allowing for wider column spacing and smaller spandrels (Figure 2.4 (a)).

A combination variation may include a shear wall and infilled frame or a braced and infilled frame. The shear wall and braced frame will tend to deflect in flexural and infilled frame tend to deflect in shear mode. In a combined wall-frame system, both the shear wall and the frames are constrained to act together, resulting in stiffer and stronger structure god for 40-60 stories rise structures. Roofs and floor can perform diaphragm action (Figure 2.4 (b)) in the buildings by transferring lateral loads to the frames or walls mentioned above, the moment of inertial will cause the floor or roof to bend in its plane; however, they are stiff enough to resist bending deformation on its plane or out of its plane (Quimby, 2014 and MacRae, 2014)

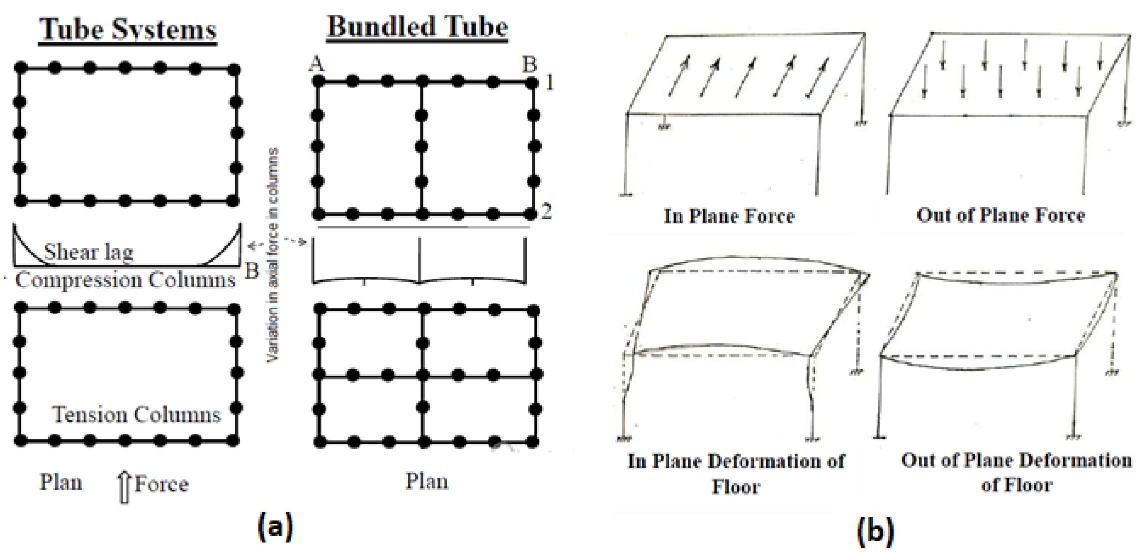

Figure 2.4 – LLRSs (a) tubular systems and (b) diaphragm action and deformation (MacRae, 2014)

Structural systems are designed in the elastic range, but these cases are few. Plastic redistribution and energy absorption are used to reduce the elastic seismic forces by as much as approximately 80%. The ductility factor can quantify the inelastic behaviour of structures. The factor is based on total hysteretic dissipated energy divided by elastically dissipated energy of a structural system at yield. High ductility is essential to ensure plastic redistribution of actions among component of lateral load resisting systems, to allow dissipation of large earthquake input energy (Elnashai and Sarno, 2008 and HAZUS 2003).

Ductile systems may resist structural damage and prevent collapse. Ductility available in a structural system less than ductility demand imposed by an earthquake will cause an imminent collapse. Elastic spectrum is the 5% damped response spectrum for each seismic level of interest, representing the maximum response of the structure, in terms of spectral acceleration, at any time during an earthquake as a function of the period of vibration.

In summary, the lateral load resisting systems include shear walls, frames, tubular systems in association with slabs diaphragm action.

2.3. Frames

Frames could be made up of steel, concrete, and wood. There are three types of frames, mainly moment resisting frames, braced frames and infilled frame, made from one or a combination of the above material. The basic form of the frame is the moment-resisting frame.

2.3.1. Braced Frames

Bracing steel frames are a common method of enhancing a frame's stiffness and strength. Bracings generally have single diagonal x-braces, k-braces, lattice, and knee bracing. The seismic resistance of steel braced frames is mainly derived from the axial force capacity of the components, much like a truss where columns are the cords, and the beam and braces act as the web members. Braced frames may be the only type of lateral load resisting system in a building, or it may be in combination with concrete or masonry walls or steel moment frames to form a dual system.

Bracing is not used in concrete frames, and instead, shear walls are employed for lateral load resistance. Bracings typically provide lower levels of stiffness and strength than shear walls, can be constructed with less disruption of the buildings, and the result has lesser weight on buildings. Braced frames can be very effective in the removal or reduction of irregularities or discontinuities such as soft-story or weak stories as well as torsional irregularities. There are two types of a braced frame including; concentrically braced frames and eccentrically braced frames.

Concentrically braced frames (CBF) resist lateral loads through a vertical concentric truss system. In CBF the axes of bracing members align concentrically at joints. Minor eccentricities due to member thickness are acceptable if accounted for in the design. CBFs are efficient lateral force resisting systems with high strength and stiffness; however, these characteristics also result in undesired seismic responses; such as attracting a larger inertia force, low drift capacity and higher accelerations. The bracings decrease bending moment and shear forces in columns to which they are connected; however, they increase axial compression in the same columns. Typical configurations of CBFs are shown in Figure 2.5.

Special CBFs are more comprehensively designed frames for seismicity. It has a special design and detailing for connections, beams and columns designed to maximise inelastic drift capacity through buckling and yielding of diagonal bracing members; however, it is used in structural steel and composite structures only (Hajjar et al. 2013).

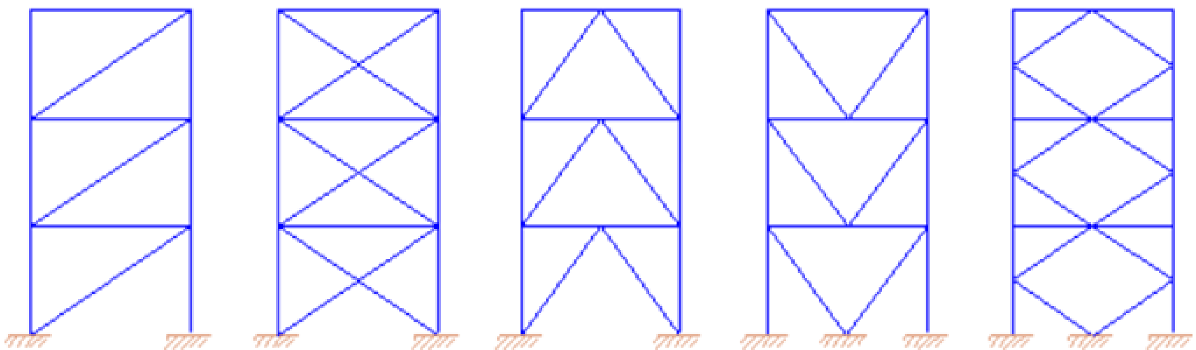

Figure 2.5 - Typical configurations of the concentrically braced frames [from www.livingsteel.org, 2014]

Eccentrically braced frames (EBF) are another type of LLRS characterised by diagonal members. The diagonal members are eccentricity located in MRFs as depicted in Figure 2.6. Eccentric bracings reduce the lateral stiffness of the system and improve the energy dissipation capacity. The lateral stiffness of the system depends on the flexural stiffness of the beams because braces are connected to the beams. The point of connection of eccentric bracings to the beam causes concentrated lateral load on the beams as a result of the vertical component of the bracing forces to the earthquakes. EBFs are known for their high-ductility and potential to offer a cost-effective solution in modern seismic regions. EBFs address the demand for lateral stiffness of the framing system with significant energy dissipation capacity to accommodate large seismic forces. The difference between a traditionally concentric frame and EBFs is that at least one end of each brace must be eccentrically connected to the frame (Tafheem and Khusru, 2013).

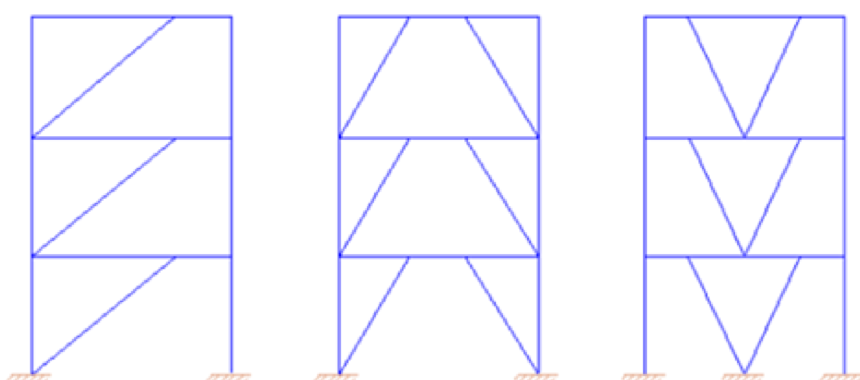

Figure 2.6 - Typical configurations of the eccentrically braced frames [from www.livingsteel.org, 2014]

2.3.2. Moment Resisting Frames

Moment resisting frames (MRFs) are often used in building between 8 to 10 stories, constructed either on the perimeter of a structural system or throughout the system. It can be used throughout the system as there is no bracing to restrict open floor space requirements. Lateral loads are transferred through axial force, shear and bending moments within its beams, columns and joints. Lateral deflection is more in moment resisting framed than as there are not braces in the system; however, the same deflection allows for ductility in the seismic design (MacGregor, 2005).

Reinforce concrete MRF is widely used in a seismic zone. The design requirement of these frames are divided into three categories based on the seismic activity location of the building; special moment frame, intermediate moment frame and ordinary moment frame. Ordinary moment frames follow standard design practice for a flexural member, columns and members in compression and bending for the buildings located in the area of low seismicity. Special moment frames are designed for areas of high seismicity. Design and detailing of concrete members are concerning increasing the building's survivability subject to a severe earthquake. Intermediate MRFs are designed and detailed for the area of moderate seismic activity such as the southern USA. The intermediate frame design was added to the code specifications after the introduction of ordinary and special MRFs to provide a guideline for structures not requiring high ductility (ACI-318, 2008).

Ductility is concentrated in areas of inelastic behaviour within the frame, which takes the form of a plastic hinge in girders or beams. The hinges absorb seismic energy and provide damping in the dynamic response of the structure. A key factor in the design of a concrete frame structure is the ability of the structure's components to develop inelastic behaviour without collapse. Failure of the frames can occur in two major forms: a soft story mechanism and a weak story mechanism. The soft-story irregularity refers to the existing of a building floor that presents a significantly lower stiffness than the others; hence, it is also called the flexible story. This effect is usually present in the modern frames buildings when a large number of rigid components are not part of the structural system. For example, masonry walls attached to the columns of the upper floor of a reinforced concrete frame structure, leaving the first story more open causing soft-first-story.

The first story is kept relatively open plan and free of walls or bracing compare to the upper floors to accommodate shops, parking or offices in modern tall buildings. The nonstructural rigid components in the upper floors limit the ability of columns to deform, modifying the structural performance of the building against horizontal forces. In a regular structure, shear forces induced by ground motion increase toward the first story. The total displacement caused by an earthquake distributes relatively homogeneously in each floor along with the height of the building and the deformation in each storey would be similar. The lower, more flexible story absorbs the bulk of the energy, and the relatively smaller remainder of the energy is distributed among upper more rigid stories. Therefore, columns of the soft floor will be subject to more extensive deformation than upper floors causing inter-story drift (Guevara-Perez 2012).

The first soft-story in the situation as depicted in Figure 2.7 (b) will be critical during an earthquake as the lowest more flexible portion in the force transmission path in comparison with Figure 2.7 (a). Stiffness discontinuity between first and upper stories might cause a collapse of the building. Examples of soft stories are evident in so-called open-floor and double-height first-stories. Open-floor in the first story is lately common in the modern residential building where structural elements are homogeneously distributed throughout the building. However, upper floors are partitioned with several masonry walls to create apartments, while the first floor is left free of partition to create vehicle parking, common area etc. Double-height first-soft-stories are desired model of modern office buildings, hotel and hospital where general public access is essential. Also, they are prevalent in mixed-use buildings where urban codes demand a higher height to accommodate shops with storage mezzanines. These stories are not flexible due to the non-existing of partitions and greater height in compare to upper floors.

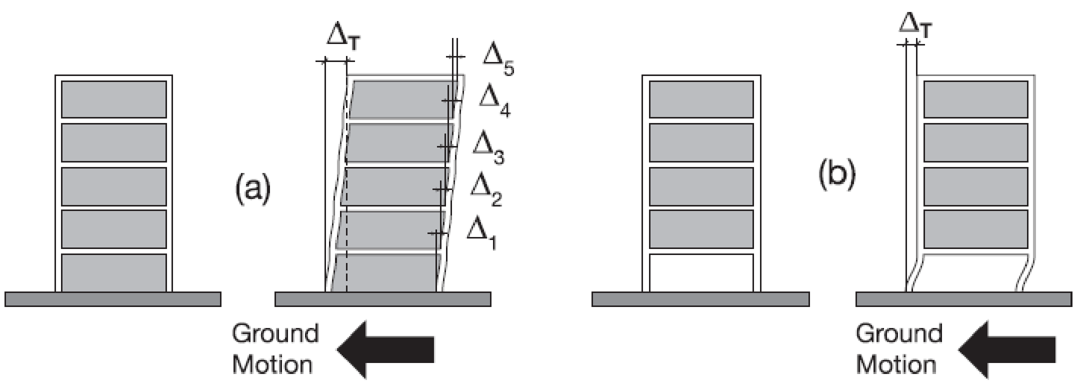

Figure 2.7 - Earthquake causing displacement in (a) regular building and (b) regular building with soft-story (Guevara-Perez, 2012)

Weak-storey is another irregularity that exists in the buildings, which means that a floor has lower lateral structural resistance than the immediate superior storey or the rest of the storeys of the building. The weakest level would be subject to more damages due to the inability to resist different types of loads (lateral, vertical and moments) exerted by ground motion. Weak-story configurations often come to existence in the hotel and hospital buildings where the first floor not only have fewer walls but also has a greater height than the rest of the storeys. Weak-story is generally come into existence by (1) elimination or weakening of seismic resistant components at first floor and (2) use of hybrid systems of the frame and structural walls, with an interruption at the second floor or intermediate floors. The irregularities can be on the first floor or middle levels. Some buildings have both types of irregularities to include a soft-story and weak-story, which make them more vulnerable to earthquakes (Guevara-Perez 2012).

2.4. Diaphragms

The diaphragm is a component of the lateral load resisting system used to transfer the lateral load to vertical structural components such as frames or shear walls; hence, the floor/roof slabs work as diaphragms placed between the vertical components. The diaphragms in the structures have double duties including (1) diaphragm to transfer lateral loads and (2) floor and roof of a building and deck of a bridge to transfer vertical loads. It can be made up of concrete such as concrete slab, metal or composite metal such as a steel deck, or plywood/oriented strand board in a timber floor. A diagrammatic view of a typical timber roof is illustrated in Figure 2.8. There are two types of the diaphragm to include; flexible and rigid type. Flexible diaphragms transfer lateral load irrespective of the flexibility of the member they are transferring the force to. Rigid diaphragms transfer load to frames or shear walls depending on their flexibility and location in the structure. To this effect, the diaphragm's flexibility affects the distribution of lateral forces in vertical components of a structure (Roskelley, 2010).

Diaphragms are assumed to be perfectly rigid in the analysis and design of three-dimensional structures under seismic loadings; however, this assumption cause discrepancy in lateral load distribution, particularly in a combined frame and wall structural system. The discrepancy is because shear walls have more stiffness and less flexibility than frames. The difference in story stiffness between adjacent vertical members diaphragm connecting the members would sustain a high shear in-plane. The high shear would cause in-plane deformation of the diaphragms (floor slab); hence, the actual force distribution to the vertical member could significantly be different from the distribution obtained by perfect rigid assumption (Huang et al. 1984 and Devarshi and Tande 2014).

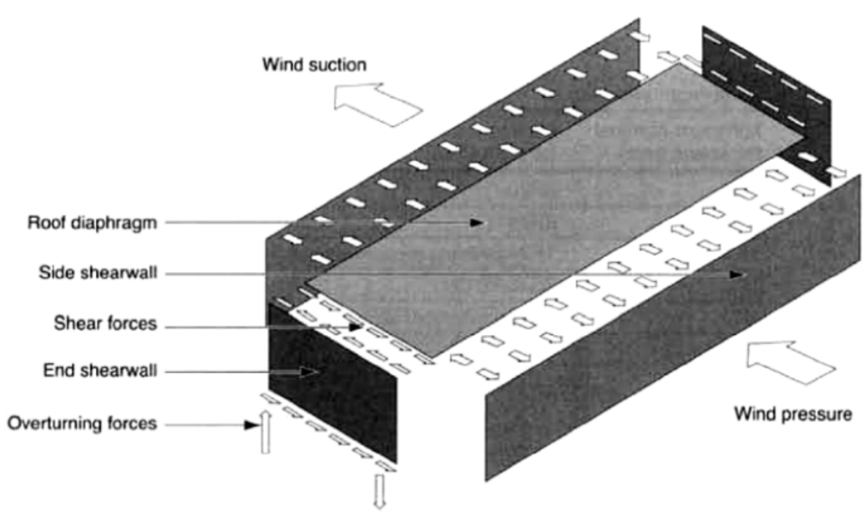

Figure 2.8 - Typical diaphragm roof illustration (Chen et al. 2013)

Design of RC building floor diaphragm is typically modelled as rigid floor diaphragm due to general provisions made in several seismic design codes where floor serve as rigid floor diaphragm with no deformation in-plane. Hence, floors are modelled with sufficient in-plane stiffness and strength as well as with efficient connections to the vertical structural elements. For a rigid diaphragm model, in-plane displacement of the diaphragm should be equal along its entire length, when subject to a lateral seismic load, which will be in turn transferred to vertical resisting elements according to their relative stiffness. For a flexible diaphragm, additional displacement along its length will happen due to in-plane bending when subject to a lateral seismic load, which can lead to overloading of structures and damage of the diaphragm as a result of high flexural stresses along its boundaries (Devarshi and Tande 2014).

Since the flexibility of the diaphragm exerts increased lateral load to vertical frames or walls, they may not be able to withstand, which can lead to a catastrophic collapse. Hence, it is essential to understand the flexibility of the diaphragm, factors causing flexure and effects on a building's seismic performance. To determine whether a diaphragm is flexible or rigid, codes specifications such as FEMA-273 (1997) and UBC-1994 sets quantitative criteria for the flexibility ratio of buildings. The flexibility ratio is the ratio of deflection of the flexible diaphragm to the rigid diaphragm.

2.5. Shear Walls

The sear wall is a vertical element of the horizontal load resisting system, resisting lateral loads parallel to the plane of the wall. Shear walls are also referred to as structural-walls in some parts of the literature as they have structural-function in a building, the only other type of vertical element resisting horizontal load is the framing system as discussed in section 2.3. Shear walls can be made up of concrete, steel, masonry, timber or thin composite walls with a length and thickness to provide lateral stiffness for the buildings. Shear walls are subdivided into coupled walls, shear wall frames, shear panels and staggered walls. Shear walls are mainly flexural members provided in high buildings to avoid the collapse of the buildings under seismic forces. Shear walls have high in-plane stiffness and strength to resist large horizontal seismic forces as well as supporting gravity loads (Chittiprolu and Kumar, 2014).

Shear walls have been used widely as a primary source of the resisting system to lateral-loads of wind and earthquake in vertical multi-storey buildings during the past sixty years worldwide. Previous research and observations show that well-designed shear walls control both structural and non-structural damages structures. Shear walls are lateral load resisting systems that also resist vertical loads, the moment about its strong axis and shear force parallel to the shear wall length. Shear walls can provide adequate strength and stiffness required for building to resist lateral loadings, and depending on the skill and precision in design, it caters for strength and ductility. The shear wall resists a large proportion of the horizontal load if not all. The shear-walls are mostly made up of reinforced concrete. They can be manipulated to resist the development of plastic hinge locations throughout the structure before failure, in addition to the resistance of lateral loads (Sittipunt and Wood, 1993).

2.5.1. Masonry Shear Walls

Masonry was usually seen as a compression type of material in the past, and the historically designed construction features such as arches, vaults and domes are evidence of this claim. The features used a compression mechanism to span spaces, and the role of masonry walls was to support floors and roofs, with little or no intention to resist lateral load due to earthquakes. By understanding the mechanical behaviour of masonry buildings from the past performance can help future analysis of the buildings. By analysing crack patterns and damages of structural masonry, the weak and strong points of structural systems can be identified. Some basic crack patterns can be generalised per Figure 2.9.

Masonry is a stiff material with almost no ductility or ability to dissipate energy, it is a heavy, and low resistance material therefor so many masonry buildings subject to severe earthquake has had severe damage or collapsed. However, there have been masonry buildings which have survived severe earthquake without severe damages or even with no damages. It should be noted that these buildings have been in the same geographic location of an earthquake, which means that these buildings must have some ductile characteristics to dissipate energy and survive in severe earthquakes in the same location (Bosiljkow et al. 2014).

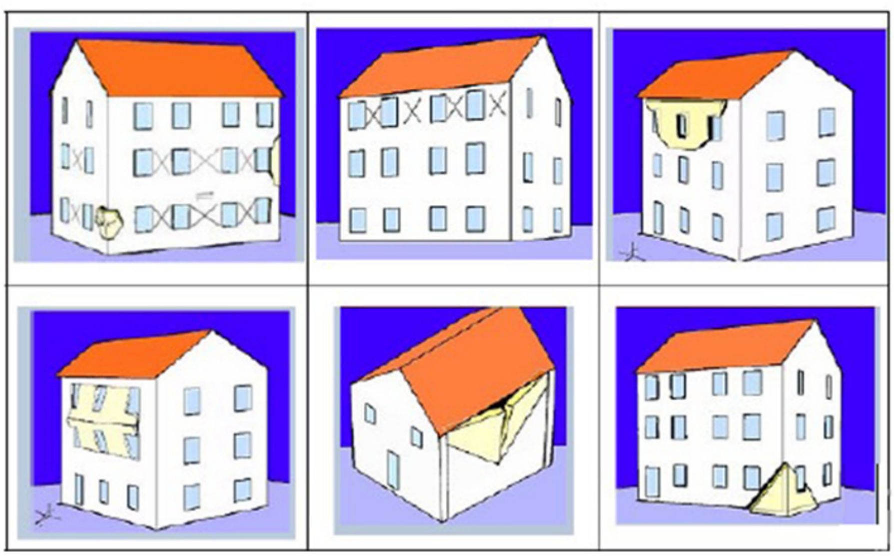

Figure 2.9 - Typical damages in masonry buildings (after Pisani, 2014)

2.5.2. Steel Shear Walls

Steel shear walls are made up of steel infill plate fixed inside steel boundary elements to resist lateral loads, also known as steel plate shear wall (SPSW). The configuration is much like the confined masonry shear wall described earlier. Vertical plate girder cantilevered from the base analogy can also be used to describe the behaviour of SPSWs; where the steel plate act as the web, the columns acts as the flanges and cross beams acts as the transverse stiffeners. Also, similar to plate girders, the SPSW optimises component performance by taking advantage of the post-buckling behaviour of the steel infill panels. In the design of this system, plate design theory will be invalid as the boundary elements have significant effects on the post-buckling behaviour of the system through facilitating relatively high bending strength and stiffness of the beams and columns (Figure 2.10).

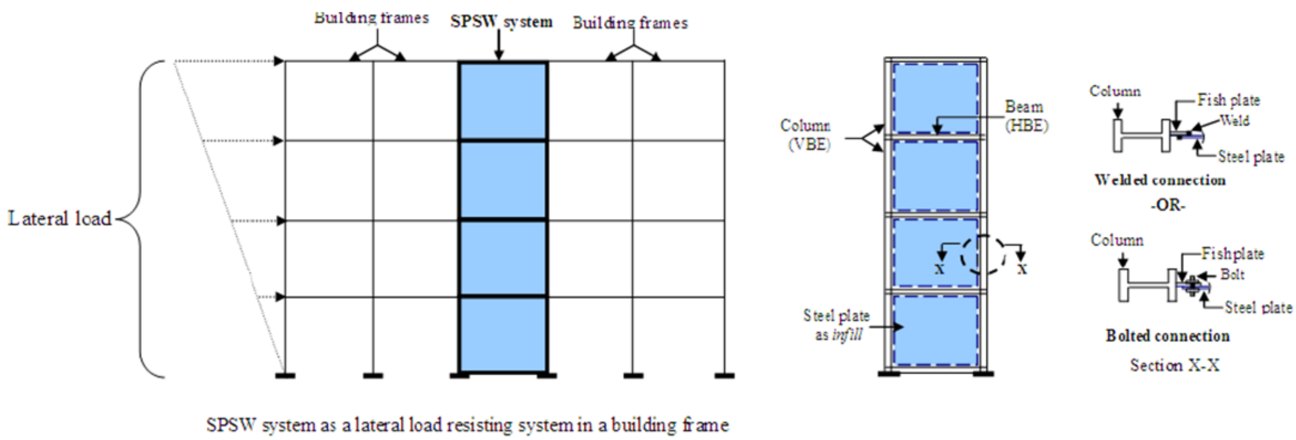

Figure 2.10 - Typical SPSW System (Ghosh and Kharmale, 2010)

Performance-based-seismic-design (PBSD) method is a general, reliable and efficient method that explicitly considers the inelastic behaviour of the SPSW. The inefficiency in design as raised earlier could be overcome by utilising the inelastic deformation capacity of the SPSW through the PBSD method, which cannot be overcome with elastic force-based or even the capacity design provisions. Ghosh et al. (2010) proposed a displacement/ductility-based design methodology for SPSW with pin-connected boundary elements. This PBSD method is based on equating the inelastic energy demand on a structural system with the inelastic work done through the plastic deformation subjected to a monotonic loading up to the target drift. The method was analytically validated by designing a four-storey steel structure with pin-connected beams with one SPSW bay. The structure was subjected to various ground motion scenarios and for different target ductility ratios.

2.5.3. Concrete Shear Walls without FRP

Reinforced concrete shear walls (RCSWs) are the most traditional type of shear walls. They are vertical plate-like reinforced concrete (RC) to provide lateral stiffness. Thicknesses of RC shear walls are typically between 150mm and 400mm depending on the building height. Shear walls are typically provided in both principal horizontal directions of a building (Figures 2.11), generally starting from the foundation level and continue throughout building height.

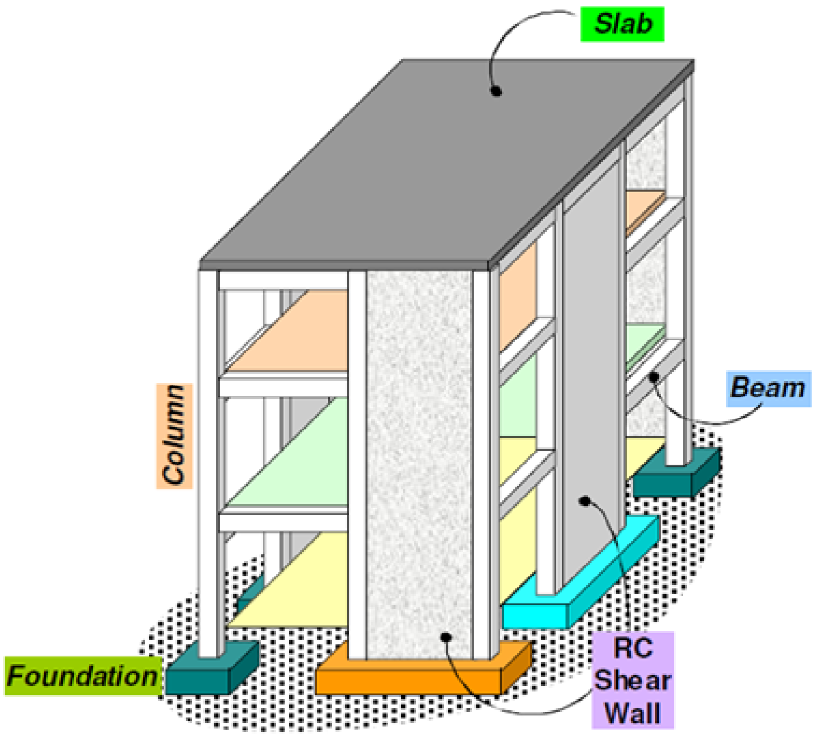

Figure 2.11 - A three-dimensional depiction of a structure with RCSWs in two principal horizontal directions (Dyavappanavar et al. 2017)

Shear walls resist lateral load like a vertically-cantilever wide beam that carry horizontal earthquake loads down to the foundation. The design of the foundation requires special attention and detailing as they are the main elements in the buildings to resist large overturning effects and transfer the load back to the ground. Shear walls in high seismic regions require special detailing; however, in the past, even buildings not especially detailed for seismic performance but had sufficient number shear walls were also able to resist collapse (Earthquake tip 23, 2014).

RCSWs are easy to construct because reinforcement detailing of the walls is relatively straight-forward and therefore easy to implement at the site for in-situ RCSWs. There are two types of RCSWs, including in-situ and precast. Precast panels are used within a concrete or steel frame as an infill plate bolted or welded to the frames respectively. RCSWs provide high strength and stiffness to the building in the direction of their orientation largely reducing lateral sway of the building; therefore, reducing structural damages and non-structural damages like a glass window and building contents. Foundation design should be carefully carried out as they are subject to large lateral forces transferred by the shear walls.

It is essential to provide a shear wall in both principal horizontal directions of a building as depicted in Figure 2.11. However, if it is provided in one principal direction of the building a proper grid of beam and columns forming frames must exist in the principal orthogonal direction of the buildings to resist horizontal earthquake loads in that direction. Shear walls must be located symmetrically in the plan of the building to avoid a twist in the building. Shear walls are more effective when located at the perimeter of the building and the farther the walls are from the centre of the building, the higher the resistance to the twisting.

Strength and ductility are the critical characteristics of shear walls to resist lateral loads. Although shear walls design procedures have been in constant improvement during recent decades, many shear walls designed before improvements are at risk of severe damage during a moderate or large earthquake due to insufficient in-plane stiffness, flexural and shear strength and ductility. The ductile response can be improved by increasing energy dissipation and adequate deformation capacity of a structural system.

In a typical floor plan, a shear wall can be located in a convenient location for construction. An example of a typical shear wall in a building plan and typical wall sections layouts is shown in Figure 2.12 (a) and typical shear wall section layouts are shown in Figure 2.12 (b). A suitable layout for the shear walls can be a location to allow lateral design loads resisting and to avoid being an obstacle to access in all areas of the buildings. The main reason why lift cores are mostly selected as a shear wall is to prevent the shear wall from affecting accessibility in the building.

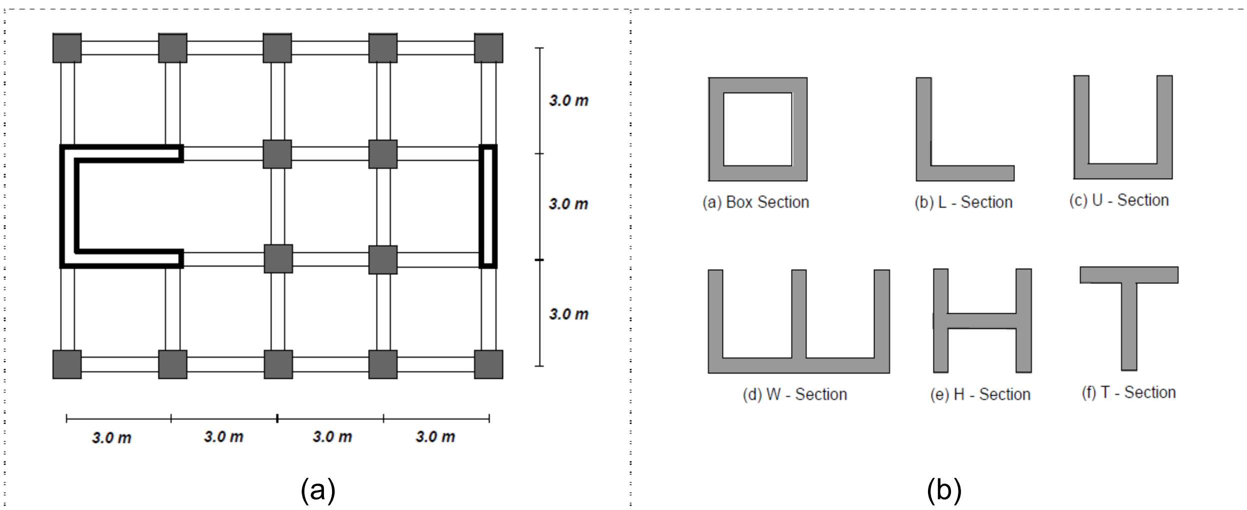

Figure 2.12 - RCSWs (a) Typical planer forms, (b) Typical sections (Akis, 2004)

RCSWs design requires special detailing for a good performance against earthquakes; however, in the past earthquakes, even buildings with a sufficient number of walls not especially detailed for seismic performance (but possessed enough distribution of reinforcement) were able to survive the collapse in earthquakes. RCSWs construction is prevalent in many earthquake-prone counties, as reinforcement detailing of the wall is relatively straightforward and easy to implement on-site. RCSWs are efficient both in terms of construction cost and minimizing earthquake damages (Murty, 2005).

The geometry of the RCSWs is oblong in cross-section if the wall contains more than one dimension in length. It means that one dimension of the cross-section will be much longer than the principal direction. Rectangular cross-section, L-shape and U-shape cross-sections are most common as shown in the picture below (Figure 2.13). Hollow reinforce concrete shafts around elevators also act as shear walls and should be taken advantage of in the earthquake design of the structures.

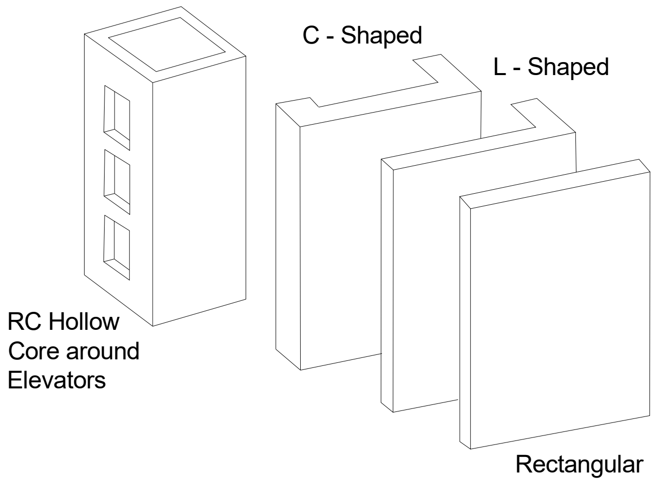

Figure 2.13 - Different geometries of reinforced concrete shear walls (after Earthquake tip 23, 2014)

The arrow indicates lateral forces acting on the edge of each floor and roof in Figure 2.14. The slab (acting as a deep beam) transfer the loads to the shear-walls A and B. The walls transmit loads to the foundation, acting like a fixed end cantilever beam. Additional loads may also act in an orthogonal direction hence demanding shear walls C and D to resist the loads in this direction. Following load could potentially act upon the wall:

i) A variable shear reaching a maximum at base
ii) Bending moment resulting in vertical tension (near the loaded edge) and compression (at the far edge)
iii) Vertical compression due to normal gravity loading from the structure

The behaviour of shear walls, concerning their typical mode of failure is influenced by their proportions as well as their support condition. Low shear walls (squat walls) having a small ratio of height-to-length are expected to fail in shear, like deep beams (Duggal, 2013).

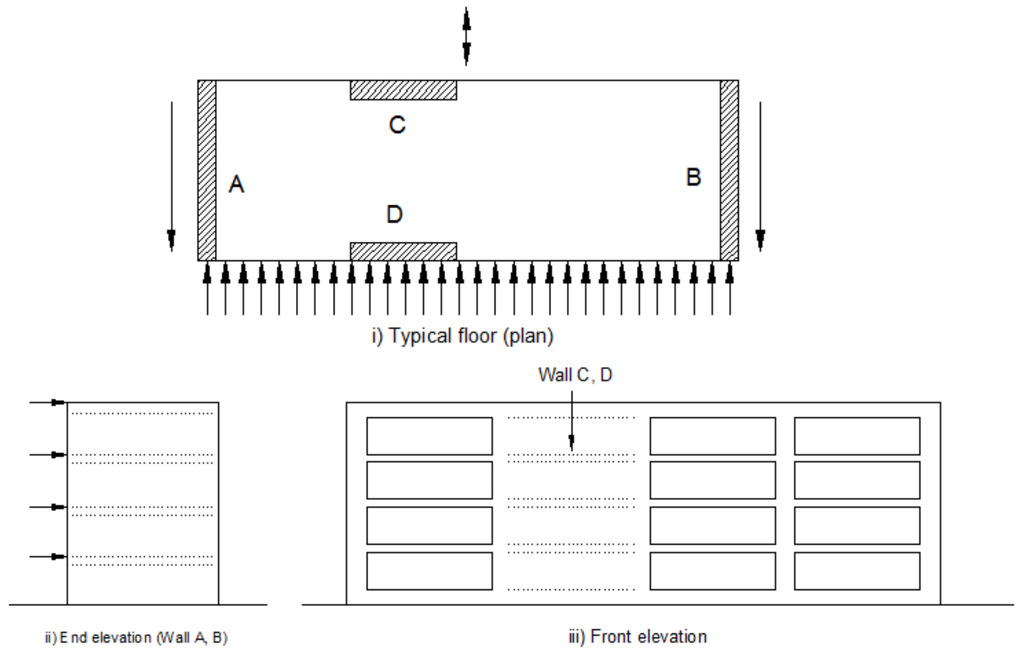

Figure 2.14 - Concrete shear wall subject to horizontal loading (Duggal, 2013)

High rise building shear walls; on the contrary, behave as cantilever beams, their strength is governed by flexure rather than shear (Figure 2.15). These walls are subject to bending moments and shear originating from lateral loads, and to axial compression (caused by gravity) hence it could be designed as a regular flexural element. The wall acting as a vertical cantilever beam which is properly reinforced for shear (diagonal tension) will be governed by the yielding of the tension reinforcement located near the vertical edge of the wall known as boundary elements. Moreover, to some degree, the vertical reinforcement distributed along the central portion of the wall.

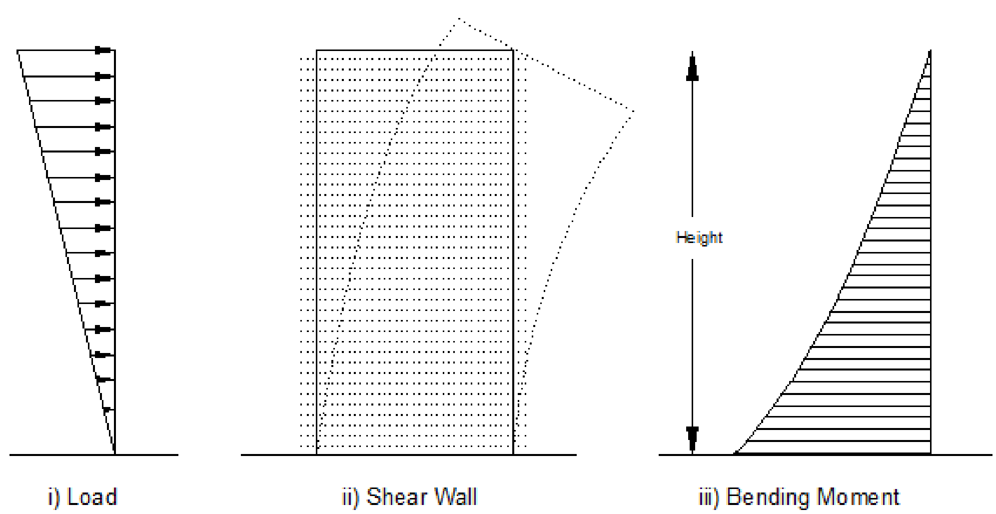

Figure 2.15 - Concrete shear wall cantilever behaviour (Duggal, 2013)

Hung et al. 2020 investigation on the behaviour of RCSWs show that shear is critical in squat walls. The squat shear walls have an aspect (height to length) ratio of less than 1.5. Flexure is critical for taller shear walls and it is further evident when uniformly distributed reinforcement is used. Figure 2.16 shows a typical shear wall of height h_w length l_w and thickness t_w. Assuming it is fixed at base and loaded horizontally at the top. Vertical flexural reinforcement of A_s is provided at the left edge, with its centroid at a distance d_w from the extreme compression face. Identical reinforcement is provided along the right edge to allow load reversal. Areas of horizontal reinforcement A_h is at a spacing of S_2 as well as the area of vertical reinforcement A_v is at a spacing of S_1 (Murty, 2005).

The ductility of tall shear walls is significantly affected by the maximum usable strain in the compression zone of the concrete. Also, concrete confinement in the form of a flanged section (Figure 2.16 iii) or a wall-return (Figure 2.16 iv) can usually be necessary to increase stability similar to I-beams where flange resists flexural stresses, and the web carries the entire shear. Inclined cracks width can be controlled with the help of vertical and horizontal minimum reinforcement distribution. The shear wall reinforcement distribution in one- or two layers depending on the wall thickness (usually over 200 mm thickness t_w would require a double layer of vertical and horizontal reinforcement).

In multi-storey buildings, the shear walls slender enough considered as cantilevers fixed at base and their seismic response is governed by flexure, hence, due to load reversals, shear wall sections necessarily contain substantial quantities of compression reinforcement. Traditionally about 0.25 per cent reinforcement is provided uniformly in both directions along with the depth of the wall; however, such an arrangement does not utilise steel efficiently because bars operate at small lever arm. In an efficient shear wall design, the flexural reinforcement is placed close to the tensile edges equally at both sides per Figure 2.16 (i) due to load reversals.

Detailing of the reinforcement will require special attention for the ductile behaviour of the shear walls. The horizontal reinforcements must be anchored near the edges of the walls where the boundary elements are; the horizontal reinforcements will act as web reinforcements for resisting the shear forces, and hence it must be anchored. Splicing of the vertical bar serving as flexural reinforcements must be avoided altogether where possible in the region with higher, yielding probability. Zone of flexural yielding may be considered to be one-sixth of the wall height, and less than a third of the vertical reinforcements must be spliced at the region.

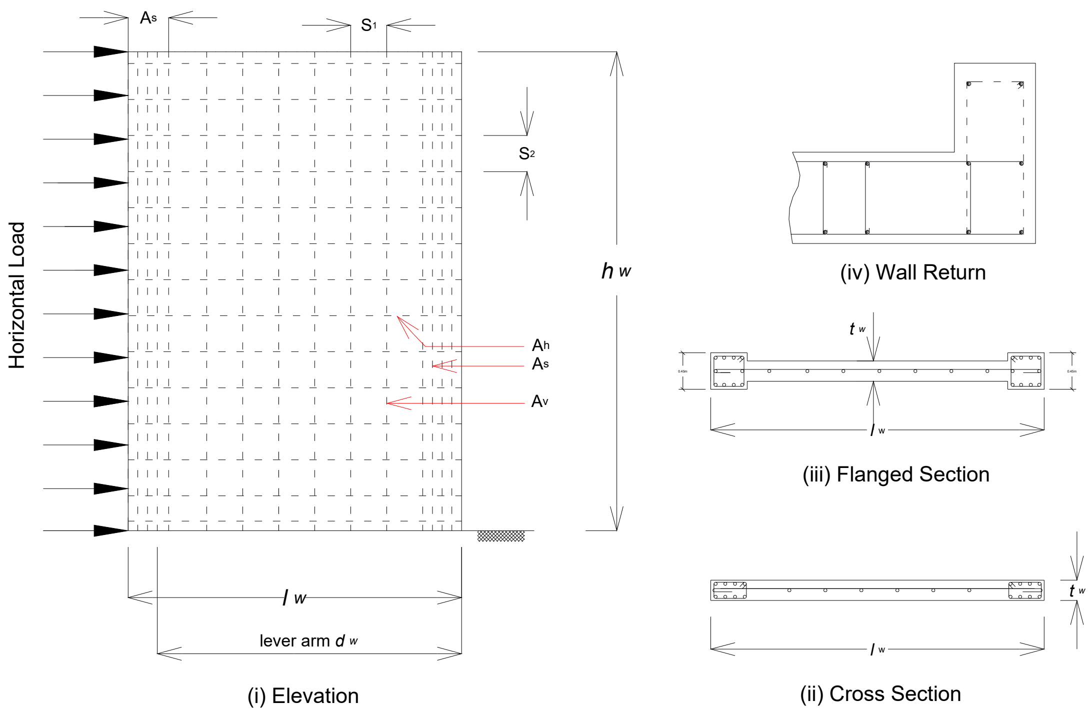

Figure 2.16 - Shear Wall Reinforcements (After Murty, 2005)

Precast concrete walls are relatively easy to manufacture, structurally efficient, durable, attractive, and provide an excellent envelope for low rise commercial and industrial buildings. Precast concrete shear walls are extremely energy efficient when it is constructed with a layer of insulation inside the wall. Lateral load resistance is another main characteristic that professionals are eager to obtain in the construction of the precast wall. In practice precast concrete wall are designed to emulated cast-in-place shear walls for the resistance of lateral loads; by using ductile vertical reinforcements coupled with splice sleeves or other devices to create continuity across horizontal joints (Bora et al. 2007).

There are other benefits to the use of precast concrete walls. The precast walls are cast in a factory-like setting; the quality of the construction is much higher than the cast-in-place structure. The factory-like setting increases the ability of the construction worker to follow design specifications and facilitate the presence of the supervisor to inspect more readily than an on-site inspector for quality control. The factory setting also makes the pre-stressing and post-tensioning duct formation easier than an on-site construction situation. Another advantage of precast concrete is the reduction of the formwork and site-labour, which results in more speed of construction on site. Installation of a precast shear wall panel is shown in Figure 2.17 below. Noise pollution, air pollution and traffic congestion decrease are the other advantages associated with the use of the precast walls (Yee, 2001).

Figure 2.17 - Precast shear wall panel being installed on-site [Source: www.housingauthority.gov.hk]

In a series of studies by Thomas and Sritharan (2004), precast construction has been described as the building process of the future because the materials are inexpensive and the factory setting of manufacturing facilitates innovative design and construction in a faster time. Advanced technology, including robotics and the use of computer-aided manufacturing, can be adapted to increase the efficiency of the construction practice and erection procedures, resulting in reduced construction costs eventually.

Limitation in the use of the precast shear wall may lead to, a design engineer discarding it as a design option and consider in-situ concrete for construction as a superior form of construction. Limitations originate from the poor performance of the precast panel in a past seismic event. This poor performance includes framed structures consisting of precast panels mainly due use of substandard material, poor construction practices and insufficient design of connections. The poor performance of precast structures attributed to substandard materials and construction practices and inadequate connection details are observed in several precast structures in the 1988 American earthquake. It is conceivable that poor performances of these structures are due to designers decrease in daring to deploy precast panels in practice for seismic subsistence of the structures (Sritharan and Vernu, 2004).

The cast-in-place emulation precast system is developed by two alternative designs as proposed by the current building codes (1) structural system that uses “wet joints” and (2) structural system based on “dry joints”. In a wet-joint system, connections are established using in-situ concrete to achieve cast-in-place emulation, and dry-joints are typically formed through bolting, welding or other mechanical means.

Wet-joints are typically provided with sufficient strength to avoid inelastic deformation within these joints, and plastic hinges are forced to develop in precast members leading to an uneconomical design. Dry-joints create natural discontinuities in the structures which are less stiff than a precast member; hence the deformations concentrate in these joints. However, these systems do not have all the economic advantages inherited in precast concrete due to the use of in-situ concrete (Ghosh, 2002).

Precast seismic structural system PRESSS which incorporates precast shear walls as primary elements of lateral load resisting system is developed in the late 1990s in the United States to unveil the potential in quality of precast concrete performance in seismic regions. The system can withstand high ground motions without much damage to the buildings. Researches in New Zealand shows that buildings with PRESSS type of construction such as the Southern Cross Hospital and Victoria University of Wellington were able to survive severe earthquakes. For example, the Christchurch earthquake magnitude 6.3(M_L) on 22 February 2011 and the Canterbury earthquake, magnitude 7.1, on 4 September 2010, without significant damages (Pampanin, 2012).

PRESSS buildings would be able to sustain high seismicity such as earthquakes happening in a thousand years. PRESSS buildings have precast walls with a series of steel strands that are anchored at the foundation and the top of the wall. In a massive earthquake as the building start shaking the walls rock in-plane direction and strands stretches a long distance without breaking, allowing a large ductility for the building. Other advantages of the PRESSS technology are that it is easy to construct, can be built with little disturbance to the neighbouring buildings, and it takes lesser time to construct than normal concrete building cast-in-place (Haverland, 2012).

The precast structural wall system tested in the PRESS programme in the USA was the unbonded post-tensioned single walls and unbonded post-tensioned jointed walls system. The unbonded post-tensioned single wall system was first studied by analytical means at Lehigh University by researchers and later on, year tests have been conducted on the single precast walls subject to lateral loads (Kurama et al. 2002 and Perez et al. 2004). Jointed precast walls were which are joined through U-shaped flexural plate-like connectors are studied by Sritharan et al. (2007). Figure 2.18 shows unbonded post-tensioned single walls units jointed together with special connectors.

The advantages of precast concrete technology are the reason for the increased use of the system. Precast concrete technology reduces the number of labours on site and making it a better-controlled environment. The advantage of the precast concrete can be summarised as below (Tolsma, 2010):

- Speed of construction; although there is a longer lead time, it reduces the cost of capital at the start and reduces the amount of nuisance to the neighbourhood.

- Small construction site; no need for storage of material, formwork etc. on-site as the panels can be installed soon as they get on site.
- Better quality; a more controlled environment of a factory can result in a better quality of the precast panels. Quality features can be; higher strength, stiffness, durability and aesthetics (better finishes).
- Environmental impact; as the panels are demountable and recyclable, they can be reused or demolished in another site other than the building's site itself.
- Reducing the risk of a contractor; panel is produced by a subcontractor at the factory hence reducing fluctuating costs of structural labour to the main contractor and provide continuity to the subcontractor.
- Reduces labour on-site; towards a better-controlled environment, and reduces the time for vertical transport of labour.

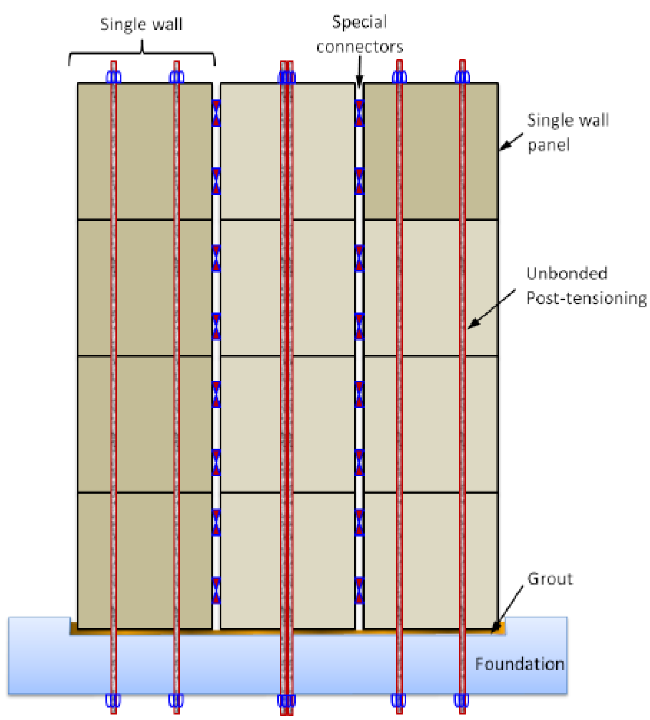

Figure 2.18 - Precast shear walls unbonded post-tensioned jointed (Sritharan et al. 2007)

Vertical transport of the precast panels can result in loss of time in high rise buildings in compare to cast-in-place concrete where the pump provides a continuous supply of the concrete throughout. The ascending and descending waste of time increase with the increasing height of the buildings. The wind is another factor that can delay the construction by making hoisting impossible on windy days. Although there will be a reduction in time for vertical transport of labour, reinforcements and formwork the vertical transport of the precast elements would be the critical path in the traditional hoisting system. Stability is another factor in the construction of the precast structural systems. Simple connections are required between the element to keep a high speed of construction. These connections are considered pinned connection hence cannot transfer moments. Precast shear walls become necessary in this case to stabilise the structures.

The connections that can resist shear, tensile and compressive forces are required for the wall to interact with other structural elements. Lack of structural continuity in precast structure in comparison with an in-situ structure means that; without proper connections, a structure built with precast components can be seen as a “house of cards”. The higher the height of the building, the larger the normal and shear stress between the precast elements. Three kinds of connection between the precast walls can be categorised (Tolsma, 2010):

- Horizontal joints between the wall elements
- Vertical joints between the parallel elements
- Vertical joints between perpendicular elements (corner connections)

Horizontal joints between the precast shear wall elements must transfer normal and shear forces. Grouted starter bar is a type of connection that has proven effective. In this type of connection, the starter bars are protruding out of the lower element, and the upper element is provided with sleeves to be filled by grout pouring (Figure 2.19 below).

Figure 2.19 - Lower precast shear wall element over protruding bars (Tolsma, 2010)

This connection has high reliability, requires no skilled labour, has relatively high fitting tolerance and can carry over the full steel stress of the starter bars. Tensile forces in the joints are transferred by protruding bars, but since the bars are in insignificant numbers, the tensile capacity can be ignored.

Mortar joints transfer the compressive forces in the joints, and the strength of the normal stiffness of the mortar is comparable with the normal stiffness of the adjoining concrete. Shear stress in the joint depends on the normal stress in the joint. Eurocode 2 section 6.2.5 estimates the design shear resistance of the horizontal joints as a function of; the roughness of the interface between the adjoining panels, tensile strength of the steel, stress per unit area, reinforcement/joint area ratio and the angle between reinforcement and the joint (FIB, 2008).

Vertical joints between parallel elements have many types; the most common methods of connections are depicted in Figure 2.20 below. In the diagram (a) and (b) the connection are concrete-filled reinforced vertical joints and form a continuous connection. In the diagram (c) and (d) are welded vertical joints which form a discrete connection. Both concrete-filled and welded connections are labour-intensive and delay constructions. Concrete filled connections have high shear strength but need time for concrete to be hardened. Welded connections have low shear capacity but can transfer forces immediately after welding. The shear stiffness of the connections is indicated in Table 2.3 below.

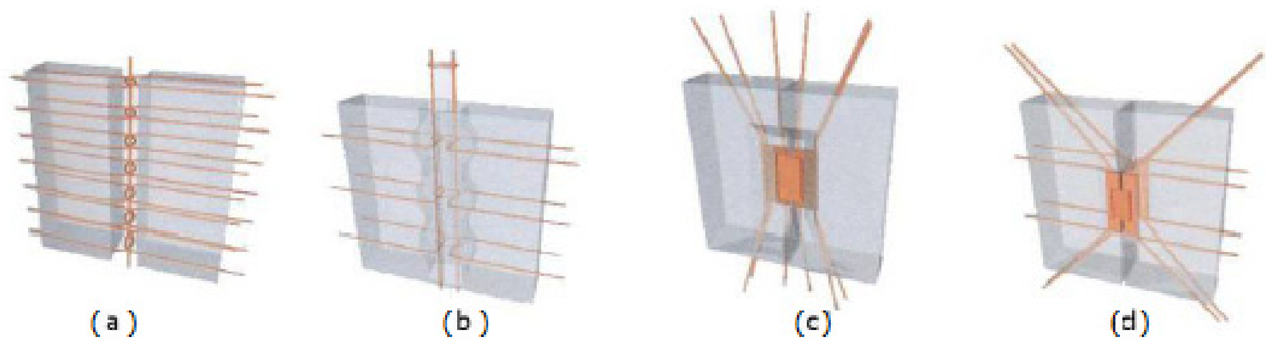

Figure 2.20 - Vertical joint between precast concrete shear walls (Tolsma, 2010)

Table 2.3 - Shear stiffness for vertical joints (Falger, 2003)

Diagram	Vertical Joint Description	Shear Stiffness K (MN/m^3)
a	Concrete filled reinforced with plain joint faces	1310
b	Concrete filled reinforced with dented joint faces	3600
c	Welded cast in steel plates	560
d	Welded cast in UNP profile	900

Vertical joints between perpendicular precast shear walls are designed to transfer shear forces at corner connections for efficient lateral stiffness of the structures. The connections along the vertical joints must be able to resist shear forces to be able to contribute to stabilising the structure. Corner connections can be of an interlocking system between the two perpendicular precast shear walls. Although, the interlocking system is used frequently in the past in the corner connections; the structural behaviour of the interlocking system is not known (Tolsma, 2010).

2.6. Shear Walls with FRP reinforcement

Fibre-reinforced polymer (FRP) is a more recent material used in the construction industry in comparison to other building materials such as masonry, timber, steel and concrete which have been around in the construction industry for a very long. FRP has been used in aerospace and marine application over the past 50 years, and recently it has found its place for application in the construction industry. Additionally, it has considerable potential for a broader application in the construction industry. Its first uses in the construction industry were the application in small building components such as dormers, windows, canopies and doors; however, new methods are the application in structures and even complete buildings (Kendall, 2014).

FRP applications to the concrete structures could be external or internal on the concrete structures. External-reinforcement applications are used to repair and strengthen reinforced concrete structures, and internal-reinforcement or prestressing elements are used in special projects to combine material strength and durability characteristics. Several national and international guidelines have become available over the past few years for the design and application of the FRP-strengthened and FRP-reinforced concrete structures. The later researches, investigations and progress clearly illustrate the extent of interest in this novel material in the construction industry. Therefore, the concrete reinforcement with FRP material can be split into two categories; (Matthys and Triantafillou, 2013).

- External reinforcement
- Internal reinforcement

Externally bonded reinforcement of the FRP to the concrete is the most common type of application of the FRP to the concrete structures. FRP is bonded to the structures as means for repairing, strengthening and retrofitting structures. FRP bonding has become more popular in the upgrading of structures due to its qualities such as; high strength, low weight, excellent durability and ease of application. FRP is externally applied to the concrete structures roughened surface in the form of an FRP sheet or FRP plate by adhesive generally epoxy (Figure 2.21 (a) and (b)). Other forms of external reinforcements are; prestressed externally bonded reinforcement, near-surface mounted reinforcement and use of textile-reinforced mortar overlays.

(a) (b)

Figure 2.21 - External bonding of FRP (a) sheet (b) laminates to concrete structures [from http://hughesbros.org, 2014]

Internally reinforcement of the concrete structures is achieved utilising FRP bars or rarely prestressing elements which are GFRP and CFRP respectively. FRP bars are best applied in a specific area for better strength, durability or non-metallic necessity and not as a general alternative to steel rebars (Figures 2.22 (a) and (b)). These specific areas could be structural components subject to environments leading to severe durability issue, building elements that need to be electromagnetically neutral, e.g. hospitals with magnetic resonance imaging equipment and other. FRP reinforcing bars offer several advantages over the traditional steel reinforcement because the FRP bars are non-corrosive and some are nonconductive. FRP bars have unique physical and mechanical behaviour of the innovative FRP material versus regular steel specific guidance on engineering and construction of the concrete structures reinforced with FRP bars are necessary (ACI-440, 2006, ACI-440, 2015).

(a) (b)

Figure 2.22 - FRP reinforcement bars (a) a winery in British Colombia 1998 (b) a bridge deck Lima Ohio 1999 (ACI-440, 2006 and ACI-440, 2015).

2.6.1. FRP Material

FRP material has been used for several decades in aeronautical, aerospace, automotive, marine, submarine and other fields. The first structural use in the construction industry date back to the 1950s when GFRP was first investigated for application; however, it was in the 1970s when the first application in structural engineer emerged, and its superior characteristics over epoxy-coated steel were recognised (Design Manual, 2007).

FRP material is made up of two constituents, including the fibre and the matrix. The fibres perform as reinforcements embedded by the matrix, which is a polymeric resin. The proportion of the fibres against the matrix must be at least 55 per cent for FRP bars and 35 per cent for FRP grids. The final quality and mechanical property of the FRP products depend on, the fibre quality, orientation, shape, volumetric ratio, adhesion to matrix and manufacturing process. Manufacturing is the most crucial element in the production of the fibres because simply mixing fibres with matrix does not guarantee a quality product; the same fibre-matrix volumetric ratio FRP material can differ significantly in their final property. Other additives such as curing agents, diluent agents, coupling agents, release agents, initiators, hardeners, promoters, catalysts, UV agents, fire retardants, wetting agents, foaming agents and pigments may be added to the fibre-matrix mix (ISIS, 2006).

Fibres are strong, stiff and lightweight, that is why they are incorporated in the FRP composites. Desirable structural and functional requirements of the fibres in composites are:

- The high elastic modulus for efficient use of reinforcement
- High ultimate strength and convenient elongation at tensile fracture
- Low variation of strength between individual fibres
- Stability of properties during handling and fabrication
- Uniformity of fibre diameter and surface
- High toughness and durability
- Availability in suitable forms and acceptable costs

FRP composites can be made with several types of fibres together with the resin matrix. The physical and mechanical properties of the different types of fibres vary significantly from each other. The most common types of fibres in the fibre-matrix composite that constitutes an FRP material are:

- Glass
- Carbon
- Aramid
- Basalt

Glass fibres are the most commonly used reinforcing fibres. There are three types: of glass fibres, including E-glass, S-glass and AR-glass. E-glass has a high amount of boric acid and aluminate which make them low alkali resistant. S-glass is stronger and stiffer than E-glass; however, it is not resistant to alkali. S-glass is more expensive than E-glass; hence, S-glass is less prevalent, albeit possessing more strength and stiffness than E-glass. Alkali-resistant (AR) glass fibres are produced by adding zirconium.

Carbon fibres are made up of pitch or polyacrylonitrile (PAN) raw materials. Pitch based fibres are made from refined petroleum or coal pitch; the pitch is passed through a thin nozzle and stabilised by heating. PAN-based fibres are made from polyacrylonitrile which is carbonised through burning. Diameters of pitch-based fibres are larger than PAN-based fibres. Pitch-fibres offer general-purpose, high-strength and high-elasticity materials, and PAN-based fibres are high strength and elasticity materials. Carbon fibres exhibit high specific strength and stiffness. They are highly resistant to aggressive environmental factors; the tensile modulus and strengths are stable as temperature rises. Carbon fibres behave elastically to failure and fail in a brittle manner. The most important disadvantage of carbon fibre is its high cost. They are 10 to 30 times more expensive than E-glass.

Aramid fibres have anisotropic structures giving higher strength and modulus in fibre longitudinal direction. The diameter of the fibre is around 12 μm. its response is elastic in tension but plastic, non-linear and ductile in compression. It exhibits good toughness, damage tolerance and fatigue characteristics. It shows a significant degree of plasticity in compression when subjected to bending. There are many manufacturers under various brand names producing Aramid fibres and Kevlar is a popular type of aramid fibre. The compressive strength of Kevlar fibre is less than 20 per cent of its tensile strength. It is brittle in tension but ductile in compression; which absorbs a large amount of energy and impact resistance. This type of behaviour is not observed in Glass or Carbon fibres.

Basalt fibres are single-component material obtained by melting crushed volcanic lava deposits of basalt rocks. They have better physic-mechanical properties than glass fibres. Advantages of basalt fibres are fire resistance, acoustic insulation, vibration isolation and resistance to the chemically active environment. They have a melting point of 1450°C and a working temperature of 982°C, making them ideal for application requiring fire resistance. The use of basalt fibres to concrete structures as reinforcement is still under development. This fibre is cheaper than carbon fibres.

Matrix element of the FRPs can be regarded both as structural and protection component. Generally, a polymer is called resin during the process and matrix after it has cured. The primary function of the matrix is to bind the fibres together, distribute loads between them and protect fibres from environmental corrosion and mechanical abrasions. It accounts for about 30-60 per cent volume of FRP and affects both the mechanical and physical properties of the final product. There are two types of matrices, including; thermosetting and thermoplastic, the first type is more common than the last one. Epoxy resin, polyester and vinyl ester are the most common type of matrices used in reinforcing fibres to make FRP. They are thermosetting polymers with excellent processability and chemical resistance. Epoxies have better mechanical properties and durability than polyesters and vinyl esters; however, epoxies are more expensive.

Table 2.4 - Properties of typical FRP material (FIB, 2007 and CIRIA, 2004)

Fibre type		**Density**	**Tensile strength**	**Young's modulus**	**Ultimate tensile strength**	**Coefficient of thermal expansion**	**Poisson's coefficient**
		(kg/m3)	**(MPa)**	**(GPa)**	**(%)**	**(10^{-6}/°C)**	**NA**
GFRP	E-glass	2500	3450	72.4	2.4	5	0.22
	S-glass	2500	4580	85.5	3.3	2.9	0.22
	AR-glass	2270	1800-3500	70-76	2.0-3.0	-	-
CFRP	High modulus	1950	2500-4000	350-650	0.5	-1.2	0.20
	High strength	1750	3500	240	1.1	-0.6	0.2
	Ultra-high strength	1910-2120	2600-4020	440-640	0.4-0.8	-1.1	-
AFRP	Kevlar 29	1440	2760	62	4.4	-0.2	0.35
	Kevlar 49	1440	3620	124	2.2	-0.2	0.35
	Kevlar 149	1440	3450	175	1.4	-0.2	0.35
	Technora H	1390	3000	70	4.4	-0.6	0.35
	SVM	1430	3800-4200	130	3.5	-	-
BFRP	Albarrie	2800	4840	89	3.1	8	-

Fibres of different types all show a linear behaviour under tensile loading until failure without showing yield, as indicated in Figure 2.23 below. Carbon, aramids are anisotropic materials and glass, basalt fibres are isotropic materials. Anisotropic materials have different mechanical and thermal properties in the main direction in comparison with their transverse direction. In contrast, the properties of isotropic fibres are similar in the main or the transverse directions (Gay et al. 2003).

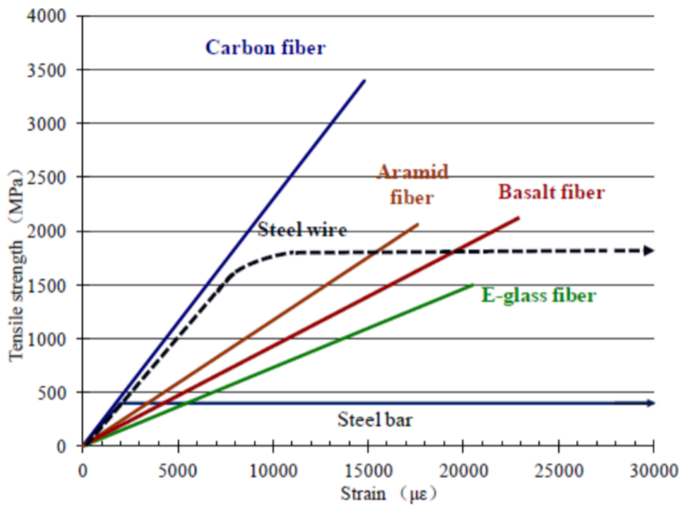

Figure 2.23 - Graphs showing tensile strength of different FRPs (ElSafety et al. 2018)

FRP materials are produced through three main processes; namely, pultrusion, braiding and filament winding. Pultrusion is common for making profile which is constant or nearly constant such as FRP bars. Braiding is the interlocking of two or more yarns to form an integrated structure. Filament winding is a process whereby continuous fibre is impregnated with matrix resin and wrapped around a mandrel. In pultrusion fibres are drawn from creels, through a resin tank where they are saturated with resin, and then through several wiper-rings into the mouth of a heated die. The speed of pulling is predetermined by the curing time need before applying dies. The surface of the bars is braided or sand-coated to have a better bonding with the concrete. Pultrusion process is shown in Figure 2.28.

Commercially available products nowadays are illustrated in the pictures complied in Figure 2.35 below. The products can be applied to reinforce the concrete structural component externally or internally. Bars and grids are shown in Figure 2.24 (a), (b), (c) and (d) are used for internal reinforcements whereas; fabrics, laminates and strips are shown in Figure 2.24 (a), (e) and (f) are used for external reinforcements.

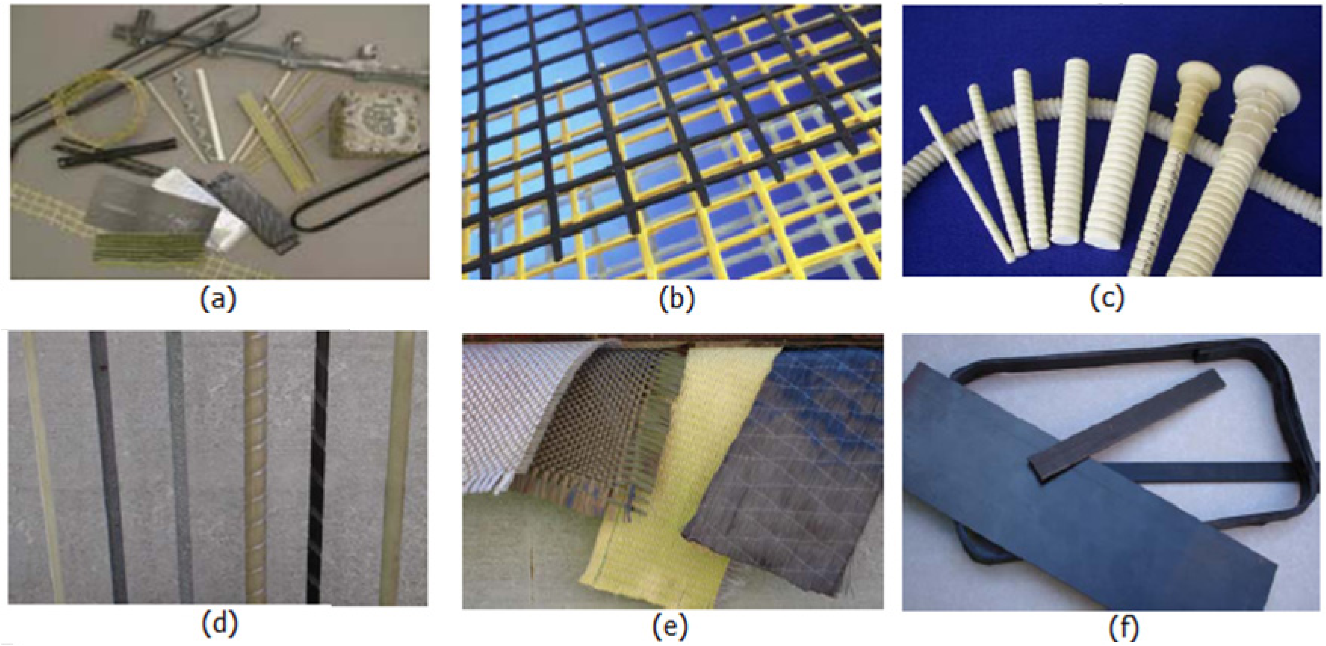

Figure 2.24 - Types of commercially available FRP (a) products, (b) grids, (c) rebars type one, (d) rebars other types, (e) fabrics, (d) plates and strips (after FIB, 2007).

Successful use of the FRP composites in many other industries such as aviation, automotive and naval resulted in the transfer of civil and structural application in the construction industry. FRPs are impacting the concrete industry by their use as internal and external reinforcement for concrete members. FRP provides an alternative better reinforcement in areas where environmental corrosion resistance or electromagnetic neutrality is required, such as seawater or hospitals (Feeser and Browen, 2005, ACI-440, 2006 and ACI-440, 2015).

In this study BFRP and GFRP rebars are selected mainly for the following reasons; (a) Access to the FRP material (courtesy of MagmaTech and Engineered Composites), (b) GFRP rebars dominating the rebar market made from FRP rebars with e.g. 85% of the market in 2015, and (c) BFRP rebars are a low-cost substitute to GFRP rebars due to large availability and easy extraction (Pulidindi and Prakash, 2017).

2.6.2. FRP External Application in Shear Walls

Retrofitting and repair of RCSWs strengthening techniques by external application of the FRPs to walls has been reported in the literature by using different kinds of materials such as steel, concrete, shape memory alloys and FRPs to improve the walls strength, stiffness, ductility or a combination of these. However, FRPs have attracted an abundant amount of attention, in the past few decades due to durability, strength, lightweight, ease of application.

The need for retrofit or repair of a shear wall stems from the requirement to improve or restore the strength of the RCSW, respectively. Improvement of the strength need arises due to a concurrent requirement for upgrading the seismic performance of the walls to meet the safety requirement of modern seismic design code. On the other hand, the restoration of strength requirement arises due to the necessity to repair and recover loss of strength due to damages that have occurred to the walls by severe earthquake lateral loads (Tremblay et al. 2001).

The strengthening techniques of the RCSWs with FRP reported in the literature include externally bonded reinforcement (EBR) and near-surface mounting (NSM). In EBR the FRP sheet or plate is attached to the surface of the walls. In NSM a groove is cut in the surface of the RC shear wall, and FRP plates or bars are inserted and glued inside the grooves (Bilotta 2011 and Bilotta et al. 2011)

The material selection for EBR strengthening is an essential process as every system designed for the fibre and resin to work together is unique. This uniqueness means that the resin system for one strengthening system will not work automatically for another system. Resin system for bonding well with fibre system will not necessarily be a good bond to the concrete surface. Today there are several types of FRP strengthening systems as outlined below (FIB, 2001):

- Wet lay-up systems
- Prefabricated elements
- Special systems (e.g. automated wrapping, prestressing etc.)

Wet lay-up system refers to the bonding and in-situ impregnation of sheets and fabrics while prefabricated elements refer to the application of the prefabricated strips and laminates and special systems provide special advantages; e.g. automated wrapping provides quality and rapid installation. The suitability of each system will depend on the type of structure that must be strengthened. For example, prefabricated elements are suitable for a plane and straight surfaces, whereas wet lay-up systems are suitable for a plane and convex surfaces because sheet and fabrics are more flexible as tabulated below.

Table 2.5 - Main characteristic of FRP EBR two basic techniques (FIB, 2001)

	Prefabricated (Pre-Cured)	**Wet Lay-Up (In-Situ Curing)**
Shape of FRP	Strips or laminates	Sheet or fabrics
Thickness	About 1.0 to 1.5mm	About 0.1 to 0.5mm
Bonding agent	Thixotropic adhesive for bonding	Low viscosity resin for bonding and impregnation

Fibre volume	About 70%	About 30%
Application	Simple bonding of the factory-made element with adhesive	Bonding and impregnation of the sheets or fabrics with resin
Applicability	If not pre-shaped only for flat surfaces	Regardless of the shape, sharp corners should be rounded
Number of layers	Normally one-layer, multiple layers possible	Often multiple layers
Surface unevenness	Stiffness of strip and use of thixotropic adhesive allows for certain surface unevenness	Often a putty is needed to prevent debonding due to unevenness
Ease of application	Simple in use, higher quality guarantee	Very flexible in use, needs rigorous quality control
Quality control	Wrong application and bad workmanship = loss of composite action between FRP and concrete, lack of system integrity in the long term etc.	

Special techniques of FRP EBR strengthening are developed along with the basic techniques tabulated above. Automated wrapping or winding of tow or tape was first developed in Japan and later on in the USA. The technique involves continuous winding of wet fibres under a slight angle around column or walls structures by mean of a robot. The key advantage of this system is its good quality and rapid installation. Other special strengthening techniques include; prestressed FRP, fusion-bonded pin-loaded straps, in-situ fast curing using a heating device, prefabricated shapes, CFRP inside slits, and FRP impregnation by vacuum. These systems are out of the scope of this review; more information can be found in FIB Bulletin 14 (2001), this review will focus on basic techniques.

The adhesive is used to FRP EBR to the RC shear walls is most commonly epoxy adhesive although there are other types of structural adhesives available. The purpose of adhesive is to provide a shear load path between the concrete surface and FRP EBR to develop a full composite action. The science of adhesive in multidisciplinary involving surface chemistry, polymer chemistry, rheology, stress analysis and fracture mechanics are out of the scope of this review; hence, key information must be sought from the manufacturers for application. The successful application of an epoxy adhesive system requires the preparation of adequate specifications including; provisions as adherent materials, mixing and application temperature and technique, curing temperature, surface preparation techniques, thermal expansion, creep properties, abrasion and chemical resistance. Epoxies normally may also contain fillers, softening or toughening additives depending on the application demand.

Cruz-Noguez et al. (2012) conducted experimental and analytical studies of RC shear wall strengthened with EBR FRP sheets. A system to transfer the load by FRP sheet to the foundation of the wall was incorporated in the study. Both slender and squat shear specimen representing the current and old design of RC shear walls were investigated. Results showed that the FRP EBR system significantly improve the flexural strength and stiffness of the walls in both repair and strengthening applications. Analysis studies confirmed that the FRP system was also useful in eliminating the brittle shear mode of failure in walls with insufficient shear reinforcement and non-ductile details.

Seismic performance of RC shear walls strengthened with FRP EBR was experimented by El-Sokkary and Galal (2012). Two RC wall panels were tested as a control specimen and a strengthened specimen. The strengthening was in an aim to increase the flexural capacity, shear capacity and effectiveness of FRP EBR up to failure. Constant axial load, cyclic moment and shear force at the top of the walls was applied. The strengthening system showed an eighty per cent increase in flexural capacity of the RC wall; however, the displacement ductility of the wall was decreased.

Perforated RC shear wall retrofitted with carbon fibre sheets (CFS), steel plate, micro defect-free (MDF) and engineered cementitious composites (ECC) was evaluated by testing six specimens by Choi et al. (2008). The results of experiments showed that; retrofitted specimens have a higher value of peak load; but, their energy dissipation capacities were lower than the control specimen. The results of the experiments showed that the failure mechanism of specimens was governed by shear fracture, and the strength of specimens was varied depending on the retrofitting strategy incorporated.

The seismic performance of RC framed shear walls strengthened with CFRP EBR strips was investigated by Hsiao et al. (2008). CFRP strips were placed in diagonal positions in RC shear walls. Six large-scale framed shear walls were tested under cyclic lateral loading. Results of the experiments showed that seismic performances of low-rise RC shear walls were significantly increased; however, the performance of the mid-rise shear wall was not relatively significant.

Composite shear wall with steel encased profile (CSRCW) was first damaged under cyclic lateral loading, thereafter retrofitted with CFRP EBR and retested to analyse the possibilities of CFRP EBR for strengthening CSRCW damaged under seismic action. Two damaged shear walls with steel encased profiles were repaired with CFRP strips and plate to restore bending resistance and to provide confinement effects at the ends. The result of the experiments shows that the performance of repaired and retrofitted elements was similar to the control element in terms of load-bearing capacity but slightly smaller in terms of stiffness and energy dissipating capabilities (Dan, 2012).

Experimental and numerical analysis of RC shear walls strengthened with CFRP EBR was conducted under cyclic lateral loading to assess the efficiency of RC shear wall to sustain the earthquake loading by Le et al. (2014). Two lightly reinforced concrete wall of different aspect ratios 0.67 (squat wall) and 2.5 (slender wall) were investigated with different CFRP retrofitting strategies. Strengthening with CFRP EBR strips allowed enhancing both strength and ductility of the tested walls and the numerical results in terms of the load-displacements were very consistent with experimental data.

The seismic performance of precast reinforced concrete wall panels (PRCWP) with cut-out openings retrofitted with FRP EBR was investigated for its shear behaviour subject to in-plane seismic loading condition. The idea was to assess shear capacity gain obtained using FRP EBR retrofitting technique and shear capacity decrease due to the cut-out openings. The wall specimens were previously damaged to simulate the post-seismic strengthening solution. The results of the experiments showed that the strengthened elements indicated increased horizontal displacement capacity and higher lateral load-bearing capacity in comparison to the control specimen (Demeter et al. 2009).

Experimental studies have been conducted to investigate the influence of CFRP EBR on RC short shear walls under lateral cyclic loading by Qazinog et al. (2011). The specimens were designed to fail in shear, and a specific scheme of FRP strengthening is proposed. A partial FRP strengthening strategy was selected to ensure concrete cracking which causes energy dissipation. Results of the experiments show that although lower stressed developed within the FRP strips, the strengthening techniques were highly efficient for seismic retrofitting. The strengthening method allowed gain in both ultimate load capacity and ductility of the RC short shear wall specimens.

Full-scale RC shear wall specimens were investigated under reversed cyclic loading to assess the effectiveness of CFRP EBR wraps and steel fibre-reinforced self-consolidating concrete (SFRSCC) jacket strengthening techniques. The walls were designed and detailed to simulate non-ductile reinforced concrete construction of the 1960s having lap spliced of the longitudinal reinforcement in the potential plastic hinge region, and having inadequate confinement of the boundary regions. The response of the original walls before strengthening was associated with the brittle failure of the lap splice. The retrofit and repair techniques improved the displacement ductility and the premature failure of the lap splices (Layssi and Mitchell, 2012).

A summary of previous researches conducted on FRP applied to RCSWs is presented in Table 2.6. below. The important elements from the researches are outlined and the key findings concerning this project are indicated.

Table 2.6 - Summary of some previous researches on FRP applied RCSWs.

No	Author	Title	Strength	Type of Load	Scale/Size	Apparatus	Key findings	Illustration
1	Le K. Nguyen, M. Brun, A. Limam, E. Ferrier, L. Michel, 2014	Pushover Experiment and Numerical Analyses On CFRP-Retrofit Concrete Shear Walls with Different Aspect Ratios	CFRP vertical and horizontal strips	Reverse cyclic loading	4xWall Specimen 2xSlinder 1.5x0.6x0.08 2xSquat 0.91x0.6x0.08 2xControl 2xRepaired	Hydraulic Jack 500kN	Two RCSW samples tested with two different aspect ratio. A limited number of experiments are conducted. Although models are produced for strengthening studies purposes as the near-surface mounting actual experiments are not conducted. The samples made are small-scale as per the authors' statement.	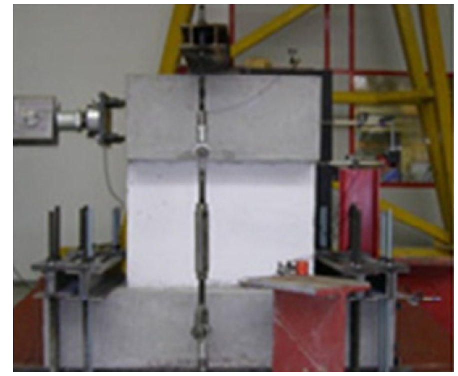 Concrete Shear Wall FRP attached
2	C.A. Cruz-Noguez, D.T. Lau & E. Sherwood 2012	Testing and Anchor System performance of RC Shear Walls Repaired and Strengthened with Externally-Bonded FRP Sheets	CFRP Sheet vertical, anchored	Reverse cyclic lateral load	9xWall Specimen 1.8x1.5x0.1m 2xControl, 2xRepaired (control wall repaired) 5xStrengthened	Hydraulic actuator jack applying in-plane load at the top of the wall	In this study, the RCSW with tow sheet are investigated. Hysteresis response and FD are considered. Cracking and failure stages are described well. The effect of anchorage is assessed. The ED and CED stages are not considered. Loading protocol not defined.	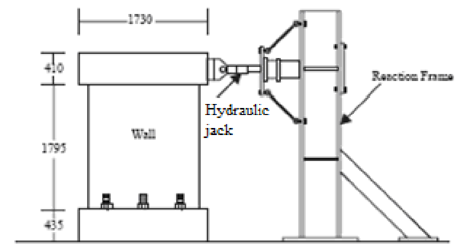 Concrete Shear Wall FRP attached
3	H. El-Sokkary & K. Galal, 2012	Cyclic Tests on FRP-Retrofitted RC Shear Wall Panels	CFRP Strips vertical at both ends, anchored	Reverse cyclic lateral load	2xWalls Specimen 1.045x1.2x.08m 1xControl, 2xRetrofited	Hydraulic actuator jack applying in-plane load at the top of the wall	The hysteresis and FD responses are considered. Cracking and failure stages are described well. The loading protocol is not defined. ED and CED stages are not considered in the study. Only two samples are used in this study.	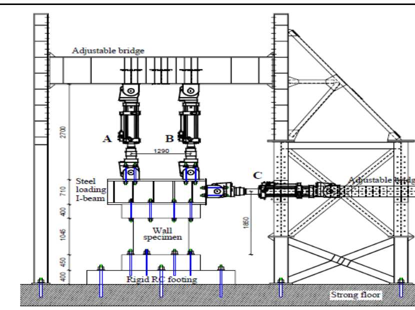 Concrete Shear Wall FRP attached

No	Author	Title	Strength	Type of Load	Scale/Size	Apparatus	Key findings	Illustration
4	D. Dan, 2012	Experimental Tests on Seismically Damaged Composite Steel-Concrete Walls Retrofitted with CFRP Composites	CFRP Anchored Steel 10@100mm vertical and 8@150mm horizontal Hoops at boundary regions 8@50mm Steel encased I profile at boundary regions	Quasi-static reversed cyclic horizontal loads cyclically increasing	6xWalls Specimen 3x1x0.1m	Hydraulic jack 400kN	In this study, 6 samples are used. hysteresis and FD responses are both considered. Cracking and crushing of concrete, as well as the failure points, are recorded. The ED of the samples is defined. A loading protocol used previously by the researcher is employed but not well defined.	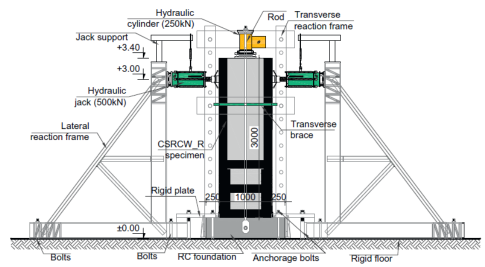 Shear wall with steel encased profiles a CFRP retrofitting
5	Hamed Layssi, And Denis Mitchell, 2012	Experiments On Seismic Retrofit And Repair Of RCSWs	CFRP and (SFRSCC) Steel Fibre-Reinforced Self-Consolidating Concrete, jacket	Reversed cyclic loading	4xWalls Specimen Full Scale Size (3.4x1.2x0.15m)	Hydraulic jacks	Four RCSW samples were tested in this study. Hysteresis response is considered but FD evaluation is not made. A custom-designed loading protocol is used. Cracking and crushing stages are not well explained. The ED and CED of samples are not evaluated.	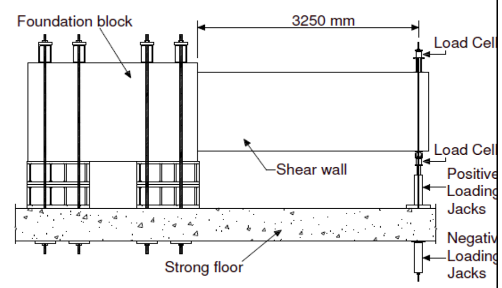 Concrete Shear Wall FRP attached
6	Fei-Yu Liao, Lin-Hai Han Zhong Tao, 2012	Performance of RCSWs with Steel Reinforced Concrete Boundary Columns	I-Section encased at boundary columns.	Cyclically increasing lateral load	6xWalls Specimens 2xSize 1.18x0.86x0.085m 4xSize 1.18x1.132x0.085m	Hydraulic actuator jack applying in-plane load at the top of the wall	In this study, six RCSWs were put to test. Hysteresis response and FD analysis are made. ED analysis of the results is made. Cracking and crushing observations are explained. No particular loading protocol is employed by the researcher. Numerical studies are also conducted by the researcher.	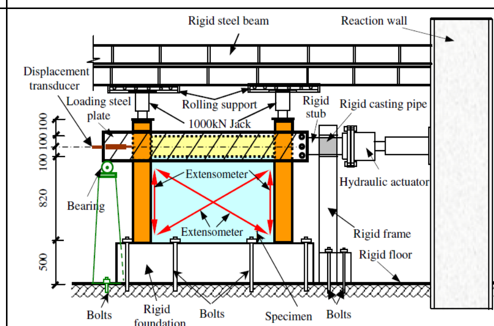 Concrete Shear Wall (Steel Encased Columns)

Summary

No	Author	Title	Strength	Type of Load	Scale/Size	Apparatus	Key Findings	Illustration
7	S. Qazi, E. Ferrier, L. Michel, P. Hamelin, 2011	Seismic retrofitting of RC Shear wall with external bonded CFRP	CFRP Strips Steel Wall 4.5@200mm vertical and horizontal Foundation 19-D6	Static and cyclic load	3xWalls Specimens 0.61x1x0.08m Scale of 1/3 1xControl 2xStrenghtened	Hydraulic Jacks	Three samples are tested in this study. Hysteresis response and ED is considered. Cracking and crushing patterns are explained. FD and CED evaluaiton are not made. No particular loading protocol is employed.	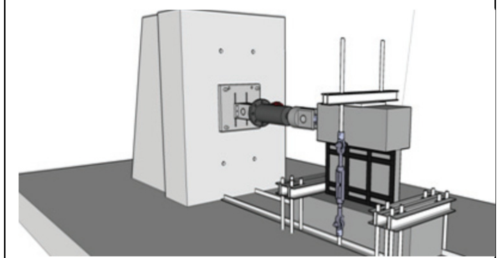 Concrete Shear Wall (Squat) FRP attached
8	Istvan Demeter Tamas Nagy-Gyorgy Stoian Valeriu Cosmin A. Daescu Daniel Dan, 2009	Seismic Retrofit Of Precast RC Wall Panels With Cut-Out Openings Using FRP Composites	CFRP Sheets Steel: Inherited from the actual wall constructed 1950-1990 in Romania	Reverse cyclic loading	8xWall Specimen 1:1.2 scaled to the actual walls	Hydraulic Jacks	Four samples are assessed in this study. Hysteresis response and FD are considered for analysis. ED and CED are not considered for analysis. No particular lateral loading is considered. Cracking and crushing are trivially pointed.	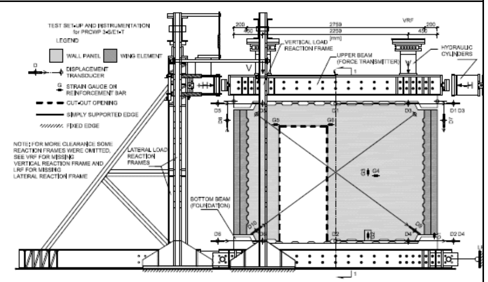 **Fig. 3** Test set-up and instrumentation. Concrete Shear Wall with Opening FRP attached
9	Fu-Pei Hsiao, Jih-Ching Wang And Yaw-Jeng Chiou, 2008	Shear Strengthening of Reinforced Concrete Framed Shear Walls Using CFRP Strips	CFRP Strips width (0.4 & 0.5m) diagonally attached Steel Wall #3@0.25cc Vertical and horizontal Columns 4- #6 vertical and #3@10mm stirrups	Reverse cyclic lateral load	7xWalls Specimen 2xWall (2x2x0.08m) 5xWalls (2x3x0.08m)	Hydraulic actuator jack applying in-plane load at the top of the wall	In this study, 5 samples are tested. Hysteresis response is considered. FD, ED, CED analysis are not considered. Crack patterns are illustrated but crushing points are not elaborated. No particular loading protocol is considered in the analysis.	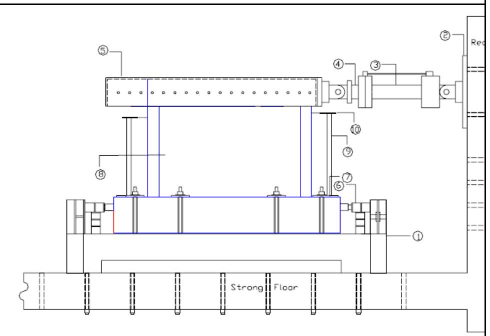 Concrete Shear Wall FRP attached

No	Author	Title	Strength	Type of Load	Scale/Size	Apparatus	Key findings	Explanation
10	Gabriel Sas et al. 2008	FRP Strengthened RC Panels with Cut-Out Openings	CFRP	In-plane horizontal cyclic quasi-static load	2xWalls Specimens Sale 1:1.2 Size (2.75x2.15x 0.10m)	Hydraulic jack	Four samples are considered in this analysis. FD analysis is conducted on the samples. No ED or CED analysis is conducted. Not particular loading protocol is considered. Cracks are described but crushing is not.	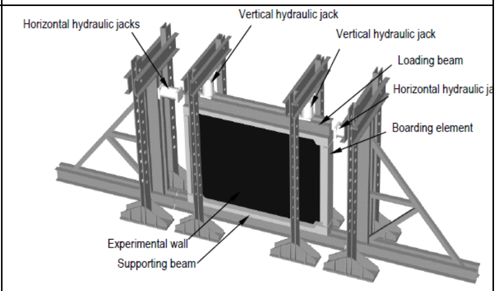 Precast CFRP attached Concrete Wall
11	H.K. Choi, Y.C. Choi, M.S. Lee, L.H. Lee and C.S. Choi, 2008	Retrofitting of Shear Walls in Different Methods	1xCFRP Sheet 1xSteel-plate 1xECC* 1MDF** Steel 6@225mm horizontal and vertical	Reverse cyclic lateral load	6Walls Specimen 3x1.3x0.1m 1xSolid 5xWith-opening (0.9x1.05m)	Hydraulic actuator jack applying in-plane load at the top of the wall	6 samples were tested in this study. Hysteresis response, FD, ED analysis are conducted. Failure pattern is assessed but cracking and crushing patterns are not described. No particular loading protocol is considered.	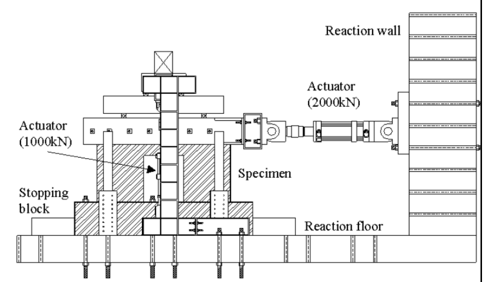 Concrete Shear Wall FRP attached
12	S. Takara, T. Yamakawa, K. Yamashiro, 2008	Experimental and Analytical Investigation of Seismic Retrofit for RC Framed Shear Walls	Steel plate, steel corner block and steel bars	Cyclic loading gradually increasing	5xWalls Specimen 1xControl 4xRetrofited Size (0.875x1.325x0.06m)	Hydraulic oil jack	5 samples are studied in this investigation. Hysteresis response and crack pattern generation are well assessed. CED analysis is also considered. No particular seismic loading protocol is considered. Failure points at different stages of loading are described.	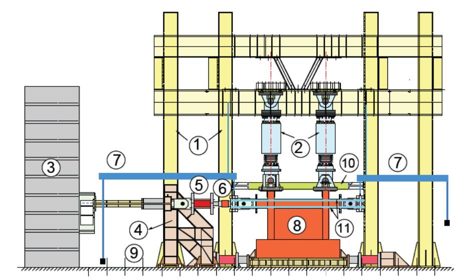 Concrete Shear Wall Steel Plate Strengthened

* ECC = Engineered Cementitious Composites
** MDF = Micro Defect Free
*** WCEE = World Conference on Earthquake Engineering
**** FRPRCS-9 = Fiber-Reinforced Polymer Reinforcement for Concrete Structures Symposium 9
***** FRPRCS-10 = Fiber-Reinforced Polymer Reinforcement for Concrete Structures Symposium 10

2.6.3. FRP Internal Application in Shear Walls

FRP internal reinforcement has been commercially available as reinforcement for concrete in the past 20 years, and over 10 million meters are used in the construction industry every year. There are many reasons why FRP reinforcement should be used as reinforcement in concrete, including electromagnetic neutrality and electrochemical durability, high strength and lightweight (FIB, 2007).

Standards and formal design deficiency are a significant barrier to extensive use of FRP in RC. First-generation guidelines for FRP RC were published in Japan (JSCE, 1992, 1993, 1997) followed by Europe's Eurocrete project (Clarke et al. 1996), Canada (CAS, 1996) and the USA (ACI, 1998). ACI committee 440 several publications, FIB Task group 9.3 of the International Federation for Structural Concrete technical reports (FIB, 2001 and FIB, 2007) in Switzerland. Several other European countries have published their codes or recommendations too (Guadagnini, 2011).

Design philosophy applied currently by developing FRP RC design guidelines with the modification of conventional RC codes of practice may look reasonable; however, it may not be entirely appropriate. Conventional RC codes of practice assume that the predominant mode of failure is always ductile due to the yielding of flexural reinforcement. However, FRP RC design guidelines assume that the predominant mode of failure would be brittle due to concrete crushing or FRP rupture (Pilakoutas et al. 2002).

Partial safety factors applied as limit state design in conventional RC design do not lead to uniform safety level in FRP RC design. It will result in a larger amount of reinforcement or larger dead to live load ratios for being safer. Additionally, the resistance capacity gap between the flexural mode of failure and other modes of failure are quite variable, and the designer will not have a reliable means of assessing them. Therefore, if there is a flexural overstrength, codes of practice do not provide information about the failure mode that will occur first and at which load level it occurs. Hence, a proposal is made for a new set of partial safety factors for use with the Eurocrete FRP bars by Neocleous et al. (2005).

Change in the traditional design philosophy of concrete structures is needed for FRP reinforcement as the mechanical behaviour of FRP reinforcement differs from the behaviour of conventional steel reinforcement. FRP materials are anisotropic and are characterized by high tensile strength and only in the direction of the reinforcing fibres, which affects shear behaviour and dowel action of the FRP bars as well as bond performance. Furthermore, FRP materials do not yield, and they are elastic until failure and design procedure must account for lack of ductility in structural concrete members reinforced with FRP bars. In the past two decades, FRP has been practically and successfully used as rebars. The research and field implementation is ongoing as well as design recommendations continue to evolve (ACI-440, 2006 and ACI-440, 2015).

Mohamed et al. (2012) conducted studies on cyclic load behaviour of GFRP RCSW. The study involved testing a shear wall reinforced with FRP bars. A large scale shear wall was experimented, to examine strength, stiffness and deformability by observing the degradation in stiffness and strength. While resisting in-plane reversed loading the energy dissipation of the system accounting for deformability of the shear wall was measured. The category of the wall was a medium-rise wall; where both flexural and shear modes of deformations were the principals. All forms of reinforcement to resist flexure, shear and sliding shear deformation was provided with GFRP bars. It was found that GFRP RCSW may qualify to resist lateral loads as the specimens showed insignificant strength degradation, reasonable stability of stiffness under reversed cyclic loading. It was found that the failure mechanism was a flexural crack followed by shear cracks and ending up with a flexural compression with a major flexure crack after the GFRP rebar rupture.

Mohamed et al. (2013a) also evaluated GFRP reinforced shear walls by conducting experiments on four large-scale specimens one reinforced with steel bars as a reference and three reinforced with GFRP bars. The samples represented a single medium-rise shear wall in a region of low to moderate risk. The specimens failed in compression reaching their flexural capacity with no strength degradation, sliding shear and anchorage failure. Specimens exhibited recoverable behaviour up to allowable drift limits before moderate damages occurred; this means that a maximum drift was achieved to meet the limitations specified in most building codes in addition to controlling the shear distortion.

In another study, Mohamed et al. (2013b) reported a strength reduction factor of GFRP reinforced shear walls. The authors proposed design guidelines by determining elastic and inelastic deformation, and evaluation of force modification factor for GFRP reinforced shear walls. Methods for estimating the virtual yield for GFRP reinforced shear wall and maximum allowable displacement is also proposed. The force modification factor was estimated based on the idealised curve of the tested GFP reinforced shear walls.

Flexure and shear deformation of GFRP RCSW was studied by Mohamed et al. (2013c) in another set of experiments. Mid-rise RC shear wall under quasi-static cyclic load was tested to investigate the interaction of flexural and shear deformation of the walls. Four large-scale specimens one reinforced with steel bars and three entirely reinforced with GFRP bars were loaded until failure where the predominant mode of failure was by flexure. It was also found that relying on diagonal displacement transducers tended to overestimate shear deformation by 30 to 50%. The proportion of flexural and shear deformation about the total deformation showed that at the early stages of loading flexure deformation was dominant and at later stages of loading shear deformation was dominant.

In their 2014 paper, Mohammed et al. reported the strength and drift capacity assessment of three GFRP and one steel RCSWs under quasi-static reversed cyclic lateral loading. It was found that the GFRP RCSWs could reach their flexural capacities without strength degradation and that shear, sliding shear, and anchorage failures were not a major problem and could be controlled. Additionally, it was found that up to a certain allowable drift limit recoverable and self-centring behaviour can be seen which meets the requirement of most buildings' codes. Furthermore, the energy dissipation along with small residual forces of the GFRP RCSWs was at an acceptable level in comparison to the steel RCSW.

The literature review shows that FRP reinforced shear walls were studied by a very limited number of researchers. Although the outcomes of the studies by the above-mentioned research team show a promising result the authors recommend further researches including the walls different sizes, dimension, aspect ratio, levels of concrete confinement, tie spacing, reinforcement ratio, axial loads, minimum reinforcement. Additionally, the recommendation is to conduct a future study of the confinement model, anchorage length, bond behaviour, ductility and deformability index and dynamic analysis of RCSWs (Mohammed, 2014).

The previous researches on the area of FRP RCSWs show that there is a major knowledge gap in the area that requires investigation. A summary of the research work conducted on the behaviour of the GFRP RCSW under quasi-static reversed cyclic loading is given in Table 2.7 which shows the limited number of researches done in the field. RCSW with BFRP reinforcement is yet to be researched and investigated in many aspects as the information about this type of RCSW is vastly scarce.

Table 2.7 - Summary of some previous researches on FRP RCSWs.

No	Author	Title	Rebars	Load Type	Scale/Size	Apparatus	Key Findings	Illustration
1	Mohamed, N., Farghaly, A., Benmokrane, B., and Neale, K. (2014)	Experimental Investigation of Concrete Shear Walls Reinforced with Glass Fiber–Reinforced Bars under Lateral Cyclic Loading	GFRP	Lateral cyclic load	Large scale specimen Size (3.5x1.5x0.2m)	Hydraulic jack	- No premature failure of GFRP RCSW - GFRP RCSWs had a pinched hysteretic behaviour - GFRP wall had a higher drift capacity - GFRP RCSW aspect ratio affected inelastic flexural and shear deformation - Cover spalling occurs at higher drifts for GFRP RCSWs.	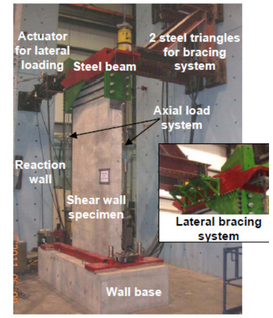Lateral loading test apparatus set up
2	Mohamed, N. (thesis, 2014)	Strength and Drift Capacity of GFRP RCSWs	GFRP	quasi-static reversed cyclic lateral loading	Large scale specimen Size (3.5x1.5x0.2m) One steel reinforced Three GFRP reinforced	Hydraulic Jack	- all specimens showed no sign of premature failure. - GFRP RCSW had pinched hysteretic behaviour without strength degradation. - hysteresis behaviour was stable and drift capacity was 3% and 2.6% for GFRP and steel RCSWs, respectively. - GFRP RCSW behaved elastically up to 2% drift. - ED of GFRP RCSW was at an acceptable level. Steel RCSWs had higher ED. – FE POA predicts ultimate load with 10% error - Lots of further researches are recommended by the author.	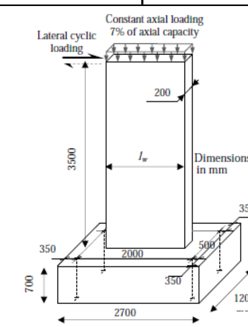Lateral loading test apparatus set up
3	Mohamed, N., Farghaly, A., Benmokrane, B., and Neale, K. (2013)	Flexure and Shear Deformation of GFRP-Reinforced Shear Walls	GFRP	Quasi-static cyclic load	4-Large scale specimen Size (3.5x1.5x0.2m) One steel reinforced Three GFRP reinforced	Hydraulic jack	- at a moderate damage steel RCSW induced higher curvature, shear strain and rotation close to the wall base due to the yielding of the longitudinal bars. - GFRP RCSW showed good distribution of shear strain. - diagonal displacement transducers overestimate shear deformation by more than 30%. Corrections reduce to less than 15% - At early loading flexural deformation was dominant at higher loading shear deformation was prominent	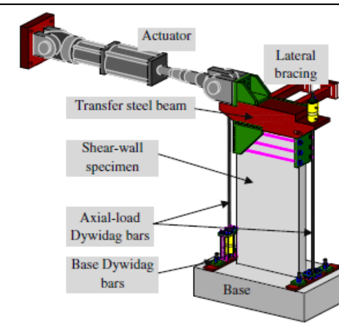Lateral loading test apparatus set up

No	Author	Title	Rebars	Load type	Scale/Size	Apparatus	Key Findings	Illustration
4	Mohamed, N., Farghaly, A., Benmokrane, B., and Neale, K. (2013)	Evaluation of GFRP-Reinforced Shear Walls	GFRP	Lateral cyclic loading	4-Large scale specimen Size (3.5x1.5x0.2m) One Steel reinforced Three GFRP reinforced	Hydraulic jack	- no sign of premature failure - aspect ratio affected inelastic flexural and shear deformations coupling. - GFRP RCSW was more flexible but its ED was at an acceptable level. - steel RCSW had more ED through inelastic deformation. - GFRP RCSWs had no permanent deformation until 80% of ultimate capacity. - GFRP RCSW had good strength and deformation capacity. - GFRP RCSW had a reasonable stiffness ratio, ED, and controlled shear distortion. - Recommendation are made by the author for further researches to implement adequate design guidelines and recommendation for GFRP RCSW structural elements.	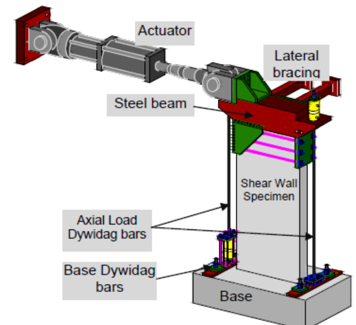 Figure 3: Test Setup Lateral loading test apparatus set up
5	Mohamed, N., Farghaly, A., Benmokrane, B., and Neale, K. (2013)	Strength Reduction Factor of GFRP-Reinforced Shear Walls	GFRP	Lateral cyclic load	Large scale specimen Size (3.5x1.5x0.2m) One steel reinforced Three GFRP reinforced	Hydraulic jack	- GFRP RCSWs reached similar drift capacities to the steel RCSWs. - The inelastic behaviour point of GFRP RCSWs corresponds to the deterioration of concrete under compressive stresses. - GFRP RCSW maximum allowable deformation was estimated as 2.5% drift. It was defined to be smaller than the actual displacement capacity. - The force modification factors are suggested as 1.5 and 1.3 for ductility and overstrength related force modification factors. - the author suggests the virtual deformation point, and maximum allowable deformation and estimation of the force modification factors to be used in the design of the GFRP RCSWs to allow for an adequate drift capacity.	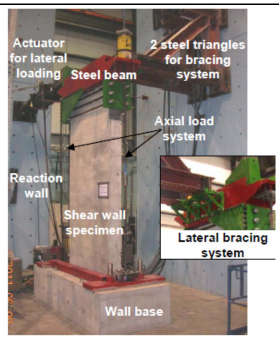 Lateral loading test apparatus set up

2.7. Shear Wall FE Modelling

Shear Wall Modelling has been conducted by researchers in the past to develop simple and accurate models. The accuracy of the analytical models has always been a concern of structural engineers too, in complex models.

Recently, an enormous amount of effort has been applied by researchers in the provision of analytical models able to simulate the behaviour of RCSWs. Development in information technology and computational efficiency of computers has further paved the way to develop more sophisticated models previously neglected due to complexities associated with such models.

Finite element models are not only used in the analysis of the newly designed structures but also it is used in the analysis of existing buildings such as ones retrofitted with CFRP. However, it is essential to construct representative models to be able to evaluate response, predict hazard and anticipate failure modes.

Clough et al. (1965) were one of the first researchers on numerical analysis of the RC structural elements proposing the very first nonlinear macro-model (Ngo and Scordelis 1967).

Nonlinear finite element analysis of RCSW based on multi-layer shell element and Microplane constitutive model was generated by Miao et al. (2006) to simulate the coupled in-plane and out-plane bending and bending-shear of the shear walls. The multi-layer shell element had several layers with various thicknesses. Concrete and rebars material models were attributed to different layers to exhibit the performance of shear walls per material properties. Additionally, a new concrete constitutive model named Microplane-model was developed to provide a better simulation of the concrete shear wall under complex stress conditions and histories. The models were tested under push-over and cyclic load. The result of simulations shows that multi-layer shell element can simulate coupled in-plane and out-plane bending failure of tall and short walls correctly. Cyclic behaviour and damage accumulation of RCSWs can be modelled precisely which was highly essential for the performance-based design of the structures under earthquake loadings (Miao et al. 2006).

Finite element nonlinear analysis of lightweight RCSW with different web reinforcement modelled three-dimensionally to predict seismic behaviour of lightweight RCSW under seismic actions. Four shear wall specimens with varying reinforcements of the web of either orthogonal grids or diagonal bars were experimentally tested and numerically simulated. The three-dimensional model was developed using Ansys Solid65 and Link180 elements for concrete and steel rebars, respectively. Comparison of the finite element and experimental models in terms of load-top displacement relationship, the shear capacity and the strain developments in steel and concrete parts shows that; the finite element analysis of the lightweight RCSW under earthquake loading can capture the nonlinear response of the model. The study also indicates that diagonal web reinforcement was effective in the transfer of the shear force to the foundation and reduction of shear force by compressive struts (Raongjant and Jing 2008).

Cortes-Puentes and Palemo (2011) modelled seismically repaired and retrofitted RCSWs to provide a quick, reliable and straightforward modelling procedure to repair and retrofit using different materials including FRP sheets. Slender, squat and slender-squat shear walls were investigated. Simple rectangular membrane element for concrete, truss bar elements for steel and FRP retrofitting material and bond-link element for the bonding interface between steel and FRP to concrete material was used. The simulations satisfactorily represented the seismic behaviour, including lateral load capacity, displacement capacity, energy dissipation, hysteretic response and failure mode of the shear walls.

The nonlinear behaviour of RCSWs incorporating macroscopic and microscopic models was studied by Jalili and Dashti (2010). Macroscopic model effectiveness in predicting the nonlinear response of the slender reinforced concrete was investigated. The model was made of the nonlinear spring element to represent flexural and shear behaviours using Abaqus finite element. The analysis shows excellent conformance of the analytical result with the experimental measurements of the specimens. Parametric studies of the model results sensitivity of the model toward different modelling parameters were not significant. The microscopic model was also created to predict the nonlinear behaviour of the specimens; although, this type of model required more CPU time. Comparing both macroscopic and microscopic models in terms of CPU time taken and lateral load-displacement curves agreement; it was determined that the macroscopic models were more efficient (Jalili and Dashti, 2010).

Nonlinear and linear analysis of RCSWs were studied by Fahjan et al. (2010). In the linear analysis, RCSWs were modelled using shell element and frame elements. In the nonlinear analysis, the theory was based on a plastic hinge concept at plastic zones. The plastic zones were located at the end of structural elements or along the member span length. In modelling with shell elements, the multi-layer property of the element was used to model nonlinear behaviour of the shear wall; where concrete was modelled in one layer and reinforcement was modelled in another layer. The comparison of a different approach to linear and nonlinear analysis of the RC shear walls showed that; the Mid-Pier frame with plastic hinge models overestimates the capacity of the structure in comparison with the multi-layer shell model (Fahjan et al. 2010).

Nonlinear finite element analysis of reinforced concrete slit-wall with shear connectors was assessed with FE application Ansys mechanical by Beatu and Ciongradi (2011). This type of wall increased energy dissipation by the yielding shear connections as structural dampers increasing the overall ductility of the structure. Static nonlinear analysis of the wall with shear connectors compared to ordinary shear walls showed that this type of wall increases ductility and easy to use in construction practice. The finite element method simulated an accurate and realistic behaviour of the reinforced concrete wall (Baetu and Ciongradi 2011).

Shear wall with flange model was developed by Greeshma et al. (2011) using Ansys FE software to model the behaviour of RCSW in practical use. The model replicated the poor design and construction practices in India, which has resulted in the collapse of the buildings under major earthquakes. The shear walls are modelled both as the discrete and smeared models formats available in Ansys under cyclic loading. The results of the analysis show satisfactory results from both discrete and smeared models. Also, it was noticed that the discrete model had a lesser amount of ductility than the smeared model on average; where the discrete model had 2.5% less deformation capacity. Hysteretic loop from both types of models shows that; discrete model shows 7.5% lower energy dissipation capacity than the smeared model. The ultimate shear capacity of both models was found to be matching and per ACI-318 empirical relationship (Greeshma et al. 2011).

Noguez et al. (2012) created an analytical model of FRP reinforced shear walls, including intermediate crack debonding mechanisms (a common debonding mechanism that is caused by the opening of flexural cracks). Nonlinear response of RC shear walls repaired and strengthened with externally bonded FRP sheets, implementing a computationally simple procedure to account for intermediate cracks. It was found that neglecting the influence of intermediate crack debonding cause substantial overestimate of the load-carrying capacity of the walls; also, it caused an overall poor correlation between the analytical and experimental nonlinear response. Intermediate crack debonding effect consideration led to close agreement between the calculated and measured ultimate strength, nonlinear hysteretic response and failure modes. The model was validated using the experimental results.

Mohamed et al. (2014) conducted a numerical simulation of mid-rise GFRP RCSW subject to lateral reversed displacement. The finite element method (FEM) was used to test and demonstrate the wall's capability to resist a lateral load. A two-dimensional model was developed using the VecTor2 FE program. The analysis was conducted on four large-scale mid-rise RC shear walls; one reinforced with steel and three reinforced with GFRP bars. The results showed the stability and compliance of the simulation procedures used and provided reasonably accurate simulations of strength and deformation capacity. Shear distortion proved the effectiveness of the elastic behaviour of the GFRP bars in controlling and reducing the shear effect. The promising results are a step forward to propose design models for such new lateral load resisting.

Nguyen et al. (2014) conducted pushover analyses on CFRP retrofitted concrete shear wall with different aspect ratios. Two numerical approaches for concrete modelling were used; one approach was

2D plane stress and with a local concrete model based on the smeared fixed crack and a classical regularization technique based on the fracture energy. The second approach investigates a coupled elastoplastic damage model using a local approach in 2D and 3D simulations. The numerical results in terms of the load-displacements turned out to be consistent with experimental data. The failure modes and crack patterns observed in experimental data were reproduced for both walls, with and without CFRP strengthening.

Sakr et al. (2017) investigated the behaviour of RCSW with three micro models in 2D and 3D. The adhesive layer was modelled using cohesive interaction methods and the results were validated using the experimental data from the literature. It was found that the FE model can predict the behaviour of strengthened RCSW and debonding of CFRP reasonably well. A parametric study was successfully conducted on the validated model.

Belletti et al. (2017) developed a crack model utilising the Abaqus user material subroutine to predict the response of RCSW. Refined material constitutive relationships were used to formulate the model accounting for plastic deformations. The model was tested under cyclic loads and the results were validated using the experimental data in the literature. The model was able to predict the specimen's behaviour with reasonable accuracy.

Husain et al. (2019) developed a nonlinear FE model using Abaqus for RCSW with opening and strengthening of FRP wraps. The model behaviour was tested under lateral monotonic loads and the results were validate using experimental data in the literature. The investigation outcomes suggest that proposed CFRP laminates configurations increase the strength, deformation capacity, ductility and energy dissipation of the shear walls substantially.

El-Kashif et al. (2019) generated a numerical model using Ansys to assess the effect of FRP sheets in enhancing the seismic behaviour of RCSWs. The model was subjected to monotonic and reversed cyclic loading until failure and the results were validated using the data from the literature. The investigation results show that FRP sheets in vertical and horizontal directions were effective in eliminating the brittle shear failure mode in walls.

The literature review shows that RCSW models are made with a focus on steel-reinforced as well as FRP external strengthened walls. RCSWs with internal FRP strengthening had very little attention (although the modelling techniques are the same) resulting in a knowledge gap in the area.

Table 2.8 shows a summary of some analytical models available in the literature. The table outlines the critical information in the development of the models and the key finding relevant to the analysis of the modelling results in this study.

Table 2.8 - Summary of some previous researches on RCSWs modelling.

No	Author	Title	Composite	Steel	Concrete	Bonding	Crack Type	Software Package	Key findings	Illustrations
1	El-Kashif O.F.K, Adly K.A., Abdalla A.H. (2019)	Finite element modelling of RC shear walls strengthened with CFRP subjected to cyclic loading	Two-node LINK180 with three DoF at each node	Smeared reinforced a ratio of the concrete volume	SOLID65 is represented by eight nodes with three translational degrees of freedom at each node	Interface element Combin39 between the concrete and FRP	Smeared	Ansys	The author has used Ansys 16, 7 models were. generated, under monotonic and cyclic loading, FRP strengthening is added. FRP addition was found to be effective in eliminating failure mode. Hysteresis response is good ins some groups but needs improvement.	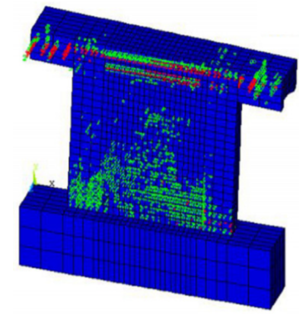 Cracking and crushing
2	Husain M., Eisa S.A., and Hegazy M.M. (2019)	Strengthening of reinforced concrete shear walls with opening using CFRP	FRP Wraps around the opening. Four-node shell element (S4R)	Two nodes truss element with three DoF at each node (T3D2)	Eight-node brick element with three DoF at each node (C3D8R)	Perfect bond assumption between the CFRP and concrete elements	Based on contours of mid-surface maximum principal strains	Abaqus	The models are verified using data in the literature. Results show an increase in lateral load strength, deformation capacity, ductility and ED. Only monotonic loading is used but not the hysteresis response, rebar bond interaction is not considered. FD correspondence is good but can be better	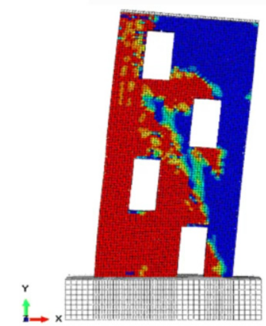 Damage of CFRP retrofitted
3	Sakr A.M., Elkhoriby R.S., Khlifa M.T. and Nagib, T.M. (2017)	Modelling of RC shear walls strengthened by FRP composites	8-node 3-D solid element (C3D8R)	2-node linear 3-D truss (T3D2)	8-node 3-D solid element (C3D8R)	Cohesive interaction model between CFRP and concrete and a perfect bond between rebars and concrete	Based on plastic strain distribution	Abaqus	A concrete constitutive damage plasticity model is used, the interaction between laminates and concrete is considered but rebars concrete interaction is not considered. The model can predict the mode of failure due to debonding. Verification is made through the literature, not the author's own experiments.	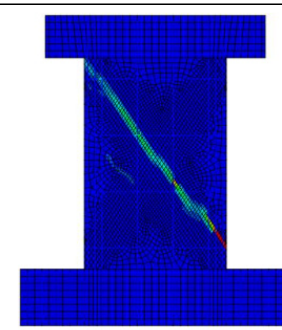 Plastic strain distribution

No	Author	Title	Composite	Steel	Concrete	Bonding	Crack Type	Software Package	Key findings	Illustrations
4	Belletti, B., Scolari, M., and Vecchi, F. (2017)	PARC_CL 2.0 crack model for NLFEA of reinforced concrete structures under cyclic loadings	Smeared reinforcement as a percentage ratio of the concrete volume	Smeared reinforcement as a percentage ratio of the concrete volume	User material PLCrack	Perfect bond between concrete and rebar elements	Fixed crack approach	ABAQUS	This author has developed his own material model for concrete which captures hysteresis response, ED and pinching effect. However, the model has not considered rebar-concrete bond interaction and the validation is through the data in the literature.	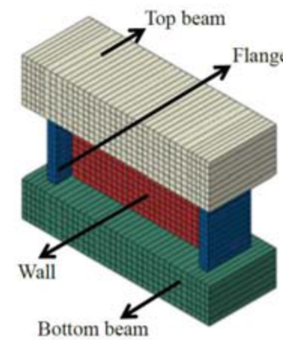 Generic FE model
5	Nguyen L.K, Brun, M., Limam, A., Ferrier, E. and Michel L. (2014)	Pushover experimental and numerical analyses on CFRP-retrofit concrete shear walls with different aspect ratio	GFRP Plate 2D and 3D uniaxial bars whose nodes are connected with the concrete nodes	2D & 3D uniaxial bars whose nodes are connected with the concrete nodes Yield Strength = 500 MPa	2D and 3D linear four nodes and eight nodes respectively Compressive Strength = 34.65 and 35.93 Mpa	Perfect bonding through nodes between concrete and the reinforcement bars	Smeared fixed crack	CAST3M	The author has conducted his own experiments, FD, failure mode and cracks pattern correspondence are good. A bond-slip model is considered between FRP and concrete but not rebar and concrete. Pushover analysis is conducted by hysteresis response is not considered in this study.	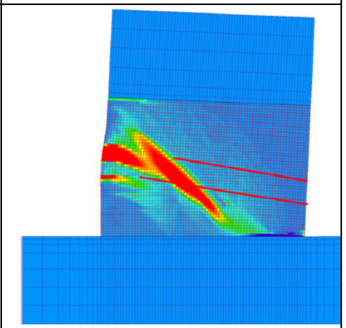 Failure Mode of FRP Retrofitted
6	Mohamed N., Farghaly S.A., Benmokrane B., Neale W.K. (2014)	Numerical simulation of mid-rise concrete shear walls reinforced with GFRP bars subjected to lateral displacement reversals	FRP bars, based on ACI-440.1R-06	Seckin and Tasson Model *	Palermo and Vecchio with decay, Vecchio-Lay, Hoshikuma et al, Bentz, Kupfer/Richart, Variable-Kupfer, Models	Perfect bond between the reinforcement and concrete	Mohr-coulomb (Stress)	VecTor2	This author has conducted his own experiments for validation, hysteresis response is considered, cracking patterns are considered. Both FD and hysteretic analysis are conducted. Rebar-concrete bond interaction is not considered. VecTor2 is a can only model in 2D and it can only take the loading as factored.	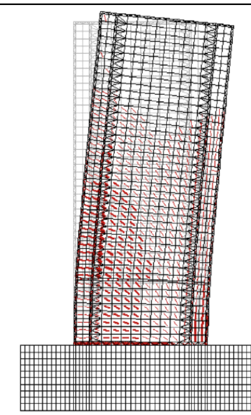 Crack pattern model

Continued...

No	Author	Title	Composite	Steel	Concrete	Bonding	Crack Type	Software Package	Key findings	Illustrations
7	Kezmane A., Hamizi M., Boukais S. and Eddine N.H (2012)	Numerical simulation of RC shear wall strengthened by external bonding of a composite material	Quadratic two-dimensional elements, 8 nodes, each having 6 degrees of freedom	Linear solid element, volumetric tetrahedron, four nodes each having 6 degrees of freedom. E = 210 GPa V = 0.3	Linear solid element, volumetric tetrahedron, four nodes each having 6 degrees of freedom	Perfect adherence assumption	Model Cracking, Isotropic reduction of stiffness	ABAQUS	The author has developed a 3D model. The author has assessed reinforcement strategies. Rebar-concrete and FRP laminate-concrete bond interactions are not considered. The model is not validated with experiments or literature data.	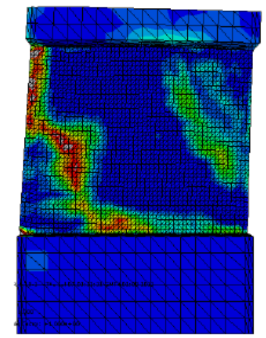 Diagonal crack pattern
8	Cruz-Noguez C.A., Lau D.T. and Sherwood E. (2012)	Analytical modelling of FRP-reinforced shear wall including intermediate crack debonding mechanism	Modelled as discreet truss elements, brittle material with zero compressive strength.	Modelled as reinforcement ratios at different regions uniformly distributed as elastic-plastic material with strain hardening	Four-node quadrilateral elements	Intermediate crack debonding model	Smeared and discreet analysis	VecTor2	The hysteresis response is well presented and has good correspondence with the experimental results. The author has not conducted his own experiments and used literature data. The is developed in 2D. Bond interaction of FRP and concrete is considered.	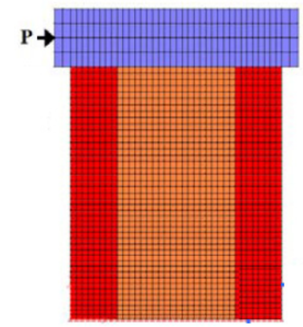 Generic FE model
9	Cortes-Puentes L.W. and Palermo D. (2011)	Modelling seismically repaired and retrofitted RCSWs	Two-node truss bars elements, four degrees of freedom; displacement in x and y directions at each node,	Two-node truss bars elements, four degrees of freedom; displacement in x and y directions at each node,	Plane stress rectangles, a four-node element with eight degrees of freedom; two degrees of freedom at each node.	Two nodes non-dimensional link element, the element contains two orthogonal springs to connect nodes of truss bars and concrete elements	smeared rotating crack approach	VecTor2	Several experimental results from the literature are compiled and used for verification of the model. Some FE results correspond well with experimental results. but the model is developed in 2D and the load type for the hysteresis response is factored load with a gradual increase.	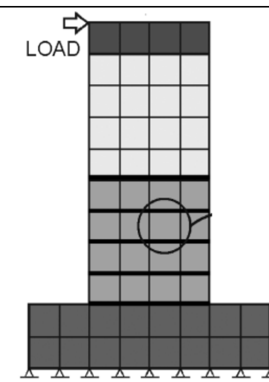 FE generic model

Continued…

No	Author	Title	Steel	Concrete	Bonding	Crack Type	Software Package	Findings	Illustrations
10	Baetu S. and Ciongradi I. (2011)	Nonlinear finite element analysis of reinforced concrete slit walls with ANSYS	Link 8, 3D spar element, two nodes, three degree of freedom at each node, translation in the nodal x, y and z directions, E_S= 2.1E+0.11 Pa, V=0.3, F_y=3.55E+0.08Pa, E'_S=2.1E+0.09 Pa	Solid65 element, eight nodes with three degrees of freedom at each node, translation at in nodal x, y and z directions, E_C=30GPa, v = 0.2	Perfect assumption	Crack pattern at each load step, where principal tensile stress exceeds the ultimate tensile strength of concrete	ANSYS	The model was developed using Ansys 12. The rebar-concrete bond interaction is not considered. Hysteresis response is not considered. A 2D model is produced. No validation is done through experiments or literature data.	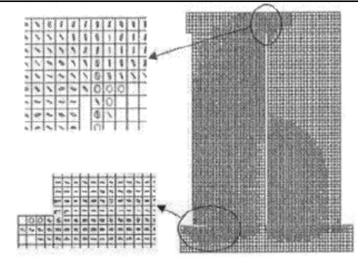 Cracking at max load
11	Greeshma S., Jaya K.P. and Sheeja L.A. (2011)	Analysis of flanged shear wall using Ansys concrete model	Link 8, three-dimensional spar element with 3DoF at each node, translation at nodal x, y and z directions. Yield stress 432 MPa, Tangent modulus = 847 MPa	Solid65 eight-node solid isoparametric 3D element, 3DoF at each node, translation in nodal x, y and z directions, Modulus of elasticity = 25GPa and Poisson ratio = 0.3	Perfect assumption	Crack pattern at each load step, where principal tensile stress exceeds the ultimate tensile strength of concrete	ANSYS	ED and FD graphs are well presented and show a good correspondence between the discrete and smeared model. A hysteresis response comparison is well made. Rebar-concrete interaction not considered. A 3D model is produced but no validation with experiments is made.	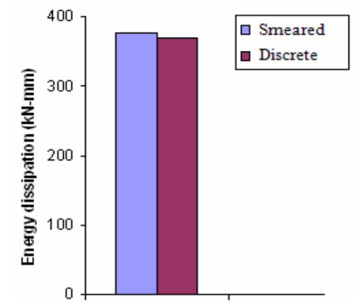 Crack pattern comparison
12	Jalili A. and Dashti F. (2010)	Nonlinear behaviour of RCSWs using macroscopic and microscopic models	Rebar layer at different orientation and angle and 3D positions	Spring element, macroscopic elements consist of vertical spring elements connected to rigid beams at top and bottom and microscopic shell element	Perfect bond	Crack initiating at the point where the tensile equivalent plastic strain is greater than zero.	ABAQUS	FD graphs show a good correspondence between the FE and experimental results. The model is verified through literature data. Hysteresis response and rebar-concrete bond interaction are not considered and only a 2D model is produced.	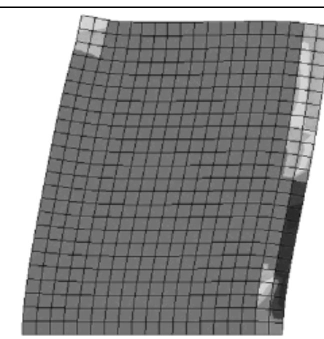 Ultimate deformation pattern

Continued…

No	Author	Title	Steel	Concrete	Bonding	Crack Type	Software Package	Key findings	Illustrations
13	Fahjan M. Y., Kubin J. and Tan T.M (2010)	Nonlinear analysis method for reinforced concrete buildings with shear walls	Multi-layer shell element with rebar layer	Multi-layer shell element concrete layer and mid-pier frame	Perfect assumption	NA	SAP2000	Well presented FD graph for a different model. A 2D model is produced. The hysteresis response or the bond interaction between the concrete and rebar is not considered. No verification or validation attempt is made and a comparison of the model to model is made.	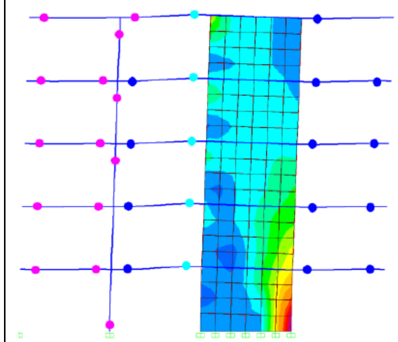 Multi-layered shell model
14	Raongjant W. and Jing M. (2008)	Finite element analysis on lightweight RCSWs with different web reinforcement	LINK 8 spar element, two-node element each node with three degrees of freedom, translation in the nodal x, y and z directions for discrete reinforcement. And Smeared reinforcement.	Solid-65 eight nodes with three degrees of freedom at each node-translation in the nodal x, y and z directions	Perfect assumption	Smeared crack	ANSYS	The researcher has produced his own experimental samples for validation. Ansys 8 is used in the production of this 3D model. The FD correspondings are ok but not very good. Hysteresis response and concrete-rebar bond interaction are not considered.	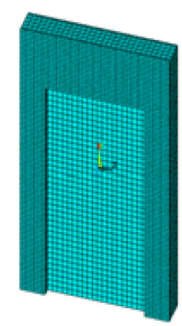 Concrete Model
15	Miao W.Z., Lu Z.X., Jiang J. J. and Ye P. L. (2006)	Nonlinear FE Model for RC Shear Walls Based on Multi-layer Shell Element and Microplane Constitutive Model	Rebar smeared layers	Multi-layer shell element	Combination	Discrete crack at the bottom of the wall	Element level	Both the POA and hysteresis response of the model is developed. Rebar-concrete interaction is considered. No validation is made but models are compared between themselves. A two-dimensional model is produced only.	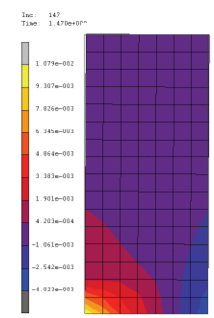 Principal major strain at peak load

2.8. Chapter Conclusions

The earthquake nature and disasters are investigated and the LLRS types are assessed. Shear walls being one of the main structural components of LLRS is further focused upon. The use of FRP material in RCSWs is investigated in details.

It was found that the internal application of FRP in RCSWs investigation is scarce in the literature. It was also found that only one researcher has conducted investigations on the internal application of the FRPs in RCSWs; even though corrosion resistance and electromagnetic neutrality of FRP rebars are important reasons that increase the demand in application of FRP in RCSWs as internal reinforcements.

The single investigation mentioned above focused on the use of GFRP rebars in RCSWs and several types of further investigations in the field are recommended. Therefore, a knowledge gap is identified in the application of FRP rebars as internal reinforcement RCSWs.

The single research carried out in the area has also conducted numerical studies in the field with successful results. Therefore, it is further decided to contribute to the knowledge body by developing analytical models for the study of FRP RCSWs.

3. Experimental Set-up

This chapter provides a detailed explanation of the experimental program conducted in the structural and concrete laboratories of Kingston University London (KUL). The chapter elaborates on; design, materials, and methodology utilized to carry out the project.

3.1. Design

The shear wall specimen represents a precast panel in a moderate-rise building made with precast panels as depicted in the diagram below. The height of all the shear wall (h_w) under the test was 1000 mm, and the horizontal length (l_w) of the wall is also 1000 mm. The wall thickness (t_w) was 100 mm.

The size of the specimen wall was chosen to represent a 1:3 scale model of a 3x3m shear wall. The sample was designed as such that the internal part of the shear wall would represent a precast panel surrounded by the boundary elements at the perimeter.

The reinforcement cage was designed so that the perimeter of the wall had a higher intensity of reinforcement bars representing the columns (vertical element) and beams (horizontal elements). The inner areas had a relatively lesser reinforcement ratio than the perimeter.

The walls were designed with 6 mm and 10 mm high yield steel rebars. The design of the BFRP and GFRP reinforcements were a replica of the steel reinforcement design. All stirrups used were 6 mm mild steel bars. Four samples were designed with tube anchorage at the end of the vertical bars to be able to analyze the effect of bond strength between concrete and reinforcement when comparing the strength of FRP with reinforcement cages.

The shear wall was designed to have higher shear strength than flexural strength to make sure that shear failure is prevented. The wall was fully fixed at the bottom to prevent sliding failure. Two steel plates were added to the top right and left surface where the load is applied to distribute the in-plane load and prevent any premature local failure of the concrete due to stress concentration.

The wall was fixed in the bottom to a Parallel Flange Channel (PFC) using 10 mm high yield steel bar anchors welded to the PFC. The PFC was welded to the Rectangular Hollow Section (RHS) to allow for the fixing bolts. The RHS was welded to a thick steel Plate. The Plate was designed to be bolted to the strong Frame where testing was conducted.

The design code (BS EN-1992-1-1:2004) for Concrete provision for minimum dimensions and reinforcement ratio were used for the design of the shear wall specimens which also meets the design requirement against flexure, shear and confinement. The reinforcement arrangement is depicted in Figure 3.1 below.

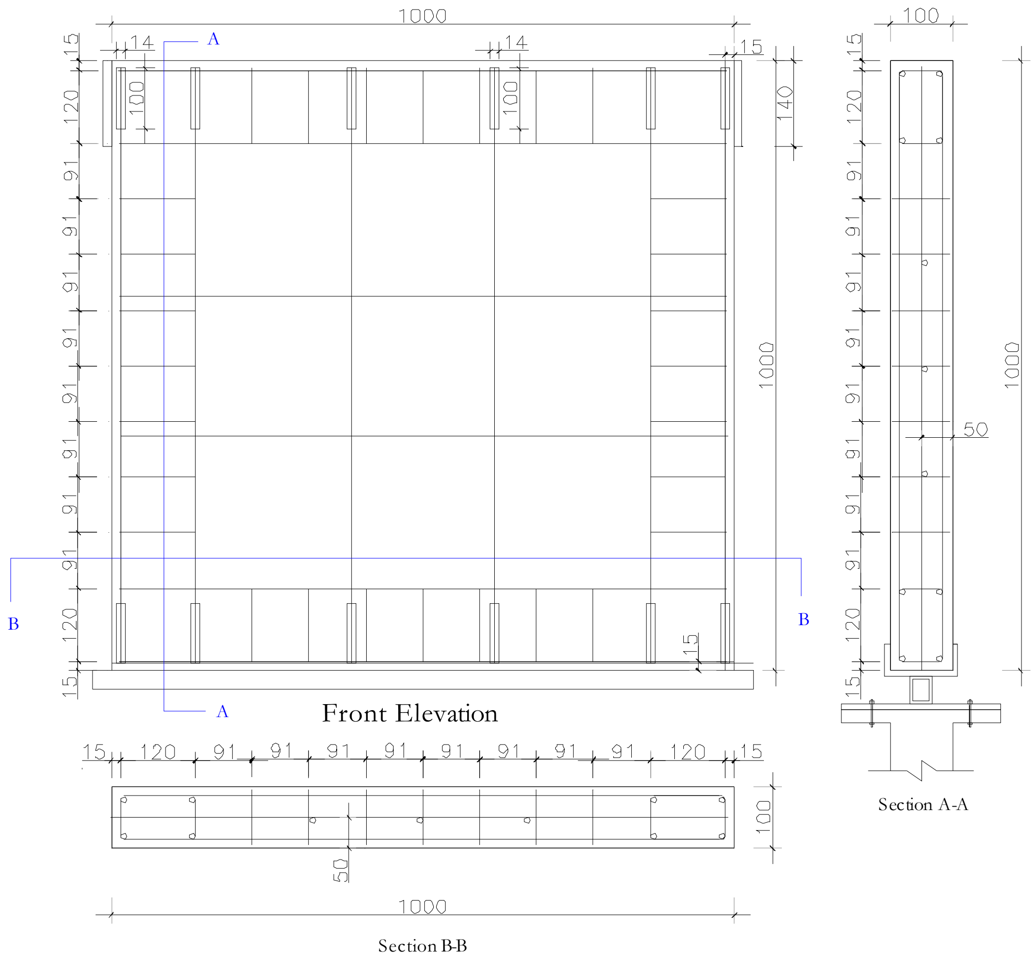

Figure 3.1 Reinforcement cage and detailing

The same reinforcement design layout was used to make the FRP rebars cage. It was made sure that there are no differences between the reinforcement layout of the two samples to enable the assessment of rebar type as the only variable in the study.

3.2. Materials

3.2.1. Concrete

To construct the shear wall specimens ready-mix concrete and the in-lab concrete mix was used. The first six samples were cast with in-lab concrete-mix, and the last six samples were cast using ready-mix concrete to analyse the benefits of both types.

The in-lab concrete-mix had the benefit of overseeing the mix proportions and the amount of water added for the workability under a controlled environment. Concrete-mix made in the lab was designed

(Figure 3.2) to achieve the characteristic strength of C30/37. The design criteria are summarized in the bullet points below:

- Characteristic strength at 28 days – 30N/mm^2
- Cement strength – 42.5 N
- Uncrushed coarse aggregate with a maximum 10 mm size
- The proportion of fine aggregate at 45%
- Water/cement ratio 0.54

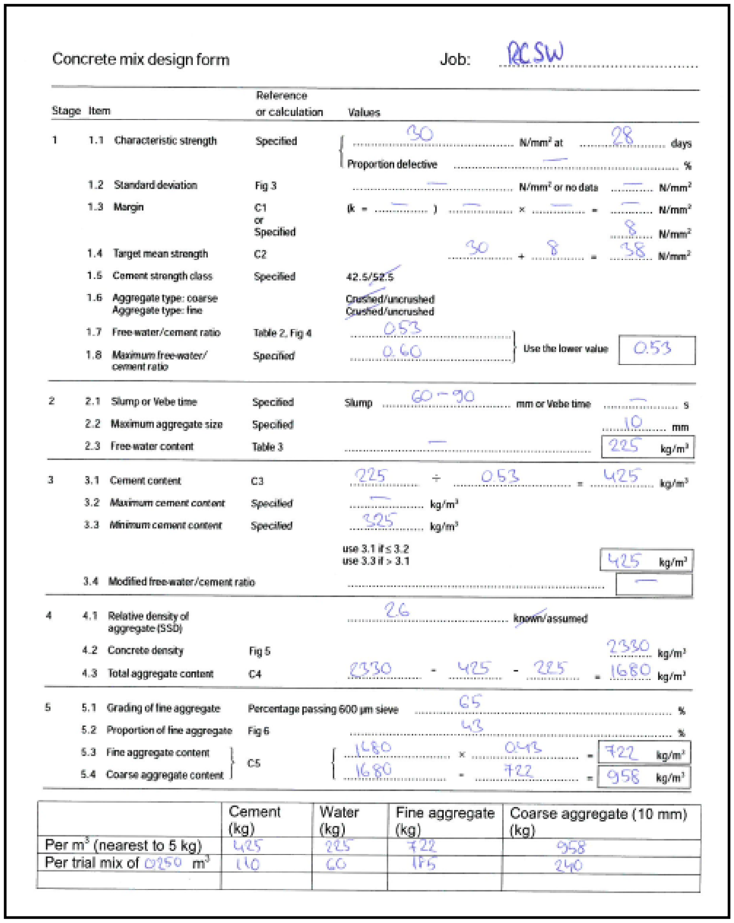

Concrete mix design form Job: RCSW

Stage	Item		Reference or calculation	Values
1	1.1	Characteristic strength	Specified	30 N/mm^2 at 28 days; Proportion defective – %
	1.2	Standard deviation	Fig 3	– N/mm^2 or no data – N/mm^2
	1.3	Margin	C1 or Specified	(k = –) – × – = – N/mm^2; 8 N/mm^2
	1.4	Target mean strength	C2	30 + 8 = 38 N/mm^2
	1.5	Cement strength class	Specified	42.5/~~52.5~~
	1.6	Aggregate type: coarse Aggregate type: fine		~~Crushed~~/uncrushed ~~Crushed~~/uncrushed
	1.7	Free-water/cement ratio	Table 2, Fig 4	0.53
	1.8	Maximum free-water/cement ratio	Specified	0.60 — Use the lower value 0.53
2	2.1	Slump or Vebe time	Specified	Slump 60 – 90 mm or Vebe time – s
	2.2	Maximum aggregate size	Specified	10 mm
	2.3	Free-water content	Table 3	– 225 kg/m^3
3	3.1	Cement content	C3	225 ÷ 0.53 = 425 kg/m^3
	3.2	Maximum cement content	Specified	– kg/m^3
	3.3	Minimum cement content	Specified	325 kg/m^3
				use 3.1 if ≤ 3.2 use 3.3 if > 3.1 — 425 kg/m^3
	3.4	Modified free-water/cement ratio		–
4	4.1	Relative density of aggregate (SSD)		2.6 ~~known~~/assumed
	4.2	Concrete density	Fig 5	2330 kg/m^3
	4.3	Total aggregate content	C4	2330 - 425 - 225 = 1680 kg/m^3
5	5.1	Grading of fine aggregate	Percentage passing 600 μm sieve	65 %
	5.2	Proportion of fine aggregate	Fig 6	43 %
	5.3	Fine aggregate content	C5	1680 × 0.43 = 722 kg/m^3
	5.4	Coarse aggregate content	C5	1680 - 722 = 958 kg/m^3

	Cement (kg)	Water (kg)	Fine aggregate (kg)	Coarse aggregate (10 mm) (kg)
Per m^3 (nearest to 5 kg)	425	225	722	958
Per trial mix of 0.250 m^3	110	60	185	240

Figure 3.2 – Concrete-mix design

The designed concrete mix provided by an external supplier had the benefit of emulating real-world building construction work. The casting of the samples was executed in one single day from one batch to ensure uniformity of the strength in samples.

It was decided to use medium strength concrete and concrete with reduced strength corresponding to deteriorated one due to atmospheric influences. Therefore, it was decided to study concrete as an additional variable in this research. Since concrete strength was an important parameter to explore it was considered to add a group of samples with high strength concrete for the planned future research investigations.

Meanwhile, a combination of the cylinders (150x300 mm) and cubes (150x150x150 mm) were cast to obtain the uniaxial compressive strength of the concrete (Figure 3.3 (a) – (d)). The concrete strength was tested for each shear wall sample on the day of testing and found to be in the region C30/37 for the in-lab cast samples and C20/25 for the ready-made design-mix (Figures 3.3 (e) and (f)).

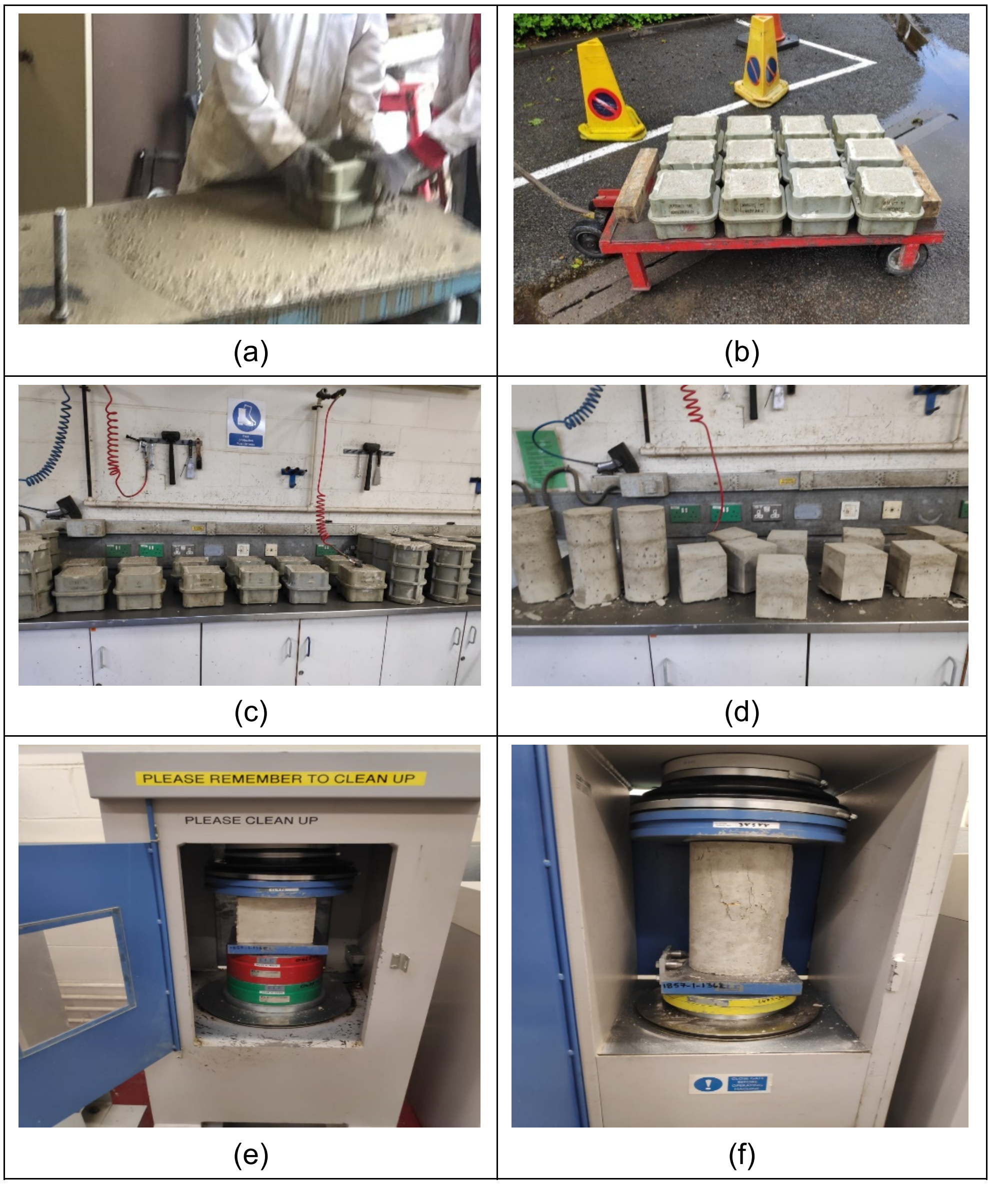

Figure 3.3 - Cubes (a) casting (b) delivery (c) demoulding (d) demoulded (e) cube test (f) cylinder test.

There were four groups of tests (G1-G4) conducted. Each group consisted of two to four samples. The samples and their associated cube and cylinder test results are enlisted in Table 3.1 below. The results of the G1 group is not included in the table below for the reasons discussed further in Chapter four.

Table 3.1 – Compressive cube and cylinder strengths for all samples

Group	Sample	Test Number	Cube Maximum Load (kN)	Cube Compressive Strength (N/mm^2)	Ave. Cube Compressive Strength (N/mm^2)	Cylinder Maximum Load (kN)	Cylinder Compressive Strength (N/mm^2)	Ave. Cylinder Compressive Strength (N/mm^2)
G2	S1	1	439.3	43.93	43.10	522.4	29.6	31.9
		2	424.3	42.43		568.2	32.2	
		3	429.5	42.95		599.2	33.9	
	B1	1	452.4	45.2	42.7	455.4	25.8	33.8
		2	414.7	41.5		660.3	37.4	
		3	414.1	41.4		674.5	38.2	
G3	SA6	1	769.7	34.21	32.21	298.6	23	20.1
		2	679.5	30.2		301.7	17.2	
	BA6	1	713.8	31.73	31.32	359.3	20.33	18.47
		2	688	30.58		293.6	16.61	
	GA6	1	744.9	33.11	31.91	379.2	20.7	20.63
		2	690.9	30.71		364.3	20.55	
	BA10	1	752.3	33.44	33.89	389.4	22.04	21.36
		2	772	34.31		365.3	20.67	
G4	S10	1	637.8	28.35	29.25	364.3	20.61	21.06
		2	678.1	30.14		385.7	21.5	
	B10	1	685	30.45	30.95	271.1	15.34	16.44
		2	707.5	30.44		309.8	17.53	

Since the result of the cube and cylinder tests for the ready-mix concrete was below expectation a further Schmidt Hammer test was conducted to confirm the strength of the concrete for the Groups G3 and G4 samples and the results are enlisted below in Table 3.2.

Table 3.2 – Schmidt Hammer Test results

Group	Sample	Point Number	Average of 10 points (N/mm^2)	Average Strength (N/mm^2)
G3	SA6	1	34.12	35.61
		2	35.91	
		3	36.8	
	BA6	1	29.33	30.7
		2	32.15	
		3	30.63	
	GA6	1	36.93	38.98
		2	41.29	
		3	38.72	
G4	S10	1	32.15	34.3
		2	38.25	
		3	32.5	
	B10	1	32.85	38.88
		2	46.05	
		3	37.75	
	BA10	1	37	33.83
		2	33.15	
		3	31.35	

3.2.2. Reinforcements

Two types of reinforcement steel were utilized for this research study including; low carbon, non-alloy mild steel and high yield steel. The properties of the steel reinforcement are enlisted in Table 3.3.

The BFRP rebars utilized in this research project is with a sanded finish to create better bonding between the concrete and the rebars manufactured by MagmaTech. The sand coating gives excellent bond-strength between the rebars and concrete (MagmaTech, 2019).

Table 3.3 – Reinforcement bars properties

No	Type	BFRP	GFRP	HY Steel	Mild Steel
1	Tensile/Yield Strength (MPa)	1000	1000	500	250
2	Elastic Modulus (GPa)	45+	40+	210	210
3	Colour	Grey	Beige	Steel	Steel
4	Surface	Sand coating	Helical recess	Threaded	Smooth

The type of GFRP rebars (Figures 3.4 (a) and (b)) used in this research study is the E-glass fibre roving with a helical recess for better bond-strength between the concrete and the rebars manufactured by Engineered-Composites (Engineered Composites 2019).

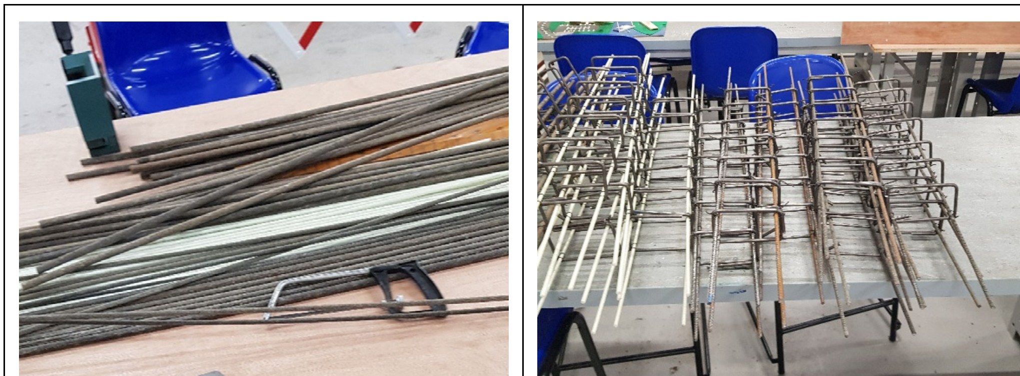

(a) (b)

Figure 3.4 - BFRP and GFRP bars (a) cut in length (b) cages made

3.2.3. Anchorage and Adhesive

The anchorage used in this study was made of 16 mm and 14 mm diameter steel round tubes with 1 mm thickness. The anchorage was applied to the rebars using EP Structural Adhesive (Figures 3.5 a-c). The adhesive was made up of two parts comprising Bisphenol A/F epoxy risen with and a modified aliphatic polyamine hardener and inert filler. The mixing ratio of the hardener to risen material is 1:2.4. The strength achieved by the adhesive in 24 hours after mixing was 30 N/mm^2 (EP Structural Adhesive, 2019).

(a) (b) (c)

Figure 3.5 – Anchorage (a) application, (b) EP-structural adhesive, (c) applied

3.3. Methodology

3.3.1. Introduction

The experimental programme comprised of testing 12 RCSW samples in four groups G1, G2, G3 and G4. Each group of the samples consisted of a BFRP and one steel-reinforced specimen as a control sample (Table 3.4).

The first group (G1) consisted of four specimens, two reinforced with 6 mm BFRP and two reinforced with Steel rebars. The concrete strength for these samples was C30/37, and no Anchorage was utilized. Initially samples i1S6 and i1B6 were tested follow by i2S6 and i2B6.

The second group (G2) comprised one steel-reinforced sample and one BFRP 6 mm diameter reinforcement with anchorage. The concrete strength for this batch of samples is C30/37 and the abbreviated names S6 and B6 for Steel and BFRP 6 mm samples respectively.

The third group (G3) included one steel, one BFRP, one GFRP 6 mm and one BFRP 10 mm reinforcement samples with anchors abbreviated as SA6, BA6, GA6 and BA10. The concrete strength of this group of samples was about C25/30.

The fourth group (G4) had two samples reinforced with 10 mm Steel and BFRP rebars; hence, abbreviated as S10 and B10, respectively. The sample had no anchorage, and the concrete strength for this batch of samples was about C25/30. All samples were cast and tested in the structural lab of the KUL.

Table 3.4 – Grouping and other details of the shear-wall samples

Groups	Sample No.	Reinforcement type	Diameter	Concrete Strength	Anchorage	Abbreviated Name
G1	1	Steel	6	C30/37	No	i1S6
	2	BFRP	6	C30/37	No	i1B6
	3	Steel	6	C30/37	No	i2S6
	4	BFRP	6	C30/37	No	i2B6
G2	5	Steel	6	C30/37	No	S6
	6	BFRP	6	C30/37	No	B6
G3	7	Steel	6	C25/30	Yes	SA6
	8	BFRP	6	C25/30	Yes	BA6
	9	GFRP	6	C25/30	Yes	GA6
	10	BFRP	10	C25/370	Yes	BA10
G4	11	Steel	10	C25/30	No	S10
	12	BFRP	10	C25/30	No	B10

3.3.2. Construction and Instrumentation

The construction process of the shear wall samples was started by cutting the wood-boards in shape for the formwork and cutting the rebars in-length to make the reinforcement cages. Each group of the samples were constructed with control samples. The control samples were reinforced with steel rebars to be able to compare the FRP reinforced samples. Details of construction are described below.

Preparation of the formwork started by choosing 1.2 m x 2.4 m x 30 mm wood-boards cut in shape to accommodate casting of 1 m x 1 m x 0.1 m reinforced concrete samples. Figure 3.6 shows the sides of the boards cut in 0.1 m width to prepare a box-shape for the casting of the concrete. Figure 3.6 (a) shows the cutting of the board edges, and Figure 3.6 (b) shows the prepared version of the box-shape for the casting of the samples.

The formwork board-joints were sealed to avoid any escape of cement slurry as can be seen in Figure 3.6 (c). Furthermore, the formwork was lightly brushed with oil to make demolding of the samples possible after the curing period as can be seen in Figure 3.6 (d).

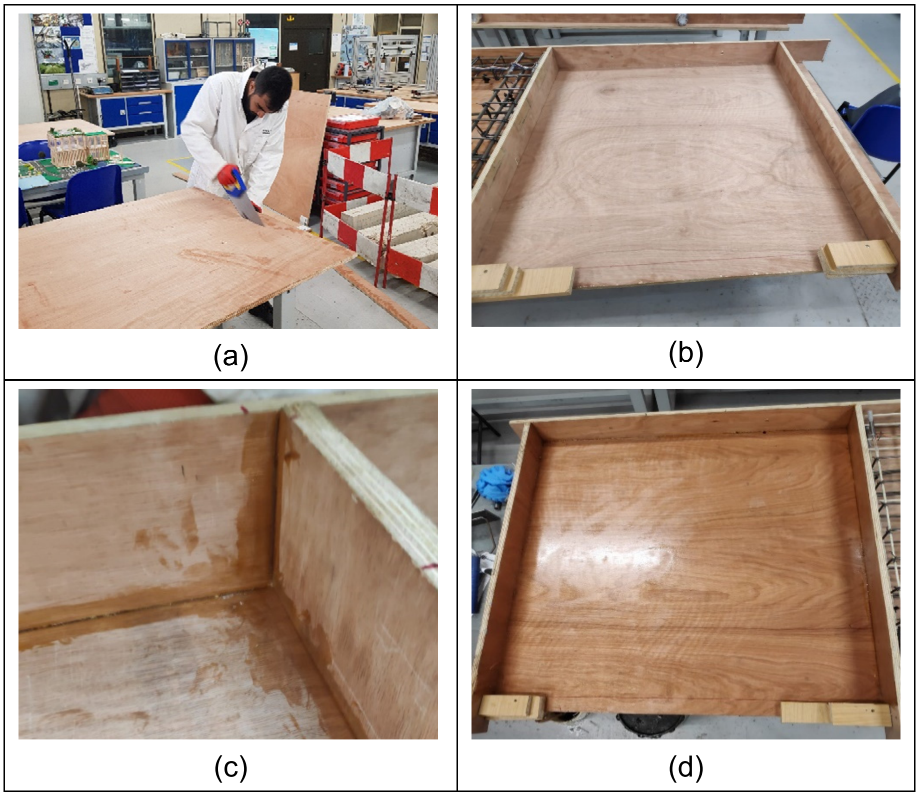

Figure 3.6 – Formwork (a) cutting, (b) constructed, (c) sealing, (d) oiling

The cages building started after the formworks were completed by cutting the bars in length, preparing the shear links, making the cages elements (beam and column reinforcements) and the full cage. The process of constructing the cages is shown in Figures 3.7 (a)-(d).

The bars were cut in length by the KUL Concrete Lab technicians after all the sizes for the reinforcement bars, shear links and dowels were given. The bars were bent using the bar-bending equipment. Smaller bar-benders (Figure 3.6 (a) top) was used to bend 6 mm bars and bigger bar-bender (Figure 3.6 (a) bottom) was used to bend 10 mm bars.

The reinforcement cages for the shear wall beam and column elements were developed by laying the reinforcement bars flat and tying the shear link to them, as shown in Figure 3.7 (b). four rebars and seven shear links were used to develop one beam or column cage (Figure 3.7 (c)).

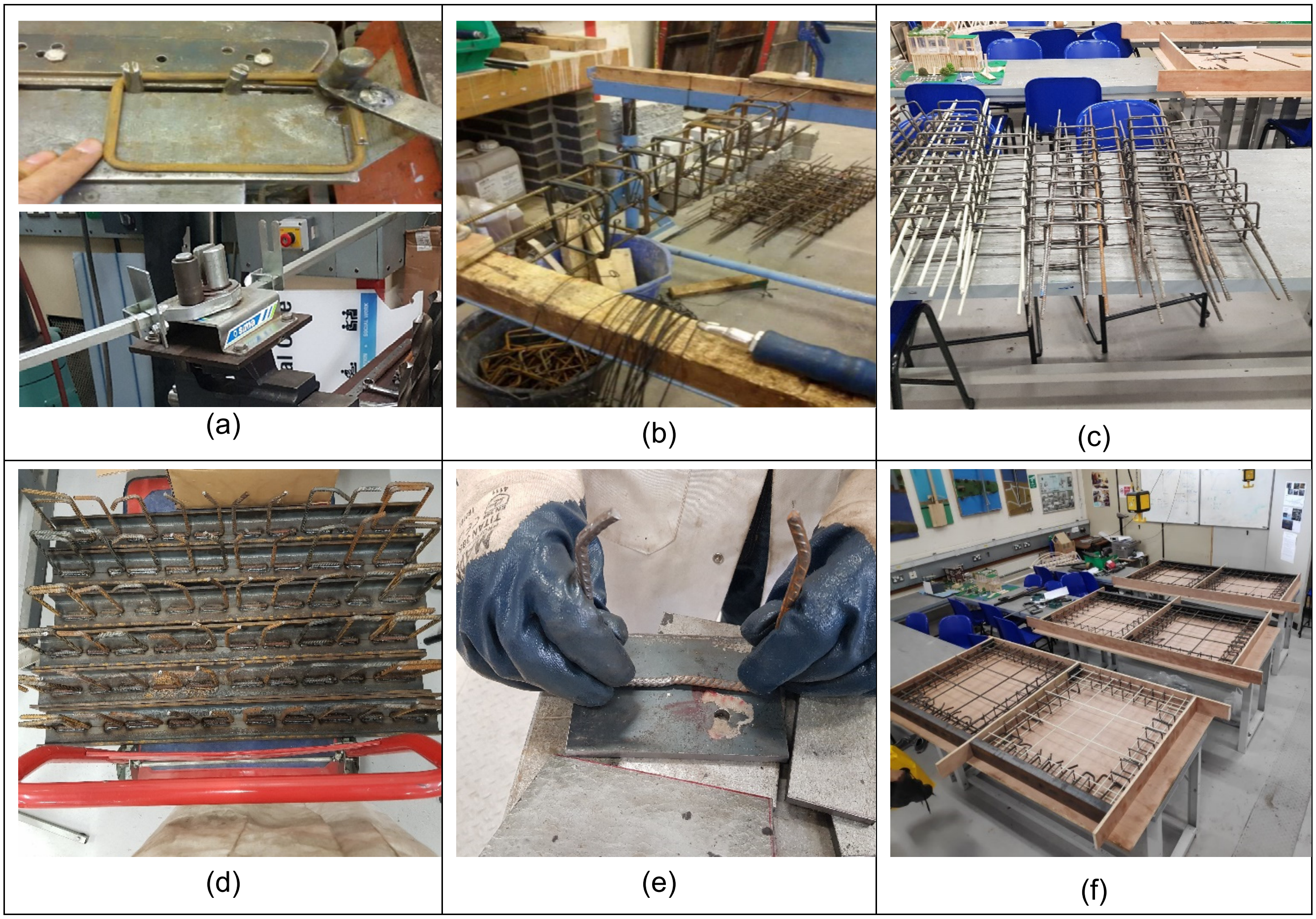

Figure 3.7 – Rebars (a) bending, (b) cage making, (c) cage parts, (d) hooks, (e) load plate, (f) full cage

The dowels (10 mm high yield steel) were bent and welded to the PFCs (Parallel Flanged Channels 100 x 50 x 10 mm) as the mechanism to hold the shear-walls in-place as shown in Figures 3.7 (d). Additionally, 10 mm bars were bent and welded to steel-plates (140 x 100 x 3 mm) to act as hooks holding the steel-plate in-place. Steel-plates were designed to serve as load-spreader at the point of lateral-loading.

The main reinforcement bars, which are the particular subject of this study, are placed in the middle of the beam and column cages, as shown in Figure 3.7 (d). Two vertical and two horizontal bars are placed at an equal distance apart from each other and tied to the beam and column cages respectively. Fully reinforcement cages for Steel, BFRP and GFRP samples are shown in Figure 3.7 (f).

Internal strain gauge by Micro Measurement VPG brand (Vishay) model CEA-06-240UZ-120 with the dimension of 24 mm x 12 mm was applied using M-Bond 200 strain gauges adhesives. Also, a gauge bond surface cleanser and preparator by the same provider were used to measure the strains in all vertical bars and a main horizontal bar (Micro Measurement A VPG Brand, 2019). Figure 3.8 (a) shows the package and (b) shows a single gauge.

(a) (b)

Figure 3.8 – Internal strain gauges (a) package, (b) single gauge

The position of the gauges was marked on the reinforcement cages before application. The surface of the locations was smoothed by file and sandpaper as can be seen in Figure 3.9 (a). The surfaces were well cleaned and cleared as is indicated in Figure 3.9 (b).

M-200 adhesive packages by Micro-Measurements (Figure 3.9 (c)) was utilized to install the gauges, which include the following solutions and material:

- GC-6 Isopropyl Alcohol
- M-Prep Conditioner A
- M-Prep Neutralizer 5A
- M-200 Catalyst
- M-200 Adhesive
- Cotton Applicators
- Gage Installation Tape

All surfaces were well cleaned using Isopropyl Alcohol and M-Prep Conditioner A (Figure 3.9 (d)) and dried using cotton; they were wiped free of chemical using M-Prep Neutralizer 5A (Figure 3.9 (e)).

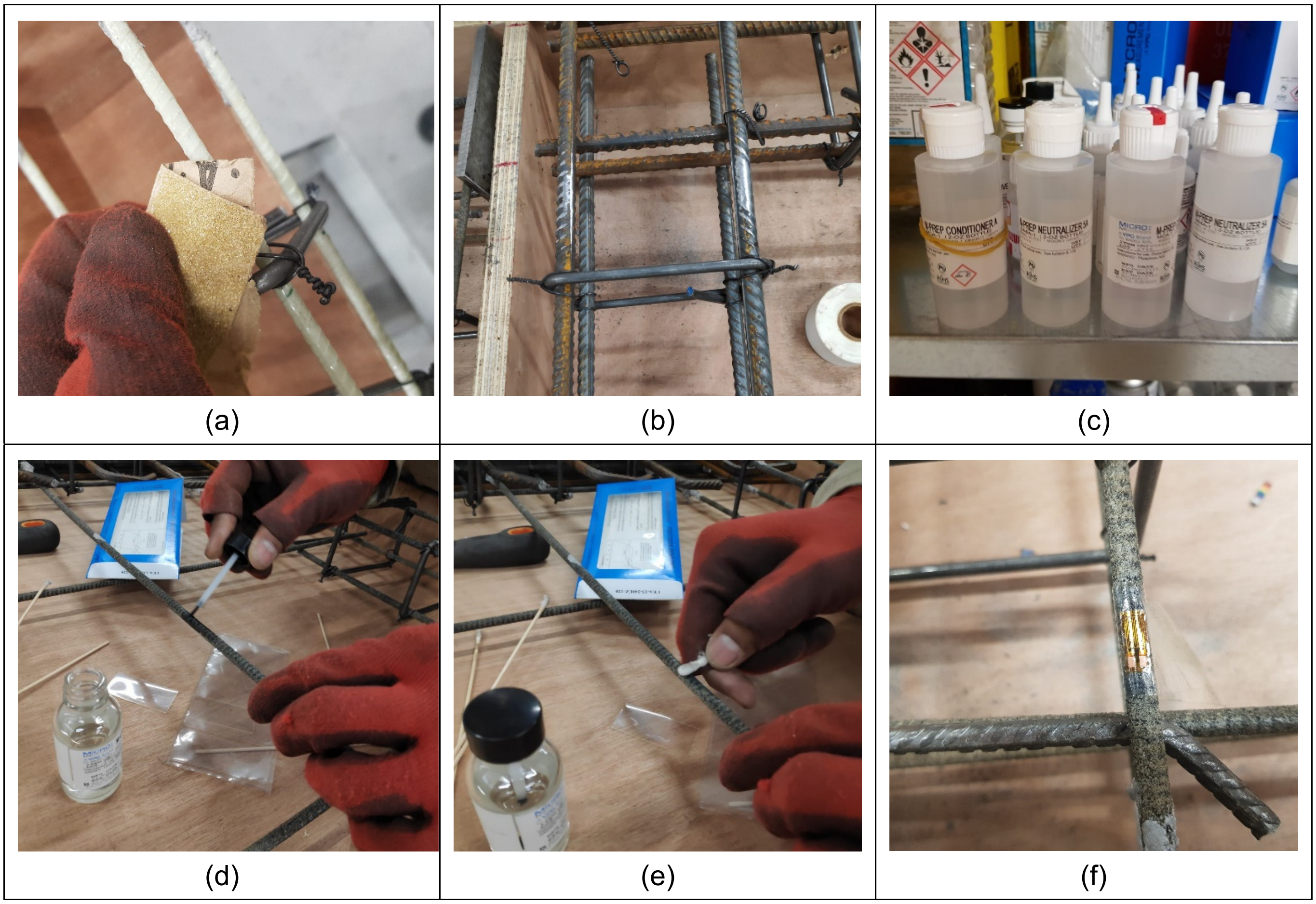

Figure 3.9 – Stains gauge installation; (a) filling, (b) smoothed surface, (c) adhesive solutions, (d) conditioner application, (e) neutralizer application, (f) adhesive applied.

M-200 Catalyst and Adhesive were applied to the clean surface, and the gauges were attached using tweezers to handle and installation tape to hold the gauges. The catalyst was used in a small thin layer for quicker hardening of the adhesive. One to two drops of M-200 adhesive was applied to the gauge to make sure even surface of the adhesive for bonding.

Gauges wire with colour-codes were soldered to the gauges using a soldering gun and the solder metal alloy (Figure 3.10 (a)). Adhesive tape was used to help with, holding the gauge wires and correct positioning of solders (Figure 3.10 (b)). The gauges were covered with silicon adhesive to protect them from moisture or damage during concrete casting (Figure 3.10 (c)).

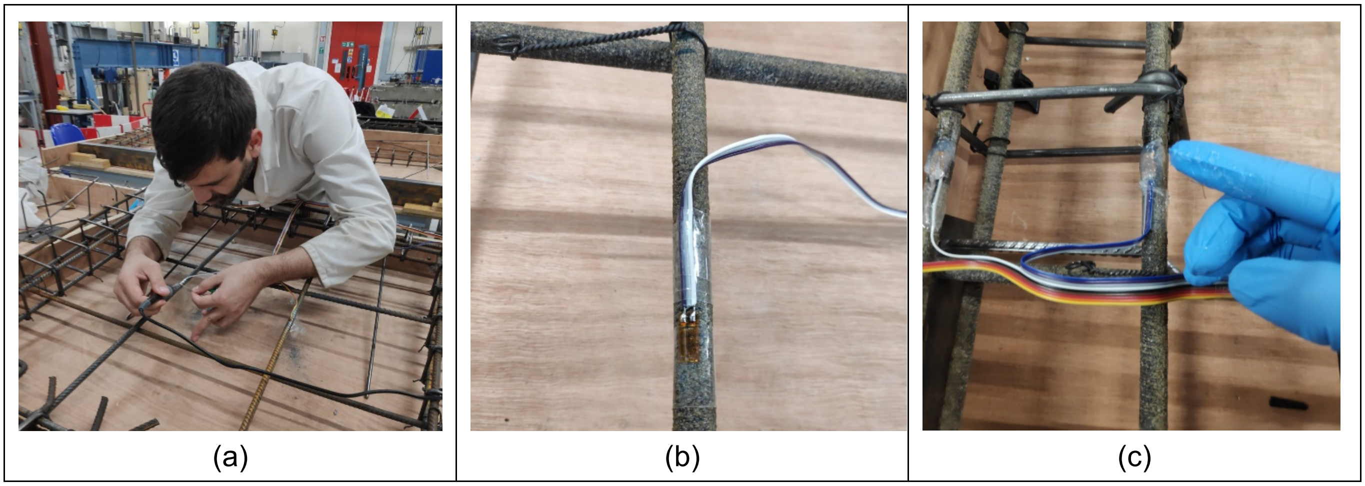

Figure 3.10 - Gauge wires (a) soldering, (b) soldered, (c) silicon cover applied on gauges

External gauges by Tokyo Measuring Instruments Lab (TML) model PL-60-11 linear single element gauge (Figure 3.11 (a) top)) purpose-built for concrete surfaces was applied to the surface of the shear wall (Tokyo Measuring Instruments Lab., 2019). RS-Pro two-part epoxy risen adhesive with chemical composition Bisphenol-A (Epichlorohydrin) and Bisphenol-F (Figure 3.11 (a) bottom) was used as an adhesive agent. The adhesive was given sufficient time to cure. A combination of three gauges in two orthogonal directions and one diagonal direction was applied in the centre of the wall to measure in-plane strain in all principal directions (Figure 3.11 (b)).

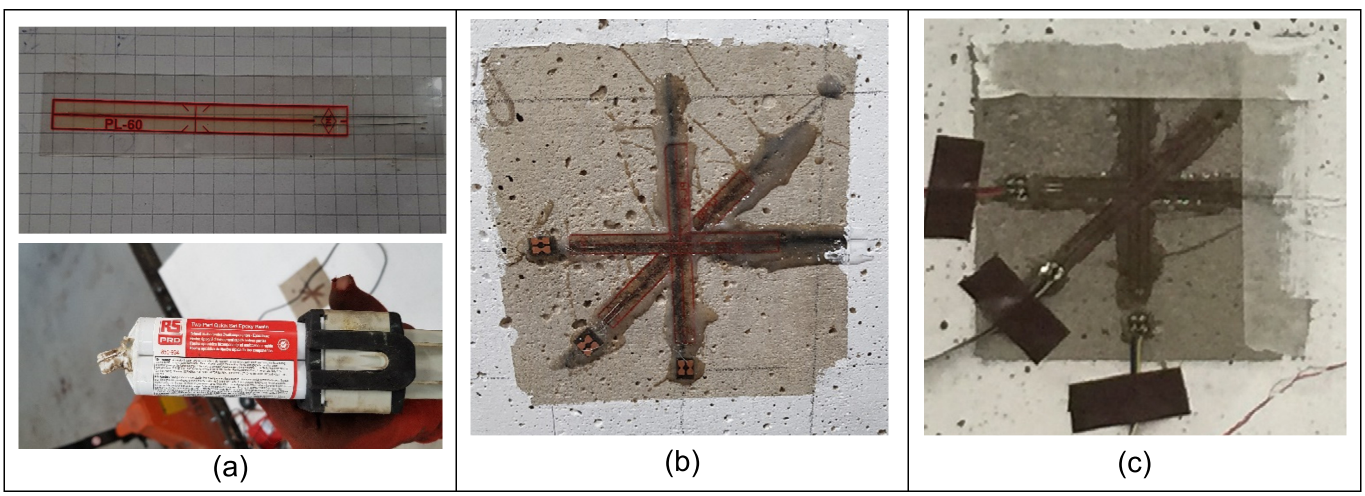

Figure 3.11 – External strain gauges (a) PL-60-11 gauge and epoxy adhesive, (b) applied on the concrete surface, (d) gauge wires connected

A small amount of solder was applied at each terminal using heat to connect the colour-coded gauge-wires (Figure 3.11 (c)). The wire to gauge connections were checked using a multi-metre (Figure 3.12 (a)) by testing the ends of the wires to be connected to the data collector (Figure 3.12 (b)). Diagrammatic locations of all the strain gauges are illustrated in Figure 3.14.

The colour-coded gauge-wires were all connected to the data-logger ("National-Instruments" model cRIO-90506 also known as the Kingston Strain Logger) as indicated in Figure 3.12 (c) per colour-code that identifies each of the internal/external strain gauges. The data-logger was connected to the PC, which was running the interface application for the data-logger.

The strain gauges were identified and as per the wires colour-code. A joint connector was used to name the gauges as 1-10. The wires from the internal-stain-gauges were marked as gauges number 1 to 7. The wires from the external-strain-gauges were named as gauges number 8-10. The PC running the interface and the data-logger set-up is shown in Figure 3.12 (d).

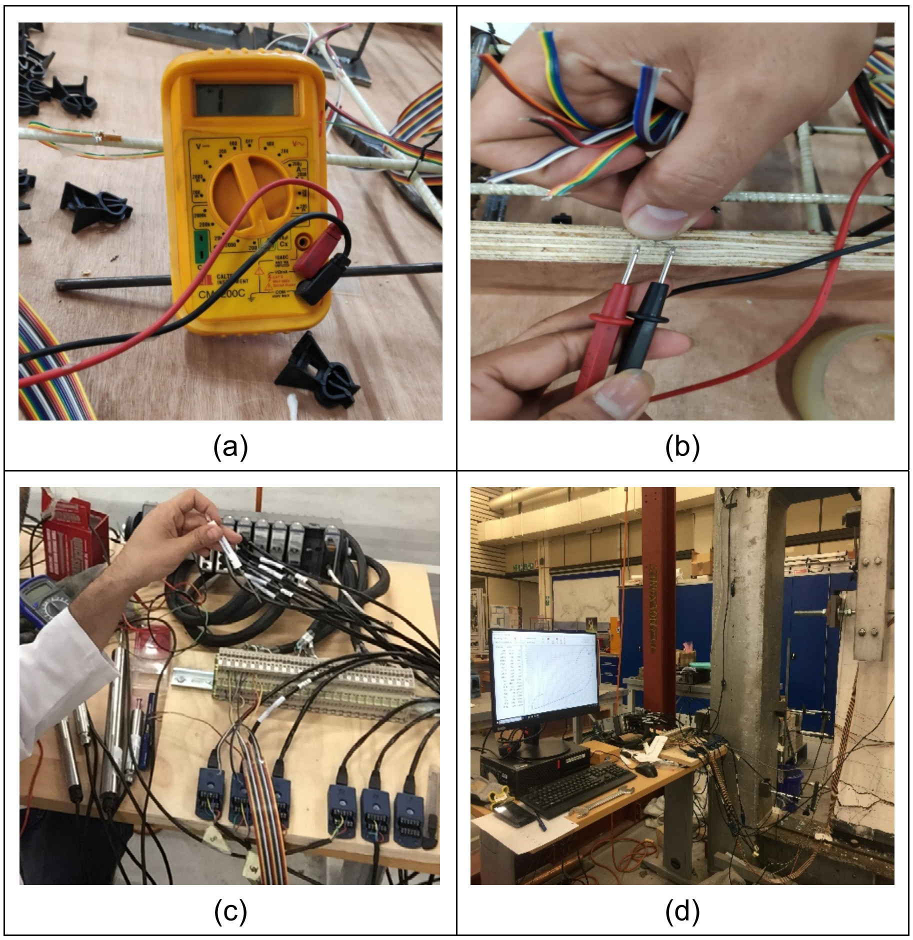

(a) (b) (c) (d)

Figure 3.12 – Gauges wires (a) multi-metre, (b) connection check, (c) data collector connection, (d) computer connected to the data collector.

In addition to the above linear variable displacement transducers (LVDTs) were also used in many critical positions to capture deformation of the wall due to the lateral loads. The LVDTs were attached to the strong frame and connected to the specimens to capture sample displacements relative to the frame. The LVDTs measured displacements of up to 50 mm.

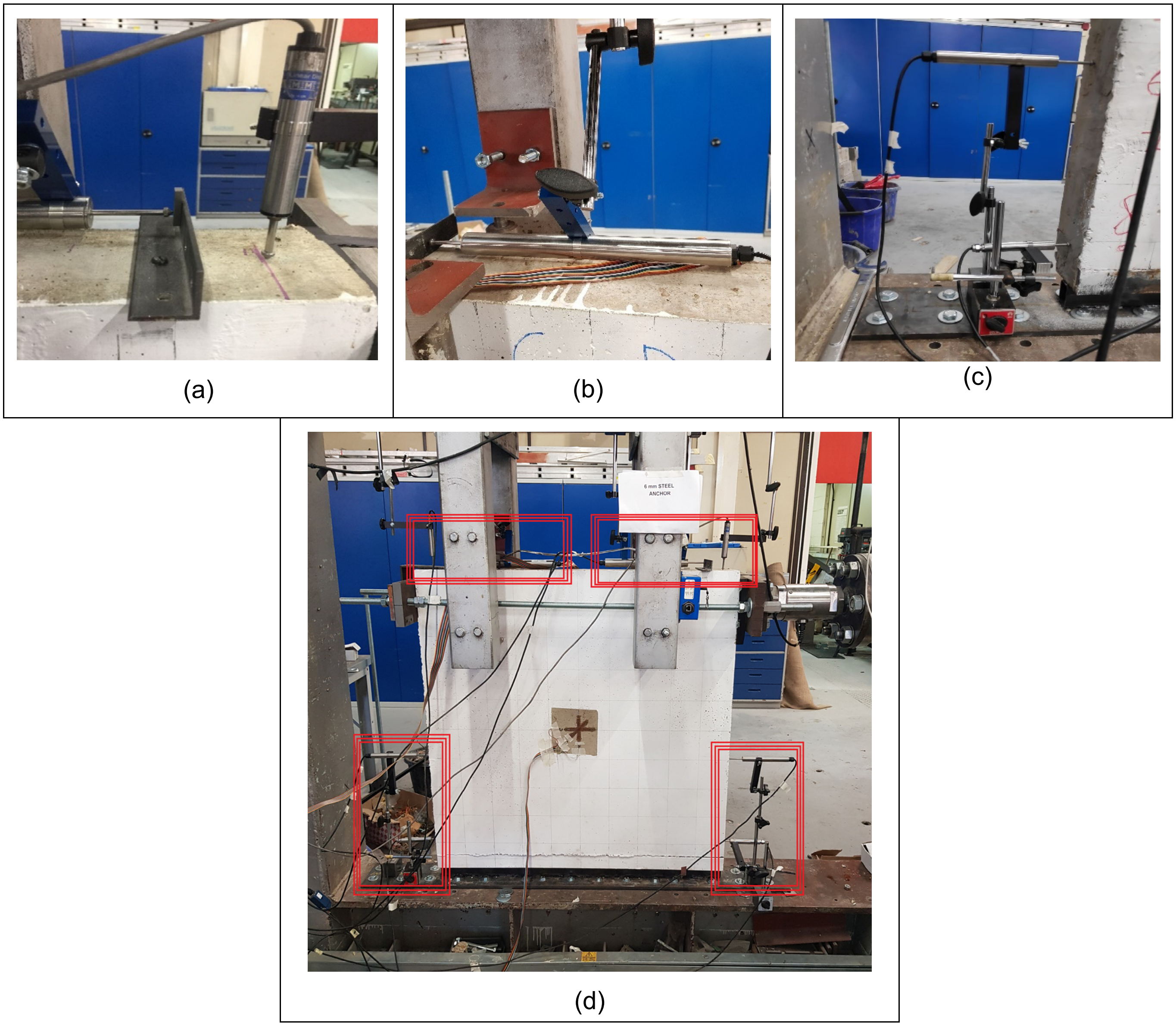

(a) (b) (c)

(d)

Figure 3.13 – LVDTs (a) vertical on top, (b) horizontal on top, (c) bottom left, (d) locations highlighted in red.

The LVDTs at the top of the wall was installed to measure the displacement of the wall in vertical (uplift) as shown in Figure 3.13 (a) and horizontal (in-plane) directions as shown in Figure 3.13 (b). L-shape angle steel was installed on top of the shear wall samples to allow installation of the horizontal LVDTs as shown in Figures 3.13 (a) and (b) stopping the tip of the horizontal gauge.

The LVDTs in the sides of the wall were installed to measure lateral displacements at critical locations. The bottom two were installed to measure movement in the bottom fixed area, and the upper two were installed to measure the displacement in the critical shear force region (Figure 3.13 (c)). All LVDTs are installed symmetrically to capture the effect of pushing and pulling forces on the symmetrical behaviour of the shear-wall; the locations of the LVDTs are shown in Figure 3.13 (d) highlighted in red and diagrammatic depiction of the LVDTs locations are shown in Figure 3.14.

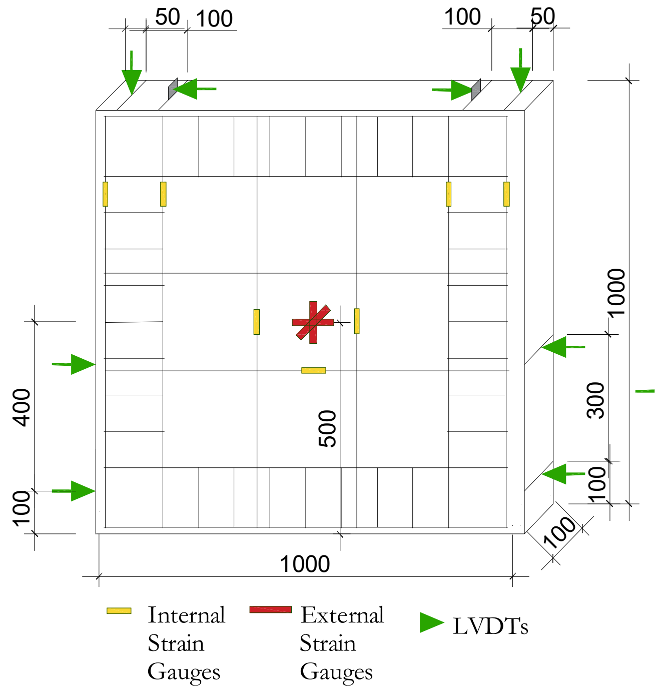

Figure 3.14 - Locations of the LVDTs, internal and external gauges

The LVDTs are calibrated utilising the gauges blocks from the gauges box shown in Figure 3.15 (a). The gauge blocks were used to check the computer-recorded-displacement caused by the block when applied between the gauge and the shear-wall samples, as indicated in Figure 3.15 (b).

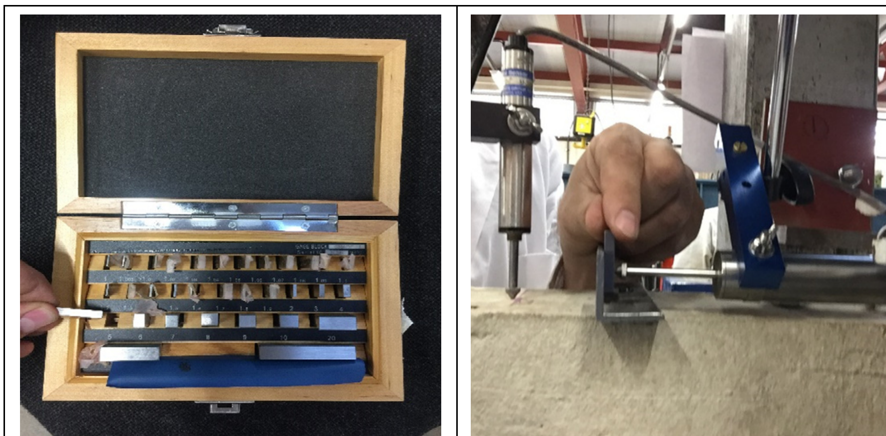

(a) (b)

Figure 3.15 – Precision (a) gauge blocks box (b) gauge block application

The concrete was cast in the structural lab using well-borrows and shovels to deliver the concrete from the concrete-mixing-truck to the formworks. The concrete casting process is shown in Figures 3.17 (a) and (b). A vibrator was used to settle the concrete in between the cage and to reduce the air traps in the concrete batch and the surface was smoothed with a using rectangular trowel (Figure 3.17 (c)).

The smooth surfaces of the samples can be seen in Figure 3.17 (d). Hessian sheets were used to cover the samples and continuously soaked to prevent moisture evaporation for 28 days (Figure 3.17 (e)). A standard slump test was carried out to ensure workability and consistency of the concrete mix slump tests were execute before casting the samples. The test was conducted per BS EN 12350-2: 2009 regulations to ensure the workability of the concrete, as shown in Figure 3.17 (f).

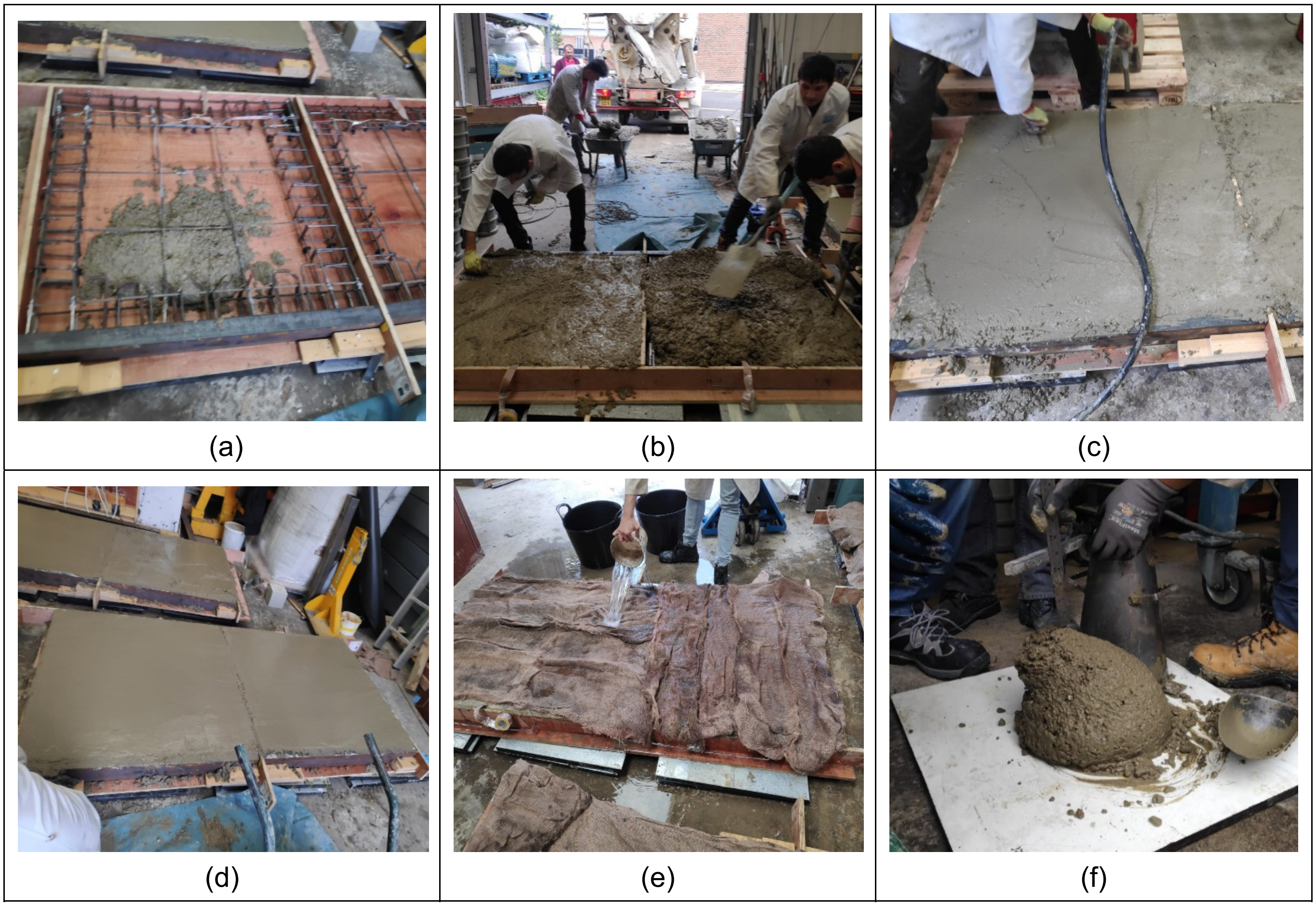

Figure 3.17 – Concrete casting (a) start of casting, (b) settle the concrete, (c) vibrating and trowelling, (d) casted concrete samples, (e) Hessian sheets and watering (f) slump test

3.3.3. Welding and Installation

The shear-wall samples were delivered to the Structural Laboratory of KUL after casting and curing to start testing. In the lab, additional steel-profiles were welded to the shear-wall sample to be able to install the sample to the Testing-Frame.

The Testing-Frame had a certain number of drilled holes to fix samples and drilling more holes were not advisable, to be able to retain the strength of the strong Testing-Frame, also known as the Reaction-

Frame. Therefore, a thick-steel-plate (12 mm) was ordered with holes to match with the frame. Design nuts and bolts of suitable size (M12, M10 and M8) was used (Figure 3.18 (a)).

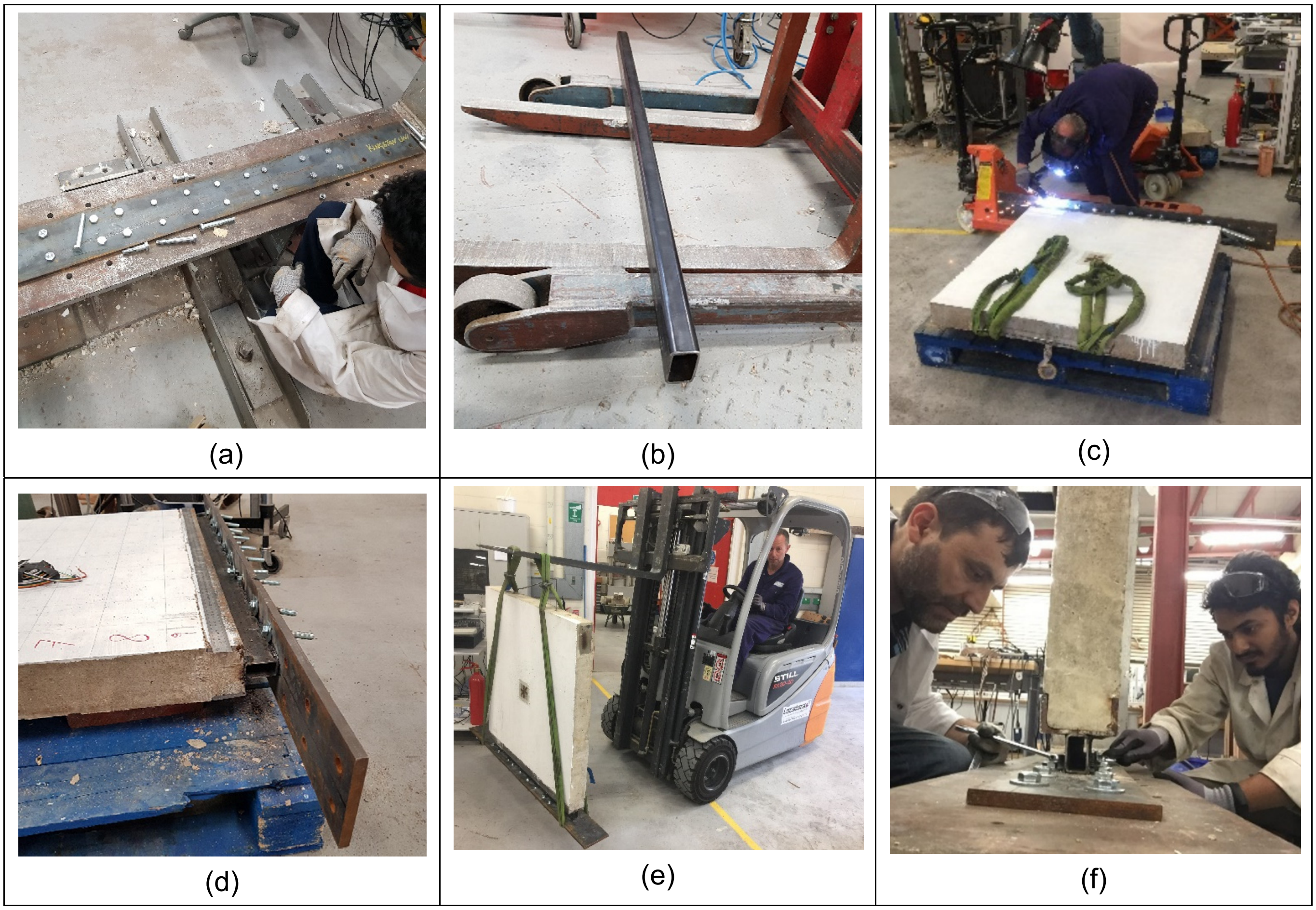

Figure 3.18 – Fixing mechanism (a) thick steel plate, (b) RSH, (c) welding, (d) mechanism welded, (e) delivery, (f) fixing to the frame

RHS size 50 x 30 x 3 mm (Figure 3.18 (b)) was welded to the thick-plate and the PFC (in-built with the shear-wall samples) at the same time. The welding process and the complete welded samples are shown in Figure 3.18 (c) and (d), respectively. All bolts were inserted into the thick-plate holes first, as shown in the photos cause the gap between the thick-plate and PFC was small.

The samples were delivered for installation to the Testing-Frame using the forklift truck in the Structural Laboratory, as shown in Figure 3.18 (e). The wall was fixed to the Testing-Frame/Reaction-Frame using the design bolts, as shown in Figure 3.18 (f). All bolts were securely tightened.

The shear wall samples were installed and fixed in the bottom steel-thick-plate to the strong Reaction-Frame, as illustrated in Figures 3.18 (f), and 3.19 (b). The load was applied at the top-right corner of the shear-wall laterally on the thick-steel-plates connected to the load-cell. The thick-steel-plate was connected to the opposite (top-left) thick-steel-plates using 22 mm steel screw rods to translate pulling tension forces to compression (Figure 3.19 (a) and Figure 3.20).

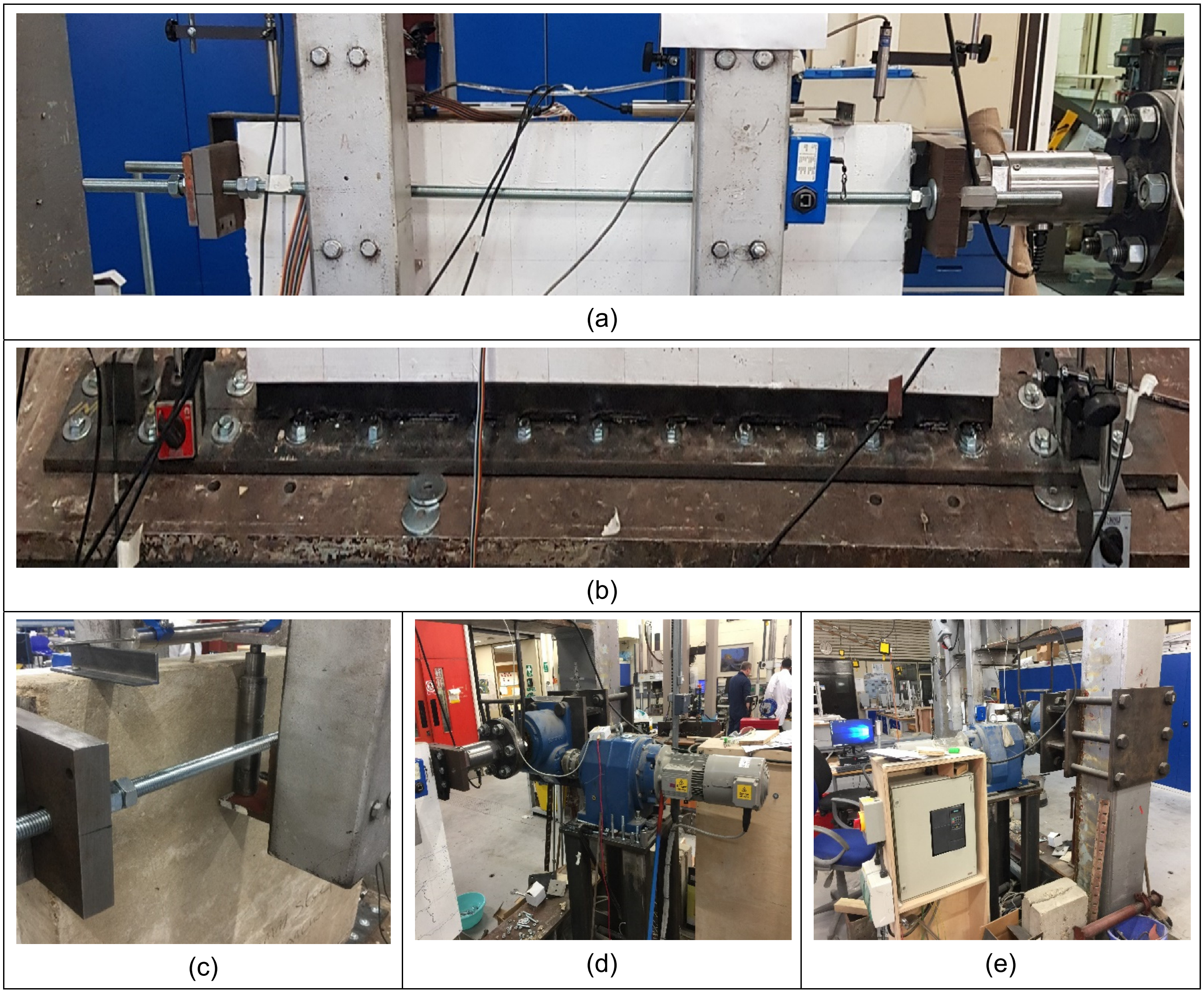

Figure 3.19 – Installation (a) loading mechanism and lateral support, (b) bottom fixity, (c) lateral support roller, (d) screw jack gear and motor, (e) screw jack clamp and power-box

Lateral-support was provided to the shear-wall samples using a roller connected to the strong-beams, which are in turn connected to the strong-frame (Figure 3.19 (c)). The screw-jack model BD Benziler 500 kN run by electric-motor, torque-increased by gearboxes and control by the load-cell was used (Figure 3.19 (d) and Figure 3.20).

The screw-jack was fully clamped to the strong reaction-frame by a rigid box made up of a 35 mm thick square flat plate fully-fixed with HSFG 42mm diameter bolts to the frame. Additionally, metallic struts were installed below to prevent any deflection of the jack due to very heavy self-weight. The motor power-button and emergency stop button were in the white box next to the motor (Figure 3.19 (e) and Figure 3.20).

The reaction frame was fully fixed in the strong concrete floor underneath, as shown in the diagrammatic illustration of the test set-up (Figure 3.20). The diagrammatic illustration also shows the position of the clamp, screw-jack, load-cell, lateral-supports, rollers, steel rod, plate, PFC, RHC, plate (bottom), bolts, shear-wall, and struts.

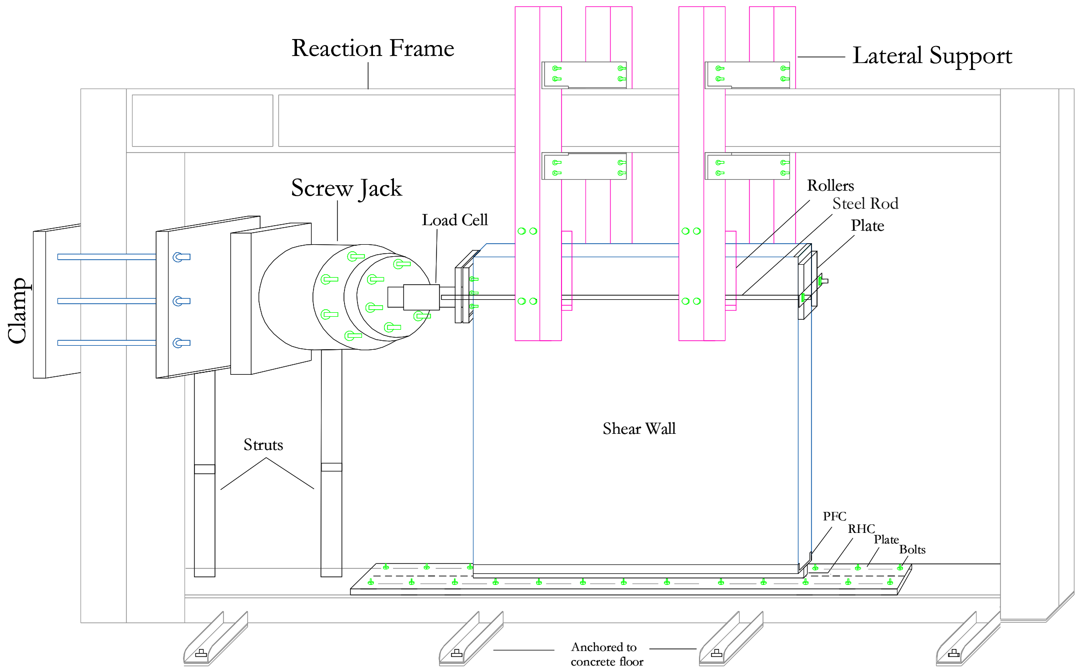

Figure 3.20 – Diagrammatic illustration of the experimental test set up

3.3.4. Loading and Data-Collection

Generally, a widely used seismic loading protocol for components of RC structures is not yet available. A unique loading history in the codes and standards is not available either because the earthquake specifications are not alike. However, the cumulative damage effects can be studied through cyclic loading (Krawinkler 2009).

There are several loading protocols in the literature that have somewhat different loading histories; however, they are different in detail but not the concept. ATC-24 (1992) protocol is one of the first protocols for seismic performance evaluation of component using a reversed cyclic loading history (Krawinkler 2009).

The loading protocol used in this study is modified ATC-24. The protocol is initially designated for steel structures and components which is very demanding on the reinforced concrete. Hence, the numbers of cycles are "modified" to one for each amplitude to allow observation of cumulative damages on the next amplitude of cyclic load.

The samples were tested under lateral quasi-static reversed cyclic loading until failure. All the loads were displacement controlled, and the loading-history for all cycles were thoroughly recorded. The load cycles were applied to the sample as smoothly as possible (3 mm/minute) per modified ATC-24 protocol (Figure 3.21). The load was controlled by using the designated application associated with the "National Instruments (NI)" data-logger cRIO-90506 (Figure 3.12 (c)).

The loading was stopped when the shear wall could not sustain more loads and failed. A maximum of 14 cycles of the load was applied to the test specimen, and cracks were recorded against each cycle and its corresponding load magnitude. One load cycle for each amplitude of displacement was applied to start from 0.2 mm going up to 40 mm displacement (Table 3.5).

Table 3.5 - Load cycle – displacement amplitude

Loading cycles	1	1	1	1	1	1	1	1	1	1	1	1
Displacement Amplitude (mm)	0.2	0.4	0.8	1.2	2.5	3.5	5	10	15	20	25	30

The displacements were controlled (by the LVDT-5) at the top-right of the samples. The loading was stopped when the sample was crushed and started rocking like a mechanism; further explanation about the "rocking" behaviour of the samples are given in Section 4.

The data-logger interface software detected all the strain-gauges and LVDTs connected to the data-Logger and required the user to "name" them. All LVDTs detected were names as LVDT 1-8 clockwise (depending on their location of installation to the sample) and all the strain-gauges were names as SG 1-10; where SG 1-7 represented the internal strain-gauges, and the SG 8-10 represented the external-gauges (Figure 3.21).

Each displacement amplitude was given a specific file-name, and for each shear-wall sample, a separate folder was created. The output files from the software were in the "Microsoft Excel Comma Separated Values File (.csv)" format which could be opened and further analysed using MS-Excel. All LVDT recordings were in millimetre (mm) and all stain-gauge recordings were in micro-strain (μStrain).

The displacement values were programmed to the software, and the load was applied to the samples through the rotation of the screw jack. All relevant variable was recorded against the given displacements. At the end of the displacement increment, the process was interrupted to save the data before the next cycle was applied, and the file was saved before the next loop of cyclic load increment was applied.

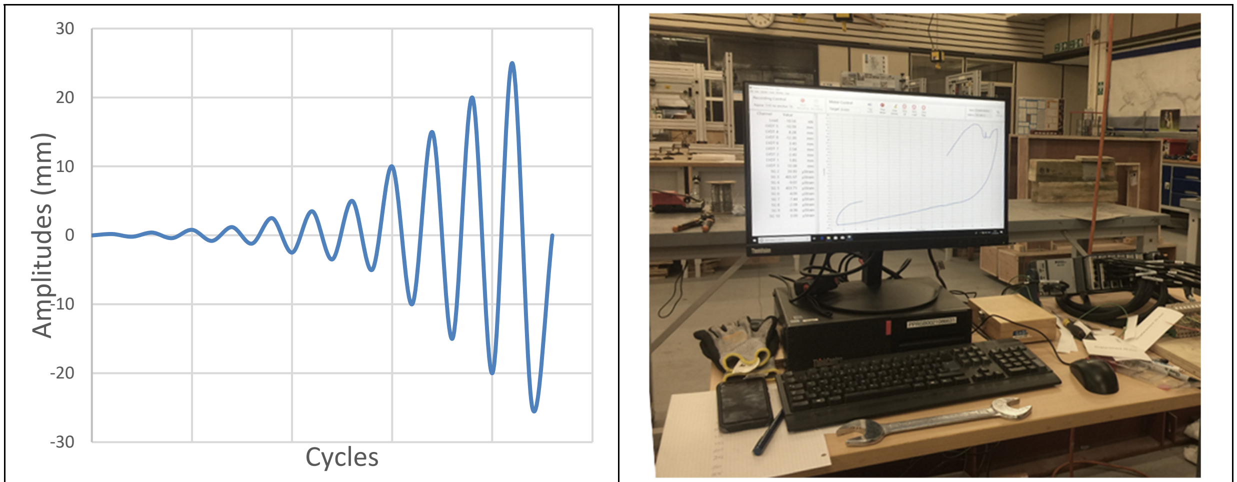

(a) (b)

Figure 3.21 – (a) ATC-24 loading protocol – displacement amplitude against cycles, (b) Designated software interface for NI Data-logger

Experimental test set-up panoramic-view is shown in Figure 3.22 as one of the shear wall samples is installed into the rig. From right to left in the Figure following major items (minor items can also be seen but not described) can be seen; electrical motor, screw-jack clump - gear-boxes - loading cell, lateral support beams, a shear-wall sample, strong frame, data-logger and the computer connected to the data-logger.

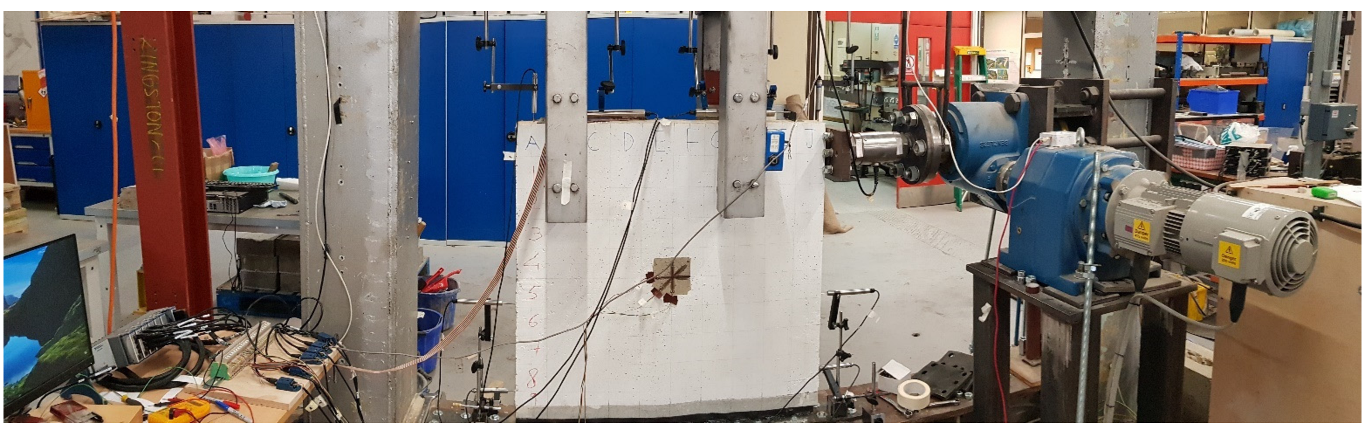

Figure 3.22 – Experimental test set-up panoramic-view.

4. Experimental Results and Analysis

The experimental results are divided into four groups as tabulated in Table 3.3.

4.1. Group One (Pilot Study)

This group consisted of four samples that were initially tested, including i1S6, i1B6, i2S6 and i2B6. There were two steel-reinforced, and two BFRP reinforced samples in this group. The reinforcement cages were built with 6 mm diameter reinforcement bars, and the concrete strength for this group was about C30/37. No rebars anchorage was applied in this group of samples (Table 4.1).

Table 4.1 – Group one samples details

Groups	Sample No.	Reinforcement type	Diameter	Concrete Strength	Anchorage	Abbreviated Name
G1	1	Steel	6	C30/37	No	i1S6
	2	BFRP	6	C30/37	No	i1B6
	3	Steel	6	C30/37	No	i2S6
	4	BFRP	6	C30/37	No	i2B6

4.1.1. Observations and Results

At the initial stages of loading, the wall deformed and some cracks were observed. However, as the load increased a premature detachment at the bottom between the wall and the connecting steel frames was observed so it was decided that additional brackets could be installed to study further the behaviour of the wall. The pictures in Figure 4.1 show the initial four samples installation of the "modification-brackets".

Figure 4.1 (a) illustrates the bottom fixity modification steel bracket and (b) shows its loading surface modification steel brackets for sample i1S6. Figure 4.1 (c) shows the bottom fixity modification, and brackets and (c) shows the loading area steel bracket addition. This is because a premature detachment occurred at the fixed-bottom of the sample to Strong-Frame and early crushing loading-surface-area

The pictures in Figure 4.1 (e) and (f) shows the front view and angle-view (respectively) for the modification of the bottom-fixity in the i2S6 sample by adding two steel-brackets. Figure 4.1 (g) shows the detachment of the sample from the bottom fixity. Figure 4.1 (h) shows the front view for the bottom fixity modification by adding two new steel-brackets to the i2B6 sample. The steel brackets were added after the early displacement of the sample in the fixed-bottom to the strong-frame. The displacement was between the concrete and the PFC.

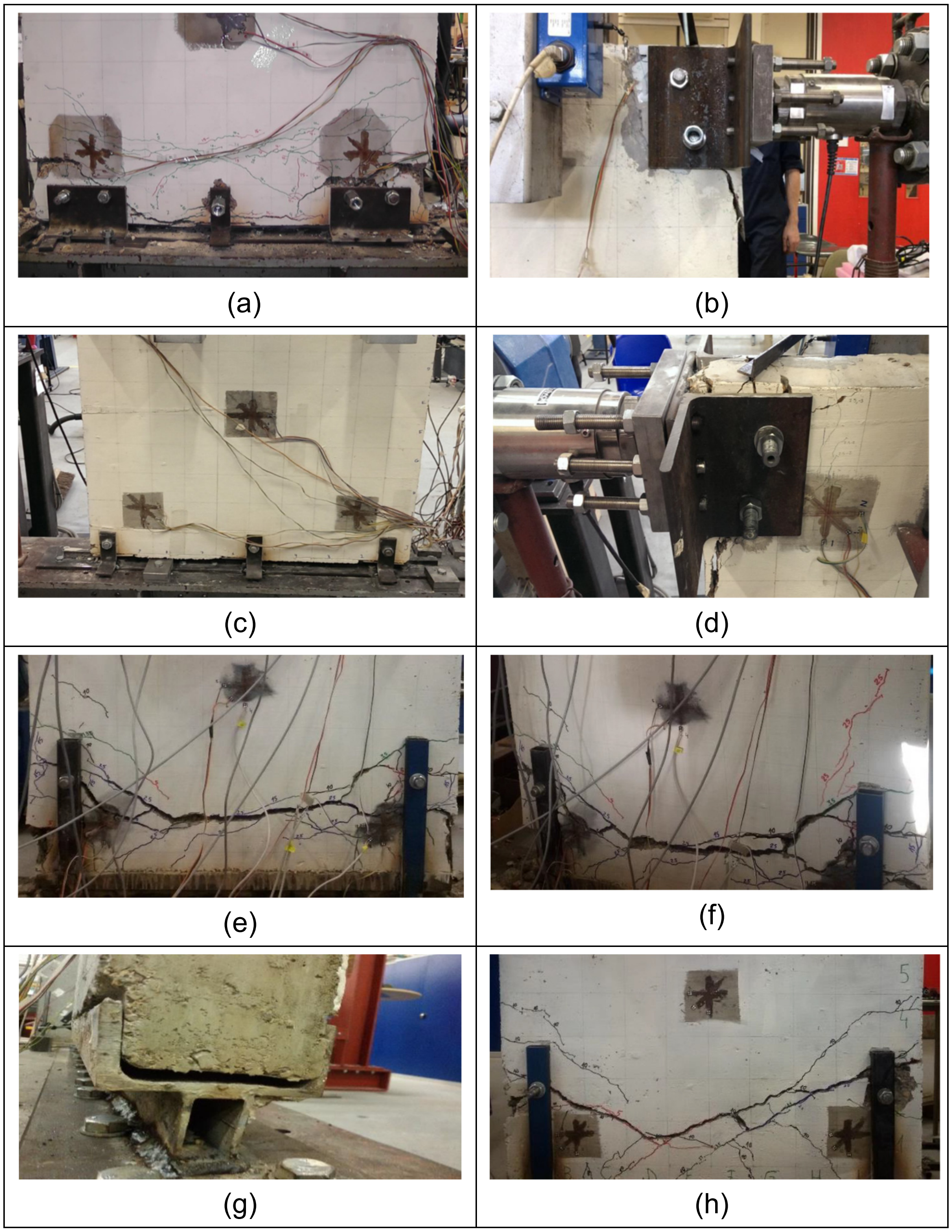

Figure 4.1 Shear walls samples (a) i1S6 bottom, (b) i1S6, top (c) i1B6 bottom, (d) i1B6 top, (e) i2S6 bottom, (f) i2S6 bottom at an angle, (g) i2B6 bottom separation, (h) i2B6 bottom modification

The initial-samples results from i1S6, i1B6, i2S6 and i2B6 are not included in the analysis due to the modifications. The modifications were necessary due to the separation of the fixed-bottom from the strong-frame and crushing of the concrete surface area attached to the loading-cell. Modifications were made by adding steel-brackets both in the fixed-bottom and the loading-area; however, the result could not be compared to new samples made as a result of the modifications. The lessons learned from the

G1 group pilots-studies were utilised in the design of the new samples cast and tested in the groups G1, G2 and G3. A greater effort had to be put into the bottom connection design, specifically to enhance the shear capacity of the wall and the steel profile.

4.1.2. Sub-Chapter Conclusions

The studies were conducted successfully and the following conclusions were made:

- The pilot studies (PS) resulted in the specimen's design improvement.
- The PS improved the experimental test setup and sample's instrumentation.

Overall, a PS project can provide a significant amount of useful information about the design, setup, instrumentation and testing in a newly devised experiment in the absence of required information.

4.2. Group Two

This group consisted of two samples S6 and B6 cast and tested in the second batch of testing which included one steel-reinforced, and one BFRP reinforced samples in this group. The steel-reinforced samples were used as the control sample. All reinforcements were 6 mm of diameter rebars, and all stirrups were 6 mm mild steel. The concrete strength for this batch of samples was close to C30/37. Rebars anchorage was not used in the design of these samples. The properties of concrete and rebars are shown in Table 4.2.

Table 4.2 – Group two samples' details.

Groups	Sample No.	Rebar Type	Diameter (mm)	Concrete Strength	Anchorage	Abbreviated Name
G2	5	Steel	6	C30/37	No	S6
	6	BFRP	6	C30/37	No	B6

The load cycles were applied using the modified ATC 24 (1992) protocol assuming one cycle for each level of amplitude. Fourteen cycles of load were programmed to be applied to the test specimens allowing for amplitudes from 0.2 mm to 30 mm, as indicated in Table 3.4. The loading was stopped when the shear wall could not sustain more loads and failed.

4.2.1. Crack and crushing patterns

Generally, all the shear wall samples started with horizontal cracks as an initial mode of response as can be seen in Figures 4.2 a-d. There was no sign of premature failures such as shear, sliding, or anchorage. At the end of each cycle, the samples exhibited a fairly symmetric lateral-load against top-displacement relationship under reversed cyclic load conditions until there was a failure at one end of the wall as can be seen in Figure 5 (d).

Figures 4.2 (a) and 4.2 (b) shows the gradual cracking pattern for S6 and B6 samples, respectively. The cracks developed as shown in the legends. At higher displacements new cracks formed in the relatively upper areas of the samples while the existing cracks propagated in the horizontal direction.

Figures 4.2 (c) and 4.2 (d) shows all the cracking and spalling zones of concrete for S6 and B6 samples, respectively. As the lateral displacement-controlled load continued to increase, spalling of concrete appeared at the boundaries under compression and tension. The concrete spalling areas are shown in green lines. The B6 sample rebars can be seen after the spalling of the concrete.

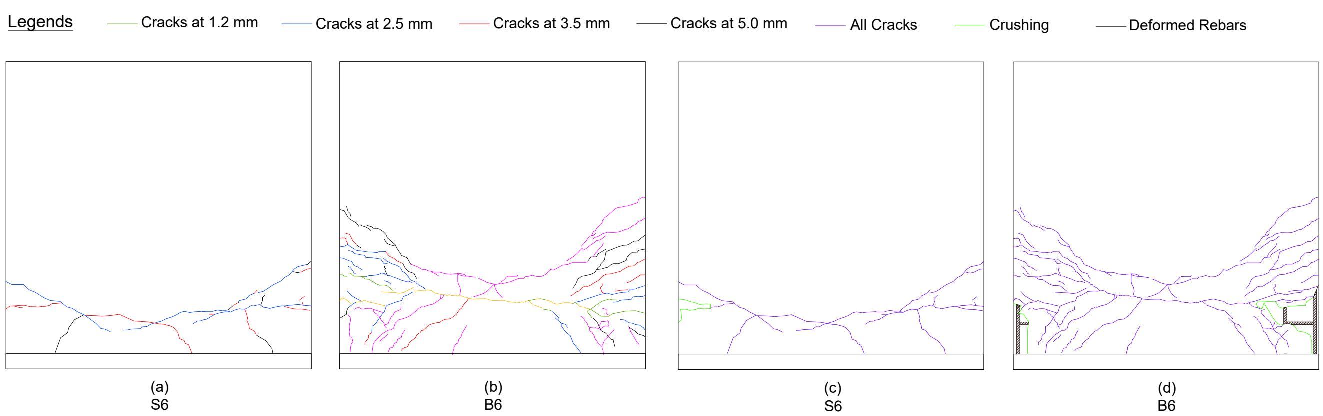

Figure 4.2. Crack pattern; (a) S6, (b) B6. Spalling and bar deformation; (c) S6, (d) B6.

Cracking and crushing of the concrete can also be seen in Figure 4.3 (a) and (b). A major crack also formed in each of the samples at about 1/4 of the height of the samples. As the displacement load increase, the crack gap increased too.

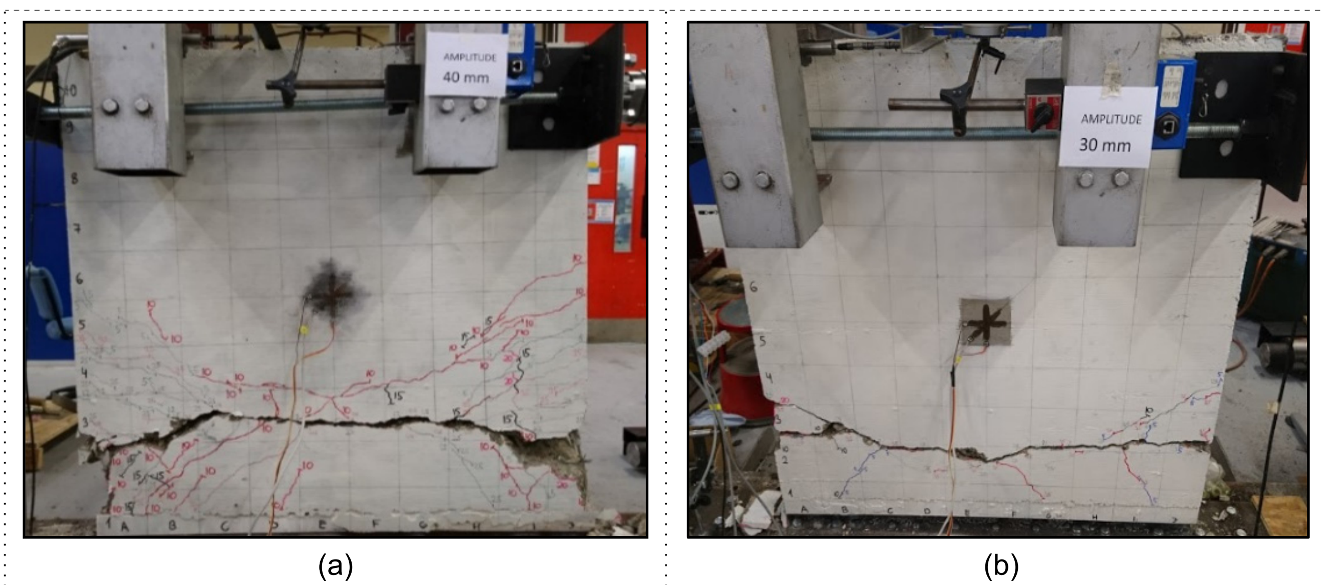

Figure 4.3. Samples cracking and crushing at final amplitude (a) S6, (b) B6

All observations made during testing of the samples are enlisted in Table 4.3. The observation started at an amplitude of 0.8 mm for B6 and an amplitude of 2.5 mm for S6.

Table 4.3 - Samples observation sheet, NOB (No Observation), CKG (Cracking), BGN (Banging Noise), CSG (Crushing), SPG (Spalling), BRD (Bars Deformation) RKG (Rocking).

Displacement/ Samples	**0.2**	**0.4**	**0.8**	**1.2**	**2.5**	**3.5**	**5.0**	**10**	**15**	**20**	**25**	**30**
S6	NOB	NOB	NOB	NOB	CKG	CKG	CKG	BGN/ CSG	BGN/ RKG	SPG/ RKG	SPG/ RKG	RKG
B6	NOB	NOB	CKG	CKG	CKG	CKG	CKG	BGN/ CSG	RKG	SPG/ RKG	SPG/ RKG	RKG

Table 4.3 and Figure 4.3 shows that cracking started at an amplitude of 2.5 mm for S6 and 0.8 mm for B6. The early cracking is because BFRP is more flexible than steel rebars as a result of lower modulus of elasticity, i.e. resulting in earlier cracking of the more deformable samples.

The cracking continued until an amplitude of 5.0 mm for S6 and B6 samples. Additionally, a banging loud noise was recorded at an amplitude of 10 mm for both samples as the crushing started. A further loud banging noise occurred at 15 mm displacement amplitude in the S6 samples. Further inspection showed that steel rebars yielded and broke during the test.

Crushing of the samples occurred at 10 mm amplitude after which the rocking of both samples started. The rocking effect was when the samples split into two part in a critical crack zone (approximately 1/5 of the height) acting as a mechanism. The rocking of the samples started at 15 mm displacement amplitude for both samples and continued till 30 mm displacement amplitude.

Spalling of the concrete cover occurred at an amplitude of 20 mm for both samples; furthermore, it continued at 25 mm amplitude for both samples in the bottom left and right of the samples.

4.2.2. Lateral Load – Top Displacement Hysteresis

The graphs in Figures 4.4 (a)-(b) show force-displacement (FD) hysteresis responses of S6 and B6 samples, respectively. The positive and negative numbers indicate the application of the load in the forward and reverse directions, respectively.

Figures 4.4 (a) shows that the initial levels of displacement lead to a linear response of almost vertical loops until 5 mm displacement and a wider loop for the S6 after a displacement amplitude of 5 mm. The loops started to become more horizontal after 10 mm displacement.

Figure 4.4 (b) shows that the initial levels of displacement until 3.5 mm amplitude the loops were also almost vertical. At 5 mm the loop started to widen and at 10 mm the loop was wider. The loops were almost horizontal after 10 mm displacement.

Figures (4.4 (a) and (b)) show that a significant amount of force is required at the initial displacements of the samples with almost vertical loops. The force required to achieve a greater displacement is reduced but there is still resistance in the system as suggested by the horizontal loops.

As the steel rebars start to yield, it causes a sharp fall of the loop. The slight continuous increase in the area of the loop for the S6 sample after 10 mm is due to the frictional forces at the rocking stage when the sample broke into two parts moving against each other like a mechanism. The residual strength is due to the contribution of the rebars still connecting the two parts with friction forces.

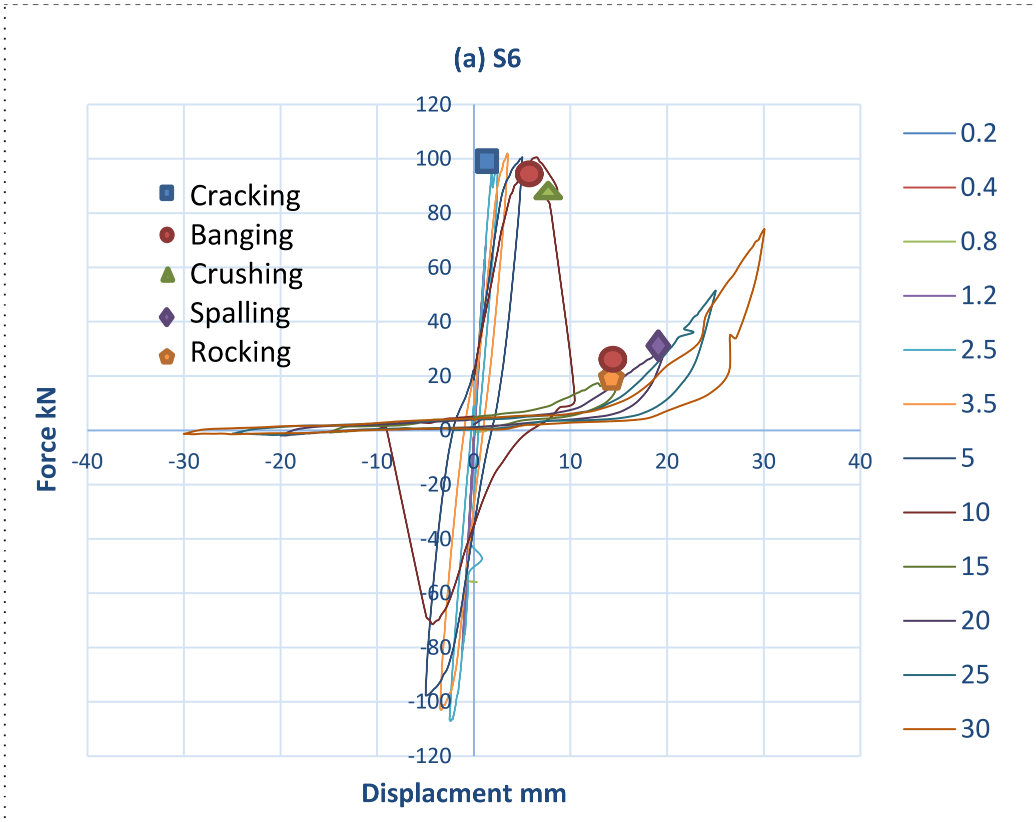

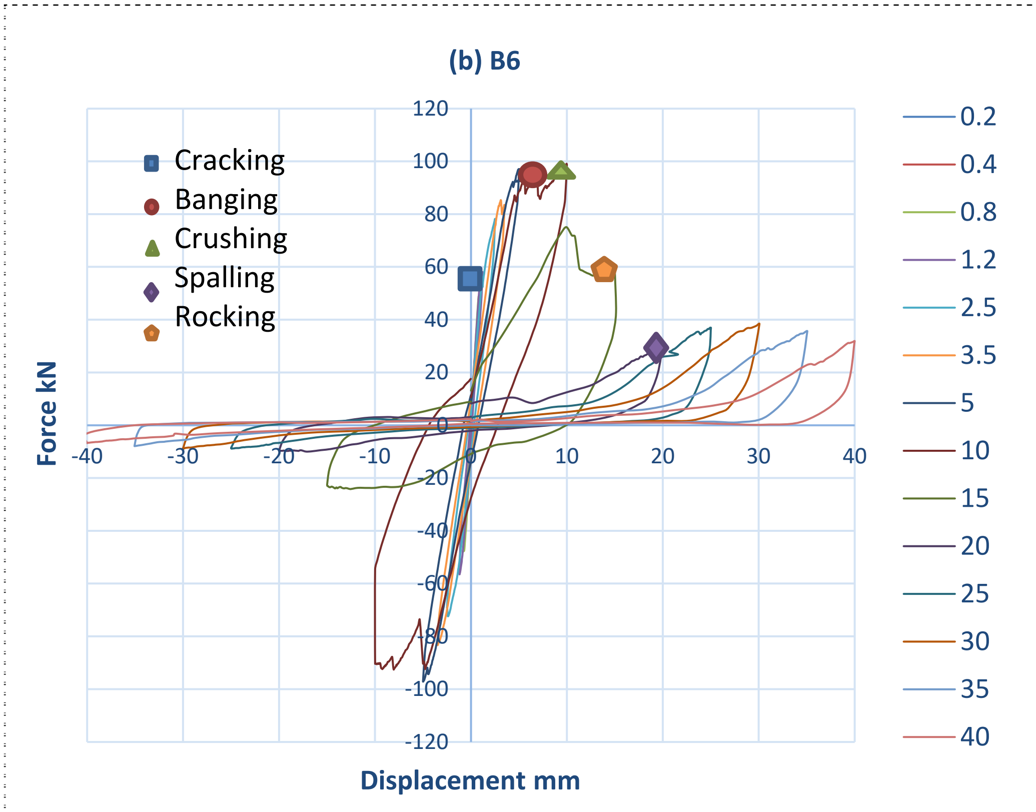

Figure 4.4 - Lateral force versus top-displacement relationship for (a) S6 and (b) B6 samples.

Loud banging noise was heard from the sample at 10 mm and 15 mm of amplitudes twice for the S6 samples, which suggests that the steel reinforcement bars were broken or the bond between the rebars and concrete was broken; hence the loop started to narrow down.

There was a banging sound at 10 mm amplitude for the B6 sample. However, an examination of the rebars after the testing showed no rupture of the BFRP bars in the sample.

Crushing of the concrete occurred at a 10 mm displacement amplitude hysteresis loop for both S6 and B6 samples. However, it was the last wide loop for the S6 sample, but there was a second-wide loop for the B6 sample, which confirmed that the BFRP reinforced sample had no rupture of the bars.

The rocking of the samples occurred at 15 mm of amplitude loops for both S6 and B6 samples (Figures 4.4 (a) and 4.4 (b)). However, the loops in the B6 samples are much wider than the B6 sample due to the yielding and breaking of the steel bars.

4.2.3. Maximum and Minimum Points

The envelope of maximum and the minimum hysteresis response loops value for all the samples are outlined in Figure 4.5 below. The graphs were created by connecting the peak values for all the displacement amplitudes.

As it can be seen from the figure, the S6 curve rise over 100 kN at about 2 mm and sharply falls at about 3 mm displacement. The B6 curve shows a more gradual rise to approximately 100 kN at less than 10 mm after which it start gradually. The curves show similar behaviour in the first and fourth quadrants of the graph. In general, the B6 curve shows a more gradual rise and fall than the S6 curve.

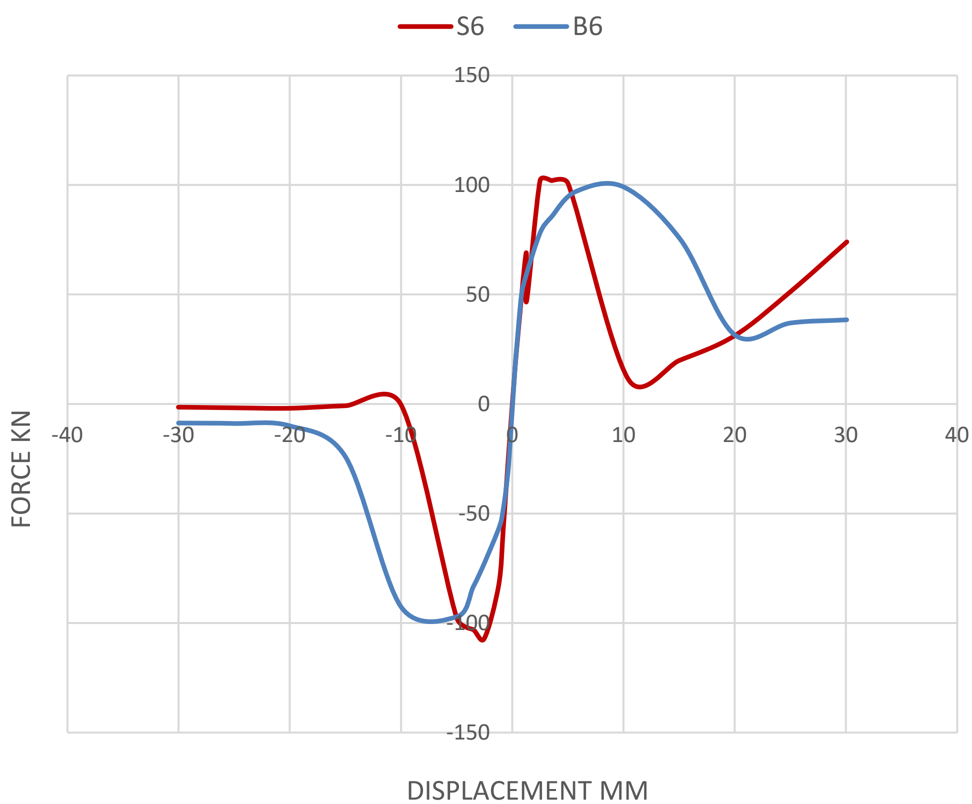

Figure 4.5 - Hysteresis maximum and minimum force against displacement graph for S6 and B6 samples.

4.2.4. Average Maximum and Minimum Points

The maximum and minimum points were taken from the previous analysis, and the averaged values from the push/pull phase are depicted in Figure 4.6.

The results show that the S6 sample has a higher force against displacement response compared to the B6 sample. However, the S6 sample loses the load-bearing capacity after taking a maximum of approximately 105 kN, and there is a sudden drop off from 100 kN to about 5 kN at 10 mm displacement amplitude due to steel reinforcement yielding and breaking.

The B6 graph reaches the peak at a greater displacement (about 100 kN force resistance at an amplitude of 9 mm) before it gradually decreases to 20 kN at about 20 mm displacement amplitude; it rises very slightly before it stops at over 20 kN at 30 mm amplitude. The S6 graph increases in force resistance from about 5 kN at 10 mm displacement to less than 40 kN at 30 mm displacement due to frictional forces when the sample was split into two-parts and was acting like a mechanism.

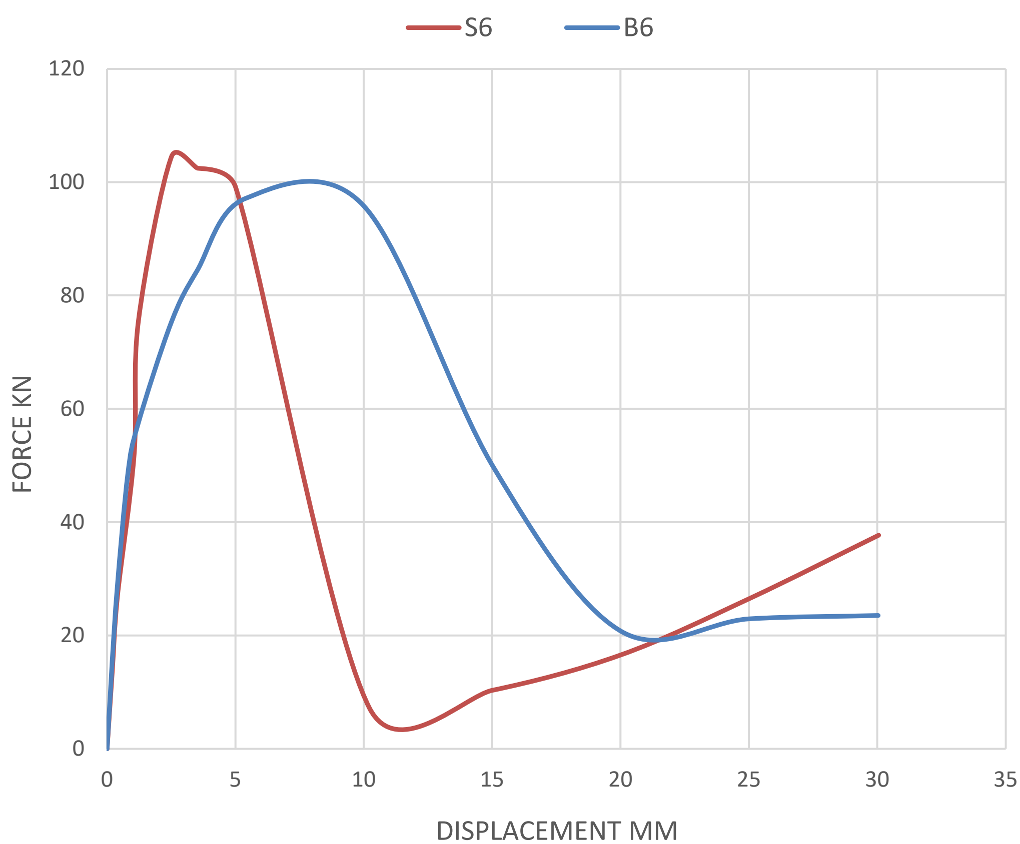

Figure 4.6 - Average maximum and minimum force against displacement graph for S6 and B6 samples.

4.2.5. Energy Dissipation

Energy dissipation (ED) of the samples was determined by calculating the areas inside the hysteresis response loops to further illustrate the response of the samples. AutoCAD platform was used to estimate the area inside the loops.

As it can be seen in Figure 4.7, the S6 sample has an initial higher ED than the B6 sample. At 12mm the ED of the B6 sample becomes greater due to the failure of the steel wall.

The initial higher ED peaking at about 1230 kNmm in around 10 mm displacement is due to the higher modulus of elasticity in S6. The ED of the B6 curve increases to just above 1080 kNmm of ED at about 15 mm displacement amplitude before it gradually drops back to about 400 kNmm at 20 mm amplitude.

The B6 sample maintains the same level of ED above 22 mm whilst the steel sample shows a drop close to about 50 kNmm followed by a small increase to 230 kNmm.

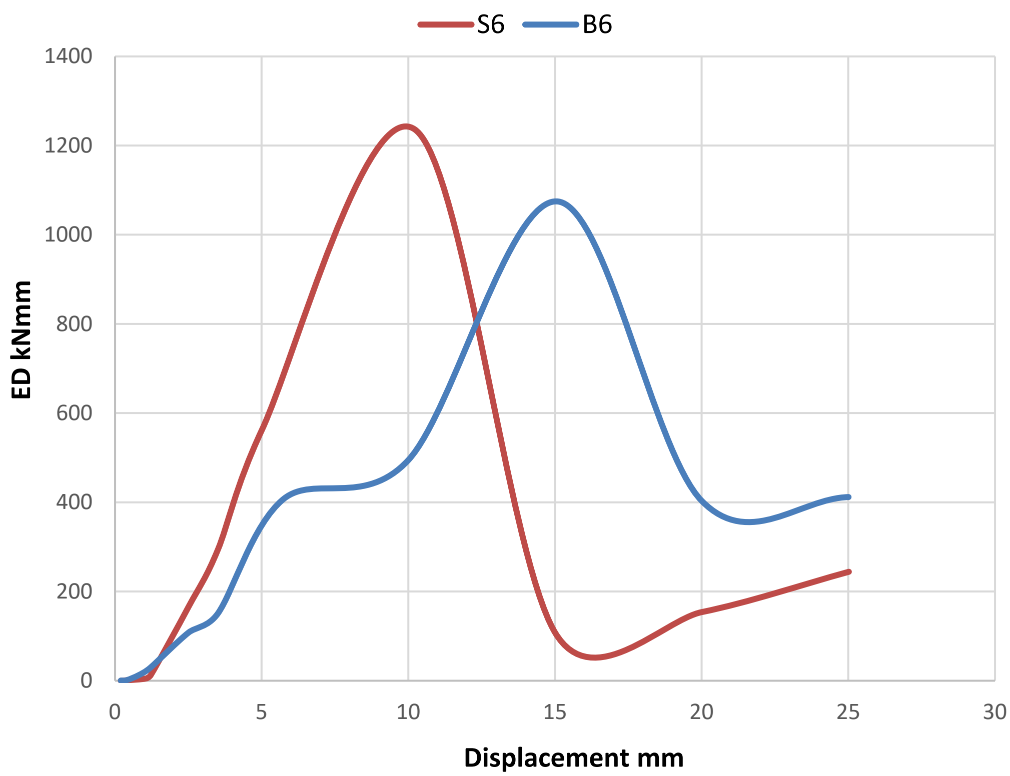

Figure 4.7. ED against displacement amplitude for S6 and B6 samples.

4.2.6. Cumulative Energy Dissipation

The cumulative energy dissipation (CED) of the samples are shown in Figure 4.8. The CED graph is a cumulative addition of the ED values per each displacement amplitude.

The B6 graph gradually increases from 0 to about 2700 kNmm as a result of higher ductility. The S6 graph increase from 0 to about 2400 kNmm CED (about 11 mm displacement amplitude) at a faster pace than B6 due to the higher modulus of the elasticity of the steel rebars. After this point, the S6 graph levels due to rebars yielding and breaking.

The B6 graph shows greater capacity above approximately 2450 kNmm CED corresponding to about 16.5 mm amplitude; this is the amplitude where the steel rebars start to break hence the CED drops below the BFRP reinforced sample. After the experiments a removal of concrete cover confirmed the rebars breaking.

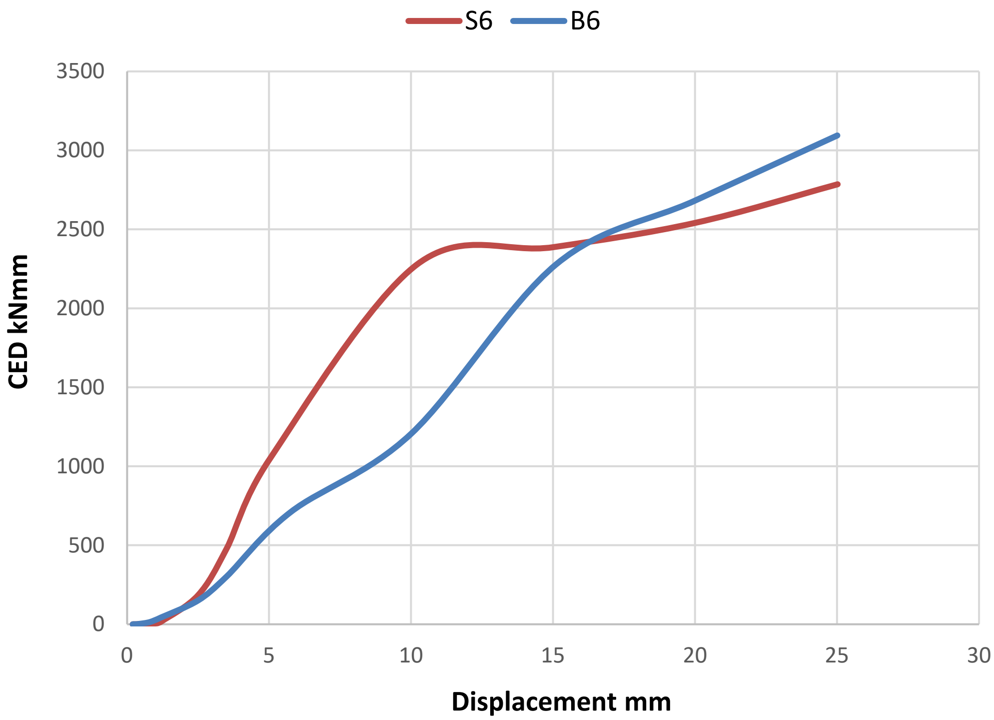

Figure 4.8 - CED against displacement for the S6 and the B6 samples.

4.2.7. Sub-Chapter Conclusions

The experiments were successfully conducted by casting and testing both samples using the structural lab at KUL, and the following conclusions were drawn:

- The hysteresis loop peak values (HLPVs) for B6 are lower than S6 due to the higher deformability of FRP and more intensive development of cracking in concrete.
- The S6 HLPVs fall faster after 5 mm amplitude displacement due to steel rebars yielding and breaking but B6 HLPVs gradually fall after 5 mm due to B6 rebar-concrete bond-slip.
- The S6 HLPVs are regaining increased reading due to frictional force and aggregate interlocking after sample splitting into two and acting like a mechanism.
- The B6 residual HLPVs after 20 mm is due to rebar-concrete friction-forces after bond-slip.
- The S6 average maximum and minimum points (AMMP) curve show a steep fall after 5 mm amplitude due to steel rebars yielding and breaking.

- The B6 average AMMP curve shows a gradual fall after about 8 mm amplitude due to rebar-concrete bond-slipping.
- The B6 ED and CED show a slower rise than S6 due to steel-rebars higher elasticity-modulus.
- The S6 ED indicate a sharper fall below B6 after about 13 mm amplitude due to steel rebars yielding and breaking.
- The S6 CED rise faster until about 11 mm displacement after which it levels off going below B6 after about 16 mm amplitude.
- The B6 shows a more gradual and constant CED rise than the S6 sample.

Generally the group two results show slightly lower FD and ED for BFRP than the steel-reinforced sample. The results are promising as an initial pace for utilisation of BFRP as an alternative to the traditional steel reinforcement in RCSWs.

4.3. Group Three

There were four shear-wall samples in this group including one steel control-sample (SA6), one BFRP and (BA6) one GFRP (GA6) 6 mm diameter reinforced. The concrete strength for this batch of samples was about C25/30. Rebars anchorage was used in this group of samples (Table 4.4).

Table 4.4 - Group three samples' details

Groups	Sample No.	Reinforcement type	Diameter (mm)	Concrete Strength	Anchorage	Abbreviated Name
G3	7	Steel	6	C20/25	Yes	SA6
	8	BFRP	6	C20/25	Yes	BA6
	9	GFRP	6	C20/25	Yes	GA6

4.3.1. Crack and crushing patterns

There was no sign of premature failure in the shear, sliding or anchorage performance of the samples. In all the samples the initial mode of response was the development of the horizontal cracks. The scale of cracks can be seen in Figure 5 a-c. Each of the samples exhibited a relatively symmetric lateral-load against top-displacement relationship under pushing and pulling cyclic load conditions until there was a failure at one end of the wall as can be seen in Figures 5 d-f.

Figures 4.9 (a-c) show that the first crack developed at 1.2 mm in BA6 and GA6 samples and 2.5 mm for the SA6 sample due to the stiffer behaviour of the steel-reinforced sample. As the loading continued the existing cracks propagated and new horizontal cracks formed. Crack developments are fairly symmetrical except in the GA6 sample (4.9 c) where a larger crushing occurred at the bottom right corner resulting in a decrease of tensile capacity in the right side of the sample. At higher displacement amplitudes, crushing and spalling of concrete appeared at the boundaries under compression and tension (Figure 4.9 d-f and 4.10 a-c). As the displacement amplitudes continued to increase more spalling of concrete cover become evident at the critical compression and tension zones (1/5 of the sample height).

Figures 4.9 (d-f) show all the cracks and spalling of concrete that occurred during the application of the 1.2 mm to 10 mm displacement amplitudes. The crushed zones are in the bottom right and left of the samples where spalling of the concrete has happened and the rebars can be seen. The crushed zones of concrete were larger in the GA6 followed by SA6 and BA6 sample due to the lower bond strength between concrete and GFRP rebars. It can also be seen from the diagrams that some rebars have deformed under cyclic loading (Figures 4.9 d-f).

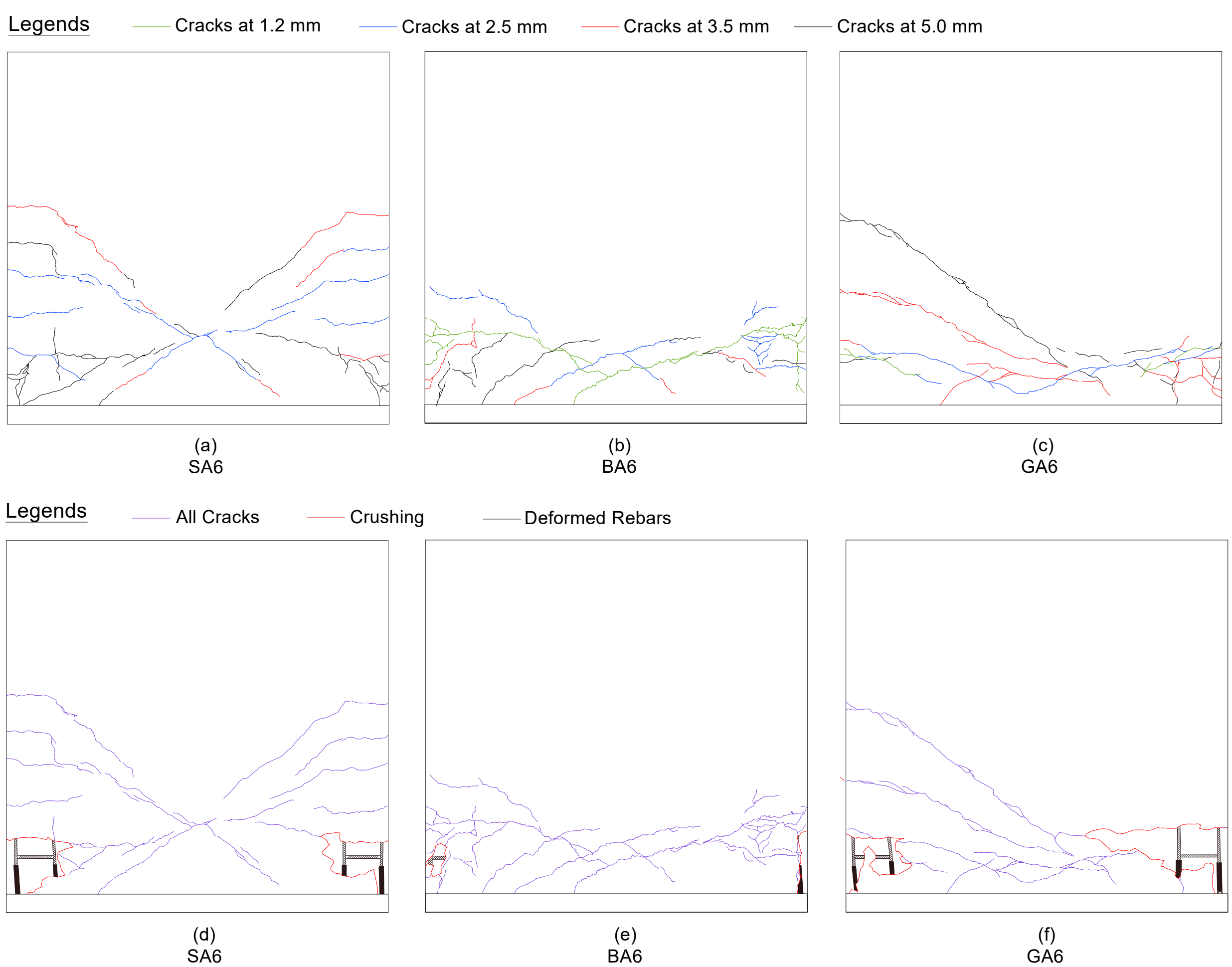

Figure 4.9 - Crack pattern (a) SA6, (b) BA6, (c) GA6. Crushing pattern, spalling and bar deformation (d) SA6, (e) BA6, (f) GA6

Cracking and crushing of the concrete can also be seen in Figure 4.10 a-c for SA6, BA6 and GA6, respectively. A major crack has also started formed in each of the samples approximately 1/5 of the height of the samples after 5 mm amplitude. As the displacement load increase, the crack gap increased followed by closing on the reverse loading.

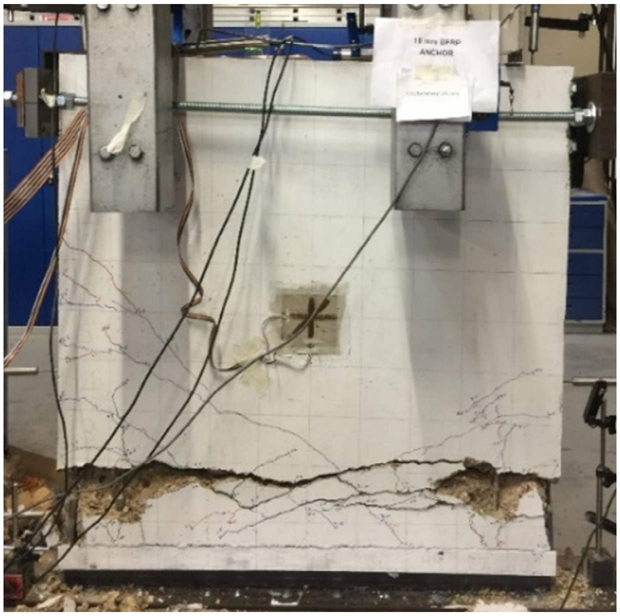

(a)

(b)

(c)

Figure 4.10. Cracking and crushing photos (a) SA6, (b) BA6, (c) GA6

All observations made during testing of the samples are enlisted in Table 4.5. The observation started at an amplitude of 2.5 mm for SA6 and an amplitude of 1.2 mm for BA6 and GA6.

Table 4.5: Samples observation sheet, NOB (No Observation), CKG (Cracking), BGN (Banging Noise), CSG (Crushing), SPG (Spalling), BRD (Bars Deformation) RKG (Rocking).

Dis/Sam	SA6	BA6	GA6
0.2	NOB	NOB	NOB
0.4	NOB	NOB	NOB
0.8	NOB	NOB	NOB
1.2	NOB	CKG	CKG
2.5	CKS/BGN	CKG	CKG
3.5	CKG	CKG	CKG
5.0	CKG	CSG	CKG/BGN
10	BGN/SPG	SPG/BGN	BGN/SPG/CSG
15	CSG/SPG	RKG	SPG/RKG
20	RKG/BRD	SPG/BRD	RKG/BRD
25	RKG/BRD	RKG/SPG	RKG

Table 4.5 and Figure 4.11 shows that cracking started at an amplitude of 1.2 mm for BA6 and GA6 samples. However, for the SA6 sample, the cracking started at an amplitude of 2.5 mm, which can be interpreted as the SA6 was less deformable than the GA6 and BA6.

A loud noise was heard at 10 mm amplitude for all samples after which the loops became wider than the previous loops. However, the peak load carrying capacity is dropped after this amplitude; SA6 had a higher drop in load-carrying capacity than BA6 and GA6 samples. Spalling of the concrete cover also occurred at an amplitude of 10 mm for all samples.

Development of critical crack following the formation of the horizontal crack occurred at 15 mm amplitude for the SA6 sample (Figure 4.11 (c)), at 5 mm of amplitude for the BA6 sample (Figure 4.11 (a)), and at 10 mm amplitude for the GA6 sample (Figure 4.11 (b)). This development means an earlier failure of concrete occurred due to higher deformability of FRP and more intensive development of cracking in concrete.

The rocking of the BA6 and GA6 started at 15 mm and SA6 at 20 mm displacement amplitude. The rocking effect occurred when the samples split into two parts, and residual capacity relied on the rebars in the vicinity of the critical crack. The rebars connected the two parts with rebars-concrete friction force resulting in observation of a residual capacity in the sample after rocking.

4.3.2. Lateral Load – Top Displacement Hysteresis

All the hysteresis graphs in Figures 4.11 a-c have an initial symmetry under the loading and unloading conditions. Relatively higher force values are required for smaller displacement until an amplitude of less than 5 mm displacement. After this amplitude, the loops start to open with relatively larger displacement amplitudes which indicates that a higher ED is occurring between these amplitudes.

Loud noise and concrete cover spalling were noticed during the application of the 10 mm amplitude in BA6, and GA6 samples which suggested some level of bond breaking between the concrete and the anchorage. In the SA6 sample, the banging noise occurred during 2.5 mm and 10 mm amplitudes due to the yielding and breaking of the steel rebars and the anchorage failure, respectively.

The sample was considered crushed when a significant loss of capacity occurred, critical horizontal crack width increased significantly, and a major spalling of concrete at the bottom left/right of the sample was observed. The BA6 sample crushed at lower amplitude (Figure 4.11 (a)) of 2.5 mm loop due to higher deformability of FRP and more intensive development of cracking in concrete. GA6 and sample had its crush at about 7 mm amplitude loop as can be seen in Figure 4.11 (b) showing more deformability than SA6. The SA6 samples had the crushing at 15 mm amplitude as can be seen in Figures 4.11 (c).

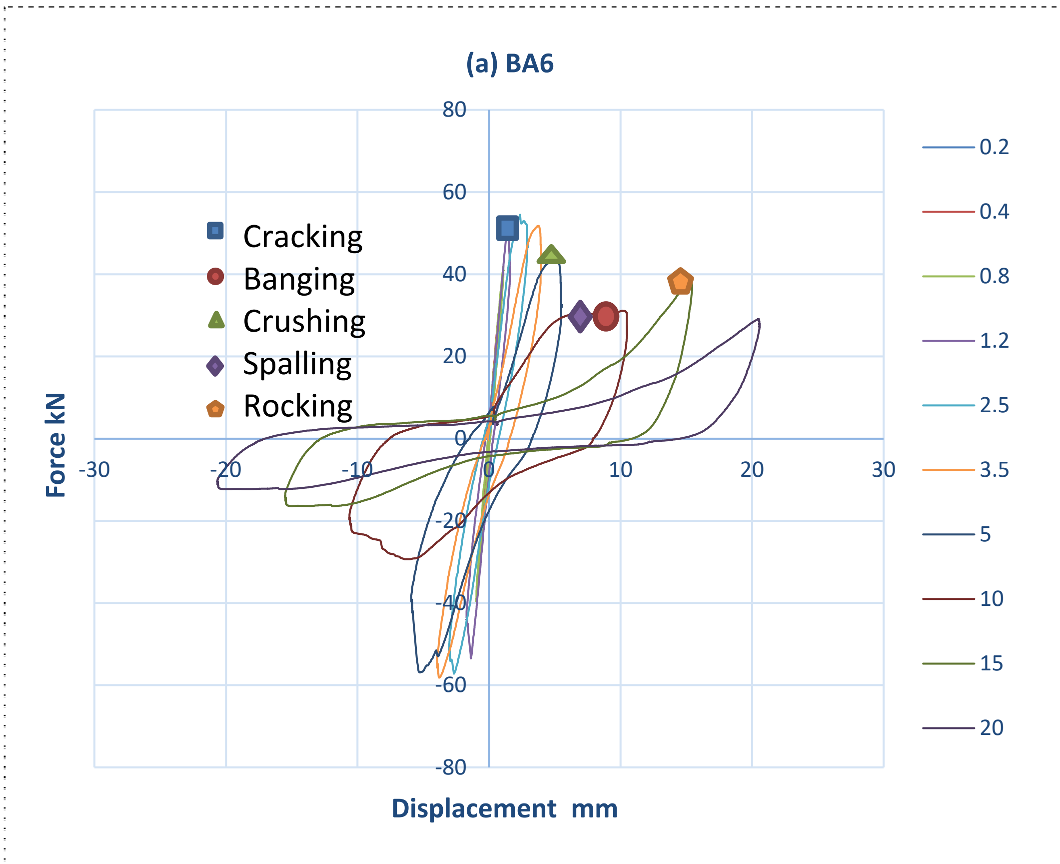

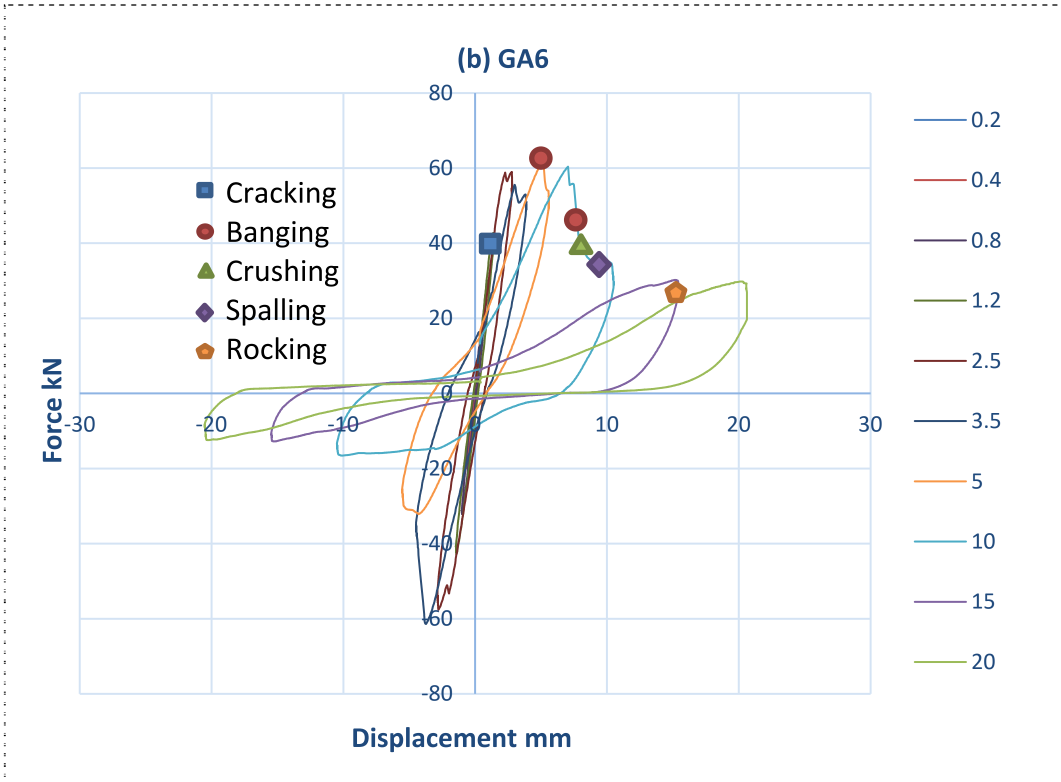

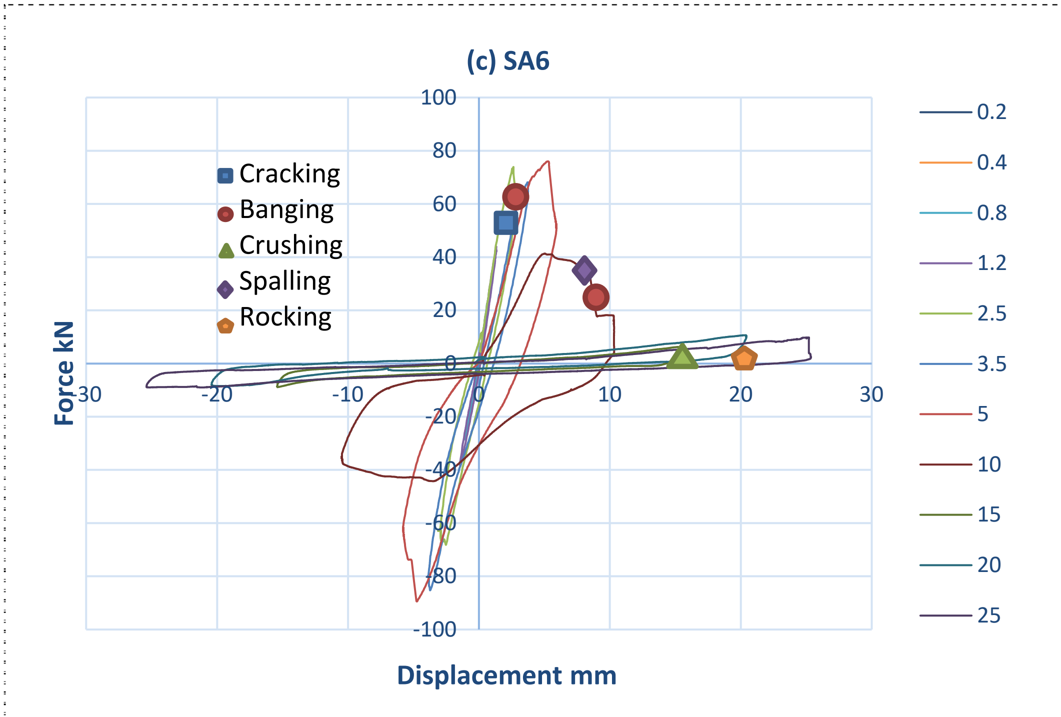

Figure 4.11 - Lateral force versus top-displacement relationship (a) BA6, (b) GA6 and (c) SA6 samples.

As the critical horizontal crack developed a rocking of the sample occurred at 15 mm of amplitude loops in the BA6 and GA6 samples as can be seen in Figures 4.11 a and b, respectively. In the SA6 sample, the rocking started at a 20 mm amplitude loop, which shows a higher energy dissipation.

Furthermore, BA6 and GA6 samples show a wider loop than the SA6 sample as can be seen in Figures 4.11 a-c. In the SA6 sample breaking of the rebars were observed in an examination after the tests which could explain the reason for the thinner loops and lesser energy dissipation.

4.3.3. Maximum and Minimum Points

The envelope of maximum and the minimum hysteresis response loops value (the envelope) for all the samples are demonstrated in Figure 8. The SA6 sample has a higher maximum and minimum response than the GA6 and followed by the BA6 sample. SA6, GA6 and BA6 had reached a maximum of 80 kN, 62 kN, 58 kN and a minimum of -90 kN, -62 kN, -59 kN respectively.

The SA6 falling envelope is significantly steeper after the maximum and minimum values. The performance of BA6 and GA6 after the maximum and minimum points show a more consistent drop.

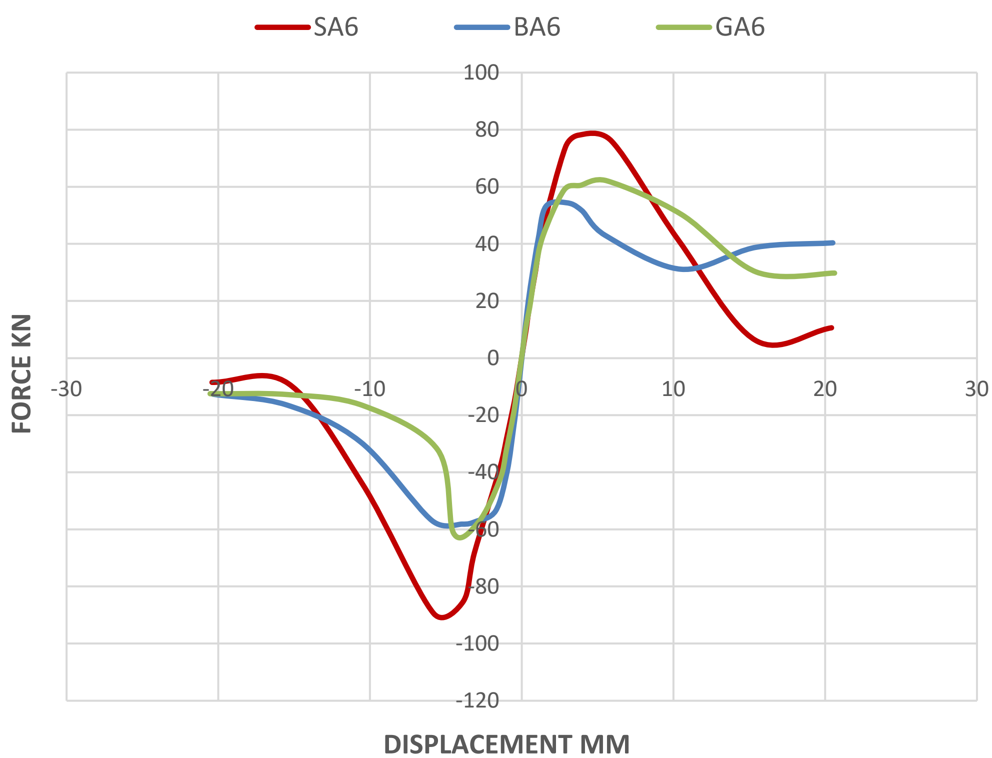

Figure 4.12 - Hysteresis curve maximum and minimum points for BA6, GA6 and SA6 samples

4.3.4. Average Maximum and Minimum Points

The maximum and minimum points were taken from the previous analysis and averaged over the push/pull values (average envelope). The average envelope (AE) peak force against displacement curves for each sample can be observed in Figure 4.13.

The results show that the SA6 sample has a higher force against displacement response followed by the GA6 and BA6 lines. Similar capacity for BA6 and GA6 was demonstrated, followed by a gradual decrease.

The post-peak performance of the FRP reinforced samples (GA6 and BA6) show a more prolonged drop than the steel-reinforced sample (SA6). After the peak forces majority of damages occurred in the samples and at this stage the FRP reinforced samples maintained a significant force.

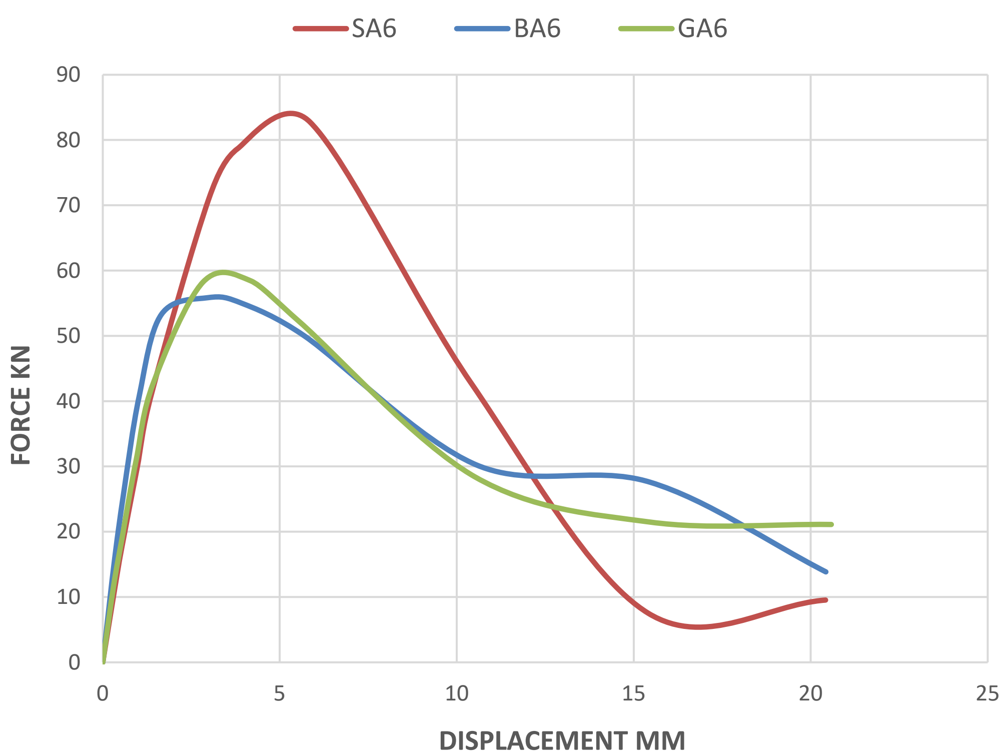

Figure 4.13 - Average maximum and minimum points for BA6, GA6 and SA6 samples

4.3.5. Energy Dissipation

Energy dissipation (ED) of the samples was determined by calculating the areas inside the hysteresis loops to further illustrate the response of the samples. As it can be seen in Figure 4.14, the SA6 sample has a higher ED followed by the BA6 and GA6 sample.

The initial SA6 ED graph is higher than the BA6 and the GA6 due to higher modulus of elasticity in steel bars; however, it drops below the BA6 and GA6 due to lower ultimate strength of steel than FRP bars. The BA6 and GA6 graphs follow each other showing similar ED response due to similar properties.

All samples show a similar initial elastic behaviour from the start to approximately 120 kNmm and 3 mm displacement amplitude this is due to initial elasticity in steel and FRP samples.

There are waves in all graphs (SA6, BA6 and GA6) between 110 – 210 kNmm ED value corresponding to about 2.5 – 3.5 mm displacement amplitudes; this is due to relatively smaller interval between 2.5 mm and 3.5 mm displacement amplitudes than higher load cycles. The displacement amplitudes are recommended values for load cycles by the ATC-24, therefore used as original values without any modification (ATC-24, 1992).

The SA6 graph rises to about 700 kNmm ED at approximately 10 mm displacement amplitude faster before the bottom at 100 kNmm and approximately 16.5 mm displacement amplitude. The SA6 graph falls below BA6 and GA6 graphs at about 500 and 450 kNmm, respectively. This is due to a higher modulus of elasticity and lower ultimate strength in steel than FRP.

The BFRP and GFRP samples start to rise a similar peak value of 520 kNmm ED at about 11 mm displacement before lowering to 440 and 400 kNmm ED respectively at about 20 mm displacement amplitude; this is because of the higher ultimate capacity of the FRP than steel reinforcements. These BA6 and GA6 graphs can be observed following each other due to the similarity in properties of the BFRP and GFRP reinforcement bars.

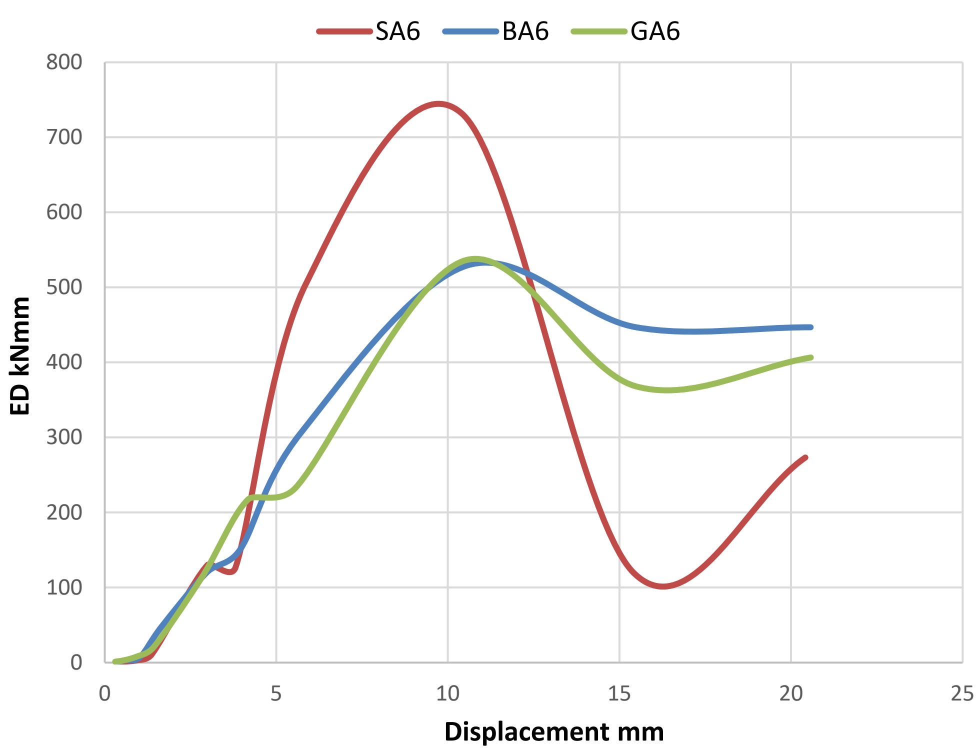

Figure 4.14 - ED graph for SA6, BA6 and GA6 samples

Overall, the FRP samples showed a consistent ED after a majority of damages occurred after the peak values. The SA6 ED gain after about 16 mm cannot be considered a reliable performance as the sample split at this stage and the gain was due to rebar-concrete friction forces connecting the two parts.

4.3.6. Cumulative Energy Dissipation

Cumulative Energy Dissipation (CED) of the samples are shown in Figure 4.15. The CED graph is a cumulative addition of the Energy Dissipation values per each displacement amplitude.

There is a steady increase of the SA6 graph to about 10 mm (22 % more CED) due to higher young modulus of steel reinforcement in the SA6 sample after which the rate is reduced and above 15 mm approaches the BA6 and GA6 graph due to yielding and breaking of the steel reinforcements.

The BA6 and GA6 closely follow each other due to similarities in the properties of BFRP and GFRP reinforcements. The BA6 graph is predominately linear after 5 mm displacement. The GA6 graph is linear between 5 mm and 12 mm after which it starts to fall slightly below the BA6 graph due to a slightly lower young modulus GFRP than BFRP reinforcement.

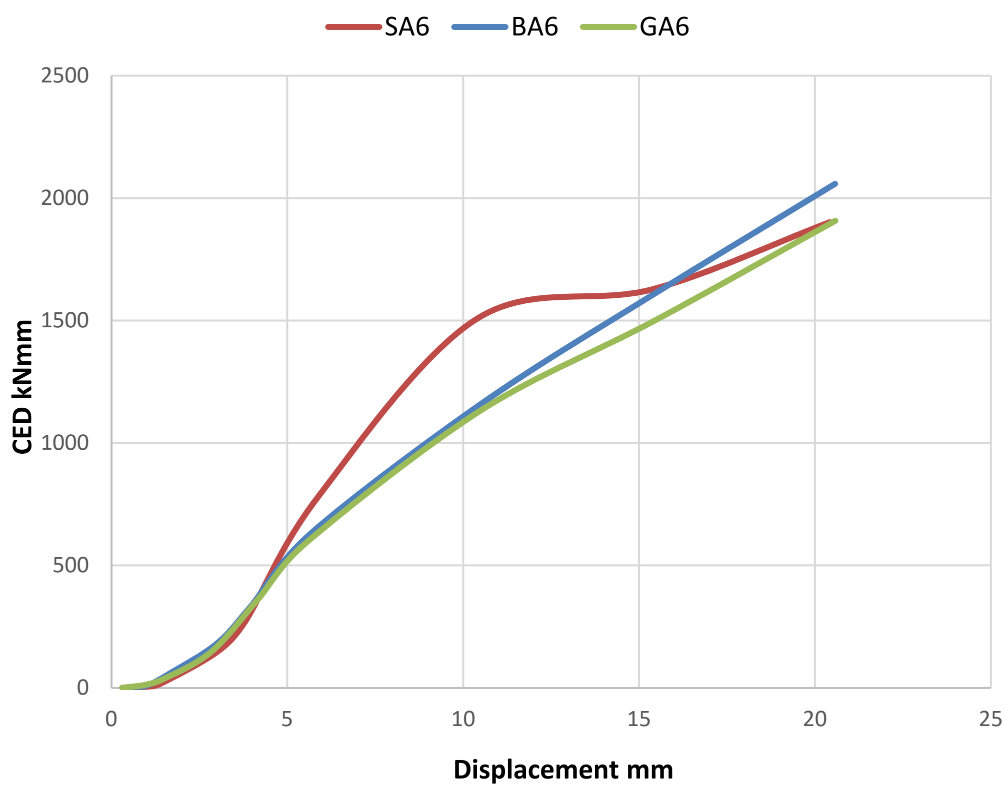

Figure 4.15 - CED of SA6, BA6 and GA6 samples

4.3.7. Sub-Chapter Conclusions

Experiments were successfully conducted in the structural laboratory of KUL. From the result of the experiments and analyses conducted following conclusion can be drawn:

- The HLPVs for BA6 were lower followed by GA6 and SA6 due to higher deformability of FRP and more intensive development of cracking in concrete followed by GA6 and BA6.
- The SA6 averaged maximum and minimum points (AMMP) curve peak is about 30% higher than SA6 and BA6. SA6 fall is faster after 5 mm displacement while BA6 and GA6 falls are gradual after 3 mm.
- The BA6 and SA6 show a similar averaged AMMP curve. BA6 and SA6 residual capacity is higher than SA6 after about 13 mm amplitude.
- The BA6 and GA6 ED fall about 29% lower than SA6. At about 13 mm amplitude SA6 ED falls below BA6 and GA6. BA6 and GA6 show similar ED.
- The BA6 and GA6 CED curves are closer to linear than SA6. The SA6 CED rise above GA6 and BA6 at about 5 mm displacement. The SA6 CED falls below BA6 and getting close to GA6 at about 16 and 21 mm, respectively.

Generally, the FRP reinforced samples peak values are lower but in close range to the steel-reinforced sample. The addition of the anchorage to the rebars prove not to be effective, therefore, a different type of rebar anchorage can be recommended for future investigations.

4.4. Group four

This group consisted of three samples including one steel (S10), and two BFRP (B10 and BA10) reinforced samples. The reinforcement cage was built using 10 mm diameter rebars, and the concrete strength for this group of samples was estimated to be C20/25 as per the concrete strength test results (Section 3.2.1). The steel-reinforced sample (S10) was used as the control sample and a rebars anchorage was applied to for BA10 sample in this group (Table 4.6).

Table 4.6: Group four samples' details.

Groups	Sample No.	Reinforcement type	Diameter	Concrete Strength	Anchorage	Abbreviated Name
G4	10	Steel	10	C20/25	No	S10
	11	BFRP	10	C20/25	No	B10
	12	BFRP	10	C20/25	Yes	BA10

Overall, all the shear wall samples started with horizontal cracks. As the displacement amplitudes increased the existing cracks propagated as well as new cracks were developed (Figures 4.16 a-c). There was no indication of a premature failure such as shear, sliding, or anchorage in samples.

Each of the samples exhibited a relatively symmetric lateral-load against top-displacement relationship under pushing and pulling cyclic load conditions until there was a failure at the bottom left/right of the samples (Figures 5 d-f).

4.4.1. Crack and crushing patterns

Figures 5 (a) – (c) show that the cracks started to appear at 1.2 mm for the B10 and BA10 samples and at 2.5 mm for the S10 sample. The existing cracks propagated in the horizontal direction and new cracks formed in further locations, as the loading continued. The cracks started merging at 2.5 mm and developed in above 50% of the height at 3.5 mm in all samples. The S10 sample continued to crack at 5 mm and 10 mm displacement amplitudes due to the higher stiffness of the sample.

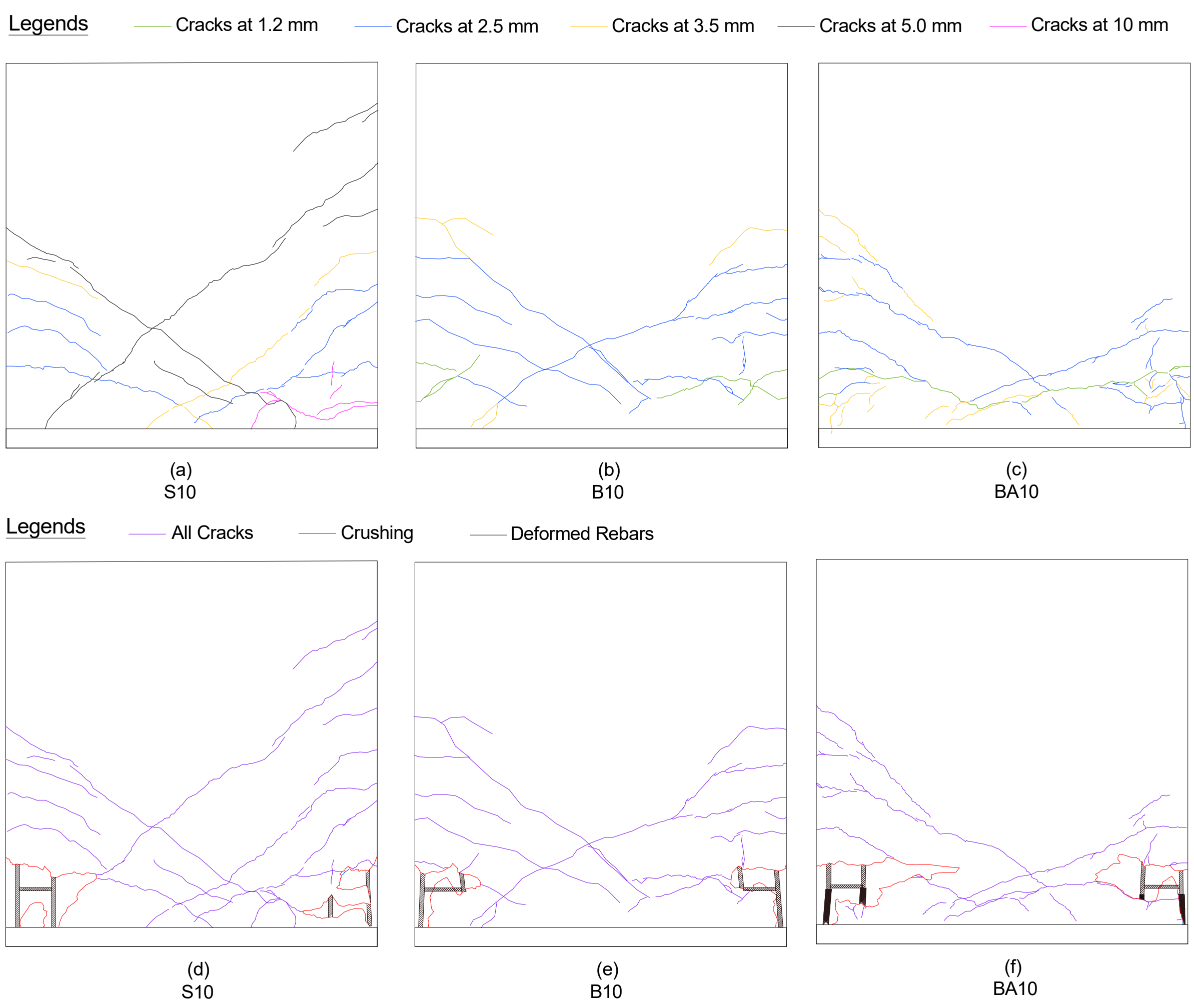

Figure 4.16 - Crack pattern (a) S10, (b) B10 and (c) BA10. Crushing pattern, spalling and bar deformation (d) S10, (e) B10 and (f) BA10

As the lateral displacement-controlled load continued to increase crushing and spalling of concrete appeared at the boundaries under compression and tension as can be seen in Figures 5 (d) – (f). As the displacement amplitudes further increased, more spalling of concrete cover become evident at the compression and tension zones (bottom left and right of the samples).

Cracking and crushing of the concrete can also be seen in Figure 4.17 (a) - (c). A major crack had also formed at 1/5 of the height of each sample. And as the displacement load increased, the crack gap increased too.

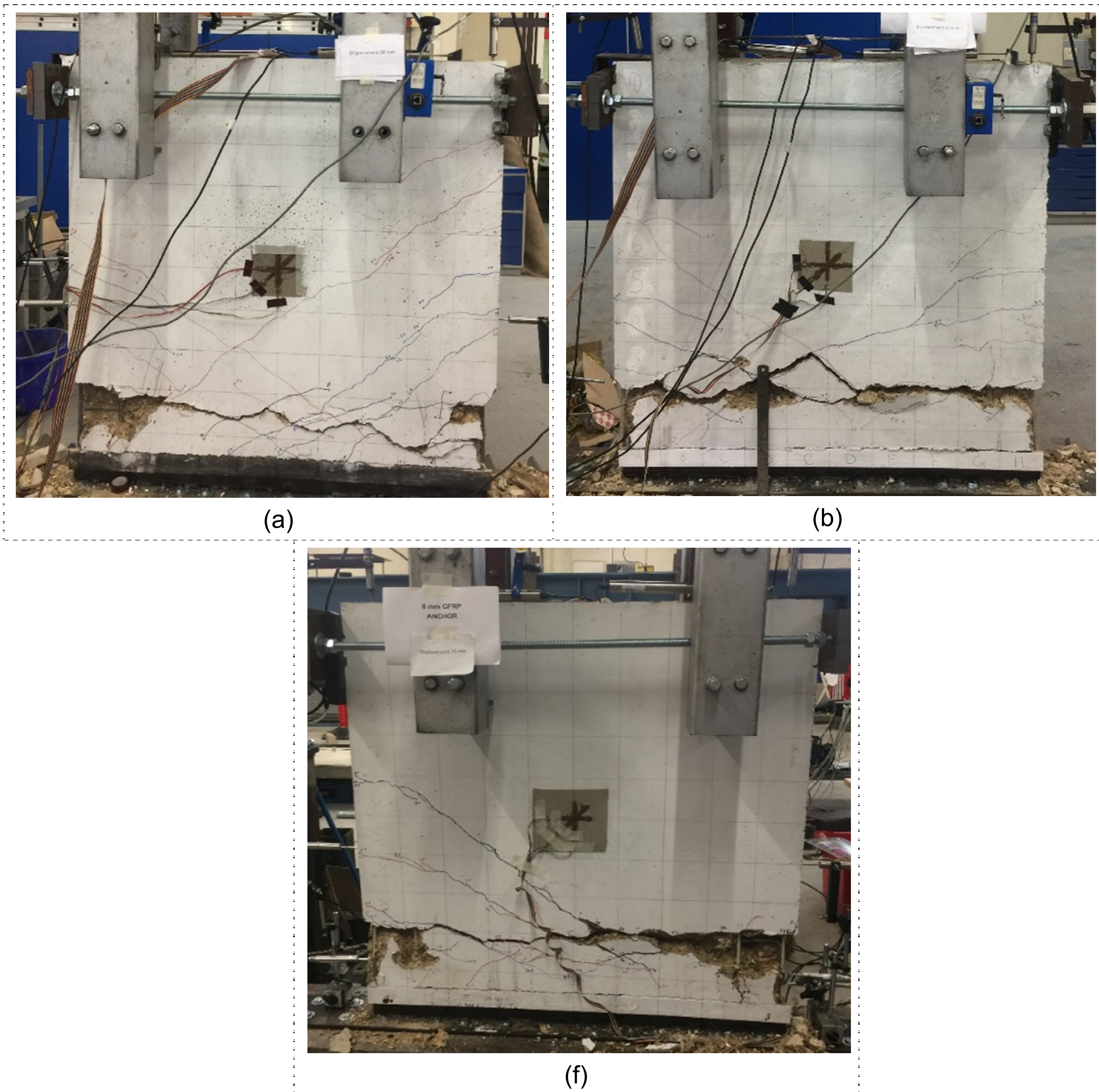

Figure 4.17 - Cracking and crushing photos at final amplitude for (a) S10, (b) B10, (c) BA10

All observations made during testing of the samples are enlisted in Table 4.7. The observation started at an amplitude of 2.5 mm for SA6 and an amplitude of 1.2 mm for B10 and BA10 samples.

Table 4.7 – Samples observation sheet, NOB (No Observation), CKG (Cracking), BGN (Banging Noise), CSG (Crushing), SPG (Spalling), BRD (Bars Deformation) RKG (Rocking)

Displ. / Samples	0.2	0.4	0.8	1.2	2.5	3.5	5.0	10	15	20	25
S10	NOB	NOB	NOB	NOB	CKG	CKG	CKG	CSG/SPG	RKG	RKG	RKG
B10	NOB	NOB	NOB	CKG	CKG	CKG	CKG/BGN	CSG/SPG	SPG	RKG	RKG
BA10	NOB	NOB	NOB	CKG	CKG	CKG	CKG/SPG	CSG/SPG	RKG	RKG/BRD	RKG

The cracking continued until an amplitude of 5.0 mm for S10 and B10 samples. However, a loud banging noise was recorded at an amplitude of 5.0 mm for the BFRP samples.

Spalling of the concrete cover occurred at an amplitude of 10 mm for all samples; however, it continued to 15 mm amplitude and again in 30 mm amplitude for the B10 samples. The prolonged spalling means that the B10 sample was more flexible than the concrete samples resulting in more spalling.

Crushing of the samples occurred at 10 mm amplitude for which means and after this amplitude rocking of both samples started. The rocking effect was when the samples split into two-part in the critical cracking zone becoming a mechanism.

4.4.2. Lateral Load – Top Displacement hysteresis

The hysteresis graphs in Figures 4.18 a-c have a fair amount of symmetry under the loading and unloading conditions. The Figures show a wider loop for the B10 after a displacement amplitude of 3.5 mm; however, for S10, the loops are starting to widen at 10 mm amplitude due to intensive plastic deformation.

The loops continue to be wider for the S10 sample, but they narrow after 20 mm displacement for the B10 sample. Both of the effects mean S10 had higher energy dissipation due to higher deformability of B10 and earlier crack developments in concrete.

BA10 sample had a sharp fall of the loops after 5 mm displacement amplitude without initial widening of the loop as a result of anchorage failure due to a thin layer of adhesive between the rebar and the anchor tubes, causing a sudden loss in the energy dissipation of the sample.

A banging noise was heard at 5 mm and 30 mm of amplitudes twice for the B10 samples suggesting a failure of the bond between the concrete and rebars.

Crushing of the concrete occurred at a 10 mm displacement amplitude hysteresis loop for all the samples. However, the S10 peak loop values are higher than B10 and BA10 due to the lesser deformability of the steel sample.

Rocking of the samples occurred at 15 mm for S10 and BA10 samples and 20 mm of amplitude for B10 as can be seen in Figures 7 (a) - (c). However, the S10 samples loops are much wider than the B10 sample due to the residual frictional forces of the threaded steel bars in the critical crack zone.

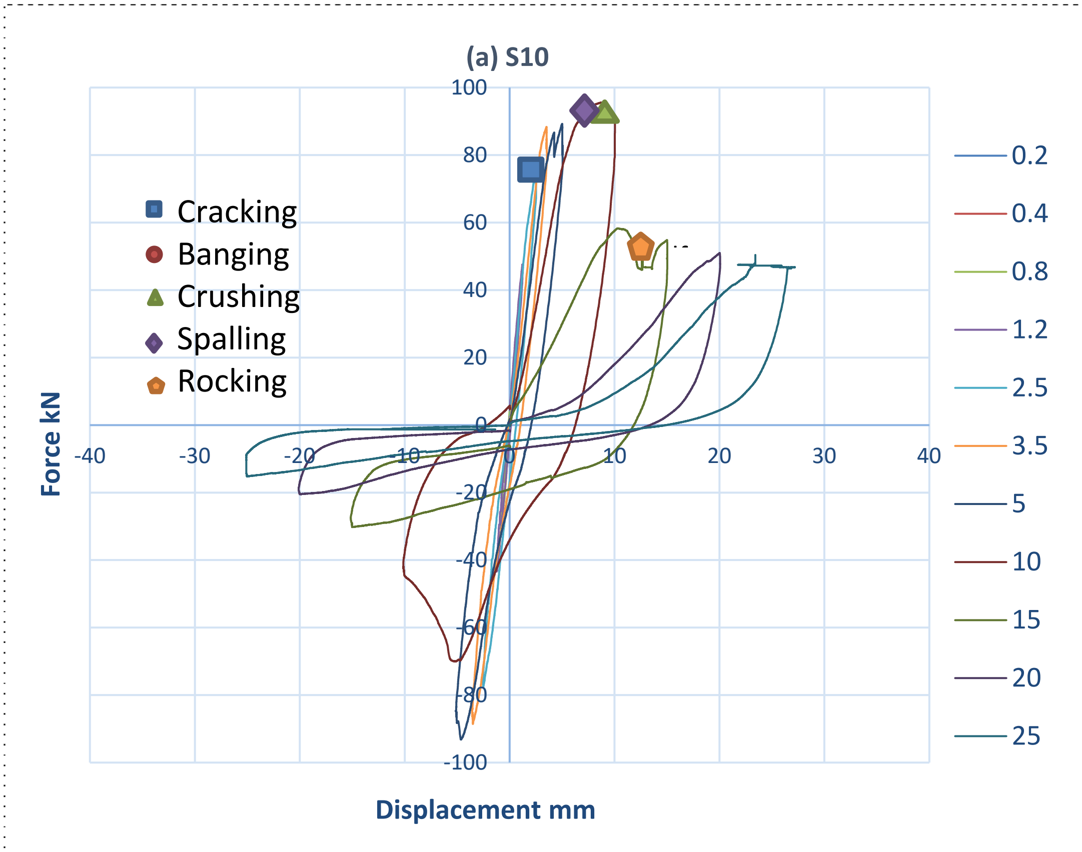

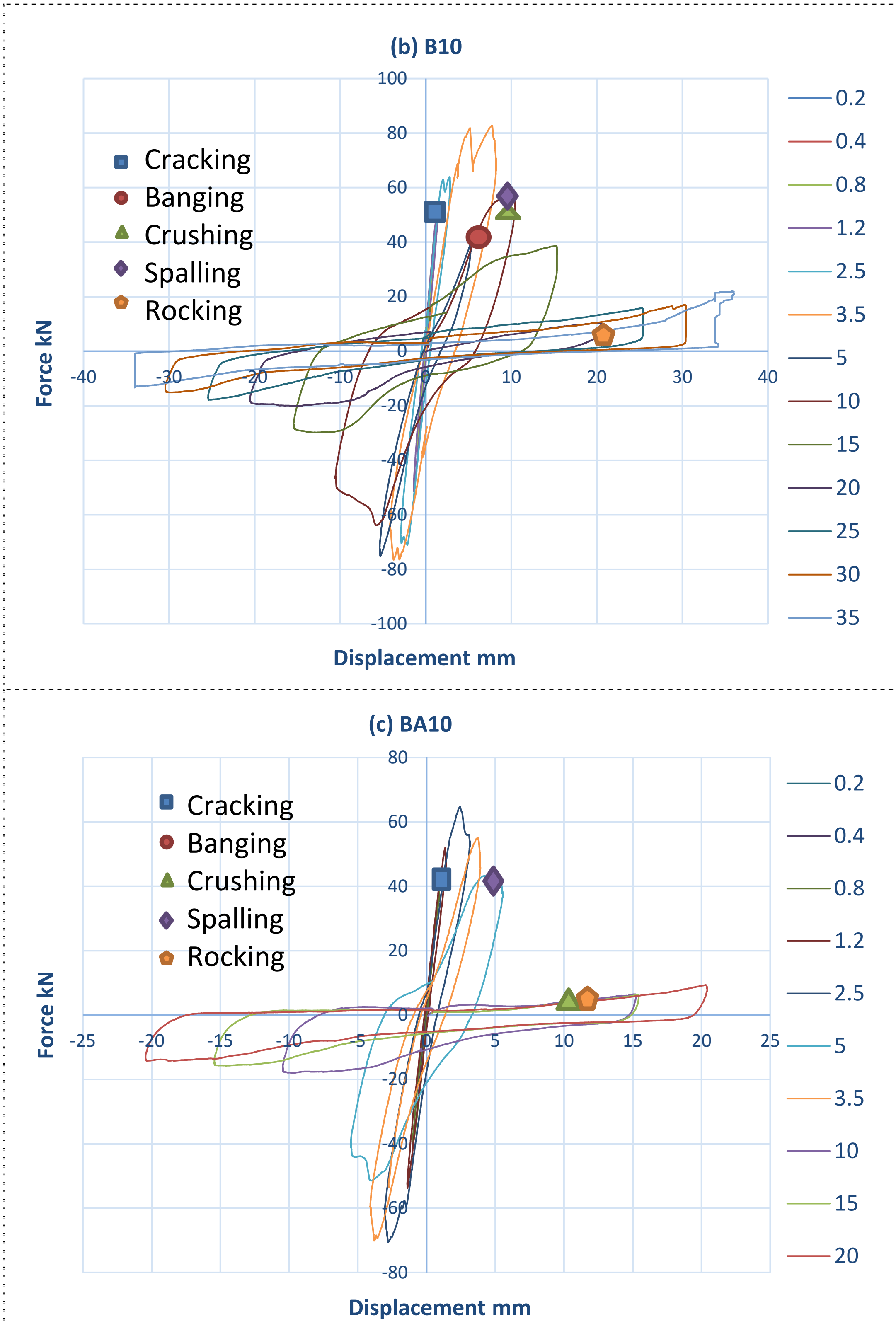

Figure 4.18 - Lateral force versus top-displacement (a) S10, (b) B10 and (c) BA10 samples.

4.4.3. Maximum and Minimum Points

The envelope of maximum and minimum hysteresis response loops value for all the samples are demonstrated in Figure 4.19 below. Due to the destruction of the steel-reinforced sample at 25 mm displacement, the comparison between shear walls is conducted only in this interval.

As it can be seen in the curves, the S10 sample has a higher maximum and minimum response followed by the B10 and BA10 samples, this means that the steel-reinforced sample was having a higher maximum and minimum response under the lateral cyclic loading due to lesser deformability. BA10 had the lowest maximum and minimum response than the two samples as a result of anchorage failure.

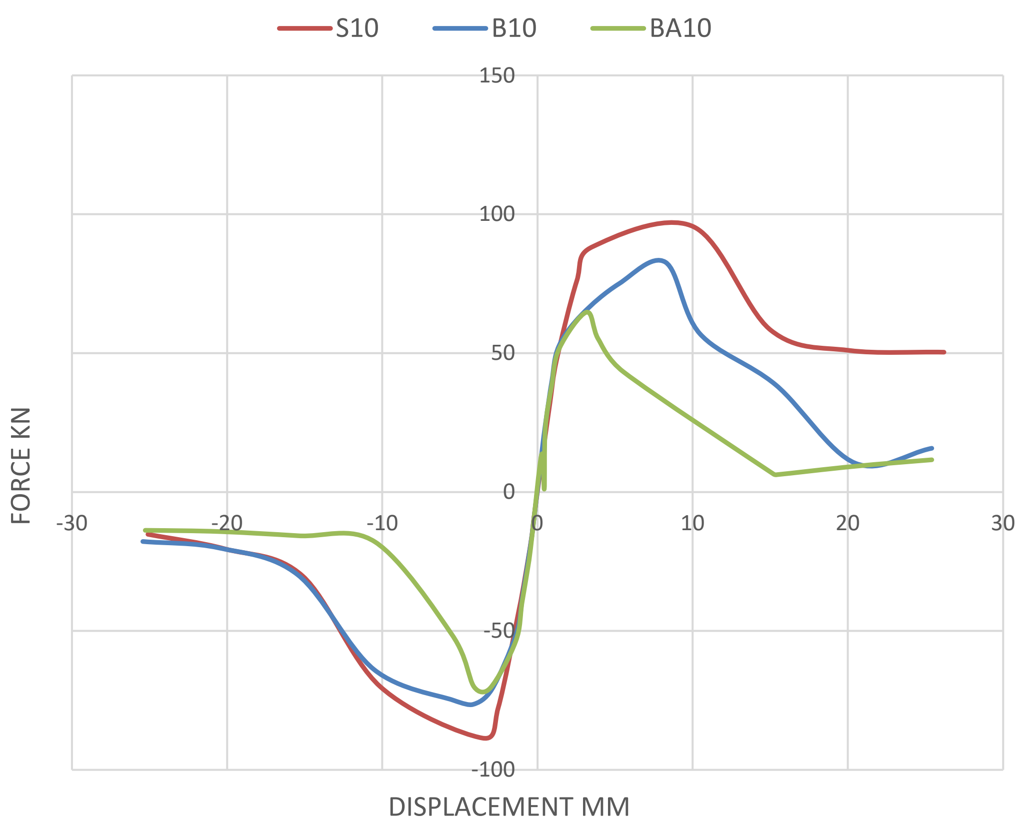

Figure 4.19 - Hysteresis envelope maximum and minimum force against displacement graph for S10, B10 and BA10 samples.

4.4.4. Average Maximum and Minimum Points

The maximum and minimum points from the previous analysis were taken and averaged over the push and pull phase to obtain an average envelope. The force against displacement curves for each sample are depicted in Figure 4.20.

The results show that the S10 sample has a higher force against displacement response in comparison with the B10 sample due to the higher deformability of the B10. Additionally, the S10 sample continues to show capacity after 20 mm displacement amplitude due to threaded steel bars connecting the sample at the critical crack zone with frictional forces.

The initial response of both samples is close to each other until a displacement amplitude of 2.5 mm. After which S10 takes about 10% to 20% higher forces per displacement amplitude. B10 and BA10 show a similar rise in force until 3 mm displacement, after which BA10 falls to 10 kN at about 14 mm. The earlier fall of BA10 is due to the anchorage failure in the sample.

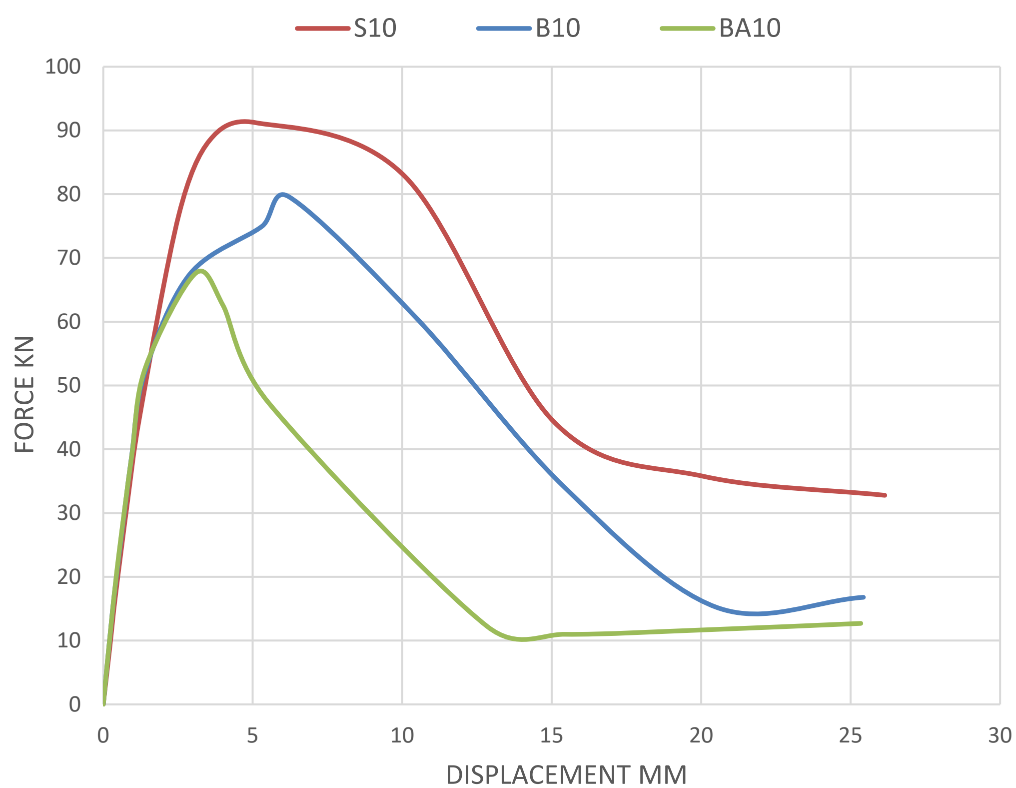

Figure 4.20 - Average maximum and minimum force-displacement graph for S10, B10 & BA10 samples.

4.4.5. Energy Dissipation

Energy dissipation (ED) of the samples were determined by calculating the areas inside each loop in the hysteresis graph to illustrate the response of the samples further. As it can be seen in Figure 4.21, the S10 sample has a higher ED than the B10 and BA10 samples.

The graphs show that S10 peaks quicker at lower amplitudes due to higher modulus of elasticity of steel than B10 and BA10 rebars. The BA10 sample has a maximum ED of about 330 kNmm at 5 mm amplitude due to an earlier failure of the anchorage. The BA10 ED graph falls to 250 kNmm at 15 mm and finishes at approximately 350 kNmm at about 25 mm amplitude.

The initial ED in all samples is similar until a displacement amplitude of 2.5 mm due to a fair amount of elasticity in the samples. However, the BA10 is slightly above the S10 and B10 due to the rebar-anchorage adding rigidity to the systems in the BA10 sample.

The B10 graph peaks at an amplitude of 14 mm due to the higher deformability in this sample. The S10 graph rises quickly to a peak ED of approximately 1160 kNmm at about 11 mm displacement amplitude due to higher stiffness in the sample.

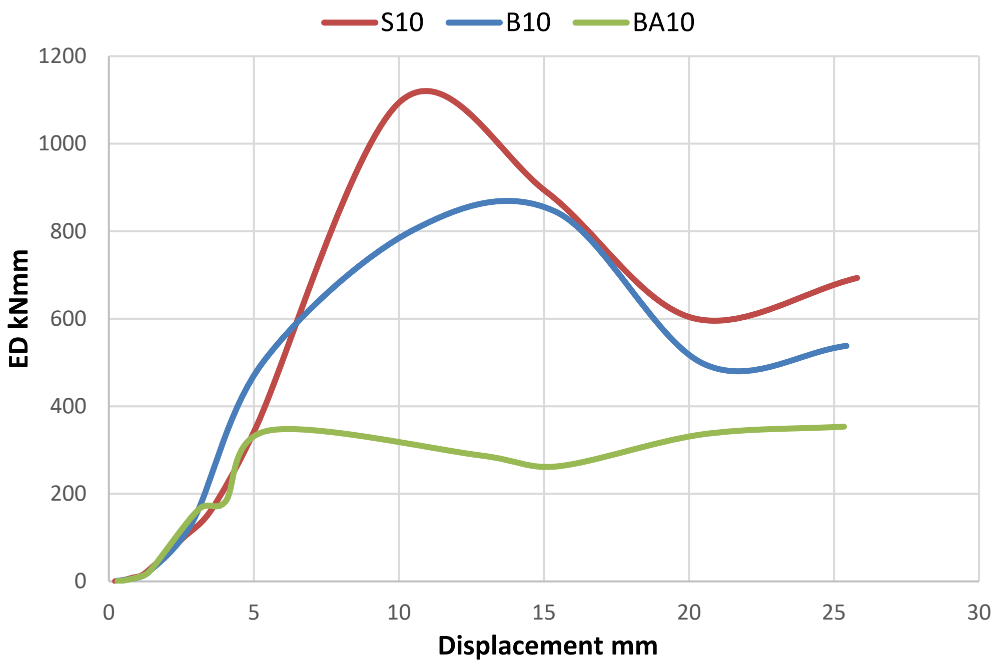

Figure 4.21 - ED against Displacement amplitudes for S10, B10 and BA10 samples.

4.4.6. Cumulative Energy Dissipation

Cumulative energy dissipation (CED) in kNmm against displacement (mm) amplitude for all the samples is shown in Figure 4.22. CED graphs are the cumulative addition of EDs at each displacement amplitude.

The curves in figure 4.22 have a similar behaviour until a CED of about 650 kNmm at around 6 mm displacement amplitude. After this point, the S10 sample shows the highest CED followed by the B10 and BA10. The S10 and B10 CED show similar behaviour although the final S10 CED is about 15% higher than B10 for the investigated interval of displacement.

The BA10 graph shows a lower CED than S10 and B10 after a displacement amplitude of about 6 mm corresponding to about 700 kNmm after which rises to just less than 2000 kNmm at 25 mm displacement amplitude. The lower CED in BA10 is due to the failure of the rebar anchorage.

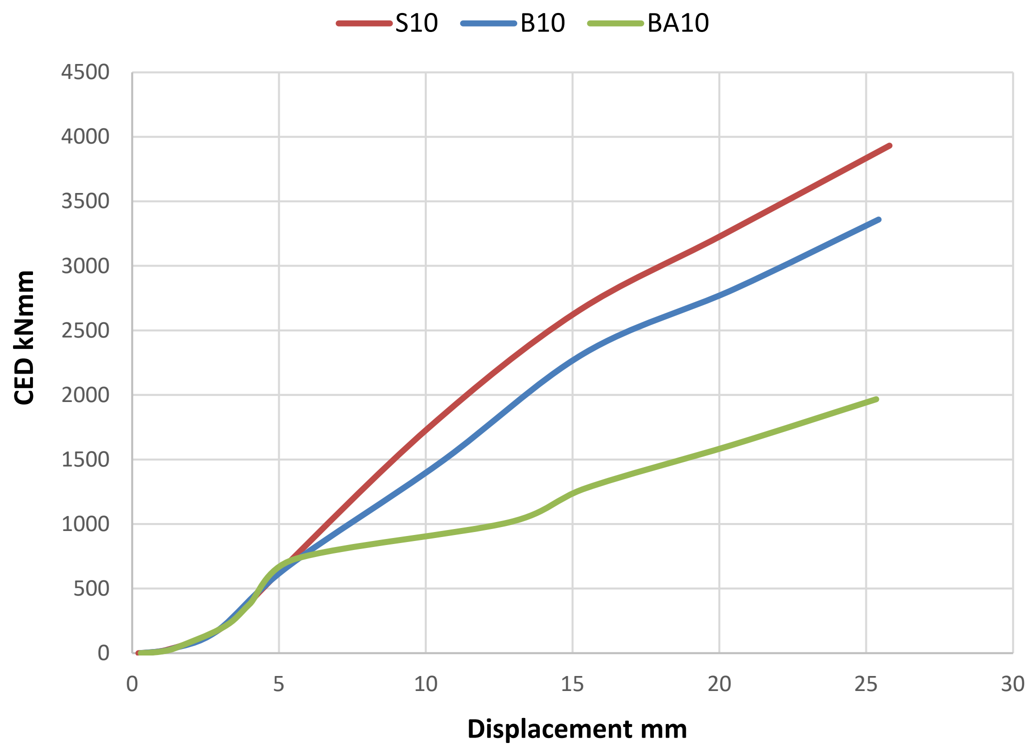

Figure 4.22 - CED against displacement for the S10 and the B10 samples.

4.4.7. Sub-Chapter Conclusions

The experiments were conducted using the structural lab at KUL, and the following conclusions can be drawn:

- The B10 HLPVs are lower than S10 due to higher deformability of FRP and more intensive development of cracking in concrete. BA10 HLPV is the lowest due to the earlier failure of the anchorage in the sample.
- The B10 and BA10 averaged maximum and minimum points (AMMP) curve is about 20% and 25% lower than S10, respectively. The B10 AE fall is more gradual than S10. BA10 AMMP curve fall is quicker than S10 and B10 due to an early failure of the anchorage in the sample.
- The B10 ED is about 30% less than S10. The BA10 ED is significantly lower due to the earlier failure of the anchorage in the sample.
- The B10 and S10 CED have a gradual rise. B10 have about 13% lower CED than S10. BA10 CED is about 30% less than S10.

Generally, the peak values of the BFRP reinforced samples are lower but in close range to the steel-reinforced samples. The result shows a promising prospect for utilisation of the BFRP rebars as reinforcement in shear walls under cyclic load. The addition of anchorage to the rebars in this specific case is not effective therefore further investigation using different types of anchorage to BFRP rebars is recommended.

5. Finite Element Modelling Bases

5.1. Introduction

The analysis of the RCSWs in this study is carried out using Ansys mechanical (Ansys), which is a three-dimensional nonlinear Finite Element Analysis (FEA) application to simulate engineering problems.

Ansys is capable of modelling RC as discrete or smeared-model. The discrete model takes the reinforcement as individual bars in the models and the smeared-model, models the reinforcement as a percentage ratio of the whole concrete model.

The concrete part of the models is discretized with Solid65 and CPT215 elements which are three-dimensional elements capable of simulating crack/crushing and strain-softening of concrete respectively. Solid65 is also capable of modelling the reinforcement bar as smeared reinforcement; however, in this study, an additional Link180 element is used to model reinforcements for a more accurate representation of the physical model.

Bond-slip behaviour between concrete and reinforcement are modelled with interface elements between the offset nodes (EINTF). Suitable interface elements were selected to model the bond-slip behaviour in the models. The performance of the interface elements was tested under the hysteresis and pushover analysis and suitable elements were selected for calibration and convergence of the results.

This chapter will encompass the representation of the model with material nonlinearity under quasi-static reversed cyclic-loading. The loading protocol used is ATC-24 which is a cyclic loading with three repetitions of a cycle. A modified version of the loading was used with one repetition per cycle as the protocol is very demanding for RCSWs. The models are then calibrated with the RCSWs specimens constructed and tested under quasi-static reversed cyclic-loading at Civil Engineering Laboratory, KUL for results validation.

The FE model is analysed in terms of hysteresis response, pushover strength, cracking patterns, deformations, reactions, failure points and strain softening. Additionally, parametric studies are conducted to examine the response of the validated model for different strength classes of concrete not tested experimentally.

The Ansys mechanical is available both commercially and at KUL networked computers. The application is highly suitable software in the analysis of engineering, nonlinear problems. There is an extensive number of elements and material models in the library of this application that can model the structural behaviours, for example, the Solid65 element and Microplane material model which is capable of simulating the behaviour of highly nonlinear and brittle natured concrete.

5.2. Fundamentals of FEA

Finite Element Analysis (FEA) is based on the Finite Element Method (FEM) to obtain approximate solutions to complex problems. The FEM is a mathematical numerical method that transforms the model into a discrete domain (Harish, 2020a).

The domain is made up of a finite number of elements interconnected through nodes, boundary lines, surfaces or a combination of these. Each element is associated with a displacement function which together with a known stress/strain material property, determines the behaviour of a given node. A matrix notation is used containing a total set of equations describing the behaviour of each node. The procedure commonly used in the FEM formulation and solution of a structural problem is summarised in this section (Logan, 2015).

Discretization involves dividing a domain into a number of finite elements. The number, size and shape of an element depend on the engineering judgement and experience. Generally, the size of an element must be small enough to give a usable result and large enough to reduce computation effort. Small elements are desirable where the change in results is rapid such as a change in a model geometry and larger elements are suitable where results are constant.

Elements selection for the discretized domain is another essential step to model the actual physical behaviour most closely. The selection depends on the physical make-up of the domain and understanding the theory behind the element. There are three main types of elements including primary bar elements, two-dimensional plane elements and three-dimensional solid elements.

The displacement function also known as the shape function describes the displacement within the element in terms of node values. The functions that are frequently used as shape function are polynomial functions including linear, quadratic and cubic functions. The higher-order elements for example a quadratic element possess additional nodes in the form of a mid-side or mid edge node that can be used to define the behaviour within the element at a shorter interval with a quadratic function (Ellobody et al. 2014).

To define the behaviour at the material level it is essential to specify the strain/displacement and stress/strain relationship for each finite element. For example in one-dimensional deformation in the *x*-direction the strain ε_x can be related to the displacement *u* as Equation 5.9 following:

$$\varepsilon_x = \frac{du}{dx} \qquad \text{Equation 5.9}$$

The stress can be related to the strain through the stress/strain law generally called the constitutive law. For example, Hooke's law which is commonly used in stress analysis given as following:

$$\sigma_x = E\ \varepsilon_x \qquad \text{Equation 5.10}$$

Where σ_x = stress in the *x*-direction and *E* = modulus of elasticity.

A stiffness matrix and element equations are developed based on the direct equilibrium (DE), work/energy (WE) or weight residual (WR) method. The DE method relates nodal forces to nodal displacements using force equilibrium conditions for a basic element along with force/displacement relationships. The WE method uses the principle of virtual work, minimum potential energy and Castigliano's theorem. Furthermore, the WR method yields the same results as WE whenever the WE method is applicable, and the method is particularly useful when the principle of potential energy is not available.

The application of any method outline above will produce the equations describing the behaviour of an element. The equations can be written in the compact matrix form as follow:

$$\{f\} = [k]\ \{d\} \qquad \text{Equation 5.11}$$

Where $\{f\}$ is the vector of element nodal forces, $[k]$ is the element stiffness matrix and $\{d\}$ is the vector of unknown element.

Once the element equations are formed the next step is to assemble the global equation for the whole model and introduce the boundary conditions. The global or assembled equation can be written in the compact matrix form of:

$$\{F\} = [K]\ \{d\} \qquad \text{Equation 5.12}$$

Where $\{F\}$ is the vector of global nodal forces, $[K]$ is the global/total stiffness matrix and $\{d\}$ is the known and unknown structures nodal DoF or generalised displacements. The boundary conditions (constraints or supports) can be introduced in the stiffness matrix [*K*] so that the body remains in place and do not move like a rigid body also known as the singularity problem.

Once the stiffness matrix [*K*] is modified to include the boundary conditions, the equations can be utilised to solve the displacements using elimination or an iterative method such as Gauss's or Gauss-Seidel methods, respectively. The displacements {*d*} are also known as primary unknowns, and secondary quantities of strain and stress can be derived using equation 5.1 and 5.2 (for one-dimensional element), respectively.

The stiffness matrices allowing cracking and crushing in Solid65 which is a comprehensive element is explained below. In the Solid65 cracking is permitted in three orthogonal directions at each integration point. The material properties at cracked integration point is adjusted to treat the crack as "smeared band" and not a discrete crack. The stress-strain matrix for this element is defined as Equation 5.1 below:

$$[D] = \left(1 - \sum_{i=1}^{N_r} V_i^R\right)[D^c] + \sum_{i=1}^{N_r} V_i^R \, [D^c]i \qquad \text{Equation 5.1}$$

Where: N_r = number of reinforcing materials (can be used if reinforcement capability is used)

V_i^R = the ratio of reinforcement volume *i* to total volume of elements.

$[D^c]$ = stress-strain matrix for concrete

$[D^c]i$ = stress-strain matrix for reinforcement i

The matrix [D^c] can be derived by specializing and inverting the orthotropic stress-strain relations and in the case of an isotropic material in can be written in the matrix form (Equation 5.2) below:

$$[D^c] = \frac{E}{(1+v)(1-2v)} \begin{bmatrix} (1-v) & 0 & 0 & 0 & 0 & 0 \\ 0 & (1-v) & 0 & 0 & 0 & 0 \\ 0 & 0 & (1-v) & 0 & 0 & 0 \\ 0 & 0 & 0 & \frac{(1-2v)}{2} & 0 & 0 \\ 0 & 0 & 0 & 0 & \frac{(1-2v)}{2} & 0 \\ 0 & 0 & 0 & 0 & 0 & \frac{(1-2v)}{2} \end{bmatrix} \qquad \text{Equation 5.2}$$

Where:

E = Young's modulus for concrete (input as EX on MP command, used in subsection 6.3.1)

v = Poisson's ratio for concrete (input as PRXY on MP command, used in subsection 6.3.1)

The matrix for the concrete material model is capable of cracking, crushing, plasticity and creep. The model can predict either elastic behaviour, cracking behaviour or crashing behaviour. When cracking or crushing behaviour is predicted the stress-strain matrix gets adjusted for each failure mode. The stress-strain relationship for the material model cracked in one direction becomes as Equation 5.3 below:

$$[D_c^{ck}] = \frac{E}{(1+v)} \begin{bmatrix} \frac{R^t(1+v)}{E} & 0 & 0 & 0 & 0 & 0 \\ 0 & \frac{1}{1-v} & \frac{v}{1-v} & 0 & 0 & 0 \\ 0 & \frac{v}{1-v} & \frac{1}{1-v} & \frac{\beta_t}{2} & 0 & 0 \\ 0 & 0 & 0 & 0 & \frac{1}{2} & 0 \\ 0 & 0 & 0 & 0 & 0 & 0 \\ 0 & 0 & 0 & 0 & 0 & \frac{\beta_t}{2} \end{bmatrix} \qquad \text{Equation 5.3}$$

Where:

β_t = the shear transfer coefficient (constant C1 applied with command TB,CONCR, later used in subsection 6.3.1). The coefficient represents a shear strength reduction factor for subsequent loads which cause shear sliding across a cracked face.

ck = the superscript signifies that the stress strain relationship refer to a coordinate system parallel to principal directions.

R^t = the slope (secant modulus) as defined in the Figure 5.1 below (controlled by key option (7), later used in subsection 6.3.1).

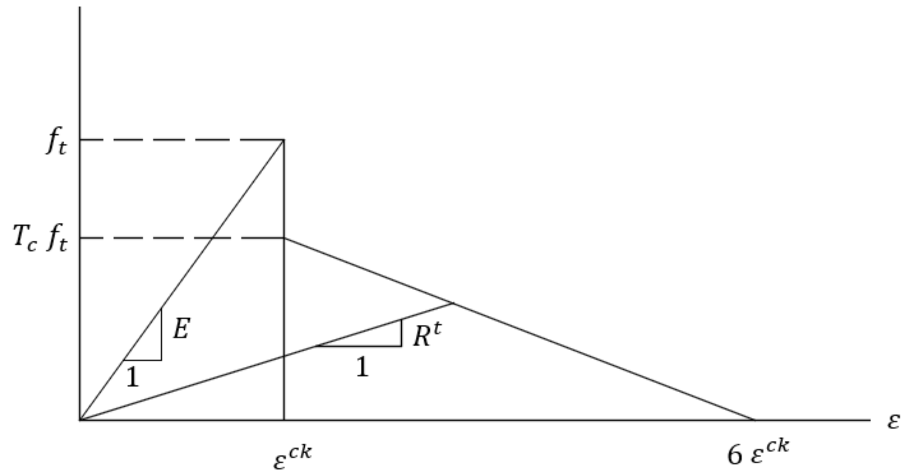

Figure 5.1 - Strength of cracked condition after (Ansys help systems, 2020)

Where:

f_t = uniaxial tensile cracking stress (input as C_3 with TB,CONCR command, used in subsection 6.3.1).

T_c = tensile stress relaxation multiplier (input as C_9 with TB, CONCR, used in subsection 6.3.1)

When the crack closes, then the shear transfer coefficient β_c (input as C_2 with TB,CONCR command, used in subsection 6.3.1) for a closed crack is used. The coefficient transmit all compressive stresses normal to the crack plane. The matrix for a closed crack can be written as Equation 5.4 below:

$$[D_c^{ck}] = \frac{E}{(1+v)(1-2v)} \begin{bmatrix} (1-v) & 0 & 0 & 0 & 0 & 0 \\ v & (1-v) & 0 & 0 & 0 & 0 \\ v & v & (1-v) & 0 & 0 & 0 \\ 0 & 0 & 0 & \beta_c \frac{(1-2v)}{2} & 0 & 0 \\ 0 & 0 & 0 & 0 & \frac{(1-2v)}{2} & 0 \\ 0 & 0 & 0 & 0 & 0 & \beta_c \frac{(1-2v)}{2} \end{bmatrix} \quad \text{Equation 5.4}$$

If the material cracks in two directions or in all directions the matrix can be written as Equation 5.6 below:

$$[D_c^{ck}] = E \begin{bmatrix} \frac{R^t}{E} & 0 & 0 & 0 & 0 & 0 \\ 0 & \frac{R^t}{E} & 0 & 0 & 0 & 0 \\ 0 & 0 & 1 & 0 & 0 & 0 \\ 0 & 0 & 0 & \frac{\beta_t}{2\,(1+v)} & 0 & 0 \\ 0 & 0 & 0 & 0 & \frac{\beta_t}{2\,(1+v)} & 0 \\ 0 & 0 & 0 & 0 & 0 & \frac{\beta_t}{2\,(1+v)} \end{bmatrix} \qquad \text{Equation 5.6}$$

If the crack closes back in all the three directions same Equation 5.4 applies. If the failure is in the integration point under uniaxial, biaxial and triaxial compression, the material is assumed to be crushed. Crushing is defined as complete deterioration of the material's structural integrity e.g. spalling of concrete. When the material crush in an integration point, the strength is assumed to have no contribution in the stiffness of the element.

The criterion at which the material crack are crush is based on the Willam and Warnke (1975) failure surface criterion due to a multiaxial stress state which can be written as Equation 5.6 below:

$$\frac{F}{f_c} - S \geq 0 \qquad \text{Equation 5.6}$$

Where:

F = a function of the principal stress states (σ_{xp}, σ_{yp}, σ_{zp})

S = failure surface in terms of principal stresses f_t, f_c, f_{cb}, f_1 and f_2 as defined in Table 6.2.

f_c = uniaxial crushing strength

σ_{xp}, σ_{yp}, σ_{zp} = principal stresses in principal directions

The cracking or crushing of the material will take place if the Equation 5.6 is satisfied. The failure surface parameters are defined and values are obtained based on the experimental test results, BS EN-1992-1-1:2004 and literature data. Although all parameters are explained here, the failure surface can be satisfied with a minimum of two constants f_t and f_c. The other three constants will default to the Willam and Warnke as shown in the Equations 5.7, 5.8 and 5.9 below:

$$f_{cb} = 1.2\, f_c \qquad \text{Equation 5.7}$$

$$f_1 = 1.45\, f_c \qquad \text{Equation 5.8}$$

$$f_2 = 1.725\, f_c \qquad \text{Equation 5.9}$$

Further detail about the Solid65 and Microplane models' development are given in sections 6 and 7, respectively. The subsections introduce the elements and then explains the material properties used from the lab experiments to develop the model for examples the stress-strain relationship based on the experimental data (Figure 6.9).

The interaction between the concrete and the rebars through the interface element and direct interactions are described in the bonding connection subsection (7.2.3). The same bonding behaviour applied to both the Solid65 and Microplane models as the bonding interaction is not a changing parameter in the development of the two models for the behaviour of the concrete material.

The final step is to interpret and analyse the results. Postprocessor in FE applications help with displaying the results in graphical form to help with interpretation. Determination of location where large deformation and large stresses occur is generally important in the analysis of results for a structure.

5.3. Finite Element Procedure

Understanding the physical model is essential in transforming the physical problem into a mathematical model. Additionally, it is essential to understand the FE procedures to be able to develop a model. In the static analysis of the problems the FEM procedures can be summarised as follows (Stolarski et al. 2006):

1. *Discretization* – to divide the domain into a finite number of elements.
2. *Selection of interpolation function* – select element order to approximate the displacement and strains in each element.
3. *Obtaining the stiffness matrices* – determine the element stiffness matrix which relates forces and displacements in each element.

4. *Assembly of stiffness matrix to global stiffness matrix* – assemble the stiffness matrices into the global stiffness matrix to relate forces and displacements in the whole body to be analysed.
5. *Rearrangement of the global stiffness matrix* – substitute boundary conditions (forces and displacements) into a global stiffness matrix to set up simultaneous equations.
6. *Derivation of unknown forces and displacements* – solve the simultaneous equations to obtain unknown force and displacement variables.
7. *Computation of strain and stresses* – compute the strains and stresses from the displacements obtained in the previous step.

In the following two sections, the above procedures are employed to develop two models including a “Solid65 model” and a “Microplane model” to simulate the behaviour of the specimens under hysteresis and pushover analysis, respectively. The model outcomes are calibrated with experimental results, and the validated model is used for parametric studies.

6. Development and Results of “Solid65” Model

The model developed for hysteresis response analysis is named as Solid65 model. The name is employed because Solid65 is a familiar name used in the analysis of concrete by the researchers.

In the following section, relevant information and explanations are given about the geometry development, element selections, material properties, meshing, boundary conditions and the analysis settings. Results are analysed and conclusions are drawn based on the evaluation of the results.

In the material properties section, concrete, FRP, steel material and bond model are described based on information available from the experimental data and relevant recent published literature. The material properties obtained from the experimental tests and manufacturers data are tabulated or shown in graphs for further elaboration.

6.1. Model Geometry

One of the essential components of defining a mathematical model is to define its geometry in the finite element method described in the previous chapter. The geometry of the model will define how the elements compile. The geometry of the shear wall in this study is modelled using Ansys. Since the shear wall is made of reinforced concrete, the Solid65 element is utilized.

In modelling the geometry of the shear wall, some feature that does not contribute significantly is removed. The model is generated in full across the x-y and z coordinates. There are steel parts (steel plate, RSH and PFC, please refer to section 3.3.3 for further details) used in the physical model to connect the model into the strong-frame in the bottom area of the shear wall. However, such a connection is not necessary to develop in the FE model as the focus of this study is the internal-reinforcement of the shear wall. Hence, connecting mechanism features are removed as part of the “defeaturing” exercise. The dimension of the RCSW is listed in Table 6.1 below.

Table 6.1 **-** The basic configuration of the RC wall models

Model no	Rebar type	Rebar size (mm)	Stirrups (mm)	Breath (mm)	Height (mm)	Depth (mm)
1	BFRP	6/10	6	1000	1000	100
2	Steel	6/10	6	1000	1000	100

DesignModeler in the Ansys Workbench environment is utilised to generate the geometric display in Figure 6.1. A geometric-display by Ansys model is a display of the model’s geometric feature including key points, lines, areas and volumes. Key points are the points that define the vertices in a solid model geometry, and they are the “lowest-order” in the geometry of the model (Ansys help systems 2020).

Three-dimensional views of the volumes created for the wall are shown in figure 6.1 below. Three types of volume were created for the model; Figure 6.1 (a) full model, (b) rebar cage, (c) half model, and (d) half model with multiple volumes. Half models were generated by removing the symmetrical half of the model along the plane of the wall to test the analysis computing time efficiency. The multiple-volume model was created to be able to use the node-merge command to connect concrete with rebars. Full-model was selected with all reinforcements (Figure 6.1 (b)) at the end for a more reliable and better display of results. Furthermore, a small difference between half and full model computing time was recorded as a result of utilising fast computer modules.

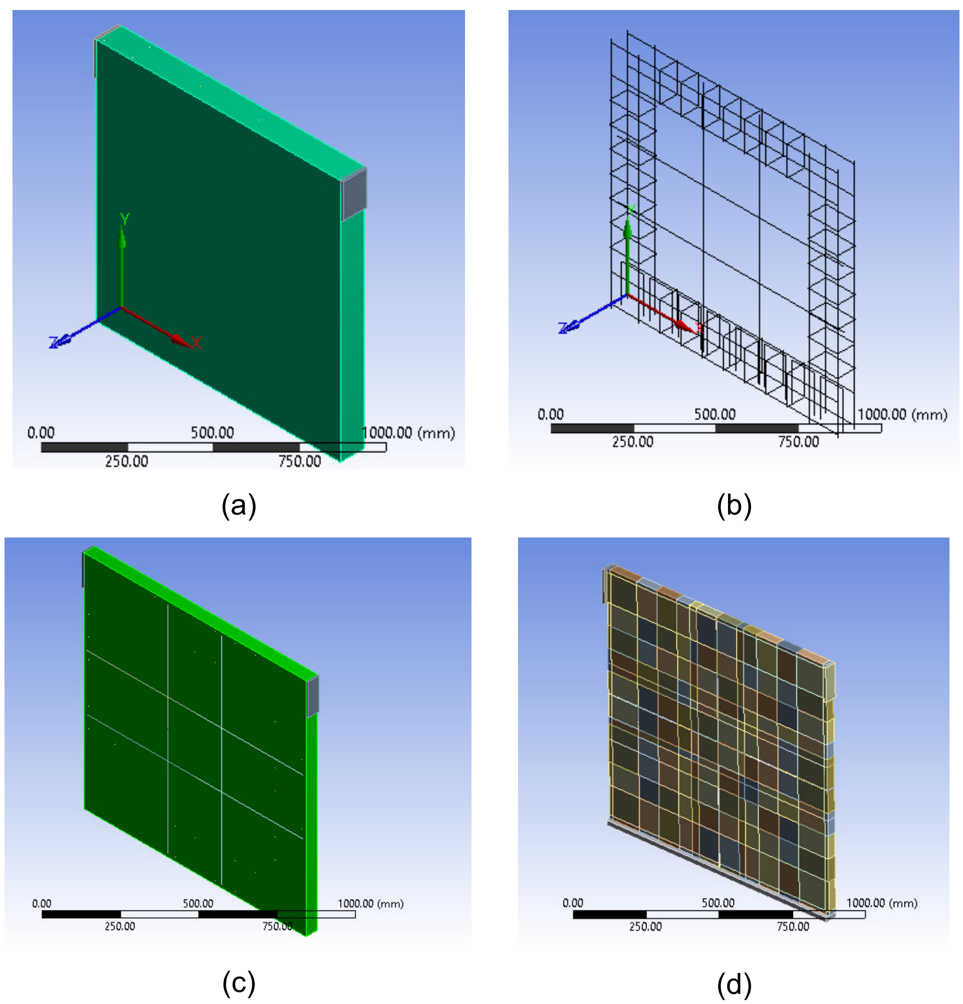

Figure 6.1- Three-dimensional volumetric illustration of the shear all FE model (a) full mode (b) reinforcements, (c) half model, (d) half model multiple-volumes (Image used courtesy of ANSYS, Inc.)

6.2. Element Selection

To analyse the cracking and crushing properties of the shear wall under quasi-static loading, the concrete, rebars and bond between the two were modelled with solid, link and spring elements, respectively. Selecting appropriate elements is the most important and fundamental decision that has to be taken before starting the analysis, which depends on the geometry, material and loading scheme applied to the model.

The advantage of 3D modelling is that it allows for a model closer to the real structure, and hence there is no need to simplify the problem by making assumptions. In some case, it is possible to simplify the problem by taking advantage of the symmetry and modelling part of the problem with appropriate boundary condition. In this analysis, the full-scale model is developed to have a better representation and illustration of the results.

6.2.1. SOLID65

Solid65 in Ansys is a three-dimensional element used to model structures, especially concrete. It is an element that can represent the concrete with or without reinforcement. The solid element is capable of cracking in tension and crushing in compression. The element is defined by eight nodes, each node having three DoF in the x, y and z directions.

The element is capable of analysing the nonlinear properties of the concrete and cracking in three orthogonal directions, crushing, plastic deformation and creep. The geometry, node locations and coordinate system are shown in Figure 6.2 for the Solid65 element. The element also has prism and tetrahedral options as well, which is not used in this study (help systems, 2020).

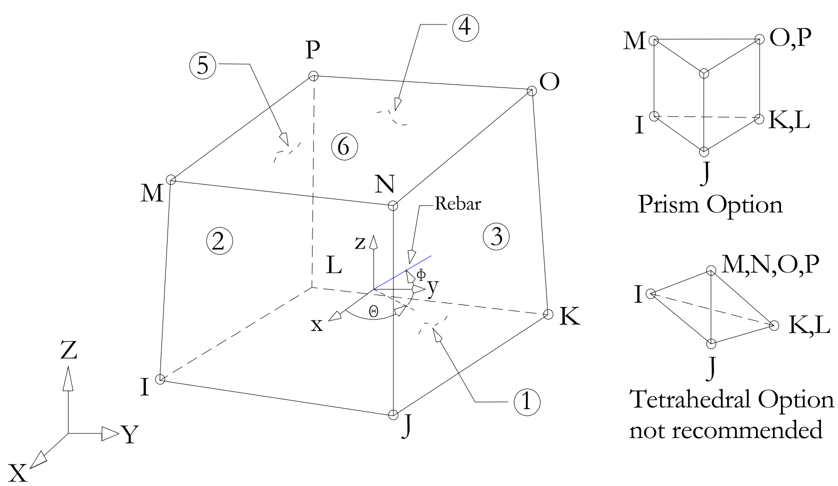

Figure 6.2 - 3D Ansys Solid65 element geometry, after (Ansys help systems, 2020)

Ansys Mechanical is formulated to choose an element type automatically depending on the defined geometry and the mesh size and shape selected. Therefore, the following command snippet is used as an object command to define the element type Solid65 and its associated key options:

```
ET,MATID,SOLID65
R,MATID,0,0,0,0,0,0
RMORE,0,0,0,0,0,0
! Element type Solid65

KEYOPT,MATID,1,1
! Extra displacement shapes:
! 0 – Include extra displacement shapes
! 1 – Suppers extra displacement shapes

KEYOPT,MATID,3,2
! Behaviour of totally crushed unreinforced concrete:
! 0 – Base
! 1 – Suppress mass and applied loads, and warning messages (see KEYOPT(8))
! 2 – Features of 1 and apply consistent Newton-Raphson load vector.

KEYOPT,MATID,5,0
! Concrete linear solution output:
! 0 – Print concrete linear solution only at the centroid
! 1 – Repeat solution at each integration point
! 2 – Nodal stress printout

KEYOPT,MATID,6,0
! Concrete nonlinear solution output
! 0 – Print concrete nonlinear solution only at the centroid
! 3 – Print solution also at each integration point

KEYOPT,MATID,7,1
! Stress relaxation after cracking:
! 0 – No tensile stress relaxation after cracking
! 1 – Include tensile stress relaxation after cracking to help convergence

KEYOPT,MATID,8,0
! Warning message for totally crushed unreinforced element:
! 0 – Print the warning
! 3 – Suppress the warning
```

The command ET is used to select the element type (Solid65) from the element library and establish it as a local type element for the current model. Information from the element type is used in the subsequent commands, so it is defined early among commands. MATID is the ITYPE argument that is selected for the concrete material model. ITYPE argument activates the element’s type name or the number for the element. Then a name (MATID) or a number (default is one if not user-selected) can be used to assign all linear and nonlinear properties of the material model to it. R,MATID defines the real constant for the concrete material (up to 6 constants), and RMORE defines real (additional six constants).

There are very helpful options (known as key-options) in the Solid65 element that can be applied in the analysis using the Keyopt command. Option (7) and option (3) can help with the convergence of the results by stress relaxation and small load increment application, respectively. If option (7) = 1 is chosen a tensile stress relaxation multiplier can be selected, but if no input is used, the solver will use the default value of 0.6. However, after convergence is achieved for the cracked state, the modulus (stiffness) normal to the crack face is set to zero. To activate a very small load increment application option (3) = 2 need to be set.

Option (8) and option (1) are used to suppress unwanted warning and extra displacement shapes, respectively. If the earlier option is set to 1, the program will suppress a warning when each unreinforced element crushes at integration points. Option (5) and option (6) are used for element print out options at each integration point or the centroid for concrete linear and nonlinear solution outputs, respectively. Option (3) allows selection for the behaviour of totally crushed unreinforced elements by suppressing mass, applied loads, a warning message and consistent application of Newton-Raphson load vector.

Rebar and nonlinear printouts will appear if their properties are defined. The printout will include all integration points if the cracking and crushing material properties are defined because cracking and crushing can occur at any integration point. The PLCRACK command in the series of General Post-processor commands POST1 can be used to display the status of the integration points.

PLCRACK use circles and octahedrons to show the location of the cracking and crushing in concrete elements, respectively. The circle will be shown in the plane of the crack and if a crack is opened and then closed the circle will have an X through it. A summary is shown below:

- Cracking – Circles
- Crushing – Octahedrons
- Closed crack – Circle with X

Each integration point can crack in up to three different planes which are displayed in a different colour as following:

- First crack – Red
- Second crack – Green
- Third crack – Blue

Symbols and colours are shown in the element centroid based on the status of all the elements’ integration points. Since Solid65 have multiple integration points, if any integration point cracks or crush the symbol will be displayed in the centroid. If more than one integration point crack a circle symbol representing the crack will outline at the element centroid showing an average orientation of all cracks.

The solution output for the Solid65 can be in two forms, including; nodal displacement and additional element outputs. The constants in Table 6.2 define the cracking and crushing capability of the concrete. If a value of -1 is selected for constant 3 or 4 no cracking and crushing capability will be activated, respectively (Ansys help systems, 2020)..

The constants C1 to C9 meanings are explained in Table 6.2. If the constants C1 to C4 is without constants C5 – C8 then the later shall resort to the default values. If even one of the constants between C5 – C8 is entered, no default values shall be used, and all the constants must be input. The above stress state is defined as a function of the principal stress in all three principal directions.

Constant that can define the cracking and crushing properties of concrete can be entered to the using TB command with *Lab* = CONCR. Up to nine constants can be defined by activating a table using the TBDATA command, data that are not input are assumed to be zero by the solver.

Table 6.2 - Cracking and crushing constants for concrete

Constant	Symbol	Meaning
C1	(β_t)	Shear transfer coefficients for an open crack.
C2	(β_c)	Shear transfer coefficients for a closed crack.
C3	(f_t)	Uniaxial tensile cracking stress.
C4	(f_c)	Uniaxial crushing stress (positive).
C5	(f_{cb})	Biaxial crushing stress (positive).
C6	(σ_h^a)	Ambient hydrostatic stress state for use with constants 7 and 8.
C7	(f_1)	Biaxial crushing stress (positive) under the ambient hydrostatic stress state (constant 6).
C8	(f_2)	Uniaxial crushing stress (positive) under ambient hydrostatic stress state (constant 6).
C9	(T_c)	Stiffness multiplier for cracked tensile condition, used if KEYOPT(7) = 1 (defaults to 0.6).

The element has some restrictions and requirements when utilizing its capabilities. A zero volume is not allowed, and the element needs an iterative solution since it is nonlinear. Slow loading is required when both the cracking and crushing capability of the element is utilized because fictitious crushing of concrete can occur through a closed crack before proper load transfer.

The integration points where crushing occurs, the output creep and plastic strains are from the previous converged substep. Also, elastic strain output includes cracking strain when cracking occurs. If the implicit methodology of reinforcing is used the shear resistance of the cracked or crushed element cannot be transferred to the rebars which have no shear stiffness anyway.

The use of stress stiffening effects, large strain and large deflection is not recommended with the element. The results either may not converge or maybe not be correct particularly if large rotation effects are involved. When the element is used in Ansys mechanical, the element “birth and death” and creep capabilities are not available.

Special features of the Solid65 element include adaptive decent. Adaptive decent is a technique the solver uses to switch to a stiffer matrix if the solution is not converged and switches back to the full tangent after the solution converges which helps in a faster convergence rate Eggert (1991).

The adaptive-decent technique is part of Newton-Raphson methodology to obtain convergence. Newton-Raphson methodology named after Isaac Newton and Joseph Raphson is a way to find a good approximation for the root of a real value function. The solver uses Newton-Raphson equilibrium iterations to obtain a solution.

Equilibrium iteration uses an incremental solution to obtain convergence. The incremental solution adjusts the stiffness matrix of the model to reflect nonlinear changes in the stiffness before going to the next increment. The size of each increment can be controlled through load steps. In nonlinear analysis total load applied to an FE model is divided into a series of increments called load steps. Smaller load increments help the convergence of the solution.

Newton-Raphson equilibrium iterations provide convergence at the end of each load increment within a tolerance limit. The default value for the tolerance limit is 0.5%. Where;

- F is the applied force
- F_1 is the internal residual force
- X is the result of convergence (F)

Each iteration is a linearized solution. Once the force F is applied, displacement X1 is calculated. From X1 the residual force F1 is calculated. Since F ≠ F1 another iteration is required where X2 and F2 are obtained. The process continues until there is no residual force (F=F1=F2…). Figure 6.3 shows three iterations and two load-steps. The load steps are converged after three iterations at point a and b in the example given below (Figure 6.3).

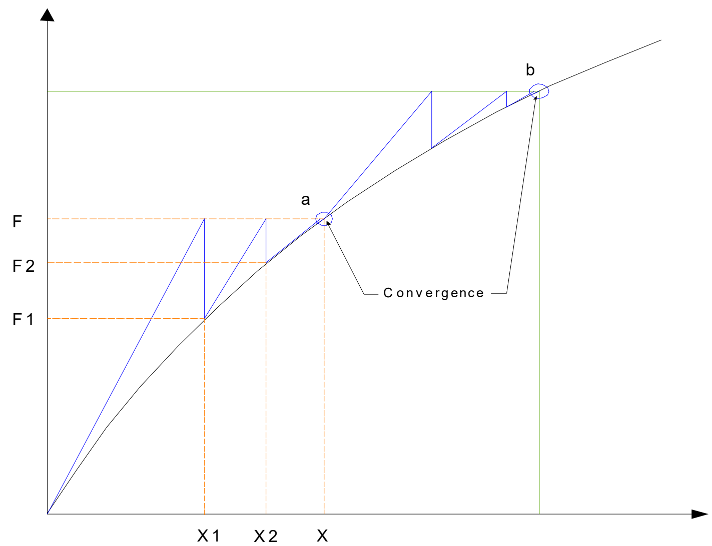

Figure 6.3 – Newton-Raphson procedure, two load steps three iterations each step

Newton-Raphson is the default option in Ansys to solve the nonlinear equations; however, if the special feature of the Adaptive Decent need to be selected, then the ADPTKY option in the NROPT command has to be scripted.

6.2.2. LINK180

Link180 was used to represent the reinforcement in the wall, which was a uniaxial tension-compression element with three degrees of freedom at each node. The three DOFs include translation in the nodal x, y and z directions. In this section, the element definition and capabilities are outlined and the material properties are defined in sections 6.3.2 and 6.3.3.

The element capacities include plasticity, creep, rotation, large deflection, and large strain capabilities. The link element has an option to represent tension-and-compression, tension-only or compression-only states as required. The geometry, node locations and the coordinate system for this element are shown in Figure 6.4.

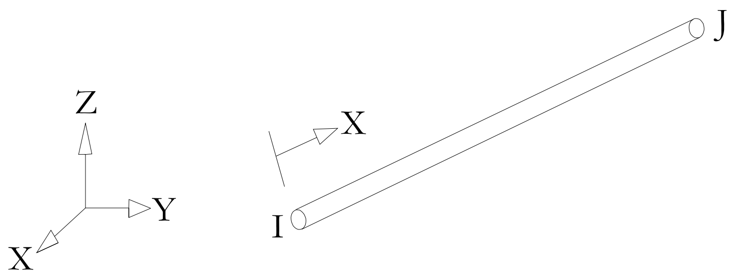

Figure 6.4 - Ansys Link180 element geometry, After (Ansys help systems, 2020)

The element (Link180) is defined by nodes labelled I and J in (Figure 6.4), cross-sectional area, mass per unit length and material properties. The element supports elasticity, isotropic hardening plasticity, kinematic hardening plasticity, Hill anisotropic plasticity, Chaboche nonlinear hardening plasticity and creep formations.

The following command snippet was applied to define the LINK180 element:

```
ET,MATID,LINK180
! Element Type link180

KEYOPT,MATID,2,0
!  Cross-section scaling (applies when large-deflection effects is on [NLGEOM,ON] )
!     0 - Sectional area changes such that the volume of the element is preserved (default)
!     1 - Section is assumed to be rigid

KEYOPT,MATID,12,0
!  Hydrodynamic output
!     0 – None (default)
!     1 – Additional hydrodynamic printout
```

6.2.3. Bonding Connection

The connection between the concrete and vertical rebars are modelled using nonlinear spring interface elements Combin39. The connection between the concrete and the steel plates are modelled using target element Targe170 and contact element Conta170, respectively.

Interface Element Combin39

Combin39 is a unidirectional element defined by two nodes with nonlinear force-deflection capability. It has longitudinal or torsional capability in 1-D, 2-D or 3-D. The longitudinal capability of the element is used in this study. The capability includes a uniaxial tension-compression up to three DoF at each node in x, y, and z directions.

The element is selected to represent the bond-slippage between Solid65 and Link180 elements in vertical (y-direction). The bond-slippage is considered in the vertical direction only because an examination of the specimens after the experiments confirmed the bond-slippage in this direction. Typical behaviour of the element in the first (compression) and fourth quadrant (tension) of the FD axis in Figure 6.5 below.

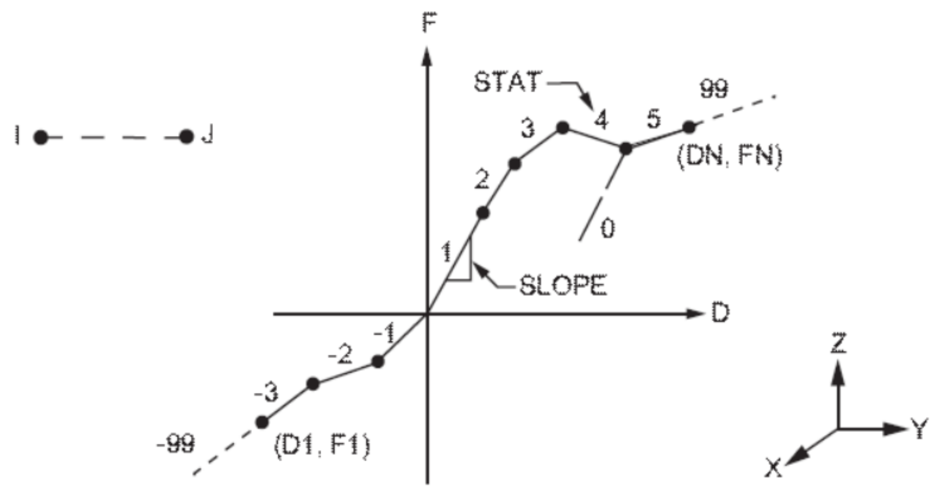

Figure 6.5 - Nonlinear Spring Element Combin39 (Image used courtesy of ANSYS, Inc.)

The real constants for Combin39 element as force-deflection points (D1, F1 to DN, FN) in 24 points as R,Matid and RMore commands as it can be seen in the snippet below. The input is in increasing order (a necessary definition requirement) from the third to the first quadrant, which is compression and tension, respectively. Essential requirements for the definition of this element are; (1) the input must be in increasing order, (2) the last input deflection must be positive, (3) the adjacent deflections cannot be nearer than 1E-7 times the total input deflection and, (4) segments tending towards vertical should be avoided. A total of 290 elements were applied to 10 vertical bars (29 elements each bar). The commands snippet and descriptions to define Combin39 element acting as the interface between Solid65 and Link180 elements is elaborated inside the dashed frame below.

```
! To create an interface element and connect the vertical bars in the y-direction

/PREP7                    ! Enter the model creation Preprocessor
```

```
CMSEL,S,CONC,ELEM  ! Select elements of concrete material
CMSEL,R,Vbars,NODE  ! Select nodes of all vertical bars

ET,MATID,COMBIN39   ! Element Type Combin39
TYPE,MATID               ! Assign element type to MATID
REAL,MATID               ! Assign all real constants sets R to MATID

! Modified Di Model
R,MATID, -30,0.0001, -15,0.0001, -5,0.0001,     ! Real constant set  (6 constants)
RMORE, 0,0, 0.0001,1950, 2.6,6824,              ! More real constant set  (6 constants)
RMORE, 5,6900, 10,6910, 15,6920,                ! More real constant set  (6 constants)
RMORE, 20,6930, 25,6940, 30,6950,              ! More real constant set  (6 constants)

KEYOPT,MATID,1,1
! Unloading path:
!     0 -- Unload along same loading curve
!     1 -- Unload along a line parallel to slope at the origin of the loading curve

KEYOPT,MATID,2,0
! Element behaviour under compressive load:
!     0 -- Compressive loading follows defined compressive curve (or reflected tensile curve if
not defined)
!     1 -- Element offers no resistance to compressive loading
!     2 -- Loading initially follows tensile curve then follows compressive curve after buckling
(zero or negative stiffness)

KEYOPT,MATID,3,2
! Element degrees of freedom (1-D) (KEYOPT(4) overrides KEYOPT(3)):
!     0, 1 -- UX (Displacement along nodal X axes)
!     2 -- UY (Displacement along nodal Y axes)
!     3 -- UZ (Displacement along nodal Z axes)
!     4 -- ROTX (Rotation about nodal X axes)
!     5 -- ROTY (Rotation about nodal Y axes)
!     6 -- ROTZ (Rotation about nodal Z axes)
```

```
!     7 -- PRES
!     8 -- TEMP

KEYOPT,MATID,4,0
! Element degrees of freedom (2-D or 3-D):
!     0 -- Use any KEYOPT(3) option
!     1 -- 3-D longitudinal element (UX, UY and UZ)
!     2 -- 3-D torsional element (ROTX, ROTY and ROTZ)
!     3 -- 2-D longitudinal element. (UX and UY) The element must lie in an X-Y plane

KEYOPT,MATID,6,0
! Element output:
!     0 -- Basic element printout (default)
!     1 -- Also print force-deflection table for each element (only at first iteration of problem)

EINTF,0.01, ,LOW,0 , 19.483,0 ,18.333 , 0    ! Create Combin39 element between offset nodes
EINTF,0.01, ,LOW,0 , 19.483,0 ,-18.333 , 0   ! Create Combin39 element between offset nodes
EINTF,0.01, ,LOW,0 , 2.93,0 ,18.333 , 0      ! Create Combin39 element between offset nodes
EINTF,0.01, ,LOW,0 , 2.93,0 ,-18.333 , 0     ! Create Combin39 element between offset nodes
EINTF,0.01, ,LOW,0 , 4.31,0 ,16.667 , 0      ! Create Combin39 element between offset nodes
EINTF,0.01, ,LOW,0 , 2.36,0 ,16.667 , 0      ! Create Combin39 element between offset nodes

ALLSEL,ALL              ! Select all entities types.
/SOLU                   ! Enter the Solution solver
OUTRES,ALL,ALL          ! Select all items for all substeps.
```

ET, TYPE and REAL command assign element type, type name and real constant set to MATID. R and RMORE command each assign one set of real constant up to six real constants to MATID. Each KEYOPT command assigns one key-option to the MATID. The type name MATID is selected to keep attribution names consistent with previous names.

The Key-options in the snippet defines how the element behaves. Keyopt (1) determines whether the energy is conserved or dissipated under cyclic loading, in this study energy dissipation option is selected, i.e. option number 1. Keyopt (2) define the element behaviour under compression; the default value is selected in this study so that the element follows the tensile curve under compression. Option two was selected for the Keyopt (3) so that the spring operates in one dimension. Keyopt (4) was set to zero to enable activation of Keyopt (3).

Target and Contact Elements

Target elements are used for the representation of 3D target surfaces in association with contact elements. Contact elements overlay solid, shell or line elements in contact with the target element.

Target element Targe170 and contact element Conta174 represent surfaces of concrete and steel plate volumes, respectively (Figure 6.6) in this study. The elements overlay the two solid surfaces describing their boundaries and are in contact with each other. The target and contact discretized and paired by sharing the real constant sets. Translation displacement capacity of the elements is utilized.

Option number 3 in Keyopt 12 for Conta174 is used to select the contact type as “Bonded”. Option number 1 in Keyopt 5 for Targe170 is used to formulate the contact as solid-solid Multi-Point Constraints (MPCs). All other key options are kept as default for both elements. “Bonded” means that no sliding or separation between the faces and edges are not allowed; this type of contact is linear as the length/area of the contact do not change. The contact interpenetration is prevented by choosing program-control contact formulation for contact-compatibility (Ansys help systems, 2020).

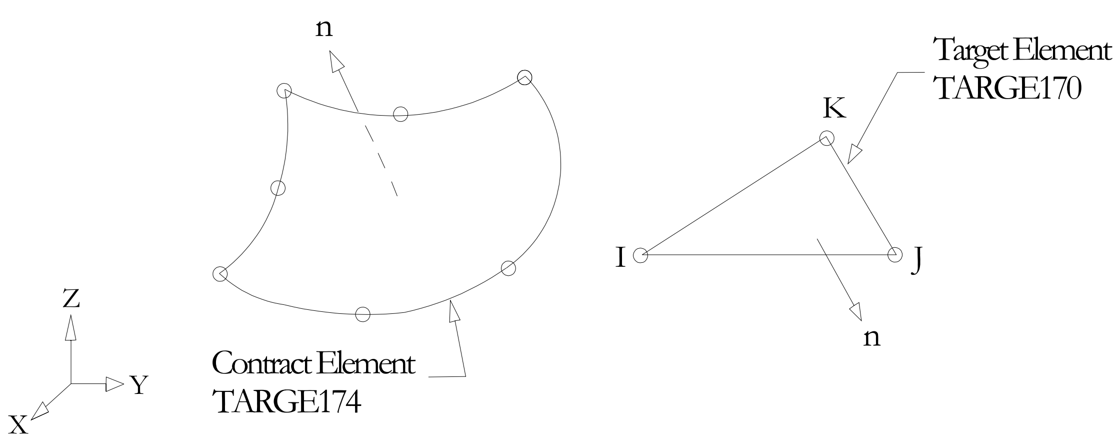

Figure 6.6 - Contact Element Conta174 and Target-Element Trage170, After (Ansys help systems, 2020.)

Constraint Equation

The connections between all the concrete and the reinforcements elements except vertical rebars are defined by applying the constraint equation using CEINTF command. Vertical rebars were constrained in x and z directions only. In the y-direction, nonlinear spring interface element combin39 was used as described earlier.

Constraint equations interface can be applied to “tie” two regions with dissimilar mesh pattern together by generating constrain equation that connects the selected nodes of the solid element with the link element at the interface between the two elements. Nodes outside the tolerance value are not considered for connection (Ansys help systems, 2020). Command snippet that ties solid and link elements together are as below:

```
! To connect the concrete and reinforcement except, the vertical bars

/PREP7                    ! Enter the model creation Preprocessor
CMSEL,S,CONC,ELEM         ! Select elements of concrete material
CMSEL,R,Obars,NODE        ! Select nodes of all rebars except vertical bars
CEINTF,0.0001,            ! Constraint equation with 0.001 tolerance
ALLSEL,ALL                ! Select all entities types.
/SOLU                     ! Enter the Solution solver
OUTRES,ALL,ALL            ! Select all items for all substeps.

! To connect the vertical bars in x and z directions
/PREP7                    ! Enter the model creation Preprocessor
CMSEL,S,CONC,ELEM         ! Select elements of concrete material
CMSEL,R,Vbars,NODE        ! Select nodes of all vertical bars
CEINTF,0.0001,UX          ! Constraint equation in x-direction
CEINTF,0.0001,UZ          ! Constraint equation in z-direction
ALLSEL,ALL                ! Select all entities types.
/SOLU                     ! Enter the Solution solver
OUTRES,ALL,ALL            ! Select all items for all substeps.
```

/PREP7 command enters the Preprocessor solver. Ansys categorise the commands into three main categories, including the Preprocessor, Solution, and Postprocessor. Before entering and commands one need to tell the solver which categories will be used because most of the commands for these categories are the same and the solver will not be able to differentiate unless it is clarified first.

The CMSEL command is a component selection command used to select the components of the model named CONC, OBars and VBars using Named Selection (NS) in the Project Tree of the Graphical User Interface (GUI). All concrete elements are named CONC, all reinforcements except vertical bars are named as OBars, and all vertical bars are named as VBars using NS.

The ALLSEL,ALL, /SOLU and OUTRES,ALL,ALL commands are used to reselect all entities, enter the Solution processor and write all solution results to the database respectively. It is always a good practice to select all entities again before entering the solution process, and after applying specific commands else, the solution processor may solve for the selected components only.

6.3. Material Properties

The material properties for each of the three components used to make the model in this study were different. The components included steel, BFRP, and concrete. The material models for each of the components are described below.

6.3.1. Concrete

Typical Behaviour of Concrete

The concrete material model is a challenging task because it is a quasi-brittle material that has different behaviour in compression. Figure 6.7 below shows a typical stress-strain relationship for normal weight concrete (Kachlakev 2001).

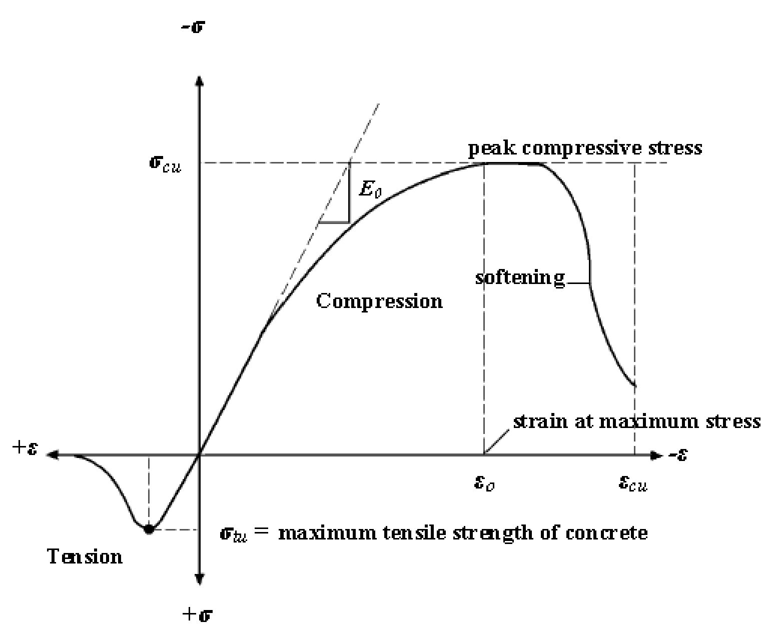

Figure 6.7 - Typical stress-strain relationship for concrete under compression and tension (Kachlakev 2001)

Tensile strength is about 8-15% of the compressive strength in concrete (Shah et al. 1995). The stress-strain relationship is linear up to about 30% of maximum compressive strength (E_0/E_c). Then, the stress gradually increases up to a maximum compressive strength σ_{cu} at a strain of ε_0. After the maximum, the curve enters the softening region and falls.

The concrete crushes at the end of the softening region (ε_{cu}) shown in Figure 6.9. The relationship is linear in the tension zone up to the maximum tensile strength of concrete (σ_{tu}). After maximum, the concrete crack and the strength of the concrete decreases to zero (Bangash 1989).

Concrete Material Model for Solid65

Defining linear and non-linear properties

The Poisson’s ratio for the concrete material was assumed to 0.2 for all models (FIB-43, 2008). Additionally, the following properties were defined to demonstrate crack behaviour when incorporating the Solid65 element for the analysis.

The characteristic compressive strength values were obtained from conducting compressive tests. The mean compressive and tensile cylinder strength and modulus of elasticity were obtained from Table 3.1 of Appendix A, BS EN-1992-1-1:2004 (2004). The calculation is per equations below:

$$f_c = f_{ck} + 8 \text{ (MPa)} \qquad \text{Equation 6.1}$$

$$f_t = 0.3 \times f_{ck}^{(2/3)} < \text{C50/60} \qquad \text{Equation 6.2}$$

Where:

- f_t is the mean tensile strength and
- f_c is the mean compressive strength.

It is recommended that the shear transfer coefficient for an open crack shall be less than 0.2 to avoid convergence problems (Kachlakev et al. 2001). The concrete property values are summarized in Table 6.3 below. The concrete properties were kept the same for all samples to make sure the types of reinforcement were the only variables under study.

Table 6.3 - Summary of concrete material properties and constants as defined in Ansys

Model	E_c (GPa)	f_c (MPa)	f_t (MPa)	β_t	β_c	v
C20/25	30	28	2.2	0.2	0.8	0.2

The Solid65 element also requires multilinear isotropic hardening material properties to model the concrete in compression. The multilinear isotropic properties of concrete are calculated utilizing the following formulae.

$f = E_c\varepsilon/1+(\varepsilon/\varepsilon_0)$ Equation 6.3

$\varepsilon_0 = 2f_c/E_c$ Equation 6.4

$E_c = f/\varepsilon$ Equation 6.5

Where:

- f = stress at any strain ε
- ε = strain at stress f
- ε_0 = strain at the ultimate compressive strength f_c.

The numerical relationships above (Equations 6.3 – 6.5) were used to generate a stress-stress curve for the concrete under compression in this study.

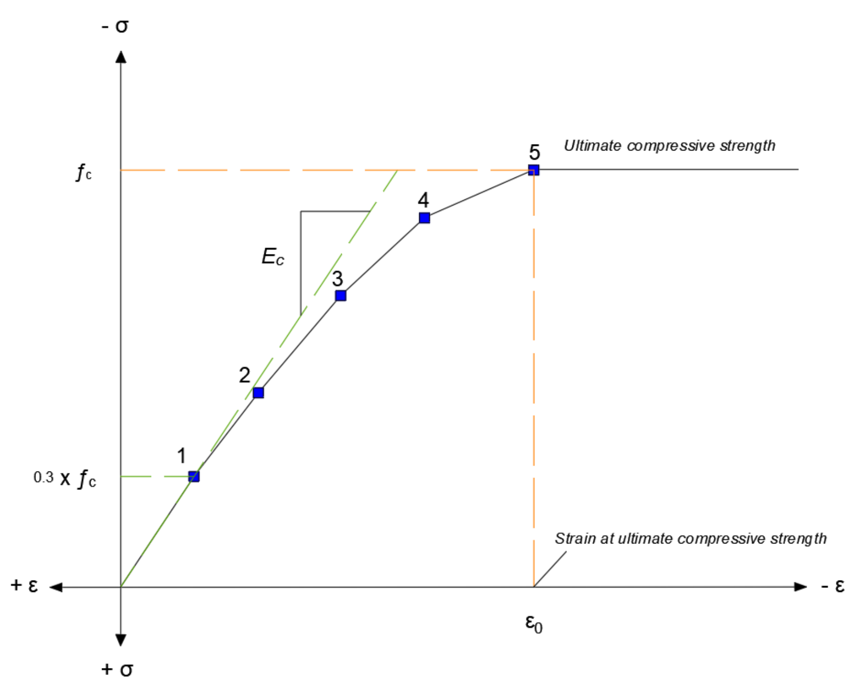

Figure 6.8 – Simplified stress-strain curve for concrete

Figure 6.8 above shows a simplified typical relationship between stress and strain in concrete. Up to approximately 30% compressive stress, the relationship is linear, which is defined as E_c (Elastic Modulus of the concrete). From point 2 until point 5 it can be seen that stress is degrading and there are sharp corners at point 2, 3 and 4; therefore, about 95 points were used between point 2-5 to using excel sheet applying equation 6.3 – 6.5 to help the convergence of the solution. The calculated stress-strain relationships established for three concrete strength classes are shown in Figure 6.9 below.

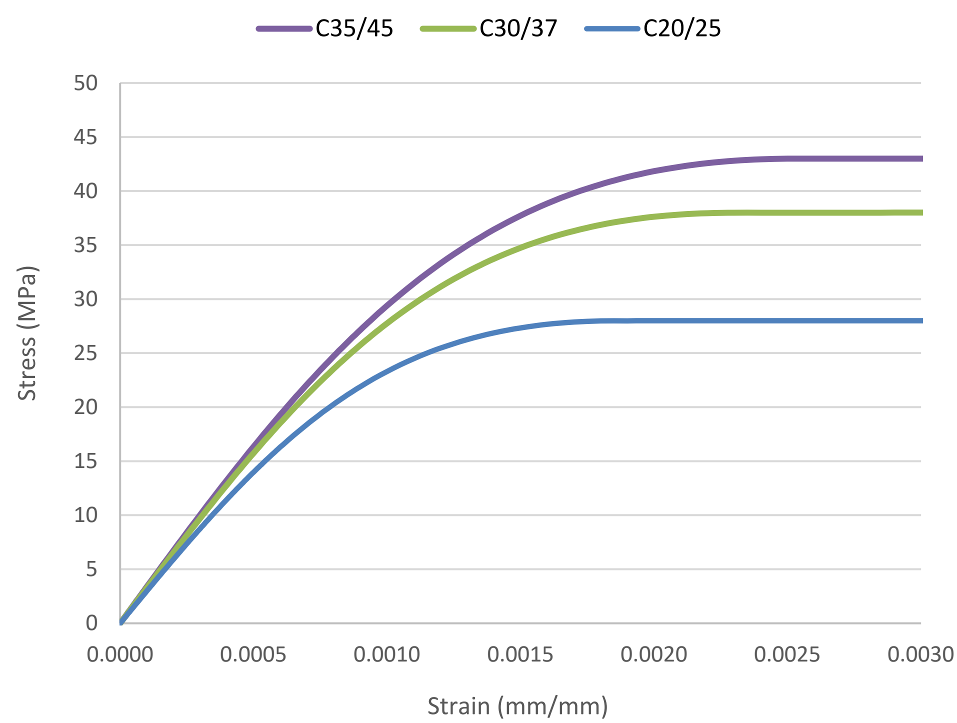

Figure 6.9 - Concrete stress-strain relationship curve for three strength classes

Defining material model using command snippet

Definition of the concrete in Ansys Mechanical need a command snippet because the Ansys Mechanical GUI does not allow insertion of the constants C1-C9 as explained in Section 6.2.1 Table 6.2; therefore, a command snippet was used to define the material as follows:

```
! Linear properties concrete material model (MATID)

MP,EX,MATID,32940        ! Material property Modulus of Elasticity for MATID
MP,PRXY,MATID,0.2        ! Material property, Poisson's ratio for MATID

! Cracking and Crushing properties concrete material model (MATID)

TB,CONCR,MATID,1,9       ! Use 1 table with 9 concrete properties (9 constants)
TBTEMP,22                ! Temperature for the concrete is 22 0C
TBDATA,,0.2,0.8,2.9,38   ! Constants 1 to 4 are defined here 5 others default

! Multilinear isotropic properties concrete material model (MATID)

TB,MISO,MATID,1,95,0     ! Use 1 table with 35 MISO data.
```

```
TBTEMP,22                    ! Temperature for the concrete is 22 0C
TBPT,,0.0001,3.294           ! Table points are enlisted
TBPT,,0.0002,6.551
TBPT,,0.0003,9.735
TBPT,,0.0004,12.813
TBPT,,0.0005,15.757
TBPT,,0.0006,18.541
TBPT,,0.0007,21.146
Continues until…….
TBPT,,0.0032,38.0
TBPT,,0.0033,38.0
TBPT,,0.0034,38.0
TBPT,,0.0035,38.0
```

MP command is used to apply the linear properties of the concrete, including the Elastic Modulus (EX) and the Poisson’s Ratio (PRXY). MATID is used to apply the properties to Solid65.

Nonlinear properties of the concrete are inserted using TB,CONCR and TB,MISO models; where the earlier is used to insert the cracking and crushing constant from Table 6.2 and TB,MISO to insert the properties from Figure 6.8.

Explaining failure surface criteria

The concrete material model will be able to predict the failure both in terms of cracking and crashing. The solver will use the constant value number C3 and C4 (tensile and compressive strengths respectively from table 6.2) to define the failure surface of the concrete due to multiaxial stress state as is shown in Figure 6.10 below (Willam and Warnke, 1975).

The most significant principal stresses are in the x and y directions represented by σ_{xp} and σ_{yp}, respectively. Three failure surfaces are shown as projections on the σ_{xp}-σ_{yp} plane. The mode of failure is a function of the sign of σ_{zp} (principal stress in the z-direction). For example, if σ_{xp} and σ_{yp} are both negative (compressive) and σ_{zp} is slightly positive (tensile), cracking would be predicted in a direction perpendicular to σ_{zp}. However, if σ_{zp} is zero or slightly negative, the material is assumed to crush (Ansys help systems, 2020).

In a concrete element, cracking occurs when the principal tensile stress in any direction lies outside the failure surface. After cracking, the elastic modulus of the concrete element is set to zero in the direction parallel to the principal tensile stress direction. Crushing occurs when all principal stresses are compressive and lie outside the failure surface; subsequently, the elastic modulus is set to zero in all directions, and the element effectively disappears (Ansys help systems, 2020).

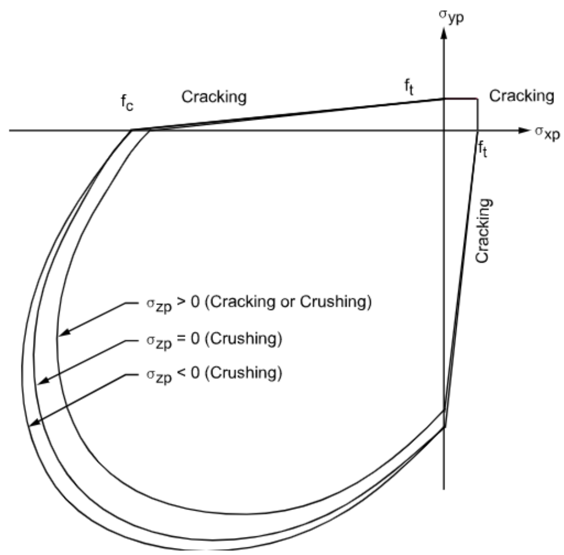

Figure 6.10 - Failure surface of the concrete in 3-D (Image used courtesy of ANSYS, Inc.)

6.3.2. Steel

The material properties for both high yield and mild steel used in this FEA were from the experiments as elaborated in section 3.2.2. Additionally, bilinear isotropic properties of the material were used to define the material model for reinforcement steel.

Poisson’ ratio was taken as 0.3, and elastic modulus was taken as 210 GPa for the steel incorporated in the reinforcement of the models (Gere, 2003). For the plates used for load distribution over a larger area of concrete, the material properties assumed to be linear. Table 6.4 below summarizes the properties for the steel reinforcement and stirrups:

Table 6.4 - Material properties of steel

No	Component	Material name	Linear Isotropic		Nonlinear Isotropic	
			Elastic modulus (E_s) / MPa	Poisson’s ratio (v)	*Yield Stress* (f_y/f_u) / MPa	*Tangent modulus* (E_s') /MPa
1	Main bars	HYSD Steel	$210x10^3$	0.3	500	0
2	Stirrups	Mild Steel	$210x10^3$	0.3	250	0
3	Plates	Structural Steel	$210x10^3$	0.3	-	-

The material model for steel rebars is based on the stress-strain relationship of steel. There are several material models available to model steel; however, typical stress-strain behaviour for the steel consists of an elastic region, plastic region, strain hardening and necking. The model in this FEA assumed to be elastic-perfectly plastic and identical both in tension and compression. A simplified bilinear stress-strain graph used for this study is shown in Figure 6.11.

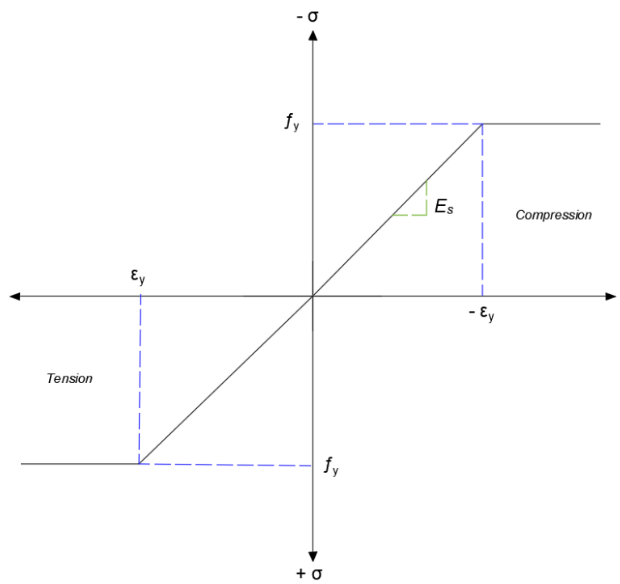

Figure 6.11 - Stress-strain curve for steel reinforcement

Definition of the steel rebars in Ansys Mechanical need a command snippet because the GUI does not allow coupling of constraint equation (CEINTF) for connection of concrete and rebars nodes; therefore, object command was used to define the material as below:

```
! Rebars

ET,MATID,LINK180               ! Element type Link 180
SECTYPE, MATID,LINK      ,     ! Section type is link
SECDATA,AREA                   ! Section property is area
AREA=28.273                    ! Area in mm2
MPDATA,EX,MATID,,2e5           ! Elastic property of steel
MPDATA,PRXY,MATID,,0.3         ! Poisson’s ratio of steel
TB,BISO,MATID,1,2              ! Bilinear property of steel
TBDATA,,500,0                  ! Tensile strength and tangent modulus

! Shear links

ET,MATID,LINK180               ! Element type Link 180
SECTYPE, MATID,LINK      ,     ! Section type is link
SECDATA,AREA                   ! Section property is area
AREA=28.273                    ! Area in mm2
MPDATA,EX,MATID,,2e5           ! Elastic property of steel
MPDATA,PRXY,MATID,,0.3         ! Poisson’s ratio of steel
TB,BISO,MATID,1,2              ! Bilinear property of steel
TBDATA,,275,0                  ! Tensile strength and tangent modulus
```

6.3.3. FRP

The material properties of the FRP bars used in this study are the properties of the bars used in the experimental studies, as explained in section 3.2.3. The linear and bilinear properties defined for the FRP reinforcement are outlined in table 6.5 below (Chansawat et al. 2009).

Table 6.5 - Material properties of BFRP

No	Material name	Linear Isotropic		Nonlinear Isotropic
		Elastic modulus (E_s) / MPa	Poisson’s ratio (v)	*Yield Stress* (f_y/f_u) /MPa
1	BRFP	$50x10^3$	0.23	1000
2	GFRP	$40x10^3$	0.26	1000

The property values were extracted from the manufacturers’ brochure for the bars. The information provided by the manufacturer showed that the Poisson’s ratio for the BFRP was 0.23, and the elastic modulus was 50 GPa (Magma Tech, 2019).

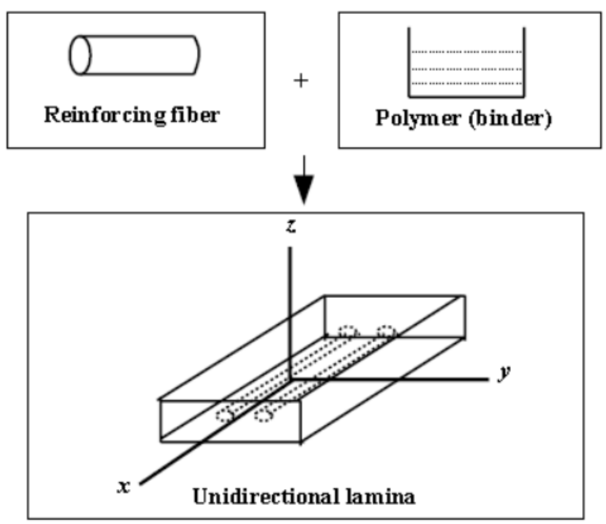

Figure 6.12 - Schematics of fibre reinforcement polymer (Kachlakev, 2001)

The elastic modulus and Poisson’s ratio for FRP materials are different in each of xy, xz and yz planes due to the direction of the fibre in the matrix (Figure 6.12). In other studies (Kachlakev, 2001) it is assumed to be the so-called “special orthotropic” material where the properties are the same in two directions (y and z) perpendicular to the fibre (x) direction. The stress-strain curve for the BFRP and GFRP is based on manufacturers data is shown in Figure 6.13 below.

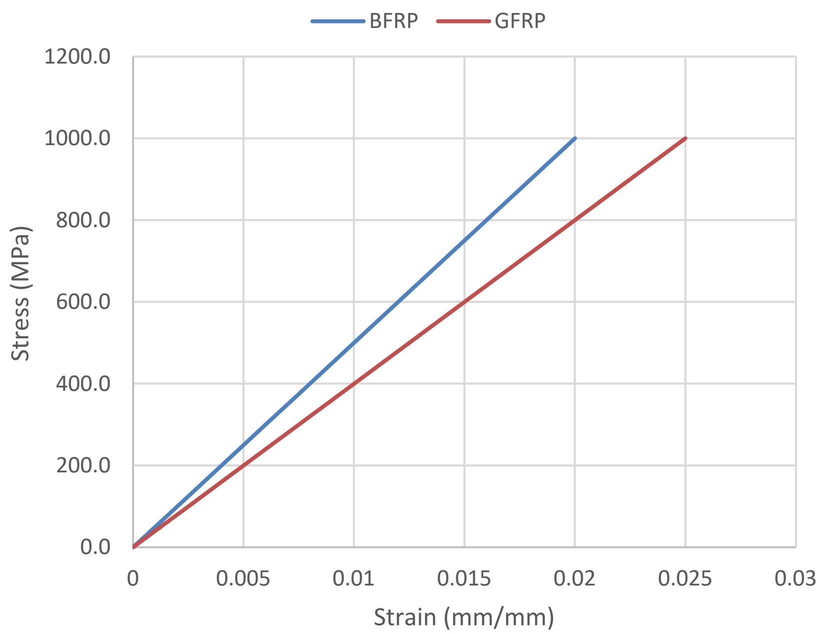

Figure 6.13 - Linear stress-strain curve for BFRP and GFRP

The definition of the FRP rebars in Ansys Mechanical need a command snippet because the GUI does not allow the constraint equation (CEINTF) for connection of concrete and rebars nodes; therefore, an object command snippet was used to define the material as below:

```
! BFRP
ET,MATID,LINK180                ! Element type Link 180
SECTYPE, MATID,LINK      ,      ! Section type is link
SECDATA,AREA                    ! Section property is the area
AREA=28.273                     ! Area in mm2
MPDATA,EX,MATID,,50e3           ! Elastic property of steel
MPDATA,PRXY,MATID,,0.23         ! Poisson’s ratio of steel
TB,BISO,MATID,1,2               ! Bilinear property of steel
TBDATA,,1000,0                  ! Tensile strength and tangent modulus
```

6.3.4. Interface Elements

The properties of the interface elements depend on the bond-slip strength. The bond strength between FRP and Steel rebars and concrete has been studied by a few researchers and generally depend on the followings:

1. Strength of the concrete
2. Reinforcement concrete cover
3. Rebars diameter and distance between rebars

4. Embedded length of the rebar into the concrete
5. Type of rebar surface including plain or deformed
6. Level of concrete confinement
7. Types of loading (cyclic or monotonic)

In this study, FRP and steel bond-slip models developed by Di et al. (2019) are utilized. Figure 6.14 (a) shows that steel curve peaks at about 21 MPa at about 0.7 mm displacement where BFRP 10 MPa at 3.5 mm; steel curve peaks about 50% higher than the FRP curves. Figure 6.18 (b) shows about 15% higher peak for 12 mm diameter curve than 20 mm diameter BFRP bars.

Since the real bond-slip behaviour depends on the seven properties of the concrete and the reinforcement enlisted above, interpolation was made to be able to find the actual bond-slip behaviour based on the optimum-response methodology until model calibration is achieved.

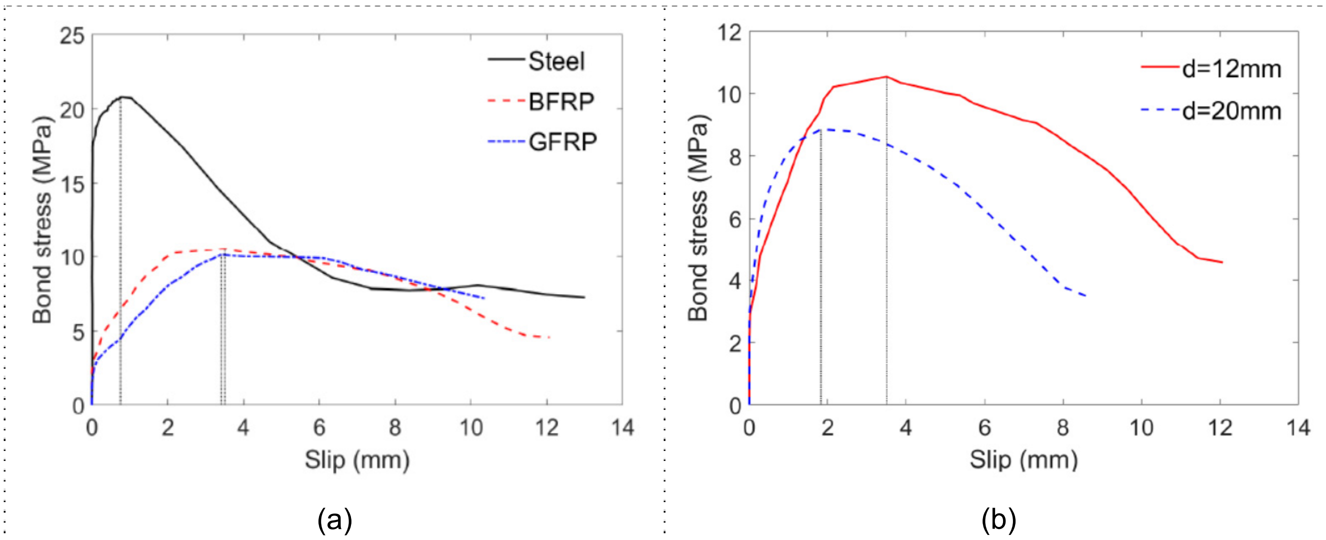

Figure 6.14 – Bond stress against slip (a) BFRP, GFRP and Steel rebars (b) BFRP rebar diameters (Di et al. 2019)

Due to the time limitation and preoccupation of the labs, it was decided to utilize the data from the literature. The available information about the bond strength of steel, BFRP and GFRP rebars was scarce; the result of recent by Di et al. (2019) work was used to obtain the bond strengths.

6.4. Finite Element Discretization

In the simulation process, meshing is an essential part to divide the geometry into simple element used as discrete local approximations of the larger domain. Accuracy, convergence and speed of simulation are influenced by mesh selection; the better the mesh, the faster and more accurate the solution (Core Skills, 2019). A total of 3933 elements and 17526 nodes were used.

Ansys provides high-performance and intelligent automated or crafted mesh that can be linear or high-order for accurate and efficient solutions. The software has built-in defaults to make meshing easier, producing dependable results by capturing solution gradients properly.

Creating an appropriate mesh is fundamental in Ansys simulations. Ansys Meshing has the appropriate criteria to create a suitable mesh base on the analysis and the geometry of the model. The mesh is automatically integrated with the solver in the Workbench environment and use all available physical cores in the computer for parallel processing to reduce time in the creation of a mesh.

Workbench meshing-tool generates mesh depending on the physics defined in parametric and persistent fashion to update automatically when the geometry is updated. Although the meshing tool is highly automated control can be added to get better quality.

The most critical factors in mesh requirement are efficiency and accuracy; a refined mesh can be used for high solution gradients and fine geometric details where coarse mesh can be used elsewhere in a geometry. The quality of mesh depends on the shape, and the accuracy and stability deteriorate as the mesh cells deviate from the ideal shape (Mesh Quality and Advance Topics, 2019).

In the global mesh settings, the following options were selected to generate the mesh for the shear wall model:

- Physics Preference – Mechanical
- Size Function – Adaptive
- Relevance Centre – Medium
- Error Limit – Standard Mechanical
- Mesh Metric – Skewness/Orthogonal Quality

The selected options above use patch conforming tetrahedrons, sweep-method or both depending on the geometry; in this case, sweep-method used to generate the mesh because the geometry was sweep-able. Figure 6.15 shows that a 100% hexahedron mesh is generated. The quality of the mesh can be seen in Figure 6.16 below.

The advantages of hexahedral mesh (over tetrahedral mesh) are that it has fewer element, faster solution time with better accuracy (Mesh Methods, 2019). Because the hexahedral mesh aligns with the geometry of the model, fewer elements per node are required, and three mostly parallel sets of faces improve the solution accuracy.

Before using the mesh, it is essential to check the mesh quality. The quality is defined through various metrics which measure the level at which each mesh cell is varying from the ideal shape.

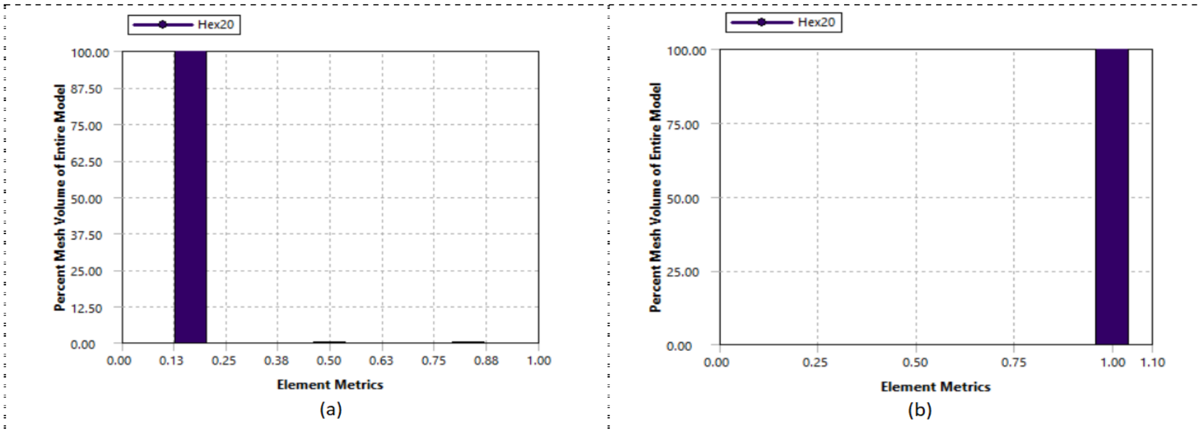

Figure 6.15 - Mesh (a) Skewness (b) Orthogonal Quality; Percentage Mesh Volume of Entire Model against Element Metrics (Image used courtesy of ANSYS, Inc.).

Mesh metrics, including the skewness and orthogonal quality results, are shown in Figure 6.15 (a) and (b) respectively. Skewness for 100% of the entire model is less than 0.2 Element Metrics, and Orthogonal Quality for 100% of the whole model is 1 Element Metrics. The mesh skewness and orthogonal quality are in the excellent range, as shown in the spectrum below (Figure 6.16 (a) and (b)).

Excellent	Very good	Good	Acceptable	Bad	Unacceptable
0-0.25	0.25-0.50	0.50-0.80	0.80-0.94	0.95-0.97	0.98-1.00

(a)

Unacceptable	Bad	Acceptable	Good	Very good	Excellent
0-0.001	0.001-0.14	0.15-0.20	0.20-0.69	0.70-0.95	0.95-1.00

(b)

Figure 6.16 - (a) Skewness and (b) Orthogonal Quality; mesh metrics spectrum (Mesh Quality, 2019)

Percentage changes in reaction results were recorded for mesh sizes 10 mm to 100 mm as can be seen in Figure 6.17. Full size reinforced concrete model with concrete strength C20/25 is used for the mesh test. The reaction is recorded at the point of applied displacement, i.e. at the top right of the wall. The graphs show that mesh sensitivity is less than 3% in the range.

The methodology employed is the Ansys parametric study tool, selecting the mesh size, the maximum value for the reaction probe, as the variables to be studied. The nine mesh sizes were then selected as independent variables, and corresponding reactions were recorded as dependant variables.

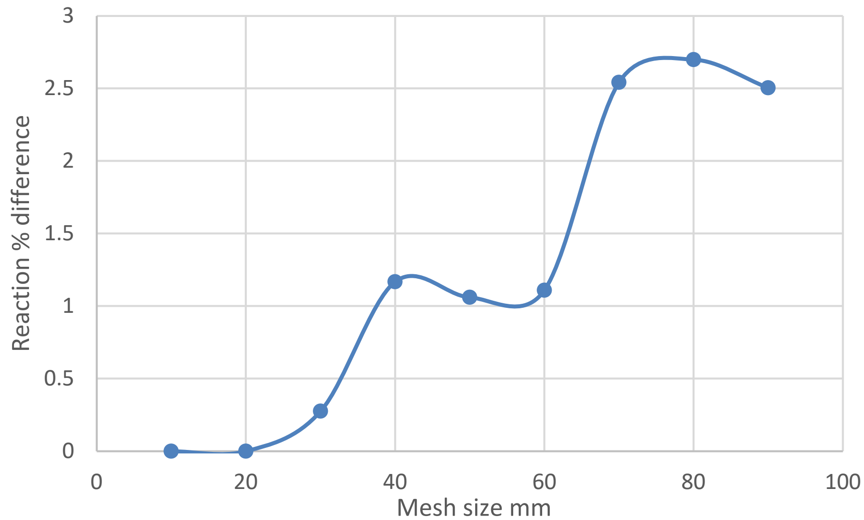

Figure 6.17 – Mesh sensitivity test results

Appropriate mesh size was selected to converge in a reasonable time; the example of a meshed model is shown in Figure 11 below. Therefore a medium size mesh recommended by the Ansys mechanical with an approximate size of 33 mm in two orthogonal directions was selected for Solid65. Medium size meshes can be used when a solution cannot converge with relatively coarser recommended mesh (66 mm) which has a higher calculation time efficiency.

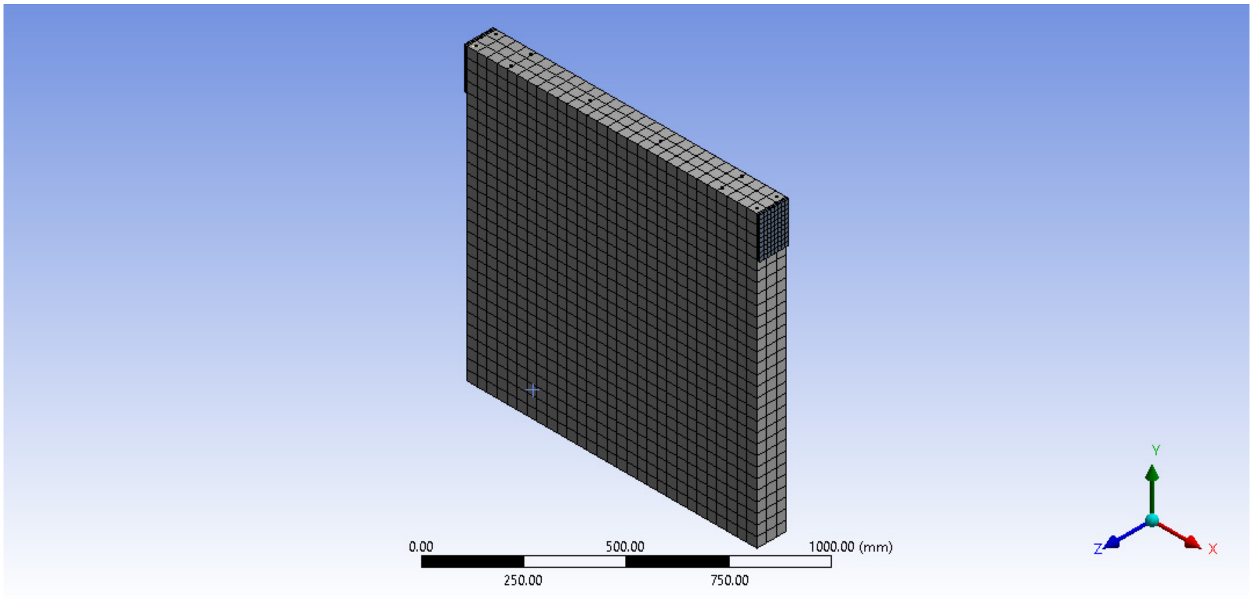

Figure 6.18 - Meshing of the RC shear wall model (Image used courtesy of ANSYS, Inc.)

6.5. Boundary Conditions

When the primary model was made, and the geometry, element, material and meshing were set, then the boundary condition was defined. Boundary conditions to constrain the model and apply appropriate displacement is required to get a unique solution per condition.

It is essential to set the boundary conditions to stop large displacements invalidating the results. The boundary condition was set as per the experimental specimens developed in the KU structures lab. Same boundary conditions were used in all specimens and models.

The bottom surface of the model’s volume was constrained in all direction to stop rotation and displacement of the base plate in all directions. The basic summary of boundary conditions is depicted in the model (Figure 6.19). The load was applied to the shear wall as in-plane displacement at the top of the wall. The load was applied to the top surface. The load was designed to push and pull the wall in-plane, until eventual failure.

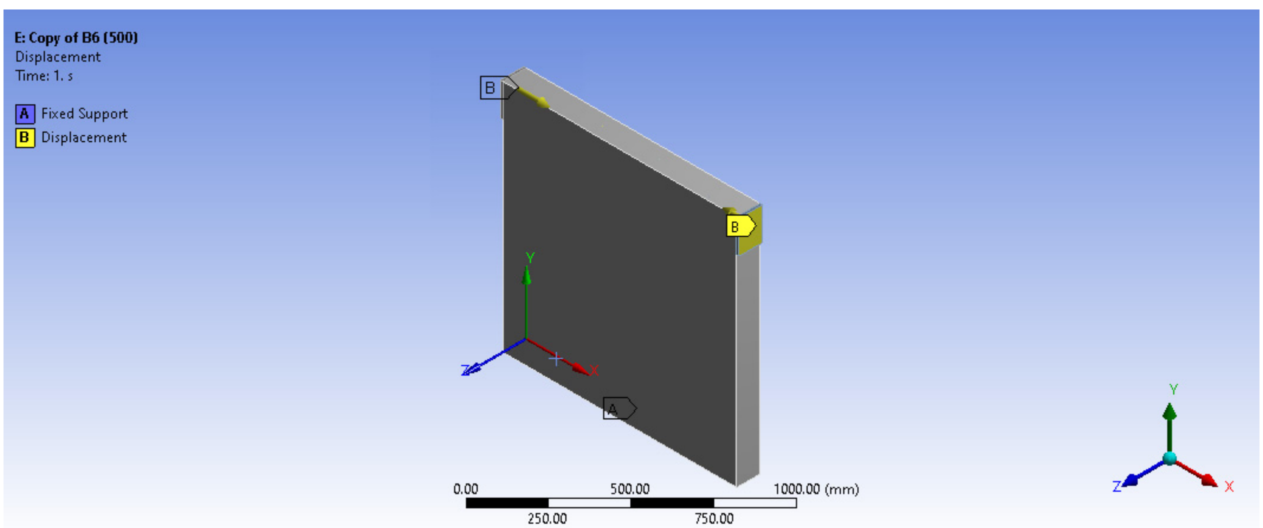

Figure 6.19 - Basic boundary conditions for the wall models fully fixed at the bottom and lateral load applied at the top.

The loading cycles applied were the modified ATC 24 protocol assuming one cycle per amplitude, the loading regime used in the experimental session. Fourteen cycles of displacement load amplitudes were sat up to be applied to the test specimen ranging from 0.2 mm to 30 mm, as indicated in Table 6.6 below. No more displacement loads were applied once the specimen failed to sustain more loads.

Table 6.6 - Load cycle – displacement amplitude

Loading Cycles	Displacement Amplitude (mm)
1	0.2
1	0.4
1	0.8
1	1.2
1	2.5
1	3.5
1	5.0
1	10
1	15
1	20
1	25
1	30

6.6. Analysis Settings

Solver settings in the Ansys mechanical GUI determine how the solver carries out the analysis. The configurations include the number of steps, substep and other linear and nonlinear analysis control.

The load is divided into 12 steps according to the experimental load setup, and each step is divided into 50 substeps. Newton-Raphson method with a maximum of 25 iterations per substep is used to help with convergence.

Weak spring was kept off to obtain a more reliable solution. The solver pivot checking error option was selected to stop the solution when such a problem occurs. The large deflection option was kept off as concrete is not a material that can sustain such deflections.

The direct solver, as opposed to the iterative solver, is usually selected when there are less than one million degrees of freedom (Harish, 2020b). A weak spring is assigned if the solver detects an unstable structure to make it withstand small external forces and obtain a solution that may not be reliable. Therefore it is turned off to make sure the solution stops if there is any instability issue in the model.

Solver pivot checking produces an error message as a result of the ill-conditioned matrix due to the under-constrained model or contact related issues; the Error option instructs the solver to stop under such conditions and issue an error message.

Large deflection property determines whether the solver should take into account a large deformation under bending, it is kept off as concrete is a brittle material and such behaviour is not expected. Inertial relief property applies to linear static structural analysis only; therefore, it is turned off.

When the out of balance force is less than the convergence criteria (0.5%) a successful solution will be obtained; displacement convergence is selected as the analysis displacement controlled. The Newton-Raphson (NR) option is kept as program-controlled. The solver can choose full, modified or unsymmetric NR options based on model nonlinearities and stiffness matrices.

The number of maximum iteration can be increased when there is no convergence, or the converged results are not smooth enough, i.e. there are jumps in the graphs of results. It can be utilized using the NEQIT command. Higher values can be selected for simpler models as the minimum number of substeps can be set low for computation time efficiently.

6.7. Solid65 Model results

6.7.1. B10 model Results

Hysteresis response

In this section, the hysteresis curves obtained from experimental testing and three FE models with a variation of the strength of the concrete are presented simultaneously. The data from EXP C20/25 and FE C20/25 is used for calibration of the model. A parametric study is conducted on the calibrated model.

The hysteresis response for all B10 model and associated different strength classes of concrete is shown in Figure 6.20 (a) – (d) below. There is an increase in the peak of the loops with increasing concrete strength class. The peak value for experimental C20/25 and FE C20/25 is about 75 and 76 kN, respectively.

The maximum loop peak for FE C20/25, FE C30/37 and FE C35/45 is less than 100 kN, about 100 kN and more than 100 kN, respectively. The difference in maximum values shows that changing the concrete strength class as a parameter changes the peak value of the loops significantly.

At lower amplitudes, both the FE and experimental models show vertical loops close to each other as a result of the initial elastic response. Above 3.5 mm, the experimental data loop shows widening due to the more significant cracking of the sample. In the FE model, smeared cracks are assumed, which, together with the limitation of the material models could explain the discrepancy between the results at the greater amplitudes. The FE C20/25 peak loop value follows the experimental results and as the concrete strength increases the peak values increase to 100 and 110 kN for FE C30/37 and FE C35/45, respectively.

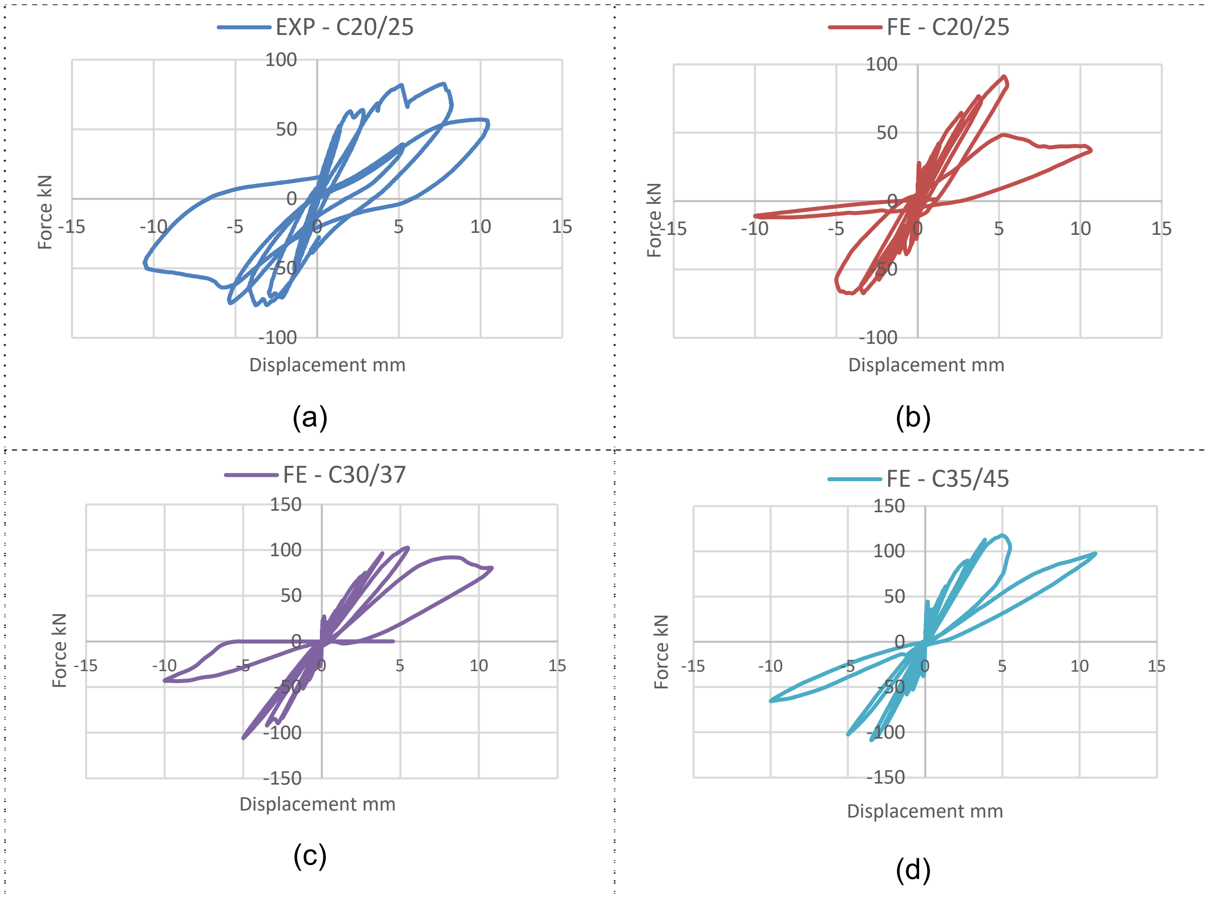

Figure 6.20 - B10 Hysteresis response (a) experimental C20/25, (b) FE C20/25, (c) FE C30/37 and (d) FE C30/35

Force-displacement envelope for model calibration

Figure 6.21 shows force-displacement (0-140 kN against 0-6 mm) curves as the envelope of the hysteresis averaged over the positive and negative values for the B10 model until the failure point. The curves (experimental C20/25 and FE C20/25) show a gradual climb from the beginning to the end showing some linear pattern followed by a curve.

The trend for the FE curve is an initial rise until about 0.2 mm due to a slightly stiffer behaviour, followed by an almost linear increase. The pattern for the experimental curve is an initial linear climb until about 1.2 mm followed by a curve until failure. The initial stiffness at the beginning of the loading process indicates that the model shows a higher stiffness at a lower displacement amplitude.

The FE curve is higher than the experimental curve at the beginning until 0.9 mm, after this it grows slightly lower until about 3.9 mm. After the 3.9 mm displacement amplitude both curves show a very close pattern until failure. The ultimate forces are 75 and 76 kN for experimental and FE curves, respectively.

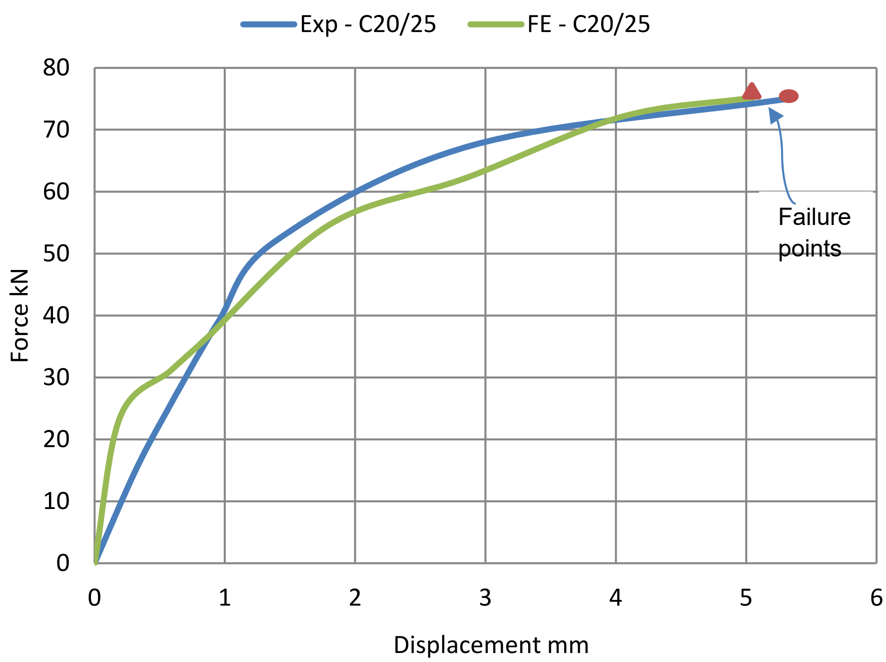

Figure 6.21 - B10 hysteresis response averaged envelope for experimental and FE results

Force-displacement envelope parametric study

Figure 6.22 shows the force-displacement envelope graph for three strength classes of concrete. All strength classes show an initial stiffness at 0.2 mm, followed by a tendency for a gradual increase. FE C20/25, FE C30/37 and FE C35/45 fail at about 80, 108 and 119 kN respectively. The FE C20/25 curve has an initial faster rise than FE C30/37 before 1.2 mm displacement. The percentage rise in the peak value from the FE-C20/25 to the FE-C30/37 and FE-C35/45 are 35 and 48 per cent, respectively.

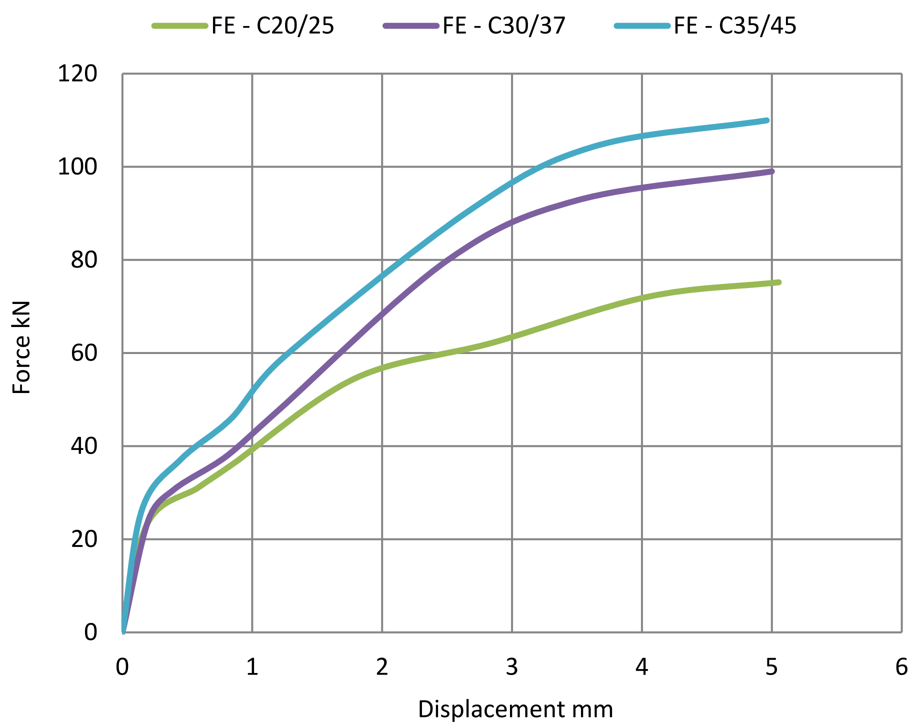

Figure 6.22 – B10 model, parametric studies, three concrete strengths

6.7.2. S10 model results

Hysteresis response

The pictures in Figures 6.23 below shows the hysteresis response for three strength classes of concrete in addition to the experimental specimen. The hysteresis loops show a more similar pattern for the displacements before 5 mm displacement than after. The difference could be due to smeared crack assumption in the FE model.

Figure 6.23 (a) to (d) shows hysteresis response for experimental C20/25 sample, and FE C20/25, FE C30/37, FE C35/45 models, respectively. It can be seen from the graphs that the maximum loop peak increases from less than 100 kN to just above 100 kN and well above 100 kN for FE-C20/25, FE-30/37 and C35/45, respectively. The difference in the maximum values signifies the effect of concrete strength as a varying parameter. Despite the deviation in loop width, the peak values follow a very similar trend in experimental and FE C20/35 graphs.

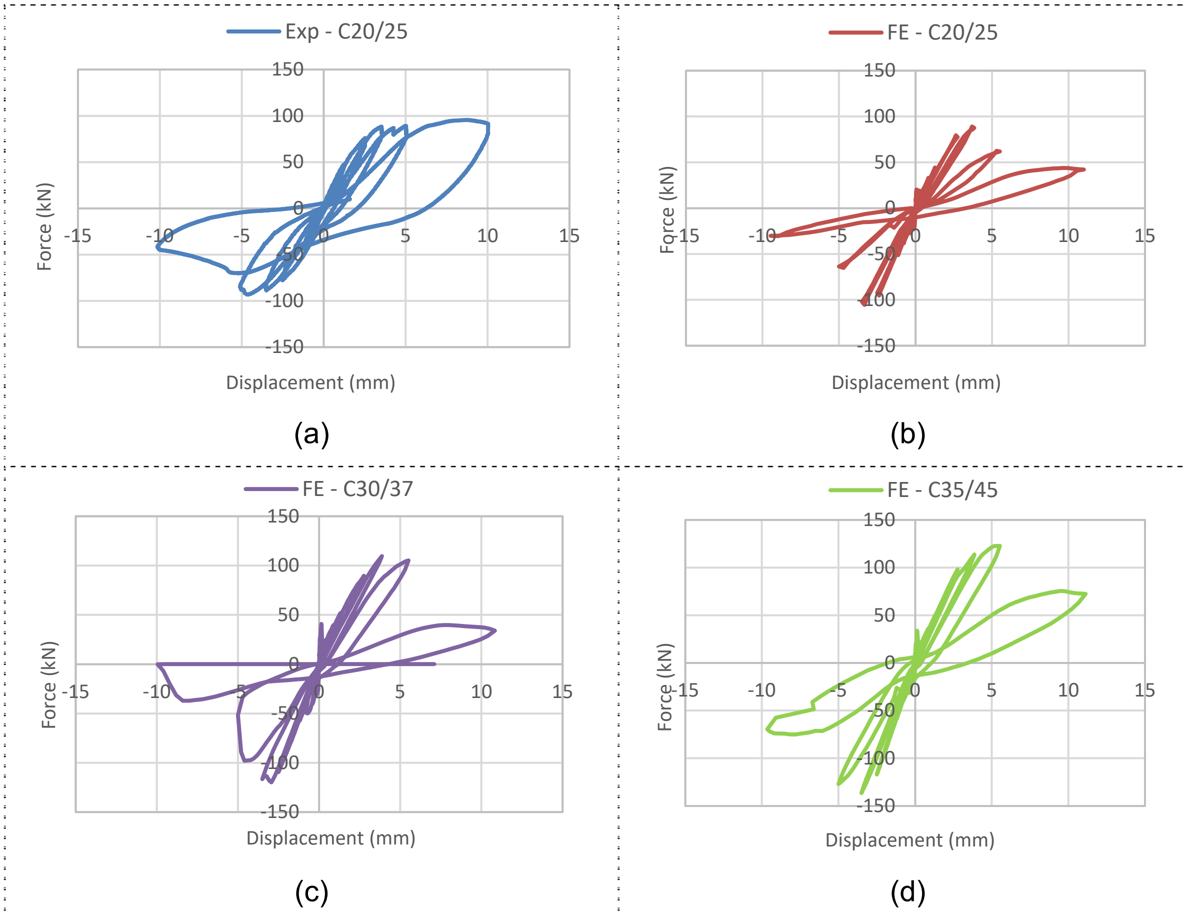

Figure 6.23 - S10 Hysteresis response (a) Experimental C20/25, (b) FE C20/25, (c) FE C30/37 and (d) FE C30/35

Force-displacement envelope for calibration

The envelope of the hysteresis response averaged over the push and pull maximum values of the hysteresis loops can be seen in the force-displacement graph (0-140 kN against 0-6 mm) of Figure 6.24 below.

Both curves show an almost linear faster rise until 3.5 mm displacement followed by a prolonged almost-horizontal climbing. There is an initial higher curve for experimental results before 1 mm displacement due to the stiffer behaviour of the FE model than the experimental specimen.

From 1.2 mm till failure point, the difference between the two curves is less than 2 per cent. At the failure point, the ultimate load is 93 and 91 kN for the FE and experimental curves. Overall the two curves show a high level of correspondence to each other until the failure point.

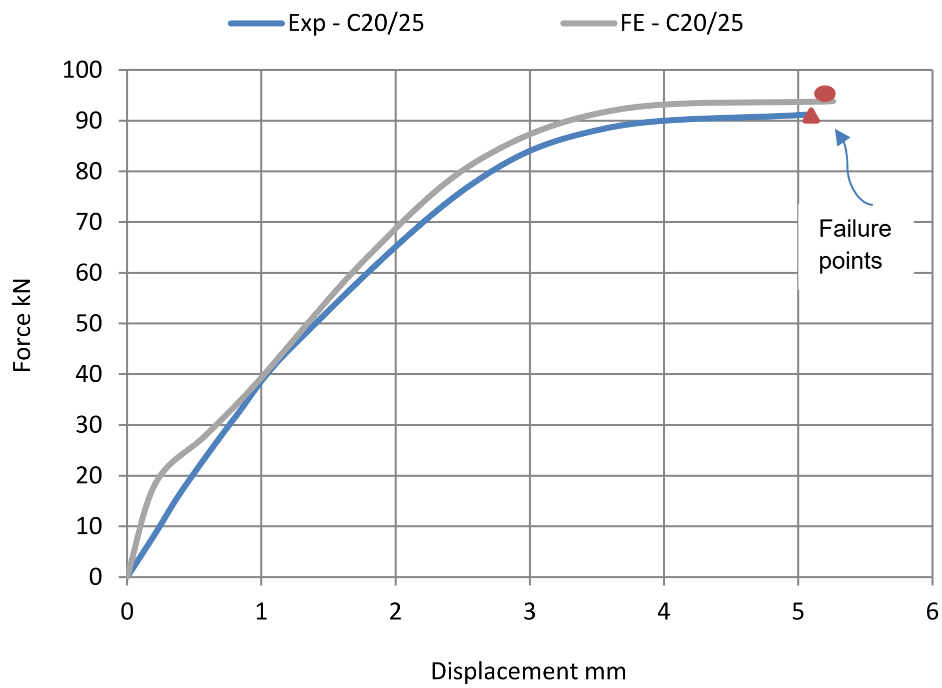

Figure 6.24 - S10 hysteresis response averaged envelope for experimental and FE results

Force-displacement envelope for parametric study

Figure 6.25 shows force-displacement graphs for three strength classes of concrete. All the FE results show an initial stiffness at 0.2 mm displacement followed by a gradual climb until 3 mm displacement, after which the curve tends to level off.

The FE-C30/37 curve rises quicker than the FE-C35/45 curve due to the stiffer behaviour of the FE-C20/25 model at the beginning. The FE-C30/37 curve declines after about 3.5 mm displacement until the failure point. FE-C20/25, FE-C30/37 and FE-C35/45 fail at about 87, 102 and 122 kN, respectively. The increase in the peak values from FE C20/25 to FE-C30/37 and FE-C35/45 are about 17 and 40 per cent, respectively.

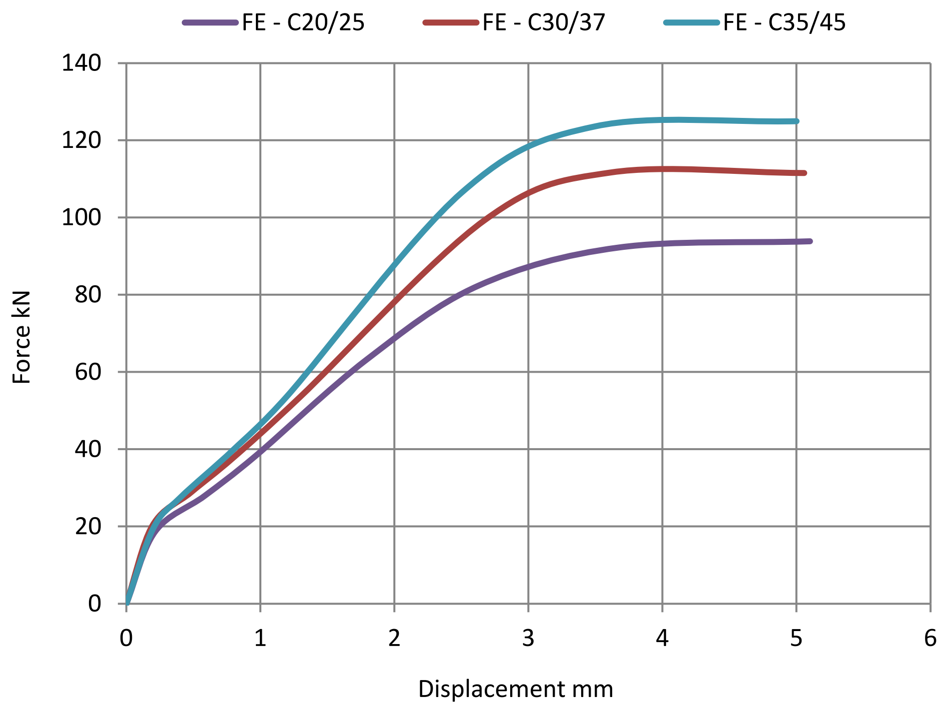

Figure 6.25 – S10 model, parametric studies, three concrete strengths

6.7.3. B6 model results

Hysteresis response

The curves in Figure 6.26 below show the hysteresis response for three strength classes of concrete, including the experimental specimen. The hysteresis loops show a more similar pattern for the displacements less than 10 mm. The difference is due to the smeared crack assumption in the FE model.

Figure 6.26 (a) to (d) shows hysteresis response for experimental C30/37, FE C30/37, FE – C20/25 and FE C35/45, respectively. It can be seen from the graphs that the maximum loop peak increases from less than 60 kN to about 100 kN and well above 100 kN for FE-C20/25, FE 30/37 and FE C35/45 respectively. The difference in maximum values signifies the effect of concrete strength as the only varying parameter. Despite some deviation in loop width the loops peak values follow a very similar trend.

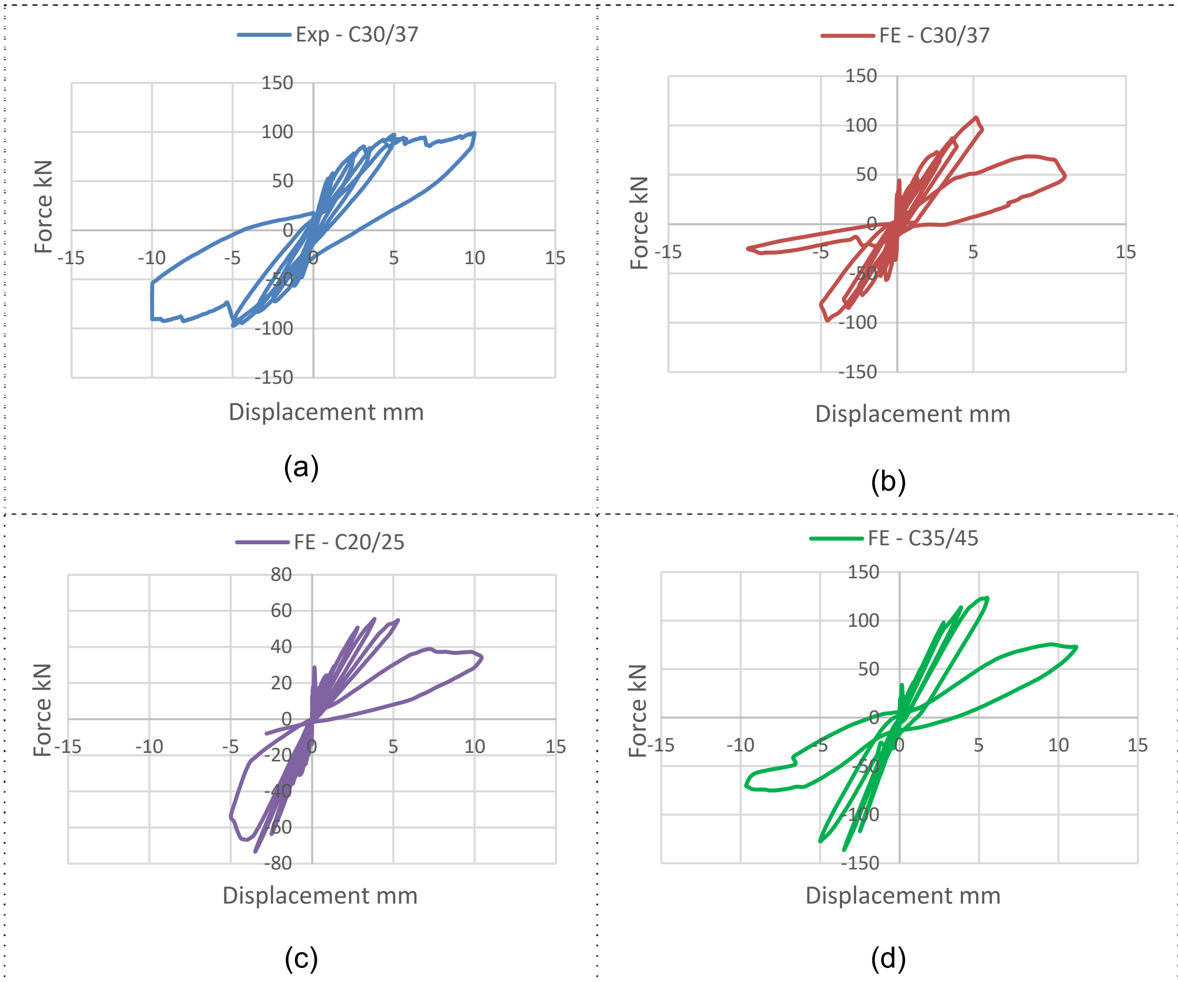

Figure 6.26 – B6 Hysteresis response (a) Experimental C30/37, (b) FE C30/37, (c) FE C20/25 and (d) FE C35/45

Force-displacement envelope for calibration

The envelope of the hysteresis response averaged over the maximum push and pull values can be seen in the force-displacement graph (0-140 kN against 0-6 mm) graph of Figure 6.27 below. The FE curve rises faster than the experimental due to the stiffer behaviour of the model before 0.8 mm displacement. From 0.8 to 3 mm displacement, the difference between the two curves is less than one per cent. After 3 mm the FE curve rises faster than the experimental until the failure point. The ultimate load is about 101 and 98 kN for FE and experimental curves, respectively. Overall there is a high level of correspondence between the FE and experimental results graphs.

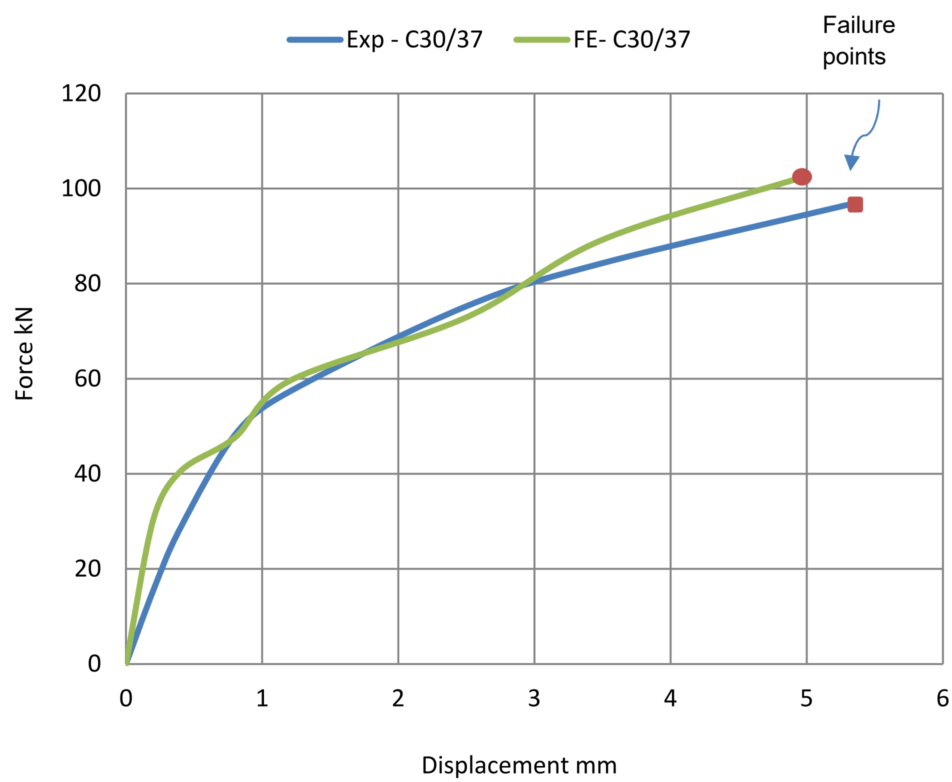

Figure 6.27 - B6 hysteresis response averaged envelope for experimental and FE results

Force-displacement envelope for parametric study

Figure 6.28 shows force-displacement curves for three strength classes of concrete. FE-C30/37 and FE-C35/45 curves show an initial faster climb due to the stiffer behaviour of the models at the beginning (less than 0.4 mm) followed by a gradual rise until failure. FE-C20/25 curve also shows a quicker rise (up to 0.2 mm) due to higher initial stiffness followed by a gradual increase until about 3.7 mm displacement after which it tends to decrease trivially due to its low concrete strengths in combination with smaller diameter rebars. FE-C20/25, FE-C30/37 and FE-C35/45 fail at about 60, 102 and 119 kN respectively. The percentage increase in the peak values in relation to the FE C20/25 are about 70% and 96% for FE-C30/37 and FE-C35/45, respectively.

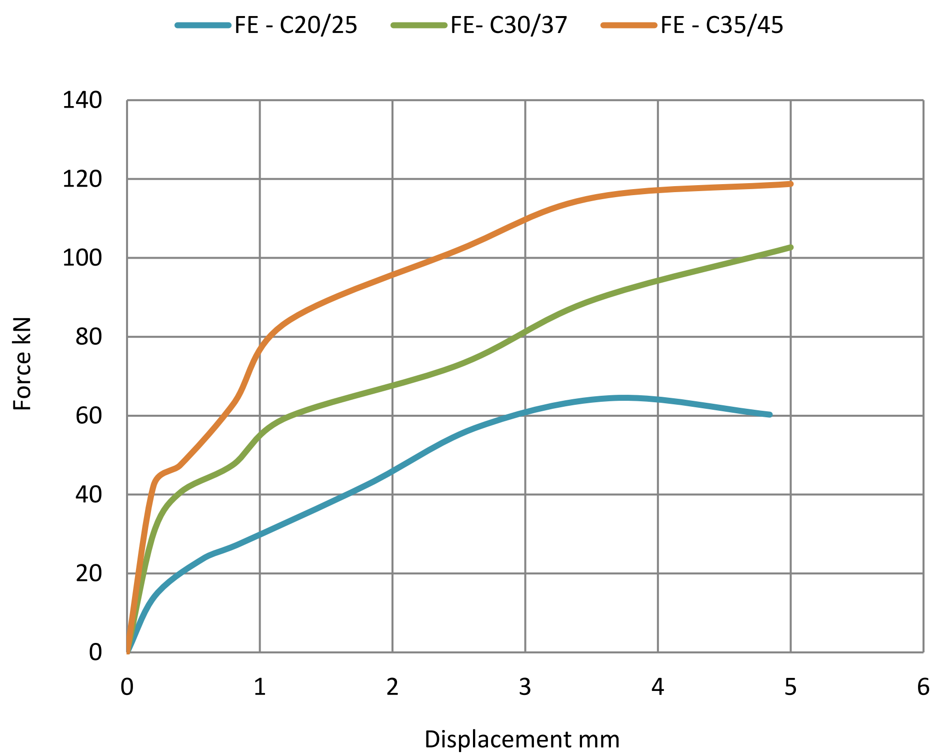

Figure 6.28 – B6 model parametric studies, three concrete strengths

6.8. Summary of FE modelling results

6.8.1. Ultimate strength

The peak strength of the hysteresis model can be seen in the bar chart depicted in Figure 6.29. The graph shows that the ultimate load-carrying capacity for different strengths of concrete. The maximum load is about 75 kN for experimental class C20/25, and 76, 99 and 110 kN for FE classes C20/25, C30/37 and C35/45, respectively. The bar chart shows a close correspondence between experimental and FE class C20/25 and a gradual increase in the peak performance of the B10 model as the strength classes of concrete increases. The percentage gain in strength relative to FE-C20/25 are about 30% and 44% in FE classes C30/37 and C35/45, respectively.

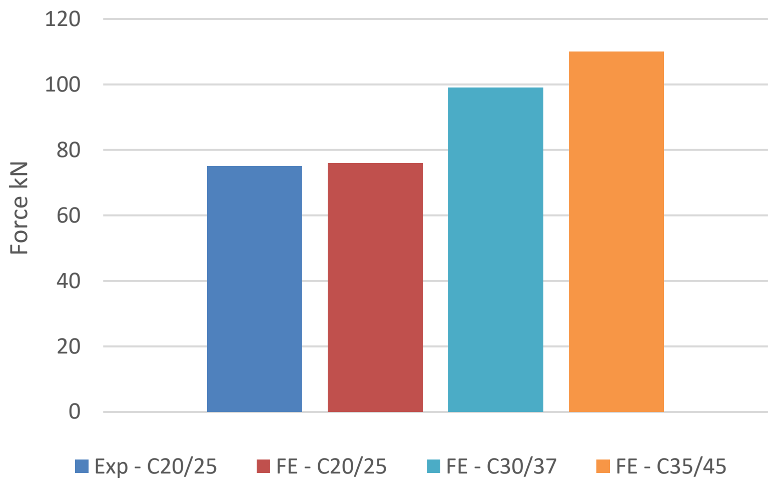

Figure 6.29 - B10 ultimate force of experimental specimen and FE Solid65 model for different strength classes of concrete

Figure 6.30 shows the peak hysteresis strength of the S10 model depending strength class of concrete. The ultimate load for the experimental specimen strength class C20/25 is 93 kN whereas for FE classes C20/25, C30/37 and C35/45 they are 92 to 113 and 125 kN, respectively. The correspondence between experimental class C20/25 and FE-C20/25 is very good (about 1% difference), and the ultimate load gradually increase with increasing strength of concrete. The FE-C30/37 and FE-C35/45 percentage strength increase in relation to FE-C20/25 is about 22% and 35%, respectively.

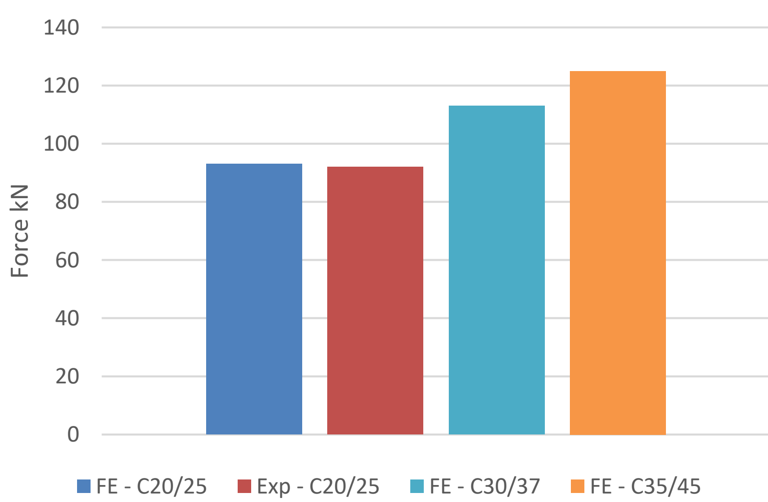

Figure 6.30 - S10 ultimate force of experimental specimen and FE Solid65 model for different strength classes of concrete

Figure 6.31 shows bar charts for the ultimate performance of the B6 model under cyclic loading. The chart shows a clear increasing trend as the strength class of concrete increases; there is a good correspondence between the ultimate performance of experimental C30/37 (97 kN) specimen and FE-C30/37 (96 kN) with about 1% difference only. The ultimate performance FE models increase from 64 to, 96 and 118 kN with increasing strength of concrete from C20/25, C30/37 and C35/45, respectively. The percentage strength increase from FE-C20/25 to FE-C30/37 and FE-C35/45 are about 50% and 84%, respectively. Overall there is an increasing trend in the ultimate performance of the B6 model with rising strength classes of concrete.

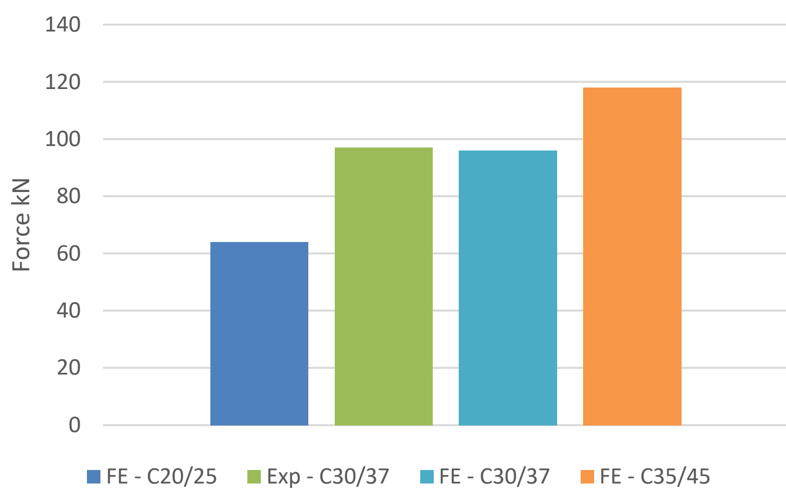

Figure 6.31 - B6 ultimate force of experimental specimen and FE Solid65 model for different strength classes of concrete

Figure 6.32 shows the ultimate force (50-130 kN) against cylindrical concrete strength (15-40). The curve shows an increase in the maximum force carrying capacity of the models against the concrete strength class. The trendlines show that the growth is approximately linear for B10 and S10, and second-order polynomial for the S6 model. The equations for the trendlines are shown in the graph.

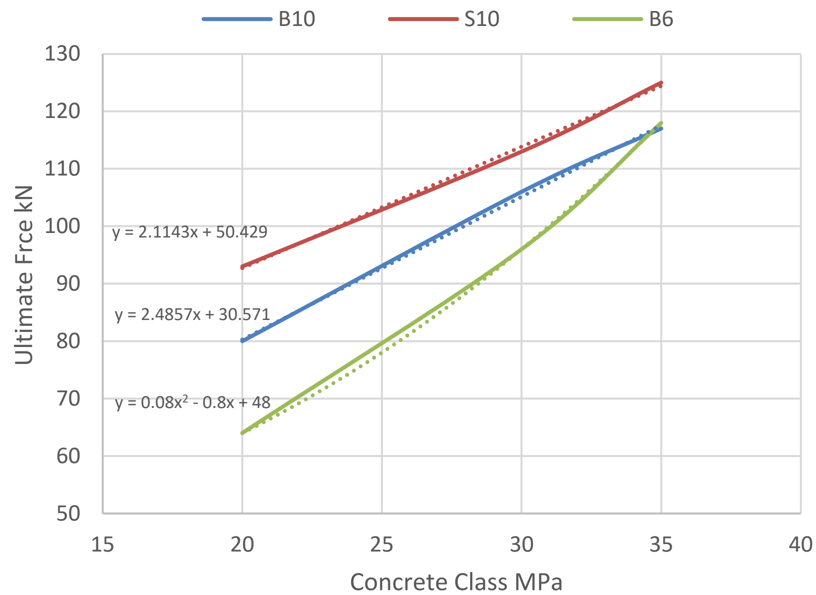

Figure 6.32 – All models ultimate force - cylindrical concrete strength trendlines

6.8.2. Crack analysis

FE Solid65 can be compared with experimental results in term of the crack pattern. The element Solid65 is capable of simulating smeared cracks. FE Solid65 figures show a crack pattern developed due to the application of the load in one direction (left side of the model). The application of the load in the opposite direction (the right side of the model) would result in a symmetrical cracking pattern, i.e. more cracks to the right than the left side of the model. The cracks shown are taken as a snapshot at indicated displacement intervals.

FE Solid65 shows crack at every integration point even the microcracks that cannot be captured by eyes as observed in the experiments. First, second and third cracks are shown in red, green and blue circles respectively for in-plane cracks and out of plane cracks are shown as diagonal dashes by the Solid65 model.

The B10 model crack patterns developed at 1.2 mm, 2.5 mm and 3.5 mm for FE Solid65 (Figure 6.33 (c), (b) and (a)) and experimental specimen (Figure 6.33 (c/), (b/) and (a/)) show a good correlation. At 3.5 mm the cracks are more than half, at 2.5 mm about half and, at 1.2 mm it is less than half of the height of the model.

Disp.	FE Solid65	Experimental
3.5 mm	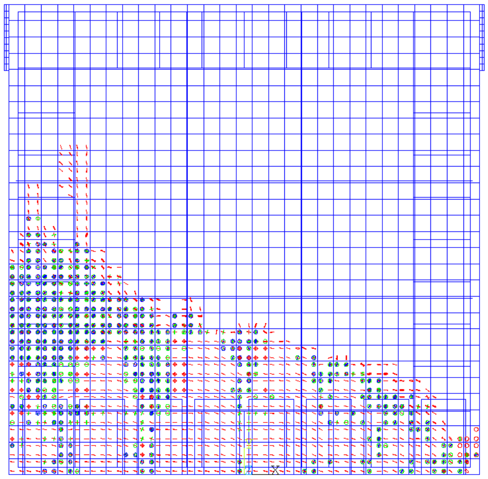 (a)	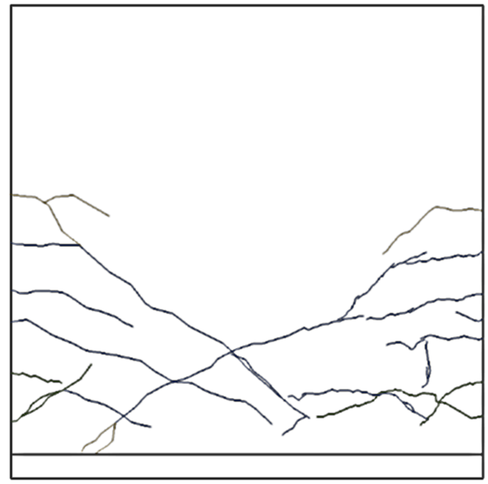 (a/)
2.5 mm	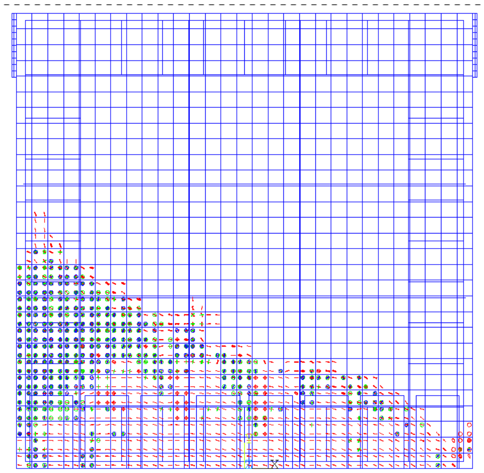 (b)	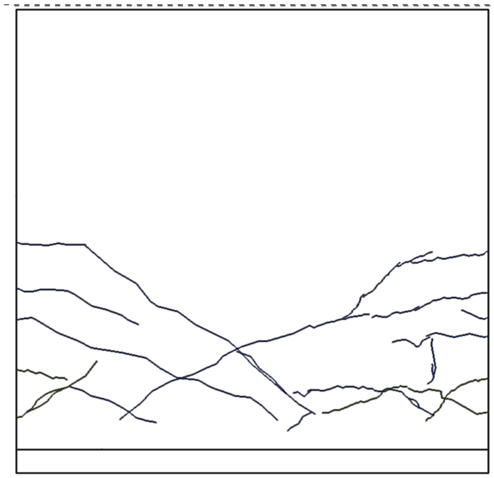 (b/)
+1.2 mm	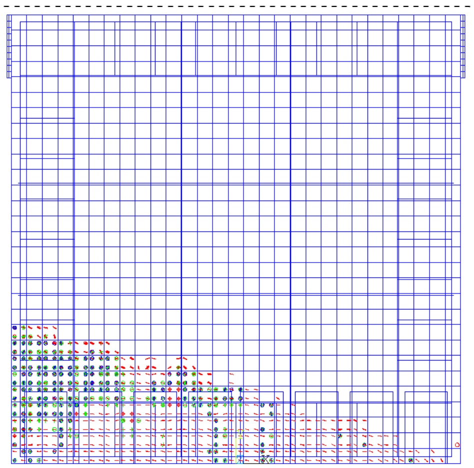 (c)	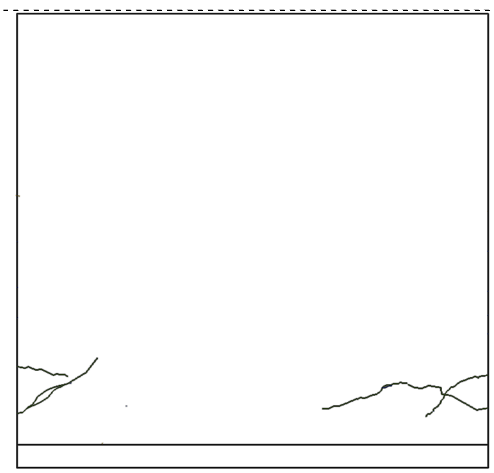 (c/)

Figure 6.33 - FE Solid65 and experimental crack patterns at displacements (a/a/) 3.5 mm (b/b/) 2.5 mm (c/c/) 1.2 mm for the B10 sample

The cracking patterns for S10 sample at 2.5 mm, 3.5 mm and 5 mm for FE Solid65 (Figure 6.34 (c), (b) and (a)) and experimental specimen (Figure 6.34 (c′), (b′) and (a′)) show a good correlation as well. At 5.0 mm the cracks are more than half, at 3.5 mm about half and, at 2.5 mm it is less than half of the height of the model.

The cracking starts later in the S10 model due to the higher bond strength between the reinforcement and the concrete. The B10 cracks stop at 3.5 mm displacement amplitude as the same cracks get wider at 5 mm displacement due to bond-slip between BFRP and concrete.

Disp.	FE Solid65	Experiments
5.0 mm	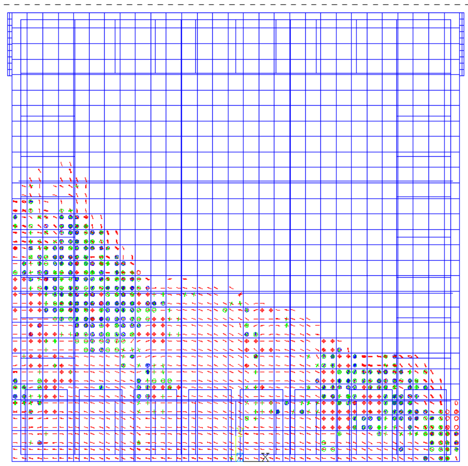 (a)	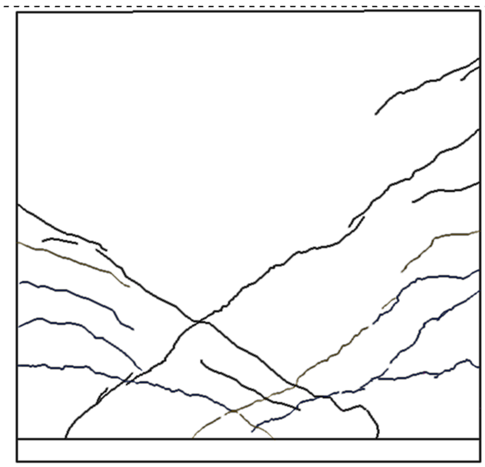 (a′)
3.5 mm	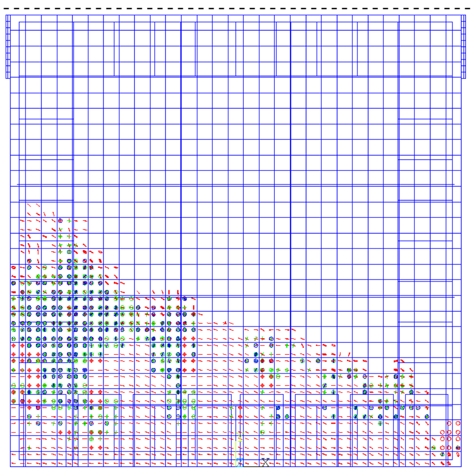 (b)	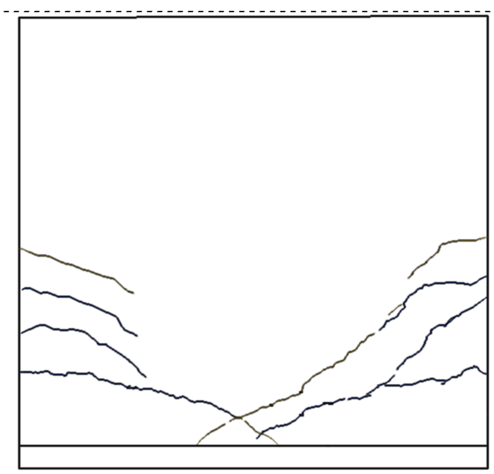 (b′)

2.5 mm	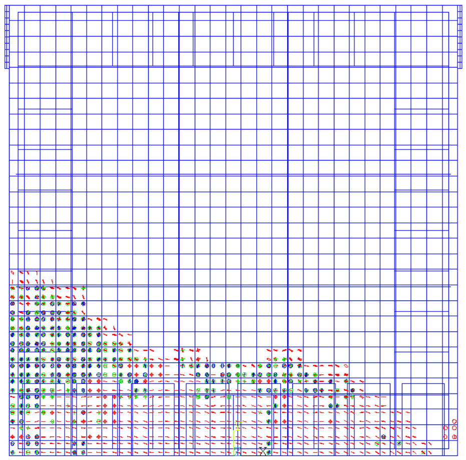 (c)	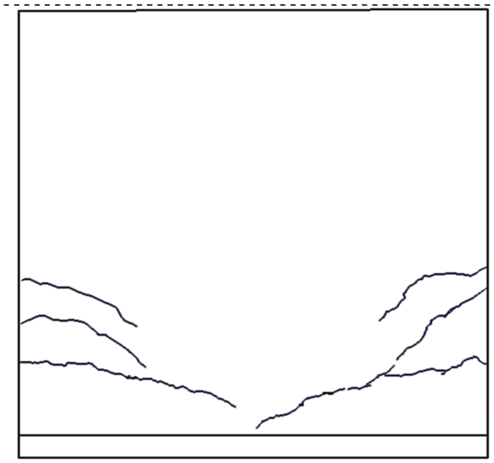 ($c^{/}$)

Figure 6.34 - FE Solid65 and experimental crack patterns at displacements ($a/a^{/}$) 5 mm ($b/b^{/}$), 3.5 mm, 2.5 mm ($c/c^{/}$) 1.2 mm for the S10 sample

6.9. Chapter Conclusions

From the results of the model’s hysteresis response following conclusion can be made:

- There is a good correspondence between FE and experimental results for the Solid65 with the existing capabilities of the material models.
- The Solid65 model can capture hysteresis response until the influence of the degree of damage becomes more pronounced, at the indicated intervals.
- The model can predict the peak performance and capture the cracking patterns developed by the experimental specimens.
- The parametric studies resulted in clarification of the process of increasing the capacity of BFRP and steel-reinforced shear walls when the strength of the concrete is increased.
- Analytical expressions reflecting the process of increase of the strength are offered.

Overall the finite element method can be successfully applied in modelling the behaviour of the RCSW and conducting parametric studies.

7. Development and Results of the Microplane Model

The model developed to simulate the behaviour of the samples conducting pushover analysis is named the Microplane model. The name is employed because Microplane is a familiar name used in analytical modelling of the concrete. The model development methodology is the same as the Solid65 model (Chapter 7) except for the sections described in this chapter.

The material model for concrete parameters based on the experimental data are calculated using the Equations 1 to 7. A concrete material behaviour based on Kachlikev work (Figure 7.4) is described and the results are tabulated (Table 7.1) for better clarification.

7.1. Element Selection

The geometrical configurations and reinforcement elements selection were the same as described in the development of the Solid65 model.

7.1.1. CPT215

For the pushover analysis element type, a Microplane damage material model was selected to represent the behaviour of the RCSW. The CPT215 element is selected from the elements library as it has elasticity, stress stiffening, large deflection and large strain capabilities. Additionally, it is one of the recommended elements for the concrete Microplane material model.

CPT215 is a 3D solid element defined by eight nodes having four degrees of freedom including; translations in the nodal x, y and z directions at each node. The geometry and node location of the element is shown in Figure 7.1 below.

The prism and tetrahedral shapes are also available as they can be seen in the diagram. However, these shapes are not used in this study (Ansys help systems, 2020).

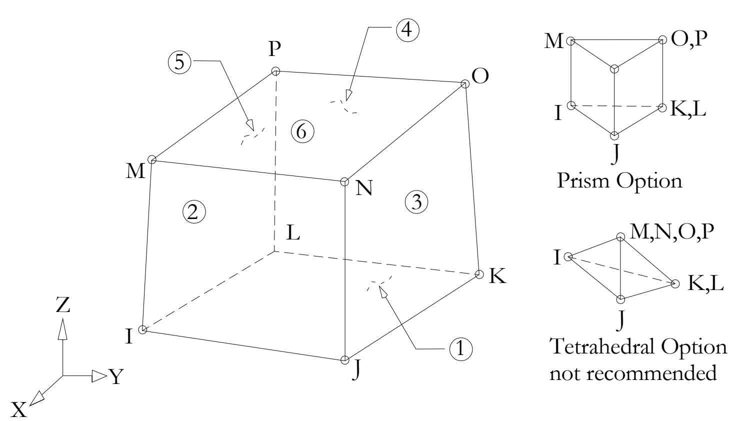

Figure 7.1 – 3D Ansys CPT215 element geometry, after (Ansys help systems, 2020)

Ansys mechanical is formulated to choose an element type automatically depending on geometry and mesh. Therefore, the following command snippet was used to define the element type CPT215.

```
ET,MATID,CPT215  ! Element type CPT215

KEYOPT,MATID,11,0
! Temperature degree of freedom:
! 0 – Disable
! 1 – Enable
```

The element can take pressure as a surface load on the element face shown by circled numbers in Figure 7.1. The effects of pressure load stiffness are included in this element which causes an unsymmetrical matrix. However, convergence difficulties can be overcome by using NROPT,UNSYM command to use the unsymmetrical Newton-Raphson method for solving.

7.1.2. Bonding Connection

The interface element used to model the bond-strength between the concrete and rebars is Combin40 described in the subsection below. The bodings with target and contact elements, as well as the, constrain equation were the same as the Solid65 model.

Interface Element Combin40

The interface element Combin40 is a two-node element that is a combination of spring-slider and damper in parallel, coupled to a gap in series. Both nodes can be associated with a mass. The element has one degree of freedom at each node, in this case, translation is selected in the y-direction in the local coordinate system, and only springer and slider capabilities are used. The element has other capabilities such as rotation, pressure or temperature not used; additionally, it has mass, damper and gap capabilities not used in this study either. All capabilities of the element are shown in the element’s geometry layout below (Figure 7.2).

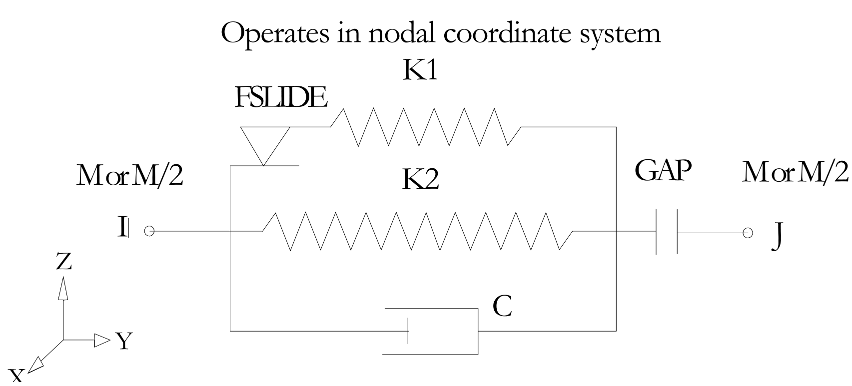

Figure 7.2 - Combin40 element geometry layout, after (Ansys help systems, 2020)

The element was selected to represent the bond-slippage between concrete CPT215 and vertical steel/FRP rebars Link180 elements in vertical (global y-direction) as observed in experimental specimens. The element was defined by two offset nodes, one from concrete and one from rebar elements. The commands their associated descriptions to define Combin40 is elaborated inside the dashed frame below.

```
! To create an interface element and connect the vertical bars in the y-direction

/PREP7                      ! Enter the model creation Preprocessor
CMSEL,S,CONC,ELEM  ! Select elements of concrete material
CMSEL,R,Vbars,NODE  ! Select nodes of all vertical bars

ET,MATID,COMBIN40   ! Element Type Combin40
TYPE,MATID              ! Assign element type to MATID
REAL,MATID              ! Assign all real constants sets R to MATID

keyopt,matid,3,2
K1=400                     ! Spring constant (Force/Length)
K2=4000                    ! Spring constant (Force/Length)
c=0                        ! Damping coefficient (Force*Time/Length)
gap=0                      ! Gap size (Length)
fslide=500                 ! Limiting sliding force (Force)
m=1                        ! Application of mass at nodes (Force/Time2/Length)
r,matid,K1,c,m,gap,fslide,K2    ! Application of real constants to MATID

EINTF,0.01, ,LOW,0 , 15 ,0 , 15, 0       ! Create Combin40 element between offset nodes
EINTF,0.01, ,LOW,0 , 15,0 ,-15 , 0       ! Create Combin40 element between offset nodes
EINTF,0.01, ,LOW,0 , 1.667,0 ,-15 , 0  ! Create Combin40 element between offset nodes
EINTF,0.01, ,LOW,0 , -1.667,0 ,-15 , 0 ! Create Combin40 element between offset nodes
EINTF,0.01, ,LOW,0 , -25, 0 ,0, 0         ! Create Combin40 element between offset nodes
EINTF,0.01, ,LOW,0 , 18.33,0 ,0 , 0     ! Create Combin40 element between offset nodes

KEYOPT,MATID,1,0
! Gap behaviour:
!    0 – Standard gap capability
```

```
!     1 – Gap remains closed after initial contact (“lockup”)

KEYOPT,MATID,3,2
! Element degrees of freedom (1-D) (KEYOPT(4) overrides KEYOPT(3)):
!     0, 1 -- UX (Displacement along nodal X axes)
!     2 -- UY (Displacement along nodal Y axes)
!     3 -- UZ (Displacement along nodal Z axes)
!     4 -- ROTX (Rotation about nodal X axes)
!     5 -- ROTY (Rotation about nodal Y axes)
!     6 -- ROTZ (Rotation about nodal Z axes)
!     7 -- PRES
!     8 -- TEMP

KEYOPT,MATID,4,0
! Element output:
!     0 – Produce element printout for all status conditions
!     1 – Suppress element printout if gap is open (STAT = 3)

KEYOPT,MATID,6,0
! Mass location:
!     0 – Mass at node I
!     1 – Mass equally distributed between nodes I and J
!     2 – Mass at node J

ALLSEL,ALL              ! Select all entities types.
/SOLU                   ! Enter the Solution solver
OUTRES,ALL,ALL          ! Select all items for all substeps
```

7.2. Material Model

The material for the Microplane model concrete elements is described in this section. The reinforcement material models are the same as the Solid65 model.

7.2.1. Concrete Material Model for CPT215

For the concrete, the Microplane material model was employed using TB,MPLANE command. The Microplane concrete behaviour is modelled through stress-strain laws on individual planes, and the stiffness degradation is modelled using damage laws on each plane. The damages are formulated macroscopic and anisotropic. The model is suited for concrete which has aggregate compositions of different properties (Ansys help systems, 2020).

The Microplane theory can be summarized as following three primary steps:

- Applying kinematic constraint to relate the macroscopic strain tensor to their Microplane counterpart.
- Defining constitutive laws on Microplane levels, where unidirectional constitutive equations (such as stress and strain components) are applied on each Microplane.
- Relating the homogenization process on the material point level to derive the overall material response. Homogenization is based on the principle of energy equivalence.

The Microplane material model formulation assumes that free microscopic energy exists at the Microplane level and the integral of microscopic free energy over all the microplanes is equivalent to macroscopic free energy. The stress and strains at microplanes decompose into volumetric and deviatoric parts based on volumetric-deviatoric split. Furthermore, it assumes elastic-isotropic elasticity is considerable for the material.

In the transferring process from the microsphere to Microplane (to approximate the sphere), forty-two planes are used for numerical integration. Still, due to the symmetry of the microplanes at every other plane with the same normal direction, twenty-one microplanes can be considered and summarized. Figure 7.3 below illustrates the approximation process (Ansys help systems, 2020).

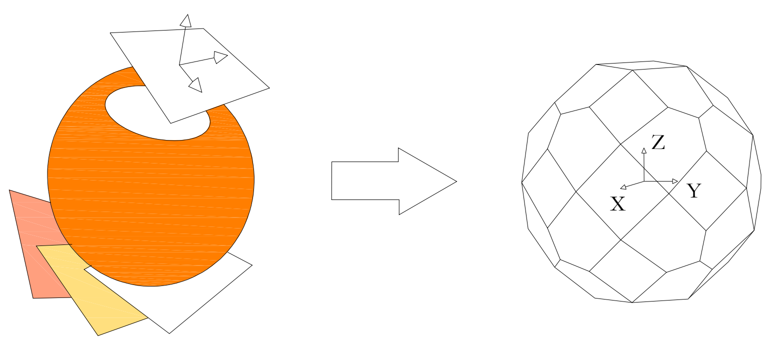

Figure 7.3 - Sphere approximation by forty-two microplanes, after (Ansys help systems, 2020)

The damage status (Φ^{mic}) of the concrete can be described by the equivalent-strain-based damage function (Equation 1) and equivalent strain (Equation 2) which characterized the damage evolution (d^{mic}) law. The equations are as followings:

$$\varphi^{mic} = \varphi\,(\eta^{mic}) - d^{mic} \leq 0$$ Equation 1

The damage function (η^{mic}) can be written in terms of equivalent strain which is a scalar measure that controls the damage. Where I_1 is the first invariant of the strain tensor, and J_2 is the second invariant of the deviatoric part of the strain tensor and k_0, k_1 and k_2 are the material parameters that characterize the form of the damage function (Equation 2):

$$\eta^{mic} = k_0 I_1 + \sqrt{k_1^2 I_1^2 + k_2 J_2}$$ Equation 2

I_1 and J_2 can be written as Equations 3 and 4 below (Groot, 1987):

$$I_1 = \varepsilon_1 + \varepsilon_2 + \varepsilon_3$$ Equation 3

$$J_2 = \frac{1}{6}((\varepsilon_1 - \varepsilon_2)^2 + (\varepsilon_2 - \varepsilon_3)^2 + (\varepsilon_3 - \varepsilon_1)^2)$$ Equation 4

Solving invariants for both parts of the tensors Equations 5 and 6 can be derived (CADFEM, 2015):

$$k_0 = k_1 = \frac{k-1}{2k(1-2\nu)}$$ Equation 5

$$k_2 = \frac{3}{k(1+\nu)^2}$$ Equation 6

In the absence of the experimental data for damage parameters, Equations 5 and 6 can be used to approximate values for the damage material parameter k_0, k_1 and, k_2. The constant k is equal to the ratio of compressive over tensile strength of the concrete, and v is the Poisson's ratio.

$$d^{mic} = 1 - \frac{\gamma_0^{mic}}{\eta^{mic}}\left[1 - \alpha^{mic} + \alpha^{mic}\, exp\left(\beta^{mic}(\gamma_0^{mic} - \eta^{mic}\right)\right.$$ Equation 7

The damage evolution (normalized) is modelled by Equation 7 above; where α^{mic} specifies maximum degradation, β^{mic} specifies the rate of damage evolution, γ_0^{mic} determines the equivalent strain on which the damage starts (damage starting boundary).

The evolution of the damage against the equivalent strain graph is shown in Figure 7.4 below as an example graph. The figure shows that as the normalized damage evolution increase from 0 to 1, the damage equivalent strain increase from 0 to 0.1, respectively.

The damage threshold γ_0^{mic} starts at 0 damage and 0.0065 strain and increase at a rate of β^{mic}. The maximum damage α^{mic} in the example graph is depicted to be about 0.98 d^{mic} against 0.1 η^{mic}.

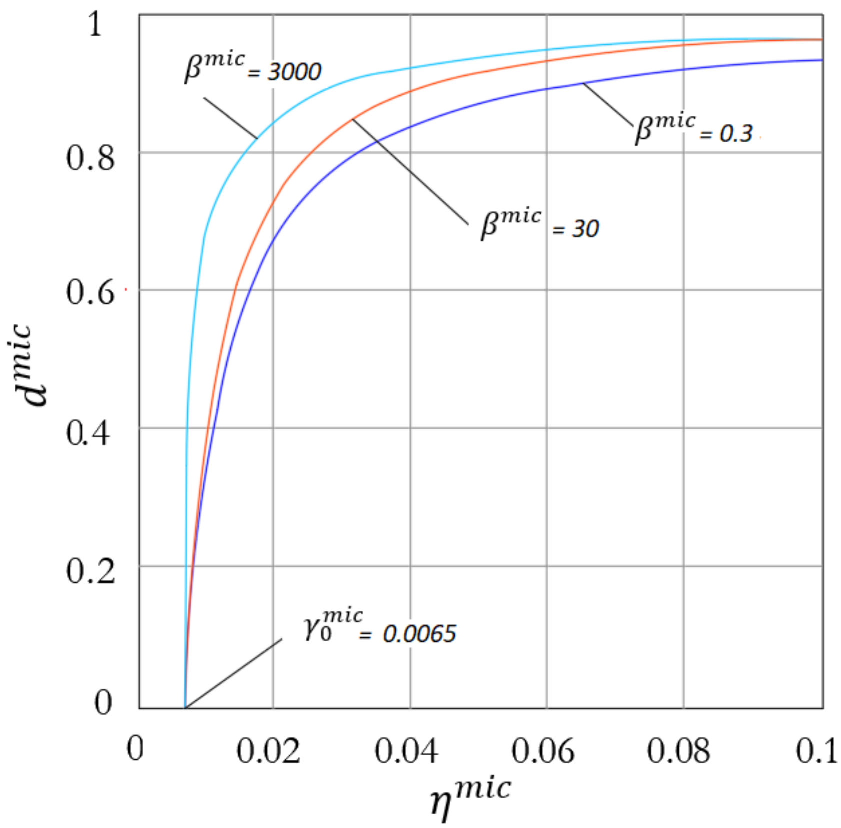

Figure 7.4 - Damage evolution against equivalent strain, after (Ansys help systems, 2020)

The constant values C1 to C6 in Table 7.1 were used to model B6, B10 and S10 models. C1 and C2 define the elasticity parameters, and C3 to C6 defines the damage evolution parameters. The damage function material parameters (k_0, k_1, k_2) were calculated based on equations 5 and 6. The damage threshold (γ_0^{mic}), maximum damage parameter (α^{mic}) and rate of damage evolution (β^{mic}) were determined based on the calibration of the model to the experimental results.

Table 7.1 - Elasticity and damage constants for concrete

Constant	Parameter type	Symbol	B6 model	B10 model	S10 model	Meaning

C1	Elasticity	E (MPa)	33000	30000	30000	Modulus of elasticity
C2		v	0.2	0.2	0.2	Poisson’s ratio
C3	Damage	k_0, k_1, k_2	Equations 5 and 6	Equations 5 and 6	Equations 5 and 6	Damage function material parameters
C4		γ_0^{mic}	2.7e-5	3e-5	2.8e-5	Damage threshold
C5		α^{mic}	1	1	1	Maximum damage parameter
C6		β^{mic}	10	30	25	Rate of damage evolution

Defining material model using command snippet

Definition of the concrete in Ansys Mechanical need a command snippet because the Ansys Mechanical GUI does not allow insertion of the constants C1-C6 as explained in Table 6.4 above; therefore, a command snippet was used to define the material as below:

```
! Linear properties concrete material model (MATID)

MP,EX,MATID,30000          ! Material property Modulus of Elasticity for MATID
MP,NUXY,MATID,0.2          ! Material property, Poisson’s ratio for MATID

! Define the Microplane damage properties concrete material (MATID)

TB,MPLANE,MATID,1,6,       ! Use 1 table with 6 concrete properties (6 constants)
fc=28                      ! Compressive strength of concrete
ft =2.8                    ! Tensile strength of concrete
k=fc/ft                    ! Constant (compressive/tensile strength ratio)
k0=(k-1)/(2*k*(1-2*v))     ! Damage function constant k0 formulation
k1=k0                      ! Damage function constant k1 formulation
k2=((2/k)/(1+v))/(1+v)     ! Damage function constant k2 formulation
gama=0.00003               ! Damage threshold
alpha= 1                   ! Maximum damage parameter
beta= 30                   ! Rate of damage evolution

TBDATA,matid,k0,k1,k2,gama,alpha,beta ! Table date (6 constants)
```

7.3. Finite Element Discretisation

A mesh sensitivity analysis was conducted for a range of 10 mm to 100 mm FE mesh sizes, and it was found that the sensitivity was below 3% for the range. The appropriate size of the mesh was selected to converge in a reasonable time. The example of a meshed model is shown in Figure 7.5 below. These mesh sizes were approximately 66 mm in two orthogonal directions. The size was also recommended by Ansys to achieve convergence of the solutions (Ansys meshing solutions, 2019).

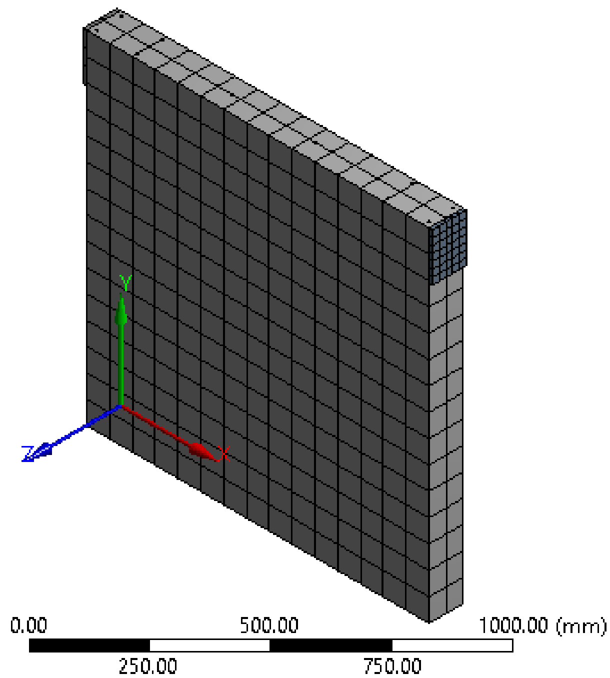

Figure 7.5 - Meshing of the RC shear wall model (Image used courtesy of ANSYS, Inc.)

7.4. Boundary Conditions

The loading regime used in the testing of the experimental samples is also used in this FEA. A monotonic pushover displacement-controlled load was applied gradually from 0.2 mm to 30 mm in according with the envelope of the modified ATC-24 following the experimental studies. Figure 7.6 below shows the applied displacements against load step numbers where each step represents a single cycle of the modified ATC-24 protocol.

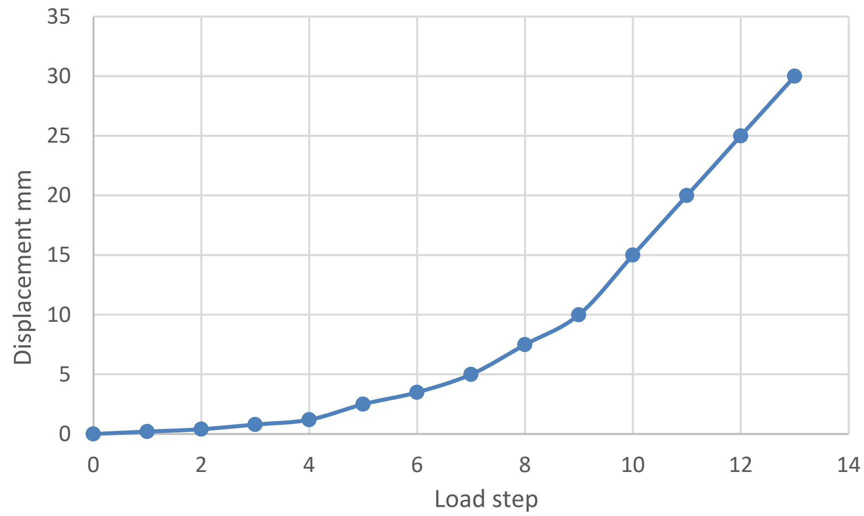

Figure 7.6 - Pushover displacement vs load steps

7.5. Analysis Settings

The Ansys mechanical solver settings are used to determine the solver's analysis configuration. The settings include the number of steps, substep and other linear and nonlinear analysis control.

The displacements curve were applied in 14 steps where each step corresponding to a load cycle. A minimum of five and a maximum of a hundred substeps was defined to help with convergence.

The solver pivot check "error" option was selected to stop the solution as soon as an error is encountered. The Newton-Raphson method was used with a maximum of a hundred iteration per substep to help with the convergence of the solution.

7.6. Microplane Model Results

The results in this section include the force-displacement comparison for validation of the model, comparison of pushover results with experimental hysteresis response, and a parametric study of the model based on the validated model.

7.6.1. Force-displacement

Force-displacement results of the FE Microplane model and experimental specimen for the B10 sample can be seen in Figure 7.7. The FE curve shows a steep rise until approximately 75 kN at about 6 mm, and the experimental curves rise to 80 kN at about 6.5 mm. After the ultimate strength, the FE curve shows a more gradual decrease compared to the steel sample which reaches its minimum at about 25 mm and maintains some residual capacity. The experimental curve shows a faster drop until about 21 mm after which it shows an almost flat pattern.

The stiffer behaviour of the FE model at the beginning is due to a fully fixed boundary condition assumption at the bottom which probably overestimates the rigidity of the connection in the experiment. At the next stage, however, the FE curve approaches the experimental curve.

The softening behaviour of the FE model is more gradual than the experimental curve due to the rate of damage evolution (β^{mic}) and maximum damage parameter (α^{mic}) which are constants resulting in more gradual softening effects as calculated by the damage evolution function (d^{mic}).

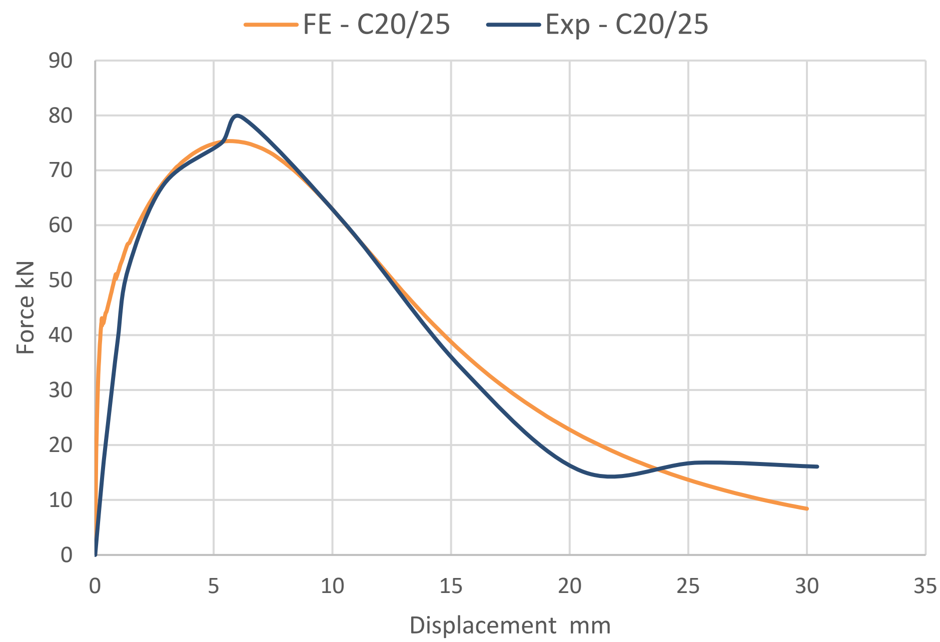

.

Figure 7.7 – B10 FE Microplane and the experimental force-displacement results

Figure 7.8 shows force-displacement curves of FE Microplane and experimental specimen for S10 sample. Similar to the previous simulation, an initially stiffer FE model is observed which is due to the fully fixed boundary condition assumption as with the B10 model. The peak strength of both curves is just over 90 kN.

The FE curve shows a gradual softening of the model from 7 to 25 mm, whereas, the experimental curve shows a slower softening between 7 to 14 mm, faster softening between 14 to 20 mm, and very slow softening after about 15 kN corresponding to about 17 mm displacement amplitude.

The comparison between FE and experimental curve up to 17 mm is more reliable. Above this value, the experimental curve is developing, readings that are higher than expected because breaking of the sample into two different parts and the interlocking effect of the aggregates is increasing during the process of movement of those two bodies against each other.

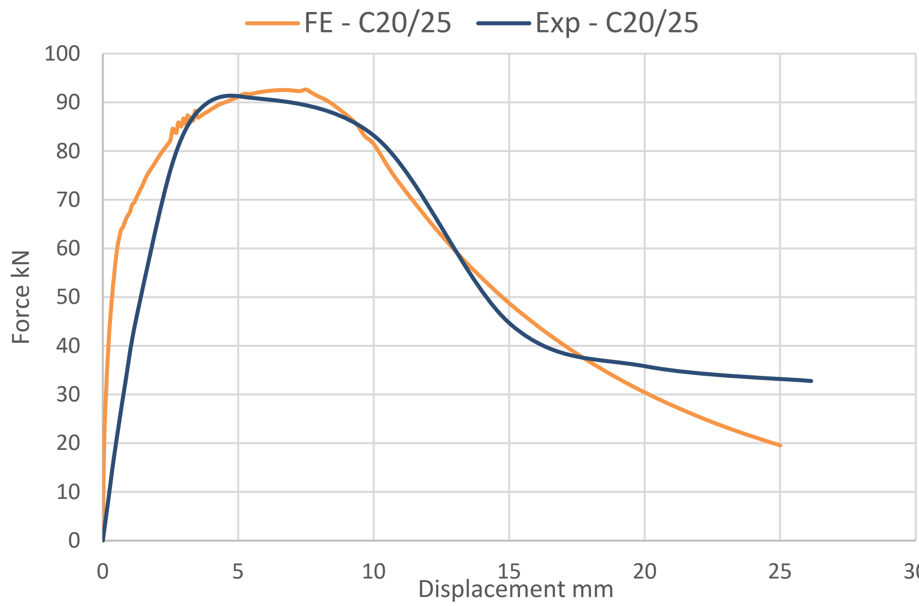

Figure 7.8 - S10 FE Microplane and the experimental force-displacement results

Figure 7.9 shows the force-displacement graph for the B6 sample. The initial stiffer behaviour of the FE model is due to the same reasons as the B10 and S10 models, and the ultimate load for both FE and the experimental curve is about 100 kN. The softening behaviour of the FE model is linear gradual from 100 to 70 kN at a rate of 4.2 kN/mm. However, the experimental curve shows a two-stage softening of the concrete. From 100 to 20 kN the curve shows an almost linear softening behaviour at a faster rate of about 3.6 kN/mm after which it levels off at about 20 mm.

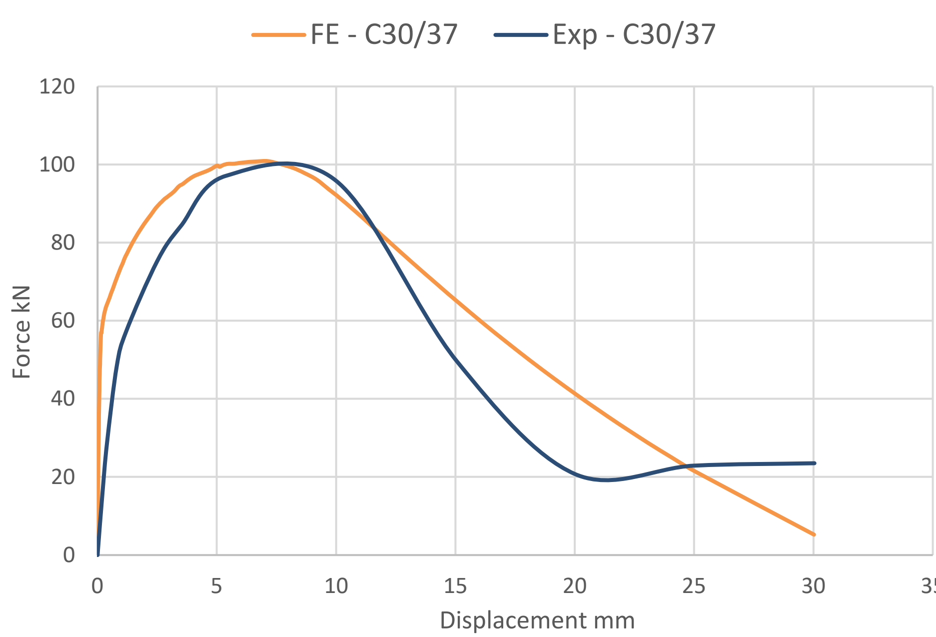

Figure 7.9 - B6 FE Microplane and the experimental force-displacement results

7.6.2. Pushover and hysteresis

Figures 7.10 (a), (b) and (c) show load-displacement graphs for hysteresis response of FE and experimental specimens up to 20 mm for B10, S10 and S6 samples, respectively. Above 20 mm the wall is significantly damaged and it is outside the scope of the FE model.

The behaviour of the FE pushover model corresponds well with the envelope of the specimens' hysteresis response. The peak performances are underestimated by 7, 4, and 2 per cent by the FE for B10, S10 and S6, respectively. Also, it can be seen that the FE results take into account the strain-softening behaviour of the samples.

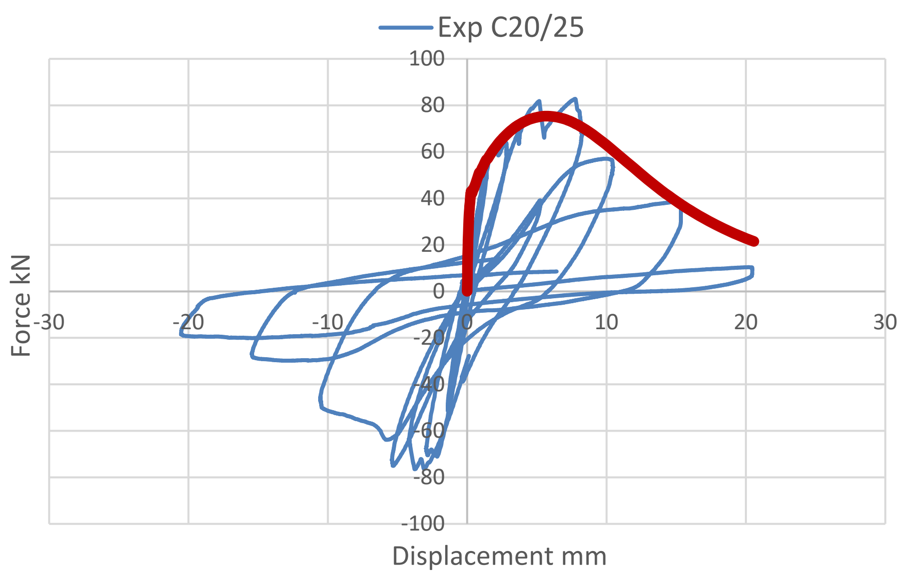

Figure 7.10 (a) - B10 experimental hysteresis response and FE Pushover results

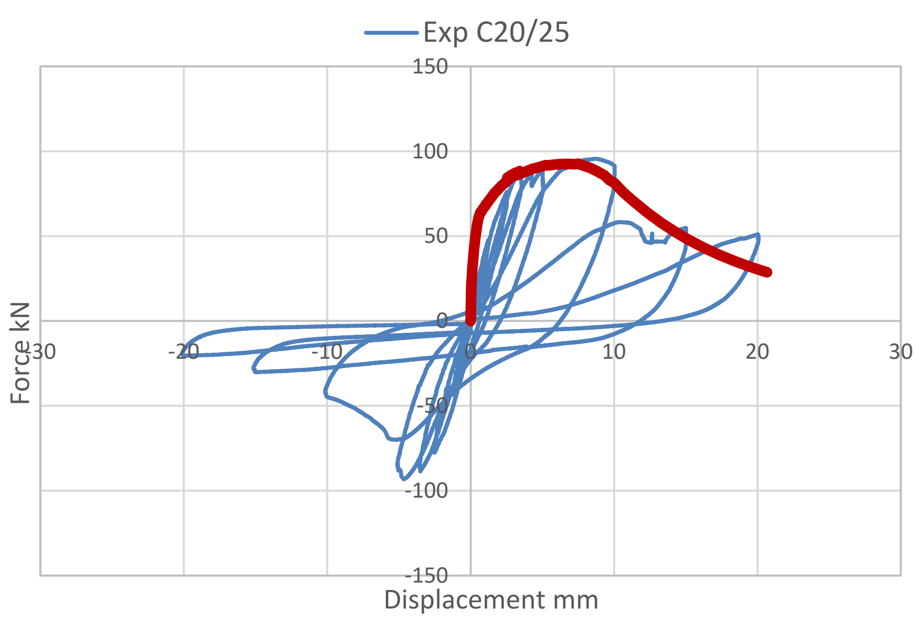

Figure 7.10 (b) - S10 experimental hysteresis response and FE Pushover results

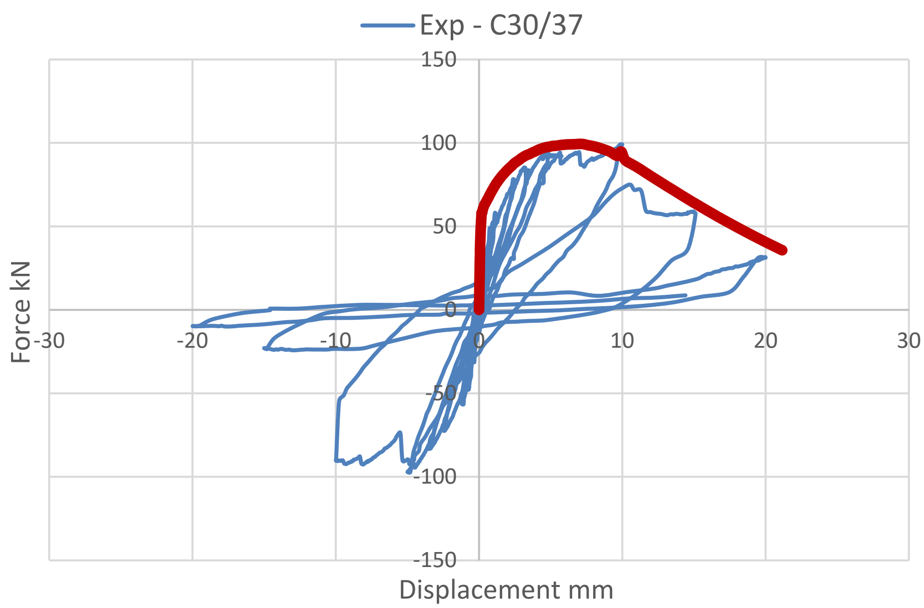

Figure 7.10 (c) - B6 experimental hysteresis response and FE Pushover results

7.7. Parametric studies

After the validation of the finite element results, the models were utilised for further parametric studies. Figure 7.11 below shows the force-displacement graph of 0-100 kN and 0-35 mm for the B10 model. Four concrete strengths (C20/25, C30/37, C40/50 and C50/60) were used as a varying parameter to study the effect of the possible design strengths on the overall capacity of the walls. The curve shapes follow the same pattern; however, the peak capacity increase from 75 to 90 kN at an increment of about 5 kN for each class of concrete.

Although the parametric study is becoming more common in FEA and can be used as a potential tool to evaluate the effect of design changes relatively quickly, cautions need to be taken in the utilisation of such “extrapolated” data for scientific purposes where a more thorough methodology like a validation of each model with actual experimental data might be essential.

The estimation of the influence of the strength of concrete as a varying parameter is obtained on basis of extrapolation within limited practical interval outside the existing data. Potential interpolation using additional experimental results for verifying the obtained characteristics can be conducted in the future.

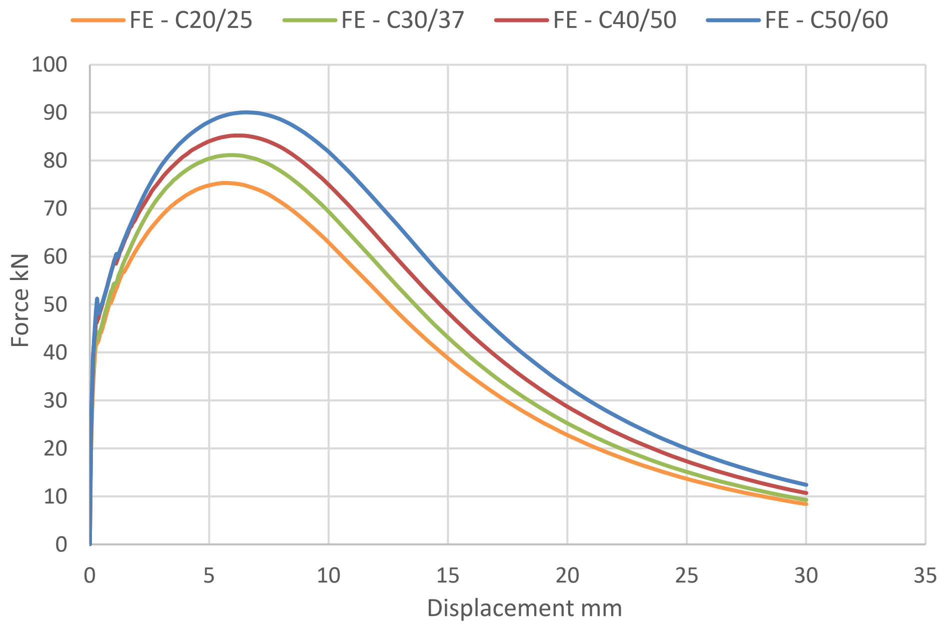

Figure 7.11 - B10 parametric studies for different strength classes of concrete

Force-displacement graph from 0 to120 kN and 0 to 30 mm for the S10 model can be seen in Figure 7.12 below; three classes of concrete were tested in addition to the strength class corresponding to the experimental concrete class. The shape of the curves follows similar patterns; however, the peak capacity increases from 91 to 110 kN. The increase is at an increment of about 7 kN for each strength class of the concrete.

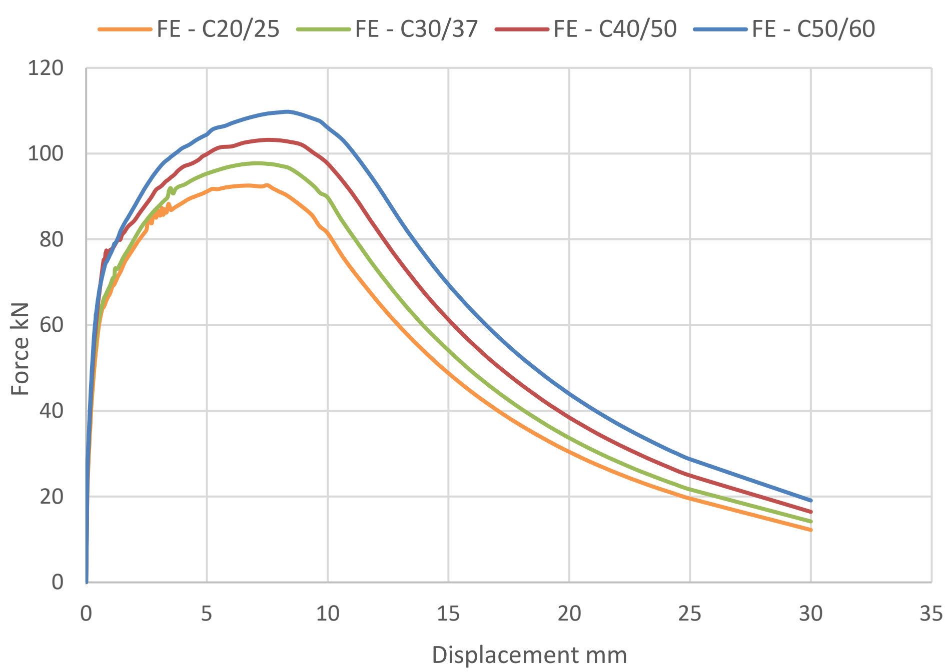

Figure 7.12 - S10 parametric studies for different strength classes of concrete

Figure 7.13 shows the force-displacement graph (0 to 120 kN against 0 to 30 mm) for the B6 model. Three strength classes of concrete were tested in addition to the strength class corresponding to the experimental specimen concrete. The shape of the curves follow similar patters; although, the peak of the capacity increase from 93 to 113 kN. The increase is at an increment of about 7 kN for each strength class increase.

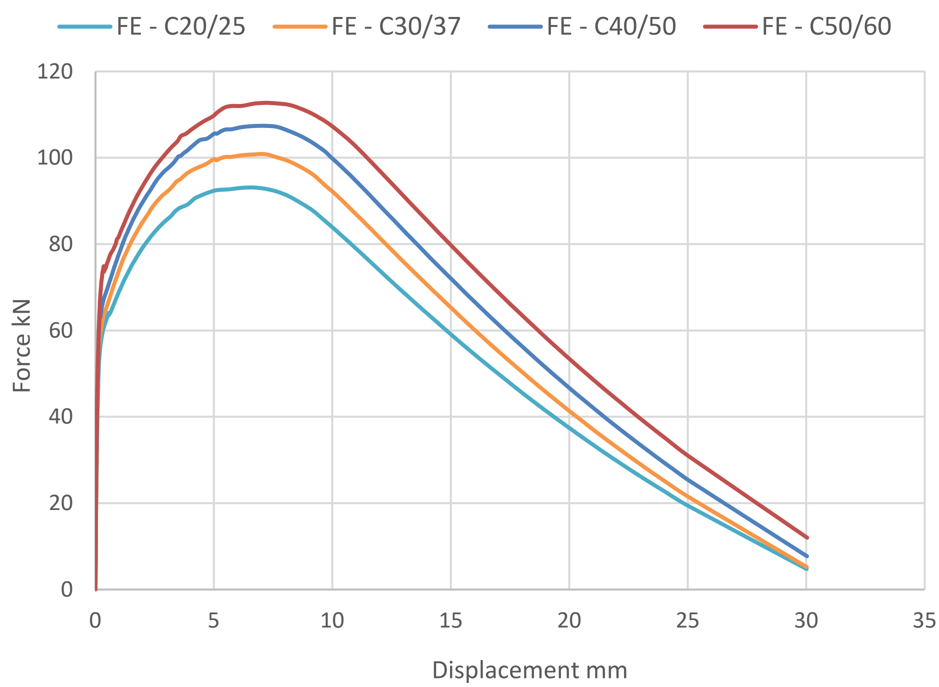

Figure 7.13 - B6 parametric studies for different strength classes of concrete

7.8. Chapter Conclusions

From the results of the model’s pushover analysis following conclusion can be made:

- There is a good correspondence between FE and experimental results for the Microplane model with the existing capabilities of the material models.
- The Microplane model can simulate the ultimate performance and the strain-softening behaviour of the specimens under pushover analysis.
- The parametric studies resulted in clarification of the process of increasing the capacity of BFRP and steel-reinforced shear walls when the strength of the concrete is increased.

Overall the finite element method using the Microplane model can be successfully applied in modelling the behaviour of the RCSW and conducting parametric studies.

8. Results Discussions

The thesis has two main parts, including the experimental researches and finite element modelling. The result of each part is discussed, and conclusions are made for the utilization of FRP reinforcement for the concrete shear wall. The experimental part includes a pilot study and three other inclusive groups of samples, the results of which are compared for FRP and steel. Shear walls FE models are developed and validated using experimental results; therefore, relevant discussions are made about each part in the sub-chapters below.

8.1. Experimental Results Discussion

The experiments were completed successfully on four groups of shear walls each group containing samples reinforced with FRP as well as traditional steel reinforcement as a control-sample. The first group was a pilot study to design and develop the specimens for the experiments. The groups two to four results were successfully obtained, evaluated and analysed using charts and graphs.

Group two had two samples with higher strength of concrete; group three had three samples with anchorage added to the vertical reinforcement bars and group four had three samples with higher diameter reinforcement than group two and three. Group three and four had the same, but group two had a higher strength of concrete.

To be able to see the effects of ground motion histories on the shear walls modified ATC-24 protocol of reversed cyclic loading was adopted as once cycle per displacement amplitude. The cracks, hysteresis graphs, load-displacement graphs, minimum and maximum points, energy dissipation and cumulative energy dissipation graphs were obtained for each group of samples.

The cracks started to develop between displacement amplitudes of 0.8 and 10 mm for all samples. All FRP reinforced samples started to crack at 1.2 mm displacement (except B6 which began at 0.8 mm), and all steel-reinforced samples started to crack 2.5 mm displacement amplitude due to lower modulus of elasticity in FRP rebars resulting in less stiff samples.

Lateral load – top displacement hysteresis response loops for all groups are close to each other with a high peaking load for a displacement of up to 10 mm except the BA10. The BA10 has a peaking load of 5 mm displacement only, as a result of 10 mm diameter rebars and anchorage added to the vertical rebars causing a high stiffness and earlier failure of the sample. All sample show lower max/min load loops at displacements higher than 10 mm amplitudes due to residual forces after samples crushing. The residual forces were due to rebars interlinking the sample along the critical horizontal crack.

Maximum and Minimum Point of the hysteresis in all the groups shows a higher and quicker peak for steel followed by a sharper fall than the FRP samples due to higher Young Modulus and lower Yielding-Strength of steel reinforcements. The difference between the Maximum and Minimum Points at the same displacement amplitude is due to the attachment of the loading jack at one side.

Average Maximum and Minimum Points in all groups show a higher average for the steel than FRP reinforced samples. In group two steel has 5%, in group three over 20% and in group four over 10% average than FRP reinforced samples. The difference is the highest in anchored samples and the lowest in higher strength concrete. All samples show a steeper graph post-peak values for steel than FRP samples due to lower Yield-Strength of steel than Ultimate-Strength of FRP.

ED in all groups for the steel than FRP reinforced samples due to higher young’s modulus and a good grip of steel rebars to concrete. In group two over 15% in group three, it is over 25%, and in group four it is over 10% higher. The fall in ED is sharper steel than FRP samples due to lower Yield-Strength of steel than Ultimate-Strength of FRP. ED for Steel reinforced samples fall below FRP for group two and three but not in group four because the latter has a larger diameter steel reinforcement, i.e. not yielding as soon as the earlier groups.

The CED in all groups shows an almost linear behaviour for FRP than steel-reinforced samples after initial elastic behaviour up to 3.5 mm displacement amplitude where all sample behave similarly except BA10 due to earlier crushing as a result of over-stiffness caused by the addition of anchorage to rebars. The graphs of steel-reinforced samples in groups two and three show an initial rise in higher rate due to higher young’s modulus in steel rebars followed by a gradual increase in a lower rate almost similar to a horizontal line after yielding of steel rebars falling below BFRP reinforced graphs at about 80% CED. In group three, the steel sample shows a more linear-like behaviour without CED decreasing rate as a result of the larger diameter of reinforcements not yielding.

8.2. FE Modelling Results Discussion

The simulations were completed successfully with two types of concrete material model, including Solid65 and Microplane model. The Solid65 model was tested under reversed cyclic load, and the Microplane model was monotonic pushover condition per modified ATC-24 loading protocol.

Ansys Workbench is used in this study which has a greater potential of modelling structural elements than classic Ansys APDL typically employed by researchers. New areas such as innovative rebars and a new structural element are modelled with unique mesh sensitivity, complex support conditions and convergence criteria. Coding is used for defining the model's behaviours and characteristics which has the benefit of unlimited ways of defining properties not restricted by the GUI.

Although Solid65 has been predominantly used in research to simulate the behaviour of reinforced concrete, this investigation explores the model further. The hysteresis response of the material model in combination with the utilisation of FRP material as reinforcement bars and the bond interaction between the concrete and the rebar have been taken into account. So the development of an RCSW model with the above characteristics would be an important contribution to the scientific knowledge.

The concrete Microplane model is a relatively new material model in the library of Ansys and has not been widely utilised in modelling of the concrete structural components. Such a model in combination with several inherent potential capabilities such as ease of geometric drawing and application of almost any type of loading histories would be another step forward expanding the "model making" knowledge.

Both Solid65 and Microplane models were tested with steel and FRP reinforcements. The interface element representing the bond-slip behaviour for the Solid65 model was Combin39 nonlinear spring element, and for the Microplane model, it was Combin40.

The models were validated with experimental results, and parametric studies are conducted examining the effects of different classes of concrete strength on the behaviour of analytical models. The results show a gradual increase in performance of both Solid65 and Microplane models with increasing strength of the concrete.

For verification purpose, all the theories behind the elements were examined using the help systems documentations in Ansys. The parameters affecting the behaviour of the model were all tested, including but not limited to the:

- Elements and element's key-option,
- Material model parameters and real constants,
- Loading steps and substeps, number of iterations,
- Bond-slip mechanism and contact formulations,
- Meshing density and quality,
- Boundary conditions, such as loading and fixing,
- Solver settings such as weak spring, large deflection and solver pivot.

The material models for the concrete was one of the most impacting factors in the behaviour of the models. Different material models were tested before selecting Solid65 and Microplane model for the representation of the behaviour for the hysteresis and pushover analysis, respectively.

The Solid65 material model was able to capture the hysteresis response of the until failure point of the model; additionally, the cracking pattern observed in the experimental specimens were captured by Solid65. The material model for the concrete is based on the TB,CONCR for defining cracking, crushing strength of the and TB,MISO which defines the stress train behaviour of the concrete.

The crushing strength of concrete was taken from the average of uniaxial compressive tests conducted on the concrete cube and cylinders. Cracking defined as the coefficient of the shear strength for Solid65 was taken 0.2 and 0.8 for open and closed cracks, respectively. The outcome of the analysis varies relative to the selection of the coefficient so, considerable experience is required for the selection of these values; additionally, the values can be adjusted until the behaviour of the model corresponds to the experimental specimens. When verifying the analysis result with experiments, the aforementioned coefficients were selected to model the behaviour of the RCSW.

Strain softening effects of the specimens were modelled using the Microplane model for concrete under pushover analysis. The Microplane material model uses a constitutive equation (such as stress-strain at the Microplane level) and the homogenisation process to draw an overall material response. Damage constants were approximated based on the invariants of the strain tensor, and the damage parameters were verified based on the behaviour of the model corresponding with experimental specimens. The damage thresholds were 3.8e-5, 2.8e-5, 2.7e-5 and the rate of damage evolution were 30, 25, 10 for the B10, S10 and B6 model respectively. The maximum damage parameter was taken as 1 for all samples which take all the strain-softening behaviour into account. The Microplane model was able to capture the strain-softening behaviour of the concrete, which represents the post-peak behaviour of the RCSW.

Modelling and validation of hysteresis response of an FRP RCSW are attempted by Mohamed et al. (2014) up to failure point, but no strain-softening for post-peak behaviour of the specimens are modelled. Belletti et al. (2017) modelled and validated the hysteresis response of RCSW but not with FRP reinforcement. The later has used his own developed material model subroutine (PARC_PL 2.0) in Abaqus using shell elements and smeared fixed crack approach. The reason behind creating a personal subroutine is the lack of the existence of suitable material models to simulate the hysteresis response of the concrete in Abaqus. Several researchers attempted to write a concrete hysteresis response material model theoretically, for example, Aslani and Jowkarmeimandi (2012) developed their own material model in Abaqus UMAT for hysteresis response of concrete under monotonic and cyclic loading. The later has verified his material model using results of experimental tests in the literature.

Since Ansys mechanical has the legacy element Solid65 and Microplane models in its material library to be used for the concrete and other brittle materials like concrete, both material models were used in this study. Solid65 was able to capture the hysteresis response of the concrete until the failure point but not beyond the peak strength of concrete because the elements lose their stiffness once their ultimate strength is reached reducing the stiffness matrix to zero. Hence the load-displacement observed in the modelling will show a sudden drop to zero after the peak performance, which means no strain-softening effects of concrete is taken into account. This deficiency and pathological mesh-sensitivity of the Solid65 is the reason for developing the Microplane model for concrete in the Ansys library of materials (Zreid and Kaliske, 2018). Therefore the Microplane model is used to see the strain-softening results of the model under compression loads. There are three types of Microplane models in the library of Ansys mechanical, including elastic regularized, elastic non-regularized and coupled damage plasticity. The regularization is used when there is instability in the solution of the stiffness matrices for the model. However, the non-regularized model can be used when the results converge well without the regularization of non-local parameters. There was no need to use a non-local parameter for convergence of results in this study, and the coupled damage plasticity model exhibited higher force-displacement values than the experimental results. The best confirming results with the experimental behaviour was from the result of the analytical model incorporating the non-regularized elastic Microplane model. The Microplane model is capable of capturing the strain-softening effects of concrete under the monotonic load of pushover analysis highly corresponding with the experimental specimens' behaviours. The later material model shows an initial stiffness in the force-displacement graph in comparison to the experimental results which will not reduce with increasing the number of substeps/reducing the size of time steps as well as adjusting the start and rate of damage evolution parameters. The initial stiffness discrepancy can be adjusted in the material model by the Ansys developer in the revised versions of the product in future hopefully looking into the frequency of revision of the product in recent years.

9. Conclusions and Recommendations.

In accordance with the aim and objectives of this project twelve medium-scaled specimens reinforced with FRP and steel rebars are made and tested under seismic loading protocol. The effects of different types of FRP reinforcement and anchorage on the behaviour of the specimens were assessed during the experiments.

Analytical shear wall models with FRP and steel reinforcements were developed and crack generation patterns were compared with experimental results. Finally, parametric studies were conducted on the behaviour of FE calibrated models.

The conclusions are divided into two sections including the experimental and analytical parts. Sections 9.1 and 9.2 give the conclusion for the experimental and the analytical parts, respectively. Section 9.3. provides some contribution of the work in the knowledge body and section 9.4. provides few recommendations for the future works in the area.

9.1. Experimental conclusions.

Based on the results of the twelve medium-scale experimental samples divided into the four groups the following conclusions can be drawn:

Group one:

- The pilot studies (PS) resulted in the specimen's design improvement.
- The PS improved the experimental test setup and sample's instrumentation.

Generally, a PS is very effective to obtain optimum specimens' design, test setup and instrumentation for the investigations.

Group two:

- The hysteresis loop peak values (HLPVs) for B6 are lower than S6 due to the higher deformability of FRP and more intensive development of cracking in concrete.
- The S6 HLPVs fall faster after 5 mm amplitude displacement due to steel rebars yielding and breaking but B6 HLPVs gradually fall after 5 mm due to B6 rebar-concrete bond-slip.
- The S6 HLPVs are regaining increased reading due to frictional force and aggregate interlocking after sample splitting into two and acting like a mechanism.
- The B6 residual HLPVs after 20 mm is due to rebar-concrete friction-forces after bond-slip.
- The S6 average maximum and minimum points (AMMP) curve show a steep fall after 5 mm amplitude due to steel rebars yielding and breaking.

- The B6 average AMMP curve shows a gradual fall after about 8 mm amplitude due to rebar-concrete bond-slipping.
- The B6 ED and CED show a slower rise than S6 due to steel-rebars higher elasticity-modulus.
- The S6 ED indicate a sharper fall below B6 after about 13 mm amplitude due to steel rebars yielding and breaking.
- The S6 CED rise faster until about 11 mm displacement after which it levels off going below B6 after about 16 mm amplitude.
- The B6 shows a more gradual and constant CED rise than the S6 sample.

Generally the group two results show slightly lower force-displacement and energy dissipation for BFRP than the steel-reinforced sample. The results are promising as an initial pace for utilisation of BFRP as an alternative to the traditional steel reinforcement in RCSWs.

Group three

- The HLPVs for BA6 were lower followed by GA6 and SA6 due to higher deformability of FRP and more intensive development of cracking in concrete followed by GA6 and BA6.
- The SA6 averaged maximum and minimum points (AMMP) curve peak is about 30% higher than SA6 and BA6. SA6 fall is faster after 5 mm displacement while BA6 and GA6 falls are gradual after 3 mm.
- The BA6 and SA6 show a similar averaged AMMP curve. BA6 and SA6 residual capacity is higher than SA6 after about 13 mm amplitude.
- The BA6 and GA6 ED fall about 29% lower than SA6. At about 13 mm amplitude SA6 ED falls below BA6 and GA6. BA6 and GA6 show similar ED.
- The BA6 and GA6 CED curves are closer to linear than SA6. The SA6 CED rise above GA6 and BA6 at about 5 mm displacement. The SA6 CED falls below BA6 and getting close to GA6 at about 16 and 21 mm, respectively.

Generally, the FRP reinforced samples peak values are lower but in close range to the steel-reinforced sample. The addition of the anchorage to the rebars prove not to be effective therefore, a different type of rebar anchorage can be recommended for future investigations.

Group four

- The B10 HLPVs are lower than S10 due to higher deformability of FRP and more intensive development of cracking in concrete. BA10 HLPV is the lowest due to the earlier failure of the anchorage in the sample.

- The B10 and BA10 averaged maximum and minimum points (AMMP) curve is about 20% and 25% lower than S10, respectively. The B10 AE fall is more gradual than S10. BA10 AMMP curve fall is quicker than S10 and B10 due to an early failure of the anchorage in the sample.
- The B10 ED is about 30% less than S10. The BA10 ED is significantly lower due to earlier failure of the anchorage in the sample.
- The B10 and S10 CED have a gradual rise. B10 have about 13% lower CED than S10. BA10 CED is about 30% less than S10.

Generally, the peak values of the BFRP reinforced samples are lower but in close range to the steel-reinforced samples. The addition of anchorage to the rebars in this specific case is not effective therefore further investigation using different types of anchorage to BFRP rebars is recommended.

Overall, the result shows a promising prospect for utilisation of the BFRP and GFRP rebars as reinforcement in shear walls under cyclic load. The bond strength between concrete and FRP was one of the governing parameters affecting the behaviour of the samples so the recommendation is to be considered as one of the major elements in the design of RCSWs.

9.2. Modelling Conclusions.

The modelling results are presented in chapter six and seven for the Solid65 and Microplane models respectively. The conclusion for each of the chapters is presented below:

The Solid65 model

- There is a good correspondence between FE and experimental results for the Solid65 with the existing capabilities of the material models.
- The Solid65 model can capture hysteresis response until the influence of the degree of damage becomes more pronounced, at the indicated intervals.
- The model can predict the peak performance and capture the cracking patterns developed by the experimental specimens.
- The parametric studies resulted in clarification of the process of increasing the capacity of BFRP and steel-reinforced shear walls when the strength of the concrete is increased.
- Analytical expressions reflecting the process of increase of the strength are offered.

Overall the finite element method can be successfully applied in modelling the behaviour of the RCSW and conducting parametric studies.

The Microplane model

- There is a good correspondence between FE and experimental results for the Microplane model with the existing capabilities of the material models.
- The Microplane model can simulate the ultimate performance and the strain-softening behaviour of the specimens under pushover analysis.
- The parametric studies resulted in clarification of the process of increasing the capacity of BFRP and steel-reinforced shear walls when the strength of the concrete is increased.
- The parametric studies show that FE C50/60 model has about 20% higher ultimate strength than FE C20/25 model.

Overall the finite element method using the Microplane model can be successfully applied in modelling the behaviour of the RCSW and conducting parametric studies.

Currently, there is a relatively small number of models developed for RCSW under quasi-static reversed cyclic loading using Solid65. Therefore, this research is a step forward in the modelling or FRP RCSWs using Solid65 in Ansys Workbench.

Additionally, there is a lack is of sufficiently developed models using the Microplane concrete material model in Ansys for such elements. Therefore, this research studied a relatively new approach in the modelling of RCSWs using the Microplane theory.

9.3. Contributions to the knowledge

Some knowledge contributions are to the body of the knowledge are outlined below:

- Significant number of bars during the process of testing are developing bond slip behaviour which allows more gradual destruction and keeping significant residual capacity for such types of BFRP RCSWs walls at high levels of displacement.
- Mixed mode of destruction for the BFRP RCSWs has been discovered as combination of breaking and bond-slip movement of the FRP bars, which allow for potential increase of capacity via improving of the anchorage.
- Initial suggestion about the connection between the strength of the concrete and capacity of the BFRP RCSWs is developed on basis of FE modelling. Further confirmation of obtained results will be developed via additional experiments.
- The utilisation of the Microplane theory for investigation of PO effect in FRP RCSWs proved to be effective.

9.4. Recommendations

A set of medium-scale samples were tested and the result of three samples was modelled using two methodologies for modelling the behaviour of FRP and steel RCSWs. The result of the experiments and modelling show that FRP RCSWs have lower but close force-displacement and energy dissipation to steel RCSWs. The effect of anchorage is also considered for some of the samples. Further research in the following area can be conducted to expand the knowledge base on the behaviour of FRP RCSWs under seismic loading:

- Further experiments can be carried out using higher strength concrete.
- Additional research can be conducted using Carbon and Aramid FRP as rebars.
- More studies can be done investigating the deformation of the surface of the FRP rebars, which affects the bond strength.
- Future research can include FRP rebars with a different type of anchorage.
- Using a large-scale model could be beneficial for a final comparison of the results.

Parametric study results for higher strengths of concrete can be used as preliminary estimated results if samples with higher concrete strengths are used.

In this study, BFRP and GFRP RCSWs were tested. There are other types of FRP rebars such as Carbon and Aramid rebars that can be used to complete the investigation of FRP rebar types commercially available.

The surface deformation for the BFRP and GFRP rebars were sand coated and helical recess, respectively. There are FRP bars with different surface deformation commercially available the effect of which can be assessed to compare with results of this study.

The samples used in this study were all medium scale samples. It would be interesting to see the results of larger-scale samples and compare the outcomes with existing results.

References

ACI-318, (2008) “Building Code Requirements for Structural Concrete”, Reported by ACI Committee 318, *ACI 318-2008*, American Concrete Institute, USA

ACI-440 (2006) “Guide for the Design and Construction of Structural Concrete Reinforced with FRP Bars”, Reported by ACI Committee 440, *ACI 440.1R-06*, American Concrete Institute, USA.

ACI-440 (2015) “Guide for the Design and Construction of Structural Concrete Reinforced with FRP Bars”, Reported by ACI Committee 440, *ACI 440.1R-15*, American Concrete Institute, USA.

Akis T. (2004) “Lateral Load Analysis Of Shear Wall-Frame Structures”, PhD Thesis, The Middle East Technical University, Ankara, Turkey.

Ansys help systems (2020), Ansys Mechanical, Ansys Inc., 2600 ANSYS Drive, Southpoint Canonsburg, PA, USA

Ansys Meshing Solutions (2019), Platform, Products, [https://www.ansys.com/products/platform/ansys-meshing, accessed on 28 March 2019]

Aslani, F. and Jowkarmeimandi, R. (2012) “Stress–strain model for concrete under cyclic loading” *Magazine of Concrete Research*, 2012, 64(8), 673–685

ATC-24 (1992) “Guidelines for Cyclic Seismic Testing of Components of Steel Structures”, Applied Technology Council, Redwood City, CA, USA.

ATC-40 (1996) “Seismic Evaluation and Retrofit of Concrete Buildings”, Volume 1, Applied Technology Council, Redwood City, CA, USA.

Bangash, M. Y. H. (1989) “Concrete and Concrete Structures: Numerical Modelling and Applications”, *Elsevier Applied Science*, London, United Kingdom.

Baetu S. and Ciongradi I. (2011) “Nonlinear finite element analysis of reinforced concrete slit walls with ANSYS” Bulletin of the Polytechnic Institute of Jassy.

Belletti, B., Scolari, M., and Vecchi, F. (2017) "PARC_CL 2.0 crack model for NLFEA of reinforced concrete structures under cyclic loadings", *Computers and Structures*, 191 (2017) 165–179

Bilotta, A. et al. (2011) "Bond Efficiency of EBR and NSM FRP systems for strengthening of concrete members", *Journal of Composites for Construction*, ASCE, October 2011.

Bilotta, A., Scolari, M., Vecchi, F. (2011) "Experimental Bond Tests On Concrete Members Strengthened With NSM FRP Systems: Influence Of Groove Dimensions And Surface Treatment", *Proceedings of 6th International Conference on Composites in Civil Engineering (CICE),* Rome, Italy, 13-15 June 2012.

Bora, C. et al., (2007) "Development of a Precast Concrete Shear-Wall System Requiring Special Code Acceptance", *PCI Journal*, 52(1), pp 122-135, January-February 2007.

Brown, L.V. and Feeser K.W. (2005) "Guide Examples for Design of Concrete Reinforced with FRP Bars", *SP-230—53, FRPRCS-7*, [www.quakewrap.com , accessed on 14 September 2014].

BS EN 1992-1-1:2004 (2004) "Eurocode 2: Design of concrete structures - Part 1-1: General rules and rules for buildings", Brussels, Belgium.

CADFEM (2015) "Reinforced Concrete Modelling with Ansys Mechanical", CADFEM, [www.cadfem-cis.ru , google translated page, accessed on 25 Nov 2019]

Chen, Z. Y., Chui, Y. H., C. Ni, Doudak, G., Mohammad, M., (2013) "Influence of diaphragm flexibility on lateral load distribution between shear walls in light wood frame buildings", *WIT Transactions on the Built Environment*, Volume 132, 2013.

Cortes-Puentes L.W. and Palermo D. (2011) "Modelling seismically repaired and retrofitted reinforced concrete shear walls", Computers and Concrete, Vol. 8, No. 5 (2011) 541-561.

Chittiprolu R., Kumar, P.R., (2014), "Significance of Shear Wall in High Rise Irregular Buildings", *International Journal of Education and Applied Researches*, Vol. 4, Iss. 2.

Choi, K.H., Choi, C.Y., Lee, H.L. and Choi, S.C. (2008) "Retrofitting of Shear Walls in Different Methods", *14th World Conference on Earthquake Engineering*, Beijing, China.

Core Skills – Module 1 (2019) "Introduction to Ansys Meshing", *Release 2019 R2*, Ansys Learning Hub 2019 [https://www.ansys.com/services/learning-hub, accessed on March 2020].

Cruz-Noguez, A.C., Lau, T.D. and Sherwood, E. (2012) "Testing and Anchor System performance of RC Shear Walls Repaired and Strengthened with Externally-Bonded FRP Sheets", *15th World Conference on Earthquake Engineering*, Lisbon, Portugal.

Dan, D. (2012) "Experimental Tests on Seismically Damaged Composite Steel Concrete Walls Retrofitted with CFRP Composites", *Engineering Structures*, Volume 45, December 2012, Pages 338-348

Demeter, I., Nagy-Gyorgy, T., Valeriu, S., Daescu A.D., Dan, D. (2009) "Seismic Retrofit of Precast RC Wall Panels with Cut-Out Openings Using FRP Composites", *FRPRCS-9*, Sydney, Australia.

Design Manual (2007) "Reinforcing Concrete Structures with Fibre Reinforced Polymers", Intelligent Sensing for Innovative Structure Canada Research Network, *Design Manual No. 3*, Version 2, September 2007, Canada.

Devarshi, A.S. and Tande N.S. (2014) "Diaphragm Flexibility in Buildings with Shear Walls", *International Journal of Latest Trends in Engineering and Technology*, Vol. 4, Issue 1, May 2014.

Di, B.; Wang, J., Li, H., Zheng, J., Zheng, Y.; Song, G. (2019) "Investigation of Bonding Behavior of FRP and Steel Bars in Self-Compacting Concrete Structures Using Acoustic Emission Method", *Sensors*, 19, 159

Duggal, S.K. (2013) "Earthquake Resistant Design of Structures", 2nd Edition, Oxford Higher Press, India.

Dyavappanavar P.S., Shashikiran.D.C, Satwik.T.S, Vishnukumar.N, Jamkhani S. (2017) "Seismic analysis of Shopping Complex with Shear walls and Bracings using ETABS", *International Journal of Innovative Research in Science, Engineering and Technology*, Vol. 6, Issue 6.

Earthquake Tip 23, "Why are Buildings with Shear Walls preferred in Seismic Regions", Learning Earthquake Design and Construction [www.iitk.ac.in accessed on 14 August 2014].

Eggert, G. M., Dawson, P. R., and Mathur, K. K. (1991) "An Adaptive Descent Method for Nonlinear Viscoplasticity", *International Journal for Numerical Methods in Engineering*. Vol. 31, Pages 1031-1054.

El-Kashif O.F.K., Adly K.A., Abdalla A.H. (2019) "Finite element modeling of RC shear walls strengthened with CFRP subjected to cyclic loading", *Alexandria Engineering Journal*, Vol. 58, Pages 189-205

Ellobody E., Feng R., Young B. (2014) "Chapter 2 – Review of the General Steps of Finite element Analysis, *Finite Element Analysis and Design of Metals"* Pages 15-13.

Elnashai, S.A., Sarno, D.L. (2008) "Fundamentals of Earthquake Engineering", John Wiley and Sons Publication, USA.

El-Sokkary, H. and Galal, K. (2012) "Cyclic Tests on FRP-Retrofitted RC Shear Wall Panels", *15th World Conference on Earthquake Engineering,* Lisboa, Portugal

Engineered Composites (2019) "GRP Pultruded Rebar Specification", Engineered Composites Ltd, Unit B4, Border 2 Industrial Park, River Lane, Saltney, Chester, UK

EP Structural Adhesive, (2019) "Moisture-tolerant epoxy adhesive for structural bonding application", Weber Saint-Gobian, [https://www.uk.weber accessed on 05 June 2019].

Fahjan M. Y., Kubin J. and Tan T.M. (2010) "Nonlinear analysis method for reinforced concrete buildings with shear walls", 14 ECEE European Conference on Earthquake Engineering, 30 August - 3 September 2010, Ohrid, Macidona.

FEMA-273 (1997) "NEHRP Guidelines for the Seismic Rehabilitation of Buildings", Federal Emergency Management Agency, USA.

FIB (2001) "Externally Bonded FRP Reinforcement for RC Structures, Bulletin No. 14", *Technical Report Prepared by a Working Party of Task Group 9.3*, Federation Internationale du Beton (FIB), Lausanne Switzerland.

FIB (2007) “FRP Reinforcement of in RC Structures, Bulletin No. 40”, *Technical Report Prepared by a Working Party of Task Group 9.3*, Federation Internationale du Beton (FIB), Lausanne Switzerland.

FIB (2008) “Structural Connections for Precast Concrete Buildings, Guide to Good Practice”, *FIB Bulletin No. 43*, Federation Internationale du Beton (FIB), Lausanne Switzerland.

Gay, D., Hoa, S.V. and Tsai, S.W. (2003), “Composite Materials. Design and Applications”, CRC Press, Boca Raton.

Gere, J.M. (2003) “Mechanics of Material (6th edition)”, Thomson Engineering, Belmont, CA, USA.

Ghosh, S.K. (2002) “Seismic Design Provisions in U.S. Codes and Standards: A Look Back and Ahead”, *PCI Journal*, Jan-Feb 2002.

Ghosh, S., and Kharmale B.S. (2010) “Research on steel plate shear wall: past, present and future, structural steel and castings”, Nova Science Publishers Inc., Hauppauge, USA Pages 57-106

Greeshma S., Jaya K.P. and Sheeja L.A. (2011) “Analysis of flanged shear wall using Ansys concrete model”, *International Journal Of Civil And Structural Engineering.* Vol. 2, No. 2.

Groot, de, R., Haan, de, Y. M., Dop, G. J., Peters, M. C. R. B (1987). “Failure stress criteria for composite resin”, *Journal of Dental Research*, Vol. 66, Iss. 12, Pages 1748-1752.

Guadagnini, M. et al., (2011) “Design Guidelines for FRP Reinforced Concrete Structures”, *Proceedings of the Institution of Civil Engineers - Structures and Buildings*, Vol. 164, Issue SB4, Pages 255-263, August 2011.

Guevara-Perez, T.L. (2012) “Soft-Story” and Weak-Story in Earthquake Resistant Design: A Multidisciplinary Approach”, *15th World Conference on Earthquake Engineering*, Lisbon, Portugal.

Hajjar F.J., Roeder W.C., and Sabelli R. (2013) “Seismic Design of Steel Special Concentrically Braced Frame Systems”, *NEHRP, Seismic Design Technical Brief No.8*, USA.

Harish A. (2020a) “Finite Element Method – What Is It? FEM and FEA Explained”, SimScale, [www.simscale.com, accessed on 10 April 2020]

Harish A. (2020b) “How to Choose a Solver for FEM Problems: Direct or Iterative”, SimScale, [www.simscale.com, accessed on 5 May 2020]

Haverland G. (2012), “Concrete Futures Part 1: PREcast Seismic Structural System, Video Published by Cement and Concrete Association of New Zealand, [www.youtube.com accessed on 1 September 2014].

HAZUS (2003) “Multi-hazard Loss Estimation Methodology, Earthquake Model”, HAZUS MR4.Technical Manual, FEMA & NIBS, Mitigation Division, Washington DC., USA.

Hoshikuma J., Kawashima K., Nagaya K, Taylor AW. (1997) “Stress-strain model for confined reinforced concrete in bridge piers”. *Journal of Structural Engineering*, ASCE 1997, Vol. 123 Iss. 5, Pages 624-33.

Hosseini, M., Rao R.V.A. (2017) “Earthquake analysis of high rise buildings with effect of box shape RC shear walls at the center, *International Journal of Engineering and Advanced Technology*, Vol. 7, Iss. 2.

Hsiao P.F., Wang, C.J. and Chiou Y.J. (2008) “Shear Strengthening of Reinforced Concrete Framed Shear Walls Using CFRP Strips”, 14th *World Conference on Earthquake Engineering,* Beijing, China.

Huang, T., Lu, L.W., and Nakashima, M. (1984) “Effect of Diaphragm Flexibility on Seismic Response of Building Structures”, *Proceedings of 8th World Conference on Earthquake Engineering*, California, USA, 1984.

Hung C.C., Chen Y.-T., Yen C.-H. (2020) “Workability, fibre distribution, and mechanical properties of UHPC with hooked end steel macro-fibres” *Construction and Building Materials,* Vol 260, 2020

Husain M., Eisa S.A., and Hegazy M.M. (2019) “Strengthening of reinforced concrete shear walls with opening using carbon fibre-reinforced polymers”, *International Journal of Advanced Structural Engineering,* Vol. 11, Pages 129-150

ISIS (2006), “Production Certification #1, Specification for Product Certification of Fibre Reinforced Polymers (FRPs) as Internal Reinforcement in Concrete Structures”, ISIS Administrative Centre, University of Manitoba, Manitoba, USA

Jalili A. and Dashti F. (2010) "Nonlinear behaviour of RCSWs using macroscopic and microscopic models", Engineering Structures Vol. 32 (2010), Pages 2959–2968.

Kachlakev, D., Miller, T. and Yim, S. (2001) "Finite element modelling of reinforced concrete structure strengthened with FRP laminates", *Final report No. SPR 316*, USA.

Kendall, K. (2014) "Fibre Reinforced Polymer (FRP) Composite Buildings – Future Opportunities, An NCN Case Review on Exploiting the Benefits of Composites", White Young Green Consulting Ltd., published by National Composite Network, [www.compositeuk.co.uk accessed on 09 September 2014].

Kezmane A., Hamizi M., Boukais S. and Eddine N.H. (2012) "Numerical simulation of RC shear wall strengthened by external bonding of a composite material", *15th International Conference on Experimental Mechanics*, Porto, Portugal, 22-27 July 2012.

Kobayashi, K. (2005) "Innovative Application of FRPs for Seismic Strengthening of RC Shear Wall", Grant-in-Aid for Scientific Research of JSPS, [www.quakewrap.com, accessed 15 May 2014].

Krawinkler, H. (2009) "Loading histories for cyclic tests in support of performance assessment of structural components", *Proceeding of 3rd International Conference on Advances in Experimental Structural Engineering*, San Francisco, USA, 15-16 October 2009.

Kupfer H., Hilsdorf HK., Rusch H. (1969) "Behavior of concrete under biaxial stress". *ACI Journal*, Vol. 87, Iss. 2. Pages 656–66.

Layssi, H. and Mitchell, D. (2012) "Experiments on Seismic Retrofit and Repair of RCSWs", *Proceedings of 6th International Conference on Composites in Civil Engineering (CICE),* Rome, Italy, 13-15 June 2012.

Lombard, D., Lau, T.D., Humar, L.J. and Cheung S.M. (2000) "Seismic Strengthening and Repair of RCSWs", 12th *World Conference on Earthquake Engineering*, Auckland, New Zealand.

Nguyen, L.K., Brun, M., Limam, A. and Ferrier, E. and Michel, L. (2014) "Pushover Experiment And Numerical Analyses on CFRP-Retrofit Concrete Shear Walls With Different Aspect Ratios", *Composite Structures*, Vol. 113, Pages 403-418.

Logan L.D. (2015) "A first course in the Finite element Method", Sixth Edition, Cengage Learning, USA.

MacGregor, G.J. and James K.W. (2005) "Reinforced Concrete: Mechanics and Design". 4th edn, Pearson Education.

MacRae G. (2014) "Lateral Load Resisting Systems Presentation", IITGN Short Course, [www.iitgn.ac.in accessed on 07 August 2014].

MagmaTech (2019) "RockBar Brochure", MagmaTech, 110 Gloucester Avenue, London, UK,

Manalo, A., Benmokrane, B., and Park, K.T., and Lutze, D. (2014) "Recent developments on FRP bars as internal reinforcement in concrete structures", *Concrete in Australia*, Vol. 40, Iss. 2, Pages 46-56. ISSN 1440-656X

Matthys, S. and Triantafillou, T. (2013) "Fibre-reinforced Polymer Reinforcement Enter FIB Model Code 2010", Technical Paper, *Structural Concrete,* Vol. 14 (2013), No. 4, Pages 335-341.

McCalpin J. P. "Earthquake Magnitude Scales" [available at www.booksite.elsevier.com accessed on 31 July 2014].

Mesh Methods – Module 2 (2019) "Introduction to Ansys Meshing", *Release 2019 R2*, Ansys Learning Hub 2019 [https://www.ansys.com/services/learning-hub, accessed on March 2020].

Mesh Quality and Advance Topics – Module 5 (2019) "Introduction to Ansys Meshing", *Release 2019 R2*, Ansys Learning Hub 2019 [https://www.ansys.com/services/learning-hub, accessed on March 2020].

Miao W.Z., Lu Z.X., Jiang J. J. and Ye P. L. (2006) "Finite element analysis on lightweight rienforced concrete shear walls with different web reinforcement", Computational methods in engineering and science, EPMESC X, Aug. 21-23, 2006, Sanya, Hainan, China

Micro Measurement A VPG Brand (2019) "General Purpose Strain Gauges – Linear Pattern", [http://www.vishaypg.com/docs/11241/125uw.pdf accessed on 05 June 2019].

Mohamed, N., Farghaly, A., Benmokrane, B., and Neale, K. (2014) “Numerical simulation of mid-rise concrete shear walls reinforced with GFRP bars subjected to lateral displacement reversals”, *Engineering Structures*, Vol. 73 (2014), Pages 62–71

Mohamed, N., Farghaly, A., Benmokrane, B., and Neale, K. (2014), “Experimental investigation of concrete shear walls reinforced with glass fiber–reinforced bars under lateral cyclic loading” *Journal of Composite for Construction*, Vol. 18, Special Issue.

Mohamed, N., Farghaly, A., Benmokrane, B., and Neale, K. (2013a) “Evaluation of GFRP-Reinforced Shear Walls”, CSCE General Conference, Quebec Canada, May 2013.

Mohamed, N., Farghaly, A., Benmokrane, B., and Neale, K. (2013b) “Strength Reduction Factor of GFRP-Reinforced Shear Walls, *4th Asia-Pacific Conference on FRP in Structures, (APFIS2013)*, Melbourne, Australia, 11-13 December 2013.

Mohamed, N., Farghaly, A., Benmokrane, B., and Neale, K. (2013c) “Flexure and Shear Deformation of GFRP-Reinforced Shear Walls”, Journal of Composite for Construction, Vol 18, Iss 2.

Mohamed, N., Farghaly, A., Benmokrane, B., and Neale, K. (2012) “Cyclic Load Behaviour of GFRP RCSW: Experimental Approach”, *6th International Conference on Advanced Composite Materials in Bridges and Structures*, Ontario Canada, May 2012.

Mohamed, N. (2014) “Strength and drift capacity of GFRP reinforced concrete shear walls” Thesis, Univeristy of Sherbrooke, Canada.

Murty, C.V.R (2005) “Learning Earthquake Design and Construction: 23 Whey are Buildings with Shear Walls Preferred in Seismic Regions”, Resonance publishing, Indian Institute of Technology, Kanpur, India.

Ngo, D. and Scordelis, A.C. (1968) "Finite Element Analysis of Reinforced Concrete Beams", *Journal of the American Concrete Institute*, Vol. 65, No. 9, Pages 152-163.

Nguyen L.K, Brun, M., Limam, A., Ferrier, E. and Michel L. (2014) “Pushover experimental and numerical analyses on CFRP-retrofit concrete shear walls with different aspect ratio”, *Journal of Composite structures,* Vol. 113.

Pande, G. (Ed.), Middleton, J. (Ed.), Kralj, B. (Ed.). (1998). "Computer Methods in Structural Masonry – 4". London: CRC Press, https://doi.org/10.1201/9781482272062.

Paisani, A.M. (2014) "Reinforced Concrete and Masonry Crack Patterns, Structural Assessment and Residual Bearing Capacity", Politechnico Di Milano [http://unina.stidue.net accessed on 23 August 2014].

Pampanin, S. (2012), "Concrete Futures Part 1: PREcast Seismic Structural System", *Video Published by Cement and Concrete Association of New Zealand*, [www.youtube.com accessed on 1 September 2014].

Pilakoutas, K., Neocleous, K. and Guadagnini, M. (2002) "Design philosophy issues of FRP RC structures". *ASCE Journal of Composites for Construction*, Vol. 6, Iss. 3, Pages 154–161.

Priestley, M.J.N. (1991) "Overview of PRESSS Research Program", *PCI Journal*, Vol. 36, No. 4, Pages 50-57.

Pulidindi, K., and Prakash, A. (2017) "Fiber Reinforced Polymer (FRP) Rebars Market Size…", Report ID: GMI698, Global Market Insights [www.gminsights.com accessed on 06 March 2020]

Qazi S., Ferrier E., Michel, L., and Hamelin, P. (2011) "Seismic retrofitting of RC Shear wall with external bonded CFRP", *Proceedings of FRPRCS-10*, Tampa, USA, 2-4 April 2011.

Quimby B.T., "Introduction to Lateral Force Resisting Systems", *Presentation on CE 636 - Design of Multi-Story Structures*, [www.soe.uaa.alaska.edu accessed on 07 August 2014].

Rahman, H., Donchev, T., Petkova, T., Jurgelans, D. and Hopartean G. (2019) "Behaviour of Concrete Shear Wall with BFRP Reinforcement for Concrete Structures", *Proceedings of FRPRCS-14 Conference*, Belfast, UK.

Rai, C.D. (2012) "Ductile Detailing of RC Structures, Short Courses on Seismic Design of RC Structures", Department of Civil Engineering, India Institute of Technology, Kanpur, India [www.iitk.ac.in accessed on 01 June 2014].

Raongjant W. and Jing M. (2008) “Finite element analysis on lightweight reinforced concrete shear walls with different web reinforcement”, Sixth PSU-Engineering Conference, 8-9 May 2008, Songkhla, Thailand.

Roskelley, A.B. (2010) “An Investigation Of The Influence Of Diaphragm Flexibility On Building Design through a Comparison of Forced Vibration Testing And Computational Analysis”, MSc Thesis, California Polytechnic State University, USA.

Sakr A.M., Elkhoriby R.S., Khlifa M.T. and Nagib, T.M. (2017) “Modelling of RC shear walls strengthened by FRP composites” *Structural Engineering and Mechanics*, Vol. 61, No. 3 (2017) 407-417

Sas, G. et al. (2008) “FRP Strengthened RC Panels with Cut-Out Openings”, Proceedings of 4th conference on Challenges for Civil Construction (CCC), Porto, Portugal, 16-18 April, 2008.

Seckin, M. (1981) “Hysteretic behaviour of cast-in-place exterior beam-column-slab subassemblies”, PhD Thesis, Department of Civil Engineering, University of Toronto, ON, Canada, Page 266.

Shah, S. P., Swartz, S. E., and Ouyang, C. (1995) “Fracture Mechanics of Concrete”, John Wiley & Sons, New York, United States.

Sittipunt C. and Wood, S.L. (1993) “Finite Element Analysis of RCSWs”, Civil Engineering Studies, Structural Research Series No. 584, University of Illinois, December 1993.

Sritharan, S. Aaleti, S. and Thomas J.D. (2007) “Seismic Analysis and Design of Precast Concrete Jointed Wall Systems”, *ISU-ERI-Ames Report ERI-07404*, Department of Civil, Construction and Environmental Engineering, Iowa State University, Ames, Iowa, USA.

Sritharan, S. and Thomas D.J. (2004) “An evaluation of Seismic Design Guidelines Proposed for Precast Jointed Wall Systems”, *ISU-ERI-Ames Report ERI-04643*, Department of Civil, Construction and Environmental Engineering, Iowa State University, Ames, Iowa, USA.

Stolarski, T., Nakasone Y., Yoshimoto S. (2006) “Engineering Analysis with Ansys Software”, Elsevier Butterworth-Heinemann, UK.

Tafheem, Z. and Khusru, S. (2013) “Structural behaviour of steel building with concentric and eccentric bracings: A comparative study”, *International Journal of Civil and Structural Engineering*, Vol. 4, No.1.

Takara, S., Yamakawa, T. and Yamashiro K. (2008) “Experimental and analytical investigation of seismic retrofit for RC framed shear walls, *The 14th World Conference on Earthquake Engineering*, October 12-17, Beijing, China.

Tokyo Measuring Instruments Lab. (2019) “Concrete Material Use Strain Gauges”, [https://tml.jp/e/product/strain_gauge/concrete.html#p_list.html, accessed on 03 June 2019].

Tremblay, R., Léger, P. and Tu, J. (2001) “Inelastic seismic response of concrete shear walls considering p-delta effects”, *Canadian Journal of Civil Engineering*, Vol. 28, Iss. 4, Pages 640-655.

Tolsma, V.K. (2010) “Precast Concrete Core in High-rise Buildings: Structural Behaviour of Precast Corner Connections”, Master’s Thesis Final Report, Delft University of Technology.

Vecchio, F.J., and Lai D. (2004) “Crack shear-slip in reinforced concrete elements”. *J Advanced Concrete Technology*, Vo. 2, Iss. 3, Pages 289–300.

Wald, L. (2014) “Science of the Earthquake, United States Geological Survey”. [available at www.earthquake.usgs.gov, accessed on 26 July 2014].

Willam, K. J. and Warnke E. D. (1975) "Constitutive Model for the Triaxial Behaviour of Concrete". *Proceedings of the International Association for Bridge and Structural Engineering*. Vol. 19, Pages 1-30, Bergamo, Italy.

Yee, A.A. (2001) “Social and Environmental Benefits of Precast Concrete Technology”, *PCI Journal*, May-June 2001.

Zreid, I., Kaliske, M. A. (2018) “Gradient Enhanced Plasticity–Damage Microplane Model for Concrete”, *Comput Mech*, Vol. 62, Pages 1239–1257

Appendix

Published and submitted papers

[1] Rahman H, Donchev T, Petkova D., Jurgelans D, Hopartean G. (2019) Behaviour of Concrete Shear Wall with BFRP Reinforcement for Concrete Structures. Proceedings of FRPRCS-14 Conference, Belfast, UK.

[2] Rahman H, Donchev T, Petkova D., (2020) Comparing the Behaviour of the FRP and Steel Reinforced Shear Walls under Cyclic Seismic Loading in Aspect of the Energy Dissipation. International Journal of Civil and Environmental Engineering, Vol. 14, No. 3, Pages 84-89

[3] Rahman H, Donchev T, Petkova D., (2019) Modelling the behaviour of concrete shear walls with BFRP reinforcement. MATEC Web Conferences 289, 09002, Concrete Solutions, Cluj Napoca, Romania, 30 Sep – 2 Oct 2019.

[4] Rahman H, Donchev T, Petkova D., Cassim H., (2020) Performance of concrete shear wall with FRP reinforcement in aspect of Ultimate Capacity and Energy Dissipation, *Engineering Structures Journal*, (Submitted)

[5] Rahman H, Donchev T, Petkova D., (2020) Modelling hysteresis response of BFRP reinforced concrete shear walls, *Engineering Structures Journal*, (Submitted)

[6] Rahman H, Donchev T, Petkova D., (2020) Modelling the behaviour of BFRP reinforced concrete shear walls using pushover analysis, *Journal of Composites for Construction*, (Submitted)